Universidade do Minho
I3Bs - Instituto de Investigação em Biomateriais,
Biodegradáveis e Biomiméticos

Ana Margarida Ribeiro Pacheco

Ureteral Stenting Using Biodegradable Metals

Março de 2026

Ureteral Stenting Using Biodegradable Metals
Ana Margarida Ribeiro Pacheco
UMinho | 2026

REPÚBLICA PORTUGUESA | CIÊNCIA, TECNOLOGIA E ENSINO SUPERIOR
fct Fundação para a Ciência e a Tecnologia
UNIÃO EUROPEIA

Universidade do Minho
I3Bs - Instituto de Investigação em Biomateriais, Biodegradáveis e Biomiméticos

Ana Margarida Ribeiro Pacheco

Ureteral Stenting Using Biodegradable Metals

Tese de Doutoramento
Engenharia de Tecidos, Medicina Regenerativa e Células Estaminais

Trabalho efetuado sob a orientação do
Professor Doutor Rui Luís Gonçalves dos Reis

Março de 2026

DIREITOS DE AUTOR E CONDIÇÕES DE UTILIZAÇÃO DO TRABALHO POR TERCEIROS

Este é um trabalho académico que pode ser utilizado por terceiros desde que respeitadas as regras e boas práticas internacionalmente aceites, no que concerne aos direitos de autor e direitos conexos.
Assim, o presente trabalho pode ser utilizado nos termos previstos na licença abaixo indicada.
Caso o utilizador necessite de permissão para poder fazer um uso do trabalho em condições não previstas no licenciamento indicado, deverá contactar o autor, através do RepositóriUM da Universidade do Minho.



Atribuição-NãoComercial-SemDerivações

CC BY-NC-ND

https://creativecommons.org/licenses/by-nc-nd/4.0/

ACKNOWLEGMENTS

My PhD was a challenging yet rewarding experience that played a significant role in my academic journey and my life. I am deeply grateful to everyone who supported me along the way and made it possible.

First, I would like to acknowledge my supervisor Prof. Rui Reis for the support and mentorship and for giving me the opportunity to pursue my PhD at a prestigious institute with excellent facilities, such as i3Bs, which were essential for this work.

I want to thank my group Alexandre, Ivo, Joana, Kardelen and Eduardo for their encouragement and expertise that helped me in the challenges of this journey and keep me motivated. A especial thank you to Beatriz for her friendship, constant support, and willingness to help whenever I needed, for the great conversations and for being the best travel partner on trips and conferences. I would like to thank the friends I made at 3Bs for the random lunchtime conversations and after-work gatherings, a very important part of my daily work life.

Part of my PhD was done in Sweden and represented one of the best experiences I ever had. I would like to express my sincere gratitude to Prof. Cecilia Persson for the warm welcoming into her group and for the valuable support she provided, which was so important to me. To Dr. Francesco D'Elia for the knowledge shared and guidance that were essential for me to understand and gain autonomy on 3D printing. To the friends I made in Uppsala, Ana, Andrea, Estefania, Lisa and Hanna for the friendship, kindness and always making me feel so good and never feel alone during my time abroad, that truly meant a lot to me.

I would like to acknowledge the *Fundação para a Ciência e Tecnologia* (FCT) for my PhD scholarship.

Finally, to my family, which I would like to thank in Portuguese

Aos meus pais e à minha irmã que me apoiaram desde sempre em todas as minhas decisões e que sem eles nunca teria chegado aqui. Ao Paulo pelo apoio, paciência e compreensão ao longo desta fase, um agradecimento muito especial.

STATEMENT OF INTEGRITY

I hereby declare having conducted this academic work with integrity. I confirm that I have not used plagiarism or any form of undue use of information or falsification of results along the process leading to its elaboration.

I further declare that I have fully acknowledged the Code of Ethical Conduct of the University of Minho.

DECLARATION ON THE USE OF ARTIFICIAL INTELLIGENCE (AI) TOOLS

I hereby declare having acted this academic work with integrity and confirm that I have not resorted to any form of undue use of AI tools, nor to the falsification or omission of information, sources, data, results or processes in any of the stages leading to its elaboration.

I further declare that any use of AI tools was done in a transparent and responsible manner, being duly noted in the work, and that I critically verified the accuracy of the content produced with their support, assuming full responsibility for what I submit.

I further declare that I have fully acknowledged the Code of Ethical Conduct of the University of Minho, as well as the applicable standards of academic integrity and data protection.

"Never get tired of trying, and never think it is impossible to conquer your fault"

Little Woman, Louisa May Alcott

RESUMO

Cateterização ureteral usando metais biodegradáveis

Stents ureterais são dispositivos médicos muito importantes e por isso muito usados para manter o fluxo de urina entre o rim e a bexiga. Apesar da sua importância clínica, os stents tradicionais estão associados com diversos problemas, como incrustação, contaminação bacteriana e a necessidade de uma segunda cirurgia para a sua remoção. De forma a contornar estas limitações, o estudo de materiais biodegradáveis, particularmente metais biodegradáveis, como ligas de magnésio (Mg), para o desenvolvimento de stents ureterais inovadores tem atraído muita atenção.

Esta tese foca-se na investigação da corrosão, biocompatibilidade e propriedades antibacterianas de ligas à base de Mg em condições que mimetizam o trato urinário, com o objetivo de se perceber o seu desempenho como potenciais materiais para stents biodegradáveis. Este estudo incluiu a análise de várias ligas de Mg, como AZ31, Mg-1Zn, Mg-1Y, Mg puro, Mg-4Ag e WE43, produzidas por diferentes técnicas de processamento, extrusão de fios e manufatura aditiva (AM, do inglês *additive manufacturing*). Os testes de corrosão em urina artificial (AUS, do inglês *artificial urine solution*) sob condições estáticas e dinâmicas revelaram que o processo de degradação dessas ligas é influenciado pela sua composição, microestrutura, processo de produção e existência de fluxo. As amostras de Mg-1Y extrudido apresentaram um perfil de degradação uniforme, mas quando o processo de enrolamento foi aplicado após a extrusão, a microestrutura desta liga foi severamente afetada, o que levou ao aparecimento de corrosão localizada. Já as amostras de Mg-1Y produzidas por AM revelaram um perfil de degradação homogéneo em comparação com as amostras extrudidas enroladas, no entanto, as amostras produzidas por AM apresentaram uma degradação muito mais rápida. Os testes de biocompatibilidade demonstraram que as amostras de Mg-1Y produzidas por AM não são tóxicas em concentrações nas quais também apresentam atividade antibacteriana face a um dos uropatogéneos mais comuns, *Escherichia coli*.

Os resultados deste trabalho contribuem para uma melhor perceção do comportamento das ligas de Mg em ambiente urinário, destacando seu potencial para o desenvolvimento de stents ureterais biodegradáveis. Esta tese apresenta uma estratégia detalhada para o desenvolvimento de um stent ureteral metálico biodegradável, e o seu conteúdo é um ponto de partida para a produção de um stent produzido a partir de Mg-1Y.

Palavras-chave: Corrosão, extrusão de fio, ligas de Mg, manufatura aditiva, stent ureteral metálico biodegradável.

ABSTRACT

Ureteral stenting using biodegradable metals

Ureteral stents are essential medical devices widely used in urology to maintain ureteral patency. Despite their clinical utility, traditional stents are associated with adverse effects, including encrustation, bacterial colonization, and the necessity of secondary procedures for removal. To address these limitations, the exploration of biodegradable materials, particularly biodegradable metals, such as magnesium (Mg) alloys, for next-generation ureteral stents has gained significant attention.

This thesis investigates the corrosion behaviour, biocompatibility, and antibacterial properties of Mg-based alloys under simulated urinary tract conditions, with the goal of understanding their behaviour as potential biodegradable stent materials. This investigation included the analysis of various Mg alloys, including AZ31, Mg-1Zn, Mg-1Y, pure Mg, Mg-4Ag, and WE43, fabricated through different processing techniques such as wire extrusion and additive manufacturing (AM). Corrosion studies in artificial urine solutions (AUS) under static and dynamic conditions revealed that the degradation behaviour of these alloys is influenced by their composition, microstructural characteristics, manufacturing processes, and flow conditions. As-extruded Mg-1Y exhibited a uniform corrosion profile but if the coiling process is applied after extrusion, the microstructure of the Mg alloy is severely affected leading to the development of localized corrosion. AM-processed Mg-1Y demonstrated a homogeneous corrosion profile compared with the extruded coiled samples, however, AM-samples degraded much faster than the extruded coiled ones. Biocompatibility assessments demonstrated that AM-processed Mg-1Y is nontoxic at concentrations where it also exhibits antibacterial activity against one of the most common uropathogens, *Escherichia coli*.

The findings of this work contribute to the understanding of Mg alloy behaviour in urinary environments and their potential for application in biodegradable ureteral stents. This thesis provides a detailed pathway for the development of a biodegradable metallic ureteral stent, and these findings are a base for the future development of a Mg1Y based biodegradable ureteral stent.

Keywords: Corrosion, wire extrusion, Mg alloys, additive manufacturing, biodegradable metallic ureteral stent.

TABLE OF CONTENTS

DIREITOS DE AUTOR E CONDIÇÕES DE UTILIZAÇÃO DO TRABALHO POR TERCEIROS ii
ACKNOWLEGMENTS iii
STATEMENT OF INTEGRITY iv
Resumo vi
Cateterização ureteral usando metais biodegradáveis vi
Abstract vii
Ureteral stenting using biodegradable metals vii
TABLE OF CONTENTS viii
List of abbreviations xv
List of figures xix
List of tables xxv
Short Curriculum Vitae xxvi
List of Publications xxvii
Introduction to the thesis format xxxi
SECTION 1 – GENERAL INTRODUCTION xxxi
Chapter I - Ureteral stents: current state and the prospects of a biodegradable metallic ureteral stent xxxi
SECTION 2 – EXPERIMENTAL SECTION xxxi
Chapter II – Materials and methods xxxi
SECTION 3 - EXPERIMENTAL STUDIES xxxi
Chapter III - Understanding the corrosion of Mg alloys in *in vitro* urinary tract conditions: A step forward towards a biodegradable metallic ureteral stent xxxi
Chapter IV - Additively manufactured WE43 for biodegradable urinary devices: exploring the corrosion profile under *in vitro* urinary tract conditions xxxii
Chapter V - *In vitro* corrosion of Mg1Y-based thin walls produced by laser powder bed fusion – influence of continuous and modulated laser modes xxxii
Chapter VI - Towards biodegradable Mg-based ureteral stents: A comprehensive *in vitro* study of two Mg-1Y stent prototypes. xxxii
SECTION 4 - GENERAL CONCLUSIONS xxxii
Chapter VII - General conclusions xxxii
SECTION 1 1

CHAPTER I 2
I-1. Ureteral stents: importance in urology and side effects 3
I-1.1. Stent associated urinary tract infections 3
I-1.2. Stent encrustation 4
I-1.3. Biomaterials for Ureteral Stents: Advances and Future Perspectives 5
I-1.3.1. Polymeric materials 6
I-1.3.2. Metallic materials 9
I-1.3.3. Biodegradable materials 11
I-1.3.4. Conclusions and future perspectives 14
I-2. Development of a Magnesium-based biodegradable ureteral stent 14
I-2.1. Requirements for a ureteral stent 17
I-2.2. Methods for the development of a Mg based ureteral stent 18
I-2.2.1. Additive manufacturing 18
I-2.2.2. Extruded wire, coiled 20
I-3. Conclusions and future perspectives 21
I-4. Bibliography 22
SECTION 2 30
CHAPTER II 31
Overview 32
II-1. Materials 32
II-1.1. Extruded Mg-based wires 32
II-1.2. Additive Manufactured (AM) samples 33
WE43 33
Mg1Y 33
II-2. Methods 33
II-2.1. Wire extrusion and coiling 33
II-2.1.1. Mg wires extrusion 34
II-2.2. Additive manufacturing 34
II-2.2.1. AM samples production 35
II-2.3. *In vitro* simulated urinary tract conditions – dynamic system 36
II-2.3.1. AUS at different pH 37
II-2.4. Samples' microstructure and powder analysis 38

II-2.5. Corrosion layer – chemical characterization 38
II-2.5.1. X-ray photoelectron spectroscopy (XPS) 39
II-2.5.2. Raman spectroscopy 39
II-2.5.3. Fourier transform infrared spectroscopy (FTIR) 40
II-2.5.4. X-ray Diffraction (XRD) 40
II-2.5.5. Scanning electron microscopy - energy dispersive spectroscopy (SEM-EDS) 40
II-2.6. Corrosion 41
II-2.6.1. Profilometry 41
II-2.6.2. Inductively coupled plasma optical emission spectroscopy (ICP-OES) 42
II-2.6.3. Micro-Computed Tomography (Micro-CT) 42
II-2.7. Interaction of Mg-based samples with cells 43
II-2.7.1. Cell lines 43
II-2.7.1.1. L929 43
II-2.7.1.2. G/G cell line 43
II-2.7.2. Cytotoxicity assay 43
II-2.8. Antibacterial activity 45
II-3. Statistical analysis 46
II-4. References 46
SECTION 3 49
CHAPTER III 50
Understanding the corrosion of Mg alloys in *in vitro* urinary tract conditions: A step forward towards a biodegradable metallic ureteral stent. 51
III-1. Introduction 52
III-2. Materials and methods 53
III-2.1. Preparation of samples – wire extrusion 53
III-2.2. Experimental setup 54
III-2.3. Corrosion rate 56
III-2.4. Profilometry 57
III-2.5. X-ray photoelectron spectroscopy (XPS) 57
III-2.6. Raman spectroscopy 58
III-2.7. Scanning electron microscopy - energy dispersive spectroscopy (SEM/EDS) 58
III-2.8. ICP-OES 58

III- 2.9. Cytotoxicity 58
III-2.10. Statistical analysis 59
III-3. Results and discussion 60
III-3.1. Microstructure 60
III-3.2. Corrosion layer – SEM analysis 61
III-3.4. Corrosion layer – Chemical characterization 64
III-3.3.1. XPS 64
III-3.3.2. Raman spectroscopy 67
III-3.4. Corrosion – Corrosion rate 73
III-3.5. Corrosion - Profilometry 78
III-3.6. Corrosion - SEM 81
III-3.7. Corrosion – ICP-OES analysis 84
III-3.8. Cytotoxicity 86
III-4. Conclusion 90
III- References 90
Supplementary information 97
CHAPTER IV 103
Additively manufactured WE43 for biodegradable urinary devices: exploring the corrosion profile under *in vitro* urinary tract conditions. 104
IV-1. Introduction 105
IV-2. Materials and Methods 107
IV-2.1. Mg alloy WE43 powder and sample preparation 107
IV-2.2. Microstructural analysis 108
IV-2.3. Corrosion test set-up 108
IV-2.4. Corrosion layer analysis 110
IV-2.4.1. Scanning electron microscopy - energy dispersive spectroscopy (SEM-EDS) 110
IV-2.4.2. Fourier transform infrared spectroscopy (FTIR) 110
IV-2.4.3. X-ray photoelectron spectroscopy (XPS) 110
IV-2.5. Corrosion rate – mass loss and ion release measurements 110
IV-2.6. Statistical analysis 111
IV-3. Results 111
IV-3.1. Microstructural characterization 112

IV-3.2. Corrosion layer analysis 113
IV-3.3. Corrosion analysis 118
IV-4. Discussion 121
IV-5. Conclusions 125
IV-6. Bibliography 125
CHAPTER V 130
In vitro corrosion of Mg1Y-based thin walls produced by laser powder bed fusion – influence of continuous and modulated laser modes. 131
V-1. Introduction 132
V-2. Materials and methods 134
V-2.1. Thin walls production 134
V-2.1.1. Powder 134
V-2.1.2. Thin walls printing and sample preparation 134
V-2.1.3. Samples's characterization SEM/EDS 135
V-2.1.4. Profilometry 136
V-2.2. Samples' corrosion 136
V-2.2.1. Fourier Transform Infrared Spectroscopy (FTIR) 136
V-2.2.2. Raman 137
V-2.2.3. Corrosion 137
V-3. Results 137
V-3.1. Mg1Y powder characterization 137
V-3.2. Thin walls characterization 139
V-3.3. Characterization of the sample's corrosion in artificial urine solution 143
V-4. Discussion 147
V-5. Conclusion 150
V-5. Bibliography 150
CHAPTER VI 153
Towards biodegradable Mg-based ureteral stents: a comprehensive in vitro study of two Mg-1Y stent prototypes 154
VI-1. Introduction 155
VI-2. Materials and methods 157
VI-2.1. Samples preparation 157

VI-2.1.1. Additive manufactured samples 157
VI-2.1.2. Extruded coiled wires 158
VI-2.2. Microstructure analysis 159
VI-2.3. Surface characterization - Profilometry 159
VI-2.4. *In vitro* dynamic conditions 160
VI-2.5. Corrosion 160
VI-2.5.1. SEM/EDS 161
VI-2.5.2. Raman spectroscopy 161
VI-2.5.3. XRD 161
VI-2.5.4. Fourier transform infrared spectroscopy (FTIR) 161
VI-2.6. Corrosion 161
VI-2.6.1. Micro-computed tomography (Micro-CT) 162
VI-2.6.2. Inductively Coupled Plasma - Optical Emission Spectroscopy (ICP-OES) 162
VI-2.7. Cytotoxicity 162
VI-2.8. Antibacterial activity 164
VI-2.9. Statistical analysis 164
VI-3. Results 165
VI-3.1. Microstructure characterization 165
VI-3.2. Corrosion layer characterization 166
VI-3.3. Corrosion characterization 171
VI-3.4. Cytotoxicity 175
VI-3.5. Antibacterial activity 178
VI-4. Discussion 178
VI-4.1. Corrosion properties 178
VI-4.2. Cytotoxicity evaluation 181
VI-4.3. Antibacterial properties 183
VI-4.4. Limitations 185
VI-5. Conclusion 185
VI-6. Bibliography 186
Supplementary information 191
SECTION 4 194
CHAPTER VII 195

General conclusions and future perspectives 196
VII-1. General conclusions 196
Future perspectives 198

List of abbreviations

2D - Two dimensions

3D - Three dimensions

A

A - Area of the specimen in cm^2

Å - Angstrom

AAS - Atomic absorption spectrometer

Ag - Silver

Al - Aluminum

AM - Additive manufacturing

ASTM - American society for testing and materials

ATCC - American Type Culture Collection

AUS - Artificial urine solution

AZ31 - Magnesium alloy composed of aluminum, zinc and manganese

B

BMUS - Biodegradable metallic ureteral stent

BUS - Biodegradable ureteral stents

C

C - Carbon

C^- - Negative control

C^+ - Positive control

$C_4H_7N_3O$ - Creatinine

Ca - Calcium

ca - From Latin circa, means approximately

CAD - Computer-aided design

CE - Conformité Européenne

CFU - Cloning forming units

CH_4N_2O - Urea

Cl^- - Chloride ion

cm - Centimeters

CO_2 - Carbon dioxide

CO_3 - Carbonate

Cu - Copper

CW - Continuous wave

D

D - Density in g/cm^3

d - Layer thickness

d50 - Refers to 50 percent of powder particles size distribution

DMEM - Dulbecco's modified eagle medium

DMSO - Dimethyl sulfoxide

DNA - Deoxyribonucleic Acid

E

EC - Extruded coiled

ED - Energy density

EDS - Energy dispersive spectroscopy

e.g. - From Latin exempli gratia, means "for example"

eV - Electron volt

F

FBS - Fetal bovine serum

Fe - Iron

FLTt - Total height of the surface profile

Fr - French

FTIR - Fourier transform infrared spectroscopy

G

g - Grams

H

h - Hours

H - Hatch distance

h - Planck's constant

H^+ - Hydrogen ion

HCl - Hydrochloric acid

HPO_4^{2-} - Hydrogen phosphate ion

Hz - Hertz

I

i.e. - From the Latin id est, stands for “that is”

ICP-OES - Inductively coupled plasma optical emission spectrometry

ISO - International Organization for Standardization

J

J - Joule

K

K - Constant for corrosion rate formula that depends on the units used

K - Potassium

KHz - Kilohertz

KH_2PO_4 - Potassium dihydrogen orthophosphate

kV - Kilovolts

L

L - Liter

Lc - Correlation length

LOM - Light optical microscopy

M

mA - Milliampere

Mg - Magnesium

$Mg(OH)_2$ - Magnesium hydroxide

Mg^{2+} - Magnesium ion

$Mg_3(PO_4)_2$ - Magnesium phosphate

$MgCO_3$ - Magnesium carbonate

MgO - Magnesium oxide

$Mg(PO_3OH)\cdot 3H_2O$ - Newberyite

MHz - Megahertz

Micro-CT - Micro-computed tomography

min - Minute

ml - Mililiter

mm - Millimeter

MN - Meganewtons

MTS - 3-(4,5-dimethylthiazol-2-yl)-5-(3-carboxymethoxyphenyl)-2-(4-sulfophenyl)-2H-tetrazolium, inner salt

MW - Modulated wave

mW - Milliwatts

N

N - Nitrogen

Na - Sodium

Na_2HPO_4 - Disodium hydrogen orthophosphate anhydrous

Na_2SO_3 - Sodium sulfite

NaCl - Sodium chloride

NaN_3 - Sodium azide

NaOH - Sodium hydroxide

ng - Nanograms

NH^{3+} - Ammonium ion

NH_4Cl - Ammonium chloride

$NH_4MgPO_4\cdot 6H_2O$ - Struvite

Ni - Nickel

Nital - Solution composed of 2% nitric acid in ethanol

nm - Nanometer

nM - nanomolar

O

O - Oxygen

O_2 - Molecular oxygen

OD - Optical density

OH^- - Hydroxide ion

OM - Optical microscopy

OPS - Oxide polishing suspension

P

P - Laser power

P - Phosphorus

PBF-LB - Powder bed fusion laser beam

PBS - Phosphate-buffered saline

PCL - Polycaprolactone

PDLLA - poly-dl-lactic acid

PGA - Glycomer-631™and polyglycolic acid

pH - Potential of hydrogen

PI - Propidium iodide

PLA - Poly-l,d-lactide

PLGA - poly-l-lactide-co-glycolide

PLLA - poly-l-lactic acid

PO_4^{3-} - Phosphate ion

ppm - Parts per million

PTFE - polytetrafluoroethylene

R

REE - Rare-earth elements

rpm - Revolutions per minute

S

S - Sulfur

s - Second

S10z - 10-point height

Sa - Arithmetic average roughness

SBF - Simulated body fluid

SD - Standard deviation

Sdq - Root mean square gradient

Sdr - Developed interfacial area ratio

SEM - Scanning electron microscopy

Si - Silicon

SiC - Silicon carbide

Sku - Kurtosis

Sp - Peak height

Sq - Root mean square roughness

SR-PLA96 - Self reinforced poly-l,d-lactide 96

Ssk - Skewness

Sv - Minimum surface depth

Sz - Total height of the surface profile

T

T - Time of exposure in hours

T004 - Tube with 0.04 mm hatch distance

T005 - Tube with 0.05 mm hatch distance

T006 - Tube with 0.06 mm hatch distance

TSB - Tryptic soy broth

U

UV - Ultraviolet

V

v - Scanning speed

W

W - Mass loss in grams

W - Watts

W005 - Wire with 0.05 mm hatch distance

W006 - Wire with 0.06 mm hatch distance

WE43 - Magnesium alloy composed of yttrium, neodymium and zirconium

X

XPS - X-ray photoelectron spectroscopy

XRD - X-ray diffraction

Y

Y - Yttrium

y - Year

YCl_3 - Yttrium chloride

Y_2O_3 - Yttrium oxide

Z

ZJ31 - Magnesium alloy composed of zinc, zirconium and manganese

ZK60 - Magnesium alloy composed of zinc and zirconium

Zn - Zinc

Zr - Zirconium

Symbols

β - Beta

υ - Is the frequency of the photon

º - Degrees

ºC - Degrees Celsius

% - Percentage

µ - micro

µA - Microampere

µg - Micrograms

µm - Micrometer

µs - Microseconds

LIST OF FIGURES

Figure I 1 Different materials used for ureteral stents development, including some examples of each class, the main advantages and disadvantages and how the different materials' properties complement each other. 8

Figure I 2 Printing parameters on PBF-LB. Scheme of the printing process and respective printing parameters in PBF-LB. 19

Figure I 3 Wires extrusion and coiling process. Scheme of the wire extrusion and wire coiling processes. 21

Figure II 1 Dynamic experimental setup. a) Photo, b) schematic. 1. Artificial urine reservoir; 2. Peristaltic pumps; 3. vessel with the tubes containing each sample; 4. Flasks collecting the artificial urine solution (AUS) after passing through the samples; 5. Thermostat to maintain 37 ºC in the vessel containing the samples. 37

Figure III 1 Dynamic experimental setup. a) Photo, b) schematic. 1. Artificial urine reservoir; 2. Peristaltic pumps; 3. vessel with the tubes containing each sample; 4. Flasks collecting the artificial urine solution (AUS) after passing through the samples; 5. Thermostat to maintain 37 ºC in the vessel containing the samples. 56

Figure III 2 Microstructure of the five extruded alloys studied in this work, obtained by optical microscopy, and respective grain size. 61

Figure III 3 Representative SEM images of the sample's corrosion layers after 1, 2, and 4 weeks of incubation with artificial urine solution (AUS), pH 6.89, in static conditions. Condition before removing the corrosion products with chromic acid. 63

Figure III 4 Representative SEM images of the sample's corrosion layers after 1, 2 and 4 weeks incubation with artificial urine solution (AUS), pH 6.89, in dynamic conditions. Condition before removing the corrosion products with chromic acid. 64

Figure III 5 Survey spectrum of all the sample's corrosion layers obtained by X-ray inducted photoelectron spectroscopy (XPS) after 4 weeks incubation in artificial urine solution (AUS), pH 6.89, in static conditions. 66

Figure III 6 Raman spectra obtained for the corrosion layers of all the samples after 4 weeks incubation with artificial urine solution (AUS), pH 6.89, in dynamic conditions. Pure Mg's corrosion layer

presented different Raman spectra for different sites on the surface and 3 representative Raman spectra are presented for this sample, Pure Mg a, Pure Mg b, and Pure Mg c. 71
Figure III 7 Representation of all the Raman spectra obtained for the corrosion layers of all the samples after incubation with artificial urine solution (AUS), pH 6.89, for 4 weeks in static conditions. 72
Figure III 8 Schematic illustration representing the reactions of Mg alloys when immersed in AUS... 72
Figure III 9 Corrosion rate (mm/y) of all the samples at different time points in static conditions representing the corrosion rate difference along the time (a), in static conditions representing the corrosion rate differences of the different alloys (b), in dynamic conditions representing the corrosion rate variation along the time (c) and in dynamic conditions representing the corrosion rate differences of the different alloys. A comparison between the static and dynamic conditions is also represented (e). The artificial urine solution (AUS) used had a pH of 6.89. 77
Figure III 10 pH evolution over 48h exposure to Mg alloys in a) acidic, b) basic and c) alkaline conditions. 78
Figure III 11 Optical images of all the metals, in triplicate, after 4 weeks immersion in artificial urine solution (AUS), pH 6.89, in static conditions. Corrosion products were removed by chromic acid before taking these images. 79
Figure III 12 3D optical images of all the samples (surface area of 1x2 mm^2 and 0.5x2 mm^2) after 4 weeks immersion in artificial urine solution (AUS), pH 6.89, in static conditions. The field of view of each optical image and the profilometric map is 0.5x2 mm^2. 80
Figure III 13 SEM images of the corroded samples after removing the corrosion layer at 1, 2 and 4 weeks incubation with artificial urine solution (AUS), pH 6.89, in static conditions..... 82
Figure III 14 SEM images of the corroded samples after removing the corrosion layer at 1, 2, and 4 weeks of incubation with artificial urine solution (AUS), pH 6.89, in dynamic conditions. 84
Figure III 15 The concentration of the different metals (mg/L) in artificial urine solution (AUS), pH 6.89, on different days of the experiment at both static and dynamic conditions for all the alloys. 86
Figure III 16 Cytotoxicity, measured by the metabolic activity of the living cells, of L929 cells after 24h exposure to Mg alloys' extracts. C- represents the negative control, 25% DMSO, C+ represents the positive control, cells with cell culture media, CTR_Nit is the condition of exposure to nitinol extract and E100, E50, E25 and E12.5 represent the different concentrations of samples' extracts exposed to cells, 100%, 50%, 25% and 12.5%, respectively. 88

Figure III 17 Microscopic images of L929 cells after exposed to Mg alloys extracts for 24h, at different concentrations, obtained by Live/Dead assay. The controls, C+ and C- as well as a reference material, Nitinol (CTR_Nit) are also represented. 89

Figure III S 1 High resolution XPS spectra of the corrosion layer of AZ31 after 4 weeks in static conditions with artificial urine solution (AUS). 98
Figure III S 2 High resolution XPS spectra of the corrosion layer of Mg-1Zn after 4 weeks in static conditions with artificial urine solution (AUS). 99
Figure III S 3 High resolution XPS spectra of the corrosion layer of Mg1Y after 4 weeks in static conditions with artificial urine solution (AUS). 100
Figure III S 4 High resolution XPS spectra of the corrosion layer of Pure Mg after 4 weeks in static conditions with artificial urine solution (AUS). 101
Figure III S 5 High resolution XPS spectra of the corrosion layer of Mg4Ag after 4 weeks in static conditions with artificial urine solution (AUS). 102

Figure IV 1 Schematic representation of the dynamic system used in this study. 109
Figure IV 2 As printed WE43-based thin structures, a) wires and b) thin-walled tubes. 112
Figure IV 3 LOM images of the samples in the planes perpendicular and parallel to the building direction, after polishing and etching with Nital. a), b) and c) refer to the tubes, printed using hatch distances of 0.04, 0.05 and 0.06 mm, respectively, and d) and e) refer to the wires, printed using a hatch distance of 0.05 and 0.06 mm, respectively. 113
Figure IV 4 Optical images of the samples' corrosion layer development over time. 114
Figure IV 5 SEM images of the samples' corrosion layer development over time. 115
Figure IV 6 FTIR spectra of the corrosion layers of all the samples tested. 116
Figure IV 7 XPS spectra obtained for the corrosion layers formed on the samples a) T004, b) T005, c) T006, d) W005, e) W006 and f) all the corrosion layer's spectra represented, after 24h in AUS. 117
Figure IV 8 XPS high resolution spectra of O1s, Y3d, P2p, Mg2s and Mg2p for all the samples' corrosion layers after 24h in dynamic conditions with AUS. 118
Figure IV 9 SEM images of the sample's surface evolution over time, after removing the corrosion layer with chromium oxide-based solution. 119
Figure IV 10 Corrosion rate (mm/y) of the WE43-based tubes and wires. 120

Figure IV 11 Concentration of the metallic ions, Mg in a), Y in b), Nd in c) and Zr in d) in AUS, released along the time by each sample..... 121

Figure V 1 Scheme of the building plate organization of the parameter's optimization phase..... 135
Figure V 2 XPS and SEM/EDS analysis of the Mg1Y powder used for printing. 138
Figure V 3 SEM of the thin walls, parallel and perpendicular to the building direction, built with continuous and modulated laser modes. 140
Figure V 4 SEM of the thin walls, parallel to the building direction (XZ plan), built with continuous and modulated laser modes. The width (µm) of four representative layers in each image is presented. ... 141
Figure V 5 Profilometry of the surface of the thin walls built with continuous and modulated laser modes. 142
Figure V 6 Profilometry values for the surface of the thin walls built with continuous and modulated laser modes. 143
Figure V 7 Photos of the thin walls produced by continuous and modulated laser after 1, 2, 3 and 7 days immersion in artificial urine solution. 144
Figure V 8 FTIR spectra of the corrosion layer obtained for both continuous (red) laser- and modulated (black) laser- based thin walls after 7 days incubation in artificial urine under static conditions. 145
Figure V 9 Raman spectra of the sample's surface, continuous laser- based (red) and modulated laser-based (grey), after 7 days incubation in artificial urine in static conditions. 146
Figure V 10 Corrosion layer percentage (a) and weight loss (b) along the time. 147

Figure VI 1 Macroscopic image of AM-mesh, a), LOM b) and SEM c) of AM-mesh sample, parallel to the building direction. Macroscopic image of Extr-coiled tubes, d), and longitudinal cross section of the extruded wires before, e), and after, f), coiling. 166
Figure VI 2 3D images of a) the AM-meshed, and b) Extr-coiled samples before immersion in AUS. 167
Figure VI 3 SEM of the AM-meshes' corrosion layer after incubation in the dynamic system with constant flow of artificial urine at different time points. 168
Figure VI 4 SEM of the coiled tubes' corrosion layer after incubation in the dynamic system with constant flow of artificial urine at different time points 169
Figure VI 5 Chemical analysis of the corrosion layer developed on the samples surface after 7 days incubation in artificial urine in dynamic conditions. a) Raman, b) XRD, c) FTIR and d) EDS analysis. For a), b) and c), grey represents the AM-meshes and blue the Ext..... 170

Figure VI 6 Sample's corrosion analysis after being in contact with AUS for 7 days in dynamic conditions. a) corrosion layer accumulated on the samples, in percentage, b) SEM images of the AM-meshes' corroded surfaces over time. The circles highlight material disintegration spots on AM-meshes, c) Relative weight of metallic stent (% of initial) after corrosion exposure and removing the corrosion products and d) SEM images of the Extr-coil samples' corroded surface over time. The rectangles highlight the shallow cavities and the arrows the spots of small corrosion pits accumulation. 171
Figure VI 7 Concentrations of Mg and Y uncovered by ICP-OES in the artificial urine samples collected over time for AM-meshed tubes and the extruded coiled tubes. 173
Figure VI 8 MicroCT scans of the AM-mesh and Extr-coil samples and corresponding remaining sample volume before the experiment and after incubation in dynamic conditions in AUS for defined time points (corrosion layer removed by chromic acid etching). 174
Figure VI 9 Cytotoxicity of AM_Mg-1Y_t, AM_WE43_t and e_Mg-1Y against L929 and G/G cell lines. a) shows the results of the direct extract and with a samples exposed surface area/ media volume ratio of 27.5 mm^2/ml and b) the direct (E100) and 50% (E50) extracts for a samples surface area/ volume ratio of 300 mm^2/ml. For this study the AM samples were in the form of tubes and the extruded ones in the form of extruded wire (not coiled). The standard deviation is presented. 175
Figure VI 10 pH variation in the cell culture media used when exposed to the tested stent prototypes (AM_Mg-1Y_t, e_Mg-1Y and AM-WE43_t) with two exposed surface area/volume ratios, 27.5 mm^2/ml and 300 mm^2/ml and antibacterial activity of AM_Mg-1Y_t against *E. coli* and *S. aureus*. 177

Figure VI S 1 EDS analysis on the SEM image of the AM-mesh cross section, highlighting the composition of the brighter and darker spots of the sample. 191
Figure VI S 2 Cell viability assay (MTS) for L929 and G/G cell lines after 24h contact with metal extracts (AM_Mg-1Y_t, e_Mg-1Y and AM_WE43_t), for 24h at a exposed surface area/volume ratio of 27.5 mm^2/ml, a), b) and c) and 300 mm^2/ml, d), e) and f). E100 represents the direct extract (100%) and E75 to E10 the different dilutions of the original extract (75% to 10%). CTR_Nit is the Nitinol control, extract with 100% Nitinol. C+ represents the positive control, cells with cell culture media only and C- the negative control, cells with 25% DMSO. 192
Figure VI S 3 Cell viability assay (Live/Dead) for L929 and G/G cell lines after 24h contact with metal extracts (AM_Mg-1Y_t, e_Mg-1Y and AM_WE43_t), for 24h at a exposed surface area/volume ratio of 300 mm^2/ml. The cels were exposed to direct extract (E100) and several dilutions of the main extract, 50% (E50), 25% (E25) and 12.5% (E12.5). A positive control (C+), without extract and a nevative control

(C-), with DMSO were used as well. Nitinol was used as reference material, only with the direct extract. 193

LIST OF TABLES

Table I 1 Polymeric ureteral stents available on the market. 9

Table I 2 Metallic ureteral stents available on the market. 11

Table I 3 Example of successful biodegradable ureteral stents. 14

Table III 1 Chemical composition, in wt%, of the extruded Mg-based wires used in this work. 54

Table III 2 Chemical composition of the artificial urine solution (AUS) used in this study and respective concentration in g/L and mol/L, and the AUS pH in acidic, neutral and alkaline conditions. 56

Table III 3 Binding energies (eV) and atomic concentrations (%at) associated with the peaks detected in the XPS high-resolution spectra of O1s, C1s, and P2p obtained for all the alloys after 4 weeks immersed in artificial urine solution (AUS), pH 6.89, in static conditions. 66

Table III 4 Chemical elements (%wt) detected on the sample's corrosion layers through EDS analysis after 4 weeks in contact with artificial urine solution (AUS), pH 6.89. 67

Table IV 1 Chemical composition of the WE43 powder, as provided by the manufacturer (NMD, GmbH, Heemsen, Germany). 108

Table IV 2 Group designations and the process parameters used to produce samples from WE43 powder in an EOS M100 PBF-LB machine (EOS GmbH, Krailling, Germany). 108

Table IV 3 Chemical composition of the corrosion layer determined by EDS. 115

Table V 1 Chemical composition of the artificial urine solution (AUS) used. 136

Table V 2 Profilometry values for the surface of the thin walls built with continuous and modulated laser modes. 142

Table VI 1 Composition of the AUS used in this study. 160

SHORT CURRICULUM VITAE

Ana Margarida Ribeiro Pacheco was born in May 4th 1994 in the city of Guimarães, Portugal. She was raised and lived in Mondim de Basto, Vila Real, Portugal. In 2015 she completed her graduation in Biochemistry by the University of Minho in the city of Braga, Portugal, and in 2017 her master's degree in applied Biochemistry, in the field of Biomedicine at the same university. Her master thesis was focused on improving the stability of a cold-adapted enzyme by genetic engineering. This project was developed in *Centro de Biologia Molecular e Ambiental* (CBMA) in the School of Sciences of the University of Minho. In 2018 she was granted with a one-year research fellowship in i3Bs Research Group from the University of Minho. During that time, she started working with urinary devices, namely, improving the antibacterial properties of silicone-based ureteral stents through curcumin impregnation by supercritical carbon dioxide (sCO_2) and the development of biodegradable haemostatic devices for minimally invasive nephrostomy. In 2019 she was awarded with an individual FCT scholarship (SFRH/BD/145285/2019) and she engaged the Doctoral Program of Tissue Engineering, Regenerative Medicine and Stem Cells (TERM&SC) at the same institute. Margarida's PhD work was in urinary devices but in a more innovative approach, which was based on biodegradable metals. The main objective of her PhD was the investigation of biodegradable metals for the development of a biodegradable metallic ureteral stent (BMUS). This work was done under the supervision of Prof. Rui L. Reis, Prof. Estêvão Lima and Dr. Alexandre Barros. This PhD journey included a 9-month period visit in Uppsala University (UU), Sweden, with the supervision of Prof. Cecilia Persson. The collaborative work was focused on the additive manufacturing (AM) of ureteral stent prototypes and respective structural characterization.

Margarida's PhD resulted in 4 publications as first author in international referee journals (2 published and 1 submitted and one finished, ready to submit), one book chapter as first author, a publication as shared first author and three publications as co-author. The work also resulted in 7 oral and 3 poster communications in international conferences.

LIST OF PUBLICATIONS

The work performed during the PhD period resulted in the publications listed below:

Papers in International Refereed Journals

Margarida Pacheco, Francesco D'Elia, Maria Nienaber, Jan Bohlen, Zahra Jafari, Sviatlana V. Lamaka, Estêvão Lima, Alexandre Barros, Rui L. Reis, Cecilia Persson, Towards biodegradable Mg-based ureteral stents: a comprehensive *in vitro* study of two Mg-1Y stent prototypes. *Submitted.*

Margarida Pacheco, Carl-Johan Hassila, Francesco D'Elia, Estêvão Lima, Alexandre Barros, Cecilia Persson, Rui L. Reis. *In vitro* corrosion of Mg1Y-based thin walls produced by laser powder bed fusion – influence of continuous and modulated laser modes. *Manuscript under revision*

Margarida Pacheco, Francesco D'Elia, Hanna Nilsson-Åhman, Estêvão Lima, Alexandre Barros, Cecilia Persson, Rui L. Reis. Additively manufactured WE43 for biodegradable urinary devices: exploring the corrosion profile under *in vitro* urinary tract conditions. Applied Materials Today. 2025. Dec. 47 102975.

Margarida Pacheco, Ivo M. Aroso, Joana M. Silva, Sviatlana V. Lamaka, Jan Bohlen, Maria Nienaber, Dietmar Letzig, Estêvão Lima, Alexandre A. Barros, Rui L. Reis. Understanding the corrosion of Mg alloys in *in vitro* urinary tract conditions: A step forward towards a biodegradable metallic ureteral stent. Journal of Magnesium and Alloys. 2023 Nov 1;11(11):4301-24.

Inês V. Gomes, **Margarida Pacheco**, Maria Nienaber, Sara C. Neves, Di Mei, Alexandre A. Barros, Rui L. Reis, José L. Alves, Helder Puga. Shielding AZ91D-1% Ca from corrosion through ultrasound melt treatment: A study for stent design. Journal of Magnesium and Alloys. 2023 Aug 1;11(8):2901-15.

Di Mei, Cheng Wang, Maria Nienaber, **Margarida Pacheco**, Alexandre A. Barros, Sara Neves, Rui L. Reis, Shijie Zhu, Jan Bohlen, Dietmar Letzig, Shaokang Guan, Mikhail L. Zheludkevich, Sviatlana V. Lamaka. Corrosion behavior of Mg wires for ureteral stent in artificial urine solution. Corrosion Science. 2021 Aug 15;189:109567.

Review Papers

Beatriz Domingues, **Margarida Pacheco**, Julia E. de la Cruz, Irene Carmagnola, Rita Teixeira-Santos, Marco Laurenti, Fusun Can, Klemen Bohinc, Fabíola Moutinho, Joana M. Silva, Ivo M. Aroso, Estêvão Lima, Rui L. Reis, Gianluca Ciardelli, Valentina Cauda, Filipe J. Mergulhão, Federico S. Gálvez. Future

directions for ureteral stent technology: from bench to the market. Advanced Therapeutics. 2022 Jan;5(1):2100158.

Book chapters

Margarida Pacheco*, Beatriz Domingues*, Estêvão Lima, Rui L. Reis, Alexandre Barros. Hydrogels as stents. In Hydrogels for Tissue Engineering and Regenerative Medicine. 2024 Jan 1 (pp. 467-482). Academic Press.

*These authors contributed equally

Margarida Pacheco, Joana M. Silva, Ivo M. Aroso, Estêvão Lima, Alexandre A. Barros, Rui L. Reis. Biomaterials for Ureteral Stents: Advances and Future Perspectives. In Urinary Stents: Current State and Future Perspectives 2022 Aug 21 (pp. 197-208). Cham: Springer International Publishing.

Communications in International Conferences

Margarida Pacheco, Francesco D'Elia, Maria Nienaber, Jan Bohlen, Estêvão Lima, Alexandre Barros, Rui L. Reis, Cecilia Persson. "Additive manufacturing of biodegradable Mg1%Y-based ureteral stents: Understanding the corrosion under simulated urinary tract environment". 15th International Symposium on Biodegradable Metals. Cetraro, Italy. 2023.

Margarida Pacheco, Ivo M. Aroso, Joana M. Silva, Sviatlana V. Lamaka, Jan Bohlen, Maria Nienaber, Dietmar Letzig, Estêvão Lima, Alexandre A. Barros, Rui L. Reis. "Biodegradable metals for ureteral stents: understanding the degradation profile under simulated urinary tract environment". 39th World Congress of Endourology and Uro-technology. San Diego, United States. 2022.

Margarida Pacheco, Ivo M. Aroso, Joana M. Silva, Sviatlana V. Lamaka, Jan Bohlen, Maria Nienaber, Dietmar Letzig, Estêvão Lima, Alexandre A. Barros, Rui L. Reis. "Towards the development of a biodegradable metallic ureteral stent: Characterizing the corrosion and encrustation tendency of Mg alloys under in vitro urinary tract conditions". 14th International Symposium on Biodegradable Metals. Alicante, Spain. 2022.

Margarida Pacheco, Ivo M. Aroso, Joana M. Silva, Sviatlana V. Lamaka, Jan Bohlen, Maria Nienaber, Dietmar Letzig, Estêvão Lima, Alexandre A. Barros, Rui L. Reis. Inside the corrosion and encrustation trend of biodegradable Mg alloys: towards the development of a biodegradable metallic ureteral stent.

European Society for Bioresorbable Implants Danube Private University for Dentistryand Medicine. Krems, Austria. 2022.

Margarida Pacheco, Ivo M. Aroso, Joana M. Silva, Estêvão Lima, Alexandre A. Barros, Rui L. Reis. "Understanding the behavior of biodegradable Mg alloys under *in vivo* urinary tract conditions". Workshop Latest Advances in Urinary Stents. Multidisciplinary approach. ENIUS - European Network of Multidisciplinary Research to Improve the Urinary Stents. Istanbul, Turkey. 2022.

Margarida Pacheco, Ivo M. Aroso, Joana M. Silva, Estêvão Lima, Alexandre A. Barros, Rui L. Reis. "Insights on the degradation and encrustation propensity of biodegradable metals in urinary tract environment". II Virtual ENIUS Workshop. Next steps for Urinary Stents Research ENIUS - European Network of Multidisciplinary Research to Improve the Urinary Stents. Online conference. 2021.

Margarida Pacheco, Ivo M. Aroso, Joana M. Silva, Estêvão Lima, Alexandre A. Barros, Rui L. Reis. Biodegradable metals for ureteral stents: understanding the degradation profile under simulated urinary tract environment. Virtual ENIUS Workshop. Latest advances in Urinary Stents Biomaterials, Technology and Coatings. Online conference. 2021. **Best Research Oral Presentation Award**

Poster Presentations

Margarida Pacheco; Sviatlana V. Lamaka,; Mikhail Zheludkevich,; Jan Bohlen, Maria Nienaber, Dietmar Letzig, Carl-Johan Hassila, Francesco D'Elia, Cecilia Persson, Estêvão Lima, Alexandre A. Barros, Rui L. Reis. "Suitability of additive manufacturing for biodegradable urinary devices: an *in vitro* study". Setting-up biobanks and regenerative medicine strategies to boost research in cardiovascular, musculoskeletal, neurological, oncological, immunological and infectious diseases" Guimarães, Portugal, 2023.

Margarida Pacheco, Ivo M. Aroso, Joana M. Silva, Estêvão Lima, Alexandre A. Barros, Rui L. Reis. "Insights on the corrosion and encrustation of biodegradable Mg alloys in urinary tract environment". Paper presented in *Final FoReCaST Conference*, 2021.

Margarida Pacheco, Ivo M. Aroso, Joana M. Silva, Estêvão Lima, Alexandre A. Barros, Rui L. Reis. "Ureteral stenting using biodegradable metals". Paper presented in *TERM-STEM* 2019.

Awarded Grants

4-year Fundação para a Ciência e a Tecnologia (FCT) PhD Scholarship (SFRH/BD/145285/2019)

ENIUS Short-Term Scientific Mission (STSM) grant - CA16217 – European Network of multidisciplinary research to improve the urinary stents.

INTRODUCTION TO THE THESIS FORMAT

This thesis is structured into four main sections, comprising seven chapters. This format ensures a clear and logical organization of the content, beginning with a general introduction, followed by an experimental section. The third section focuses on the experimental work, presented across four chapters that detail the results obtained in the exploration of biodegradable metals for a biodegradable metallic ureteral stent development. The final section presents the main conclusions and outlines future perspectives for this research.

The main body of the thesis consists of a series of manuscripts that have been published in international journals or submitted for publication. Each chapter follows the structure of a scientific publication, i.e., an abstract, introduction, materials and methods, results, discussion, and conclusion. A list of relevant references is provided at the end of each chapter to support the findings and facilitate further reading.

SECTION 1 – GENERAL INTRODUCTION

Chapter I - Ureteral stents: current state and the prospects of a biodegradable metallic ureteral stent

This chapter provides a general introduction to the thesis topic, emphasizing the characteristics and side effects of currently available ureteral stents. It underscores the pressing need for a novel ureteral stent concept: the biodegradable metallic ureteral stent. Furthermore, it outlines the key features and considerations for the development of future metallic ureteral stents.

SECTION 2 – EXPERIMENTAL SECTION

Chapter II – Materials and methods

This section outlines the materials and methods employed in this thesis for the development and characterization of biodegradable metals and ureteral stent prototypes.

SECTION 3 - EXPERIMENTAL STUDIES

Chapter III - Understanding the corrosion of Mg alloys in *in vitro* urinary tract conditions: A step forward towards a biodegradable metallic ureteral stent

This chapter presents an investigation of five biodegradable metals, specifically five magnesium alloys, in a simulated urinary tract environment. It details the corrosion behavior of each alloy and assesses their respective cytotoxicity.

Chapter IV - Additively manufactured WE43 for biodegradable urinary devices: exploring the corrosion profile under *in vitro* urinary tract conditions

This chapter introduces additive manufacturing for ureteral stent development. It presents a preliminary investigation into the additive manufacturing of simple thin structures using WE43 powder, along with an analysis of the corrosion behavior of these samples.

Chapter V - *In vitro* corrosion of Mg1Y-based thin walls produced by laser powder bed fusion – influence of continuous and modulated laser modes

This chapter discusses the optimization of printing parameters for Mg-1Y-based thin structures, with a focus on evaluating the differences between two laser modes for developing thin structures. The findings from this study serve as the foundation for the subsequent chapter.

Chapter VI - Towards biodegradable Mg-based ureteral stents: A comprehensive *in vitro* study of two Mg-1Y stent prototypes.

This chapter details the development of two biodegradable ureteral stent prototypes using two manufacturing techniques, additive manufacturing and extruded and coiled wire, made from the same base Mg alloy, Mg-1Y. Their corrosion characterization in dynamic conditions and evaluation of cytotoxicity and antibacterial activity is explored in this study.

SECTION 4 - GENERAL CONCLUSIONS

Chapter VII - General conclusions

This chapter summarizes the key conclusions of the research conducted in this thesis and outlines potential directions for future work.

SECTION 1

GENERAL INTRODUCTION

CHAPTER I

URETERAL STENTS: CURRENT STATE AND THE PROSPECTS OF A BIODEGRADABLE METALLIC URETERAL STENT

I-1. URETERAL STENTS: IMPORTANCE IN UROLOGY AND SIDE EFFECTS

Ureteral stenting is one of the most performed procedures in modern urology. When the ureter becomes obstructed it can lead to serious consequences, such as kidney failure or even death if left untreated. In such cases, a ureteral stent is inserted to restore the flow of urine from the kidney to the bladder, preventing further complications. Thus, ureteral stents play a crucial role in safeguarding kidney function and are indispensable tools in urological practice. The pioneering insertion of a ureteral stent was first reported by Zimskind and his colleagues in 1967. They successfully used an endoscopically placed silicone tube to relieve ureteral obstruction, which marked the beginning of modern ureteral stenting(1). Another significant milestone came in 1978 with the introduction of the double pigtail, or double-J, stent design, which addressed the major issue of stent migration, which was a major problem at the time(2). Since then, the use of ureteral stents has greatly increased, with the double pigtail design becoming the most common and widely adopted in modern practice(3). Currently, the typical ureteral stents design consists of a 22-24 cm long flexible polymeric or metallic tube with side holes punched along the stent wall with J-shaped ends (double J or double pigtail model)(4–8). Nowadays the stents are used to treat several conditions where the urine passage in the ureter is, or is predicted to be, obstructed. These conditions include ureteral stricture, urolithiasis, maintenance of ureteral patency when there is an external ureteral compression (e.g. tumour), post operatively when the surgery involved ureter manipulation that would cause swelling and consequent obstruction, among others(3,4,9,10). Despite this unquestionable role, ureteral stents are associated with several side effects that in the first days of implantation include pain, irritation of the bladder mucous membrane which results in dysuria, voiding urgency, haematuria and urinary tract infections (UTI)(9) and in cases of long-term treatments other symptoms occur, such as hydronephrosis, encrustation, reflux, stent migration and inflammation(5,7,11).

I-1.1. Stent associated urinary tract infections

Ureteral stent-associated urinary tract infection (USAUTI) is a highly prevalent effect of ureteral stent placement. The symptoms associated with the USAUTI vary from patient discomfort to life-threating complications such as sepsis(12). The prevalence of bacteriuria is lower (around 27-30%) than the cases of biofilm formation on ureteral stents' surface (which is about 68-90%). This means that biofilm formation is difficult to detect using conventional urine analysis, therefore, negative urine cultures do not necessarily indicate the absence of biofilm formation(13–15). Additionally, the prevalence of biofilm formation increases with the duration of the treatment, so the incidence can be around 24-58.6% for indwelling time of less than 1 month but then increases to 71-75.1% for treatments longer than 3 months, achieving 100% for patients with permanent ureteral stents(7,12,16). Even though there are no specific guidelines

concerning the administration of antibiotics for ureteral stenting, the standard practice is to administrate an antibiotic prophylaxis, especially if the patient has a positive preoperative urine culture or patients at higher risk of infection(17,15). Then, during stent use, the antibiotics are prescribed only if symptoms of infection emerge or on patients with recurrent urinary tract infections. To prevent the development of severe USAUTI and the antibiotic-resistant microorganisms, some institutions recommend the replacement of ureteral stent in short periods of time(18). However, the approach adopted varies among countries and healthcare institutions(16,17,19).

Studies indicate that within 24h after stent placement, bacteria start to adhere to the stent surface, which later develops into a biofilm(12,15,18). The biofilm is a complex, organized microenvironment rich in proteins, nucleic acids and polysaccharides that allow the bacterial survival and proliferation, protects the microbial community against host's immune defense and antimicrobial drugs, which make it very difficult to treat once the biofilm is established(16). After the stent is implanted, a conditioning film forms on the implant surface by the host urinary components, which constitutes the first step of biofilm formation, facilitating the bacterial adhesion on the stent surface and future biofilm development(16,18). For this reason, it is very common that antibiotic treatments fail to eliminate USAUTI. Additionally, there is an increase in the incidence of antibiotic-resistant bacteria due to the overuse of these drugs, making it even more challenging to treat infections(18).

Therefore, there is an urgent demand to develop ureteral stents with inherent antibacterial properties, especially, able to inhibit the biofilm establishment, which minimizes the incidence of infections and antibiotics use.

I-1.2. Stent encrustation

Similarly to USAUTI, the incidence of ureteral stent encrustation increases with dwell time. The reported rates of encrusted stents are around 9.2-26.8% before 6 weeks of implantation, increasing to 47.5-56.9% between 6 and 12 weeks, achieving 75.9-76.3% for stents implanted for longer than 12 weeks(16,20,21). Encrustation can become very serious if it accumulates to the point of obstructing the stent lumen or becomes so severe that multiple procedures are needed for its removal(22). These extreme situations occur mostly in cases or prolonged dwell times when the patient fails to attend the follow-up doctor's appointments for stent removal or in cases of forgotten stent. These cases cause considerably patient morbidity(16,23).

The encrustation formation mechanisms are still unclear, but it is believed that it forms after a urinary conditioning film formation on the stent surface. This conditioning film can be composed of different

biomolecules, depending on the patient's urine composition, therefore, the different components of the conditioning film will have different tendencies on interacting with the urine components, which makes that encrustation composition can be highly variable(22–25). This phenomenon shares similarities with biofilm formation(23). In fact, the development of bacterial biofilms and encrustation are closely interrelated, though the mechanisms underlying this relationship remain poorly understood. Encrustation can provide a suitable substrate for biofilm deposition, while bacteria can actively induce crystal precipitation(23). In both cases, the formation of a conditioning film on the stent surface is a critical initial step(23). As a result, understanding the conditioning film and how it develops is a significant advance in research on preventing encrustation formation(23).

Over the last few years, the research has been focused on improving ureteral stents performance through the development of innovative materials, stent designs or stent surface features that would prevent or avoid stent symptoms(26–28). Nowadays there are several ureteral stents available in the market, with different characteristics, providing a plethora of choice to adapt to each patient's case(6–8,26,27). The following chapter will address some of the current stents characteristics, specifically the materials and their main characteristics.

I-1.3. Biomaterials for Ureteral Stents: Advances and Future Perspectives

The content of this sub-chapter was published as an original book chapter in *"Urinary Stents: Current State and Future Perspectives"*.

Pacheco, M., Silva, J. M., Aroso, I. M., Lima, E., Barros, A. A., & Reis, R. L. (2022). Biomaterials for Ureteral Stents: Advances and Future Perspectives. In Urinary Stents: Current State and Future Perspectives (pp. 197-208). Cham: Springer International Publishing.

Ureteral stents play a fundamental role in the relief of several symptoms associated with common urinary diseases in modern society, such as strictures, obstruction or promotion of ureteral healing(29,30). Even though ureteral stents have been used for more than 40 years and their performance had a huge development over time, they are still related with complications that include stent encrustation and urinary tract infections(29,30). Therefore, efforts from the research community continue to better meet the clinical needs. Ureteral stent's materials have a great influence on their efficacy, mostly in terms of mechanical and physicochemical properties(31). Thus, understanding the stent material's properties is fundamental to address problems of encrustation, bacterial adhesion, patient discomfort and the troubles during insertion, by working on the softness, flexibility and surface properties of the device(31).

Ureteral stents were described for the first time by Herdman back in 1949(32). Among the various biologically and chemically inert polymers that were popular at that time, polyethylene was used owing to its considerable tensile strength, flexibility, biocompatibility and hydrophobic properties. However, during the first animal studies tube blockages and hydronephrosis were detected as the main drawbacks(32). Another suitable polymer that was at the time used for the manufacture of ureteral stents was silicone, which can withstand high temperatures, facilitating the sterilization process that, in turn, prevent infections(1,33). Silicone based stents were less likely to promote encrustations and infections while still being effective in different urological conditions. Nonetheless, due to the low radial strength, silicone-based stents were inefficient in bearing with high external compression(1,33). Thereby, the research efforts have turned the tide to merge the flexibility and elasticity of silicone with the rigidity of polyethylene, which resulted on the development of polyurethane as raw material for ureteral stents. Indeed, polyurethane mechanical properties were promissory, but this polymer also demonstrated higher predisposition for encrustation than silicone-based materials(34). Metals and biodegradable materials have been also used for ureteral stents manufacturing due to their remarkable properties. Metallic ureteral stents are very efficient in situations of high compression forces and when long term treatments are required(29). A recurrent disadvantage with metallic stents is tissue hyperplasia and increased propensity to develop encrustation due to longer indwelling time periods(31). On the other side, biodegradable ureteral stents (BUS) provide the uniqueness of self-degradation but obtaining a controlled and homogeneous is still the main obstacle for development of BUS (**Figure I 1**). On the next sections of this chapter, the three main classes of materials used for ureteral stents manufacture will be individually addressed and most recent findings will be discussed in order to shed the light on the advances and future perspectives in this field.

I-1.3.1. Polymeric materials

Polymers are attractive base materials for biomedical applications due to their inert nature, and constitute the first materials explored for ureteral stent development(35). Currently, polymeric ureteral stents are the most common in the market, known by being inexpensive and well-tolerated by patients(31). Certainly, the extensive research on polymers lead to a widespread understanding of their properties, the companies developed proprietary blends and high-quality polymeric ureteral stents are now commercially available(36). The aim of the current studies on polymeric ureteral stents are focused on improving the biocompatibility, the indwelling time without significant encrustations and infections, and the ease of insertion and retrieval, maintaining the appropriate mechanical properties and radiopaque nature(31,35). Polyethylene was the first material employed on the design of ureteral stents, that is not

used anymore due to the substantial drawbacks associated to it, namely the easy fragmentation caused by the brittleness of the material and the high rates of encrustation and infection(31,37). Currently, silicone and polyurethane are the most used polymers for ureteral stents manufacture(31,35) (**Figure I 1**). Silicone has been extensively used, since the earlier beginning of ureteral stents production. Zimskind and colleagues, in 1967, studied for the first time the suitability of silicone for ureteral stents, describing the application of a piece of silicone tube with open ends and side holes to promote long term ureteral drainage of compromised ureters(1). Nowadays, silicone is considered as a gold standard due to its unique properties, such as the less propensity of encrustation and bacteria contamination, non-toxicity and the improved comfort due to its softness and high lubricity(31,38,39). Besides the aforementioned features, silicone is also easy to shape and process, facilitating the production phase. However, the high flexibility and elasticity is also a disadvantage during the placement on tight and tortuous ureters or when high compression (e.g. tumors) is present(31). Additionally, difficulties in maneuvering it with the guidewire were also reported(37). The use of polyurethane in the urologic field is popular since the earlier beginning due to the suitable mechanical properties, however, as a stiff material, causes discomfort and pain to the patients, being also reported epithelial erosion and ulceration when compared to other materials(30). The problems encountered in ureteral stents also instigated companies to develop optimized polyurethane-based proprietary formulations, like Sof-Flex®, Tecoflex®, Hydrothane® and ChronoFlex®(40). Nowadays, polyurethane's chemical characteristics can be tuned, such as the surface wettability and surface energy, which allows the control of other properties like encrustation and bacterial adhesion propensity(41). Other polymers were also developed, such as the polyester copolymer, Silitek®, a proprietary polymer that becomes soft and flexible at body temperature, with a reported excellent biocompatibility, Perculfex®, polyethylene-vinyl acetate and Styrene/ethylenebutylene/styrene block copolymers, F-Flex®, and poly(methyl methacrylate)/poly(hydroxyethyl methacrylate) (PMMA/pHEMA) with improved mechanical properties than silicone(42). Albeit all the reported polymer's formulations, the available ureteral stents are not devoid of clinical complications, thereby, investigations aiming to modify the base polymers are still on going. A recent work presented by Rebl *et al.* addressed the influence of physical properties of different polymers' samples on their propensity to develop encrustation(41). The data revealed that the encrustation degree is correlated with the surface charge and hydrophobicity of the polymer samples, a lower encrustation propensity was observed for polymers with strong negative surface charge and good hydrophilicity(41). This behavior is justified by the fact that the most common components of the infectious urinary stones are negatively charged, and, consequently, can be repelled by strongly negative charged polymers' samples(41). Rosman *et al.* also explored the bacterial resistance

and anti-biofilm properties of a polyacrylonitrile based ureteral stent (pAguaMedicina™, Pediatric Ureteral Stent, Q Urological) where a considerable reduction on bacterial colonization and biofilm formation in Broth (Trypticase Soy Agar broth), Broth with human urine, and Broth with swine blood was observed when compared with a commonly used commercial ureteral stent (BostonScientific)(43). An interesting approach is a combinatorial approach of different materials, taking advantage of the properties of the individual counterparts. For example, Silhouette® ureteral stent consist on a nitinol wire covered with a synthetic polymer, thus this stent present an improved resistance due to the presence of metal on its structure and a good biocompatibility provided by the polymeric revetment(8,31). **Table I 1** presents examples of the polymeric commercial ureteral stents available on the market.

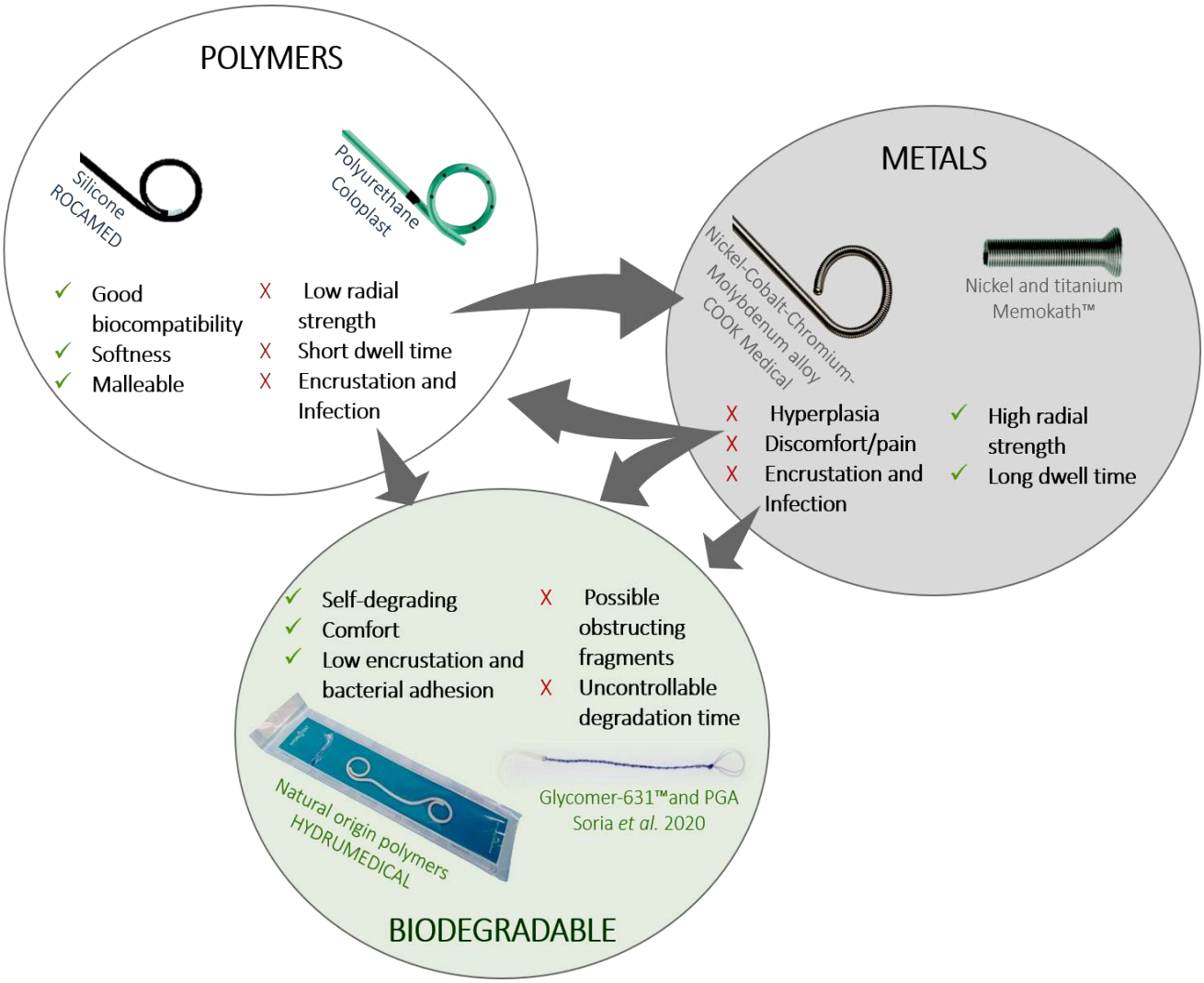


Figure I 1 Different materials used for ureteral stents development, including some examples of each class, the main advantages and disadvantages and how the different materials' properties complement each other.

Table I 1 Polymeric ureteral stents available on the market.

Commercial name	Company	Material
LithoStent	OLYMPUS	Tecoflex®
Classic closed tip ureteral stent	OLYMPUS	Silicone
UroGuide	OLYMPUS	Silicone
Lubri-Flex	OLYMPUS	Tecoflex®
Classic Double Pigtail	OLYMPUS	Tecoflex®
Sof-Curl™	OLYMPUS	Tecoflex®
Endosil® Silicone double loop ureteral stent	ROCAMED	Silicone
Amecath double loop stent	Amecath Medical Technologies	Tecoflex® (short term use) or Carbothane (long term use)
Silhouette® ureteral stent	Applied Medical	Synthetic polymers, proprietary materials and coil reinforced nitinol
Yellow Star Tumour Stents Green Star Stents White Star Stents	GBUK Healthcare	Aliphatic polyurethane
Ureteral stent medadvDJ	MEDAS INC	Polyurethane
Double pigtail ureteral stent	MEDNOVA	Polyurethane
MEDpro Ureteral Stents	MEDpro	Tecoflex® for short term use and Carbothane for tumour compression cases
Biosoft® duo ureter Stent	Coloplast	Rigid proprietary material
Silicone double loop ureteral stent	Coloplast	Silicone
Polyurethane (PU-R & PU-S) double loop ureteral stents	Coloplast	Soft or rigid, proprietary polyurethane
Tumor stent	Coloplast	Proprietary formulation with a reinforced internal layer for excellent resistance to compression
Ureteral stent Polaris™ Ultra	Boston Scientific	Percuflex with dual durometer
Pyelostent	Coloplast	Silicone
Sof-Flex® Double Pigtail Stent	COOK Medical®	Proprietary radiopaque soft polyurethane
Percuflex®	Boston Scientific	Proprietary copolymer - Modified polyurethane
Single J Urinary Diversion Stents	OLYMPUS	Silitek®

I-1.3.2. Metallic materials

Metallic based ureteral stents were developed to treat ureteral obstruction caused by a malignant external compression, usually a tumor, and for patients needing chronical indwelling ureteral stents(44,45). In this context, polymeric ureteral stents are ineffective due to the inadequate drainage and requirement of replacement in a short time period, causing discomfort and extra hospital

costs(45,46) (**Figure I 1**). A metallic ureteral stent has an improved radial strength that provides long-lasting ureteral patency - 12 months to 2 years - tackling the problem of low compression strength and shorter indwelling time - usually 3 months - of polymeric stents(47,48). The success rate of a treatment with a metallic stent is between 37% and 100%(45,48,49). Current metallic ureteral stents could be double-J shaped as the traditional polymeric ones (Resonance®), self-expandable (Wallstent™, Allium), balloon expandable (Uventa™), thermo-expandable (Memokath 051) and/or covered with a polymer (Uventa™)(29,50). Resonance® has a double-J shape with an occluded lumen and, even though this exclusive design makes the stent insertion and retrieval more difficult, it assures ureteral patency and urine flow under high external compression(51). Blaschko *et al.* have reported a significant higher flow rate for Resonance® when compared with a 6Fr standard stent under high extrinsic compression, 5.15 ml/min and 0.64 ml/min respectively(52). In another study, Christman et al. compared the radial compression resistance of different ureteral stents - Silhouette®, Sof-Curl™, Resonance®, Polaris™ Ultra, and Percuflex®. The data indicated that Resonance® had a significant higher resistance to compression, followed by Silhouette®, which could be justified by the nitinol wire coil present on Silhouette®(8). Resonance® is currently seen as a reference for malignant ureteral obstructions owing to the numerous advantages already reported, such as good biocompatibility, suitability for magnetic resonance imaging examination, inhibition of endogenous tissue growth and high flexibility due to the tightly coiled wire of the spiral shaped design(31,53,54). Additionally, Resonance® is soft and, more importantly, has an indwelling time of more than 12 months, during which it retains its suitable features(53). Chen *et al.* conducted a study where they compared the performance of Resonance® with an ordinary polymeric stent on patients with malignant ureteral obstruction(48). The authors confirmed that after 1 year of stent placement, the stents patency decreased 60% in the polymeric stent group and only 9.3% metallic stent group, indicating that metallic stents with good drainage effect for a long period of time are superior to the traditional polymeric stents for patients who require long term stenting(48). Up to now, different metallic ureteral stents were developed and accessible on ureteral stents market. Memokath 051 is a thermo-expandable nickel titanium alloy with a very tight coil design(46). Memokath 051 deploys in warm saline and shrinks in cool saline, which is an attractive benefit for placing and retrieving them from the body(31). Complications such as stent migration and encrustation were reported, together with tissue ingrowth and stent occlusion(42,55). Uventa is another commercially available metallic ureteral stent composed of a double layer of nickel and titanium alloys with polytetrafluoroethylene (PTFE) layer between them, designed to prevent migration and tissue adhesion(56). The success rates of Uventa for malignant ureteral obstructions are between 64.8-81.7% and the associated complications include tumour

progression beyond the stent, tissue ingrowth and pain(57). Another metallic stent model is WALLSTENT, a self-expanding stent composed of cobalt-based microfilaments woven in crisscross pattern(58). Unfortunately, WALLSTENT is also associated with pain, stent migration and tissue ingrowth(56). Allium Ureteral Stent is made of nitinol and covered with a copolymer, with the purpose to prevent encrustation and tissue growth(59). The major advantage of Allium Ureteral Stent is the easy removal owing to its particular design(59). Passage™ is a coil-based metallic ureteral stent with improved flexibility and comfort and higher resistance to radial compression when compared with Resonance® and Silhouette®(29,60). Nitinol is a biocompatible material, composed of titanium oxide and nickel with a better corrosion resistance than stainless steel - a material that was previously seen as a reference for stents - possessing also memory shape, i.e. it can be manipulated as needed for stent insertion and afterwards recovers its original shape(47). Most of the currently available metallic ureteral stents are made of nitinol. Table 2 presents metallic ureteral stents currently available on the market and their composition.

Table I 2 Metallic ureteral stents available on the market.

Commercial name	Company	Material
Resonance®	Cook Medical	Nickel-Cobalt-Chromium-Molybdenum alloy
Allium Ureteral Stents	Allium™Medical	Nitinol wire covered with a polytetrafluoroethylene (PTFE)
Passage™	Prosurg	Nitinol
WALLSTENT™	Boston Scientific	Cobalt-based microfilament
UVENTA™ Ureteral Stent	TaeWoong Medical	Double layer of nickel and titanium alloys with a layer of PTFE in between
Memokath 051	Memokath™	Nickel and titanium alloys

I-1.3.3. Biodegradable materials

Biodegradable ureteral stents are an appealing alternative since its use eliminates the need of a second surgery for the stent removal, avoid additional ureter damage, pain and discomfort, and diminishes the treatment costs(29,31,47). These exceptional features and decreased propensity for bacterial adherence and encrustation motivated the investigations on biodegradable materials for ureteral stents development(29,47) (**Figure I 1**). A crucial concern when producing a BUS is that the degradation profile of ureteral stents should occur in a controllable and adequate form, i.e. efficient mechanical properties must be assured during the treatment time and the degradation has to occur in an homogeneous way, avoiding additional ureteral obstruction(36,47,61). In fact, these are very challenging features to obtain and constitute a critical point during the development process(31,61). BUS have been

fabricated from synthetic polymers, naturally origin polymers, biodegradable metals or a combination of biodegradable polymers and metals(31,61). The concept of biodegradable material applied for ureteral stents date back to 1997, in which Schlick and Planz evaluated the degree of dissolution in acidic and alkaline artificial urine of two polymers (G100X-15LB and G100X-20LB)(62). With these raw materials, they aimed at producing an ureteral stent with controlled degradation by alkalinizing the urine through medication. However, in clinical practice this concept is risky as a basic urine pH can lead to extra complications, such as precipitation of urine salts and also the development of a suitable environment for the uropathogens growth(29,47). Olweny *et al.* in 2002 introduced the use of poly-l-lactide-co-glycolide (PLGA) as BUS material in a porcine model(63). Other studies followed this direction and BUS were developed using PLGA, Poly-l,d-lactide (PLA), poly-l-lactic acid (PLLA), polycaprolactone (PCL) and poly-dl-lactic acid (PDLLA), nonetheless problems of inadequate degradation and toxicity were frequently found, with the exception of some promising results obtained in dogs with poly-l,d-lactide (SR-PLA96) where reduced inflammation and good biocompatibility was obtained(29,47,64–66). Some concerns affecting the stent degradation are the size and shape, the molecular weight of the polymer, the presence of other ingredients and the respective proportions, among others, and improvements of BUS's characteristics are made by optimizing these features(29,61). Yang *et al.* proposed the use of PLGA for ureteral stents with a particular stent design that is different from the ones usually employed for BUS -braided and spiraled. The data suggested an homogeneous and controllable degradation and better radial compression strength when compared with a commercial stent(67). This design is based on a multilayer immersion method using PGLA, zein -a natural protein- and barium sulfate(67). Later on, Zhang *et al.* reported the use of a novel biodegradable polymer, methoxypoly(ethylene glycol) -block-poly(l-lactide-ran-Ɛ-caprolactone) (mPEG-PLACL), that present less propensity for encrustation and superior biocompatibility(68). Soria *et al.* scrutinized the performance of an innovative anti-reflux BUS, BraidStent, in 24 female pigs where only part of the ureter was intubated(69). The stent degraded in 3-6 weeks without obstructive fragments and favorable anti-reflux properties(69) (Table 3). Uriprene™ is a radiopaque glycolic acid-based stent that start the degradation process after 3 weeks, while after 7 and 10 weeks 60% and 100% of the stent was degraded, respectively, in porcine models(70). This stent was designed to degrade in a specific direction, from the bladder to the kidney end, thereby preventing also the obstruction-formation fragments(29). Uriprene™ provides similar drainage capacity as ordinary stents with less ureteral dilatation and microbial contamination(70) (Table 3) The reported problem associated with this stent is the difficulty of insertion(47). An improved version was later developed with a shorter degradation time (i.e., 4 weeks)(71). Lingman *et al.* conducted clinical trial studies using a BUS produced

from a proprietary formulation based on the natural origin polymer alginate(47,72,73). The stent was biocompatible and presented appropriate patency up to 48 hours, after that time the stent starts to degrade. The main problem of these stents is the permanence of fragments inside the patients for long periods, which required surgical intervention for removal. Recently, Barros *et al*. successfully reported the use of gelatin and alginate to produce an hydrogel BUS using the supercritical carbon dioxide technology in the production process, which proved to be beneficial for the mechanical properties(74). In the first studies encouraging results in terms of biocompatibility and low propensity for bacterial contamination and encrustation were reported(74). This model then showed good performance *in vivo*, in pig models, with better biocompatibility than a commercial ureteral stent and an homogeneous degradation profile(75,76). These works resulted in a patented BUS and the development of HydrUStent™, a biodegradable hydrogel stent for temporary treatments (**Table I 3**). HydrUStent™ was already validated in porcine model and is being currently preparing to start clinical trials(77).

Biodegradable metals can be used for prolonged time treatments, given the slower degradation rate when compared with biodegradable polymers. The potential of biodegradable metals for ureteral stents was studied for the first time by Lock *et al*. that investigated the antibacterial activity of magnesium (Mg)-4%Yttrium(Y), the Mg alloy AZ31 and commercially pure Mg. A decrease in *Escherichia coli* viable colonies was observed for all the tested Mg alloys when compared with commercial polyurethane stents(78). Zang *et al*. studied the alloy ZK60 and pure Mg in terms of corrosion, in artificial urine, and histocompatibility in rat's bladder where they verified that ZK60 had a faster degradation both in vitro and in the animal's bladder and both metals reveal to be biocompatible(79). Recently, Tie *et al*. reported for the first time the use of a Mg based alloy, ZJ31, in a large animal model for ureteral stent application(80). The data indicated a homogeneous corrosion rate, good biocompatibility and antibacterial activity, when compared with stainless steel. The studies conducted up to now using biodegradable metals for ureteral stents application are still very scarce but promising. Thereby, it is envisioned the clinical translation of a biodegradable metallic ureteral stent in the near future.

Another appealing approach to improve the mechanical properties and degradation time of BUS is the combination of biodegradable polymers with biodegradable metals. Jin *et al.* evaluated the performance of a BUS based on filaments of Mg alloys covered with biodegradable polyurethane and a coating composed of a biodegradable polymer and barium sulphate(81). The stents started to degrade after 1 week implantation on pig's ureter and degraded completely after 4 weeks. The degradation process is not explained but the authors highlight the better drainage ability of the developed stents(81).

Table I 3 Example of successful biodegradable ureteral stents.

Commercial name	Company	Material
BraidStent	n/a	Glycomer-631™and polyglycolic acid (PGA)
Uriprene™	Poly-Med Inc.	l-glycolic acid
HydrUStent™	HYDRUMEDICAL	Natural origin polymers

I-1.3.4. Conclusions and future perspectives

Considerable progress has been done on ureteral stent's properties with the aim to meet the clinical problems encountered. Even though this progress does not end up with an ureteral stent without associated complications, it allows to understand the behavior of different materials and designs in the urologic environment. Indeed, the vast amount of work done and respective outputs have been proven that the different materials can complement each other's disadvantages, for example, the metals can bear with the high compression that polymeric stents cannot. The goal is to combine the advantages of each material without their associated complications. Indeed, promising works have been validating the success of this approach, such as the combination of polymers and metals (Silhouette®) or biodegradable polymers and biodegradable metals. Biodegradable materials seem to be a superior alternative due to their undoubtedly outstanding advantages, the only concern that still needs to be optimized thorough is the degradation rate. However, it should be highlighted the outstanding progresses that have been made in the design of ureteral stents by tailoring their composition. Therefore, the use of biodegradable materials and combination of different raw materials and design adjustments appears to be the future of ureteral stents design.

I-2. Development of a Magnesium-based biodegradable ureteral stent

Despite the considerable advancement, ureteral stents still present side effects that restrict the optimal function of these devices, so novel stent materials are required to provide stents with increased biocompatibility and decreased susceptibility for encrustation and infection.

Biodegradable materials have emerged as a significant innovation in the biomedical sector, offering an appealing alternative over traditional implants(7,27). Biodegradable implants will gradually dissolve in the body, avoiding the need for surgical removal after the treatment. Besides, the physical characteristics of biodegradable stents are constantly changing as the stent degrades, which is expected to decrease the bacteria interaction and adhesion, condition film deposition and encrustation(3). Biodegradable metals

are recognized as revolutionary biomedical implants due to their compatibility and superior strength and ductility when compared to polymers(82). The most investigated biodegradable metals for biomedical applications are Mg-based alloys, Fe-based alloys and Zn-based alloys, mainly because they are also essential nutritional elements and naturally available in the human body, making them of easy translation to the clinical environment(82–84). There are some limitations associated with these metals, Zn, for example, has a toxicity limit lower than Mg, and some adverse reactions have been reported(85,86). Fe has a very long degradation time that sometimes becomes much longer than the needed for the treatment, besides the fact that it produces a large volume of iron oxide that is unlikely to be safely metabolized(87). Also, the ferromagnetic degradation product is not compatible with the magnetic resonance imaging. Regarding Mg, the major problem is the fast corrosion, which leads to premature implant failure, and a higher accumulation of corrosion products that, if in high amounts, could become toxic(88). The degradation mode of Mg is through its corrosion process, which occurs by an electrochemical reaction to produce oxides, hydroxides, hydrogen gas or other compounds, depending on the media it is immersed in. In physiological environment, Mg corrosion involves the following reactions(84,89):

$$Mg + 2H_2O \rightarrow Mg(OH)_2 + H_2 \uparrow$$

$$2Mg + 2H_2O + O_2 \rightarrow 2Mg(OH)_2$$

The corrosion products generated during Mg corrosion may be problematic when produced in high amounts in confined spaces, for example due to localized alkalinity caused by the release of OH^- ions, gas pocket accumulation resulting from hydrogen evolution, or excessive Mg^{2+} ion release(90). However Mg has several advantages over the other counterparts, namely the higher compatibility and the density, which is very important for specific applications such as bone implants(91). These unique characteristics increased the use of Mg as base material for biodegradable implants, so this metal has been the main focus of research on biodegradable metallic-based implants especially on fast corrosion control(90,91). Nowadays, Mg-based biodegradable implants have already reached the market and are currently used with success as bone implants and cardiovascular stenting(90). Magmaris is a biodegradable vascular stent composed of a Mg alloy containing the rare-earth metals Zr and Y, composition that confers it decreased corrosion rate, increased radial strength and improved biocompatibility(92). MAGNEZIX® is a Mg-Y-RE (rare earth)-Zr-based screw, the first CE approved biodegradable osteosynthesis implant with very good outcomes in terms of absorption, biocompatibility

and degradation rate(93–95). The U&I Corporation provides the Resomet bioresorbable bone screw and Resomet bioresorbable K-wire and pin, made of Mg-Ca alloy(96). In an experiment led by Shin *et al*, the absorption time for Resomet products was between 6-18 months and no complications and successful bone union after one year follow-up was achieved(96). For urinary applications, however, the research is more limited, even though some works have been shown great potential for its application in urology. In the work published by Lock *et al*. the suitability of biodegradable metals for ureteral stents was explored by investigating the antibacterial activity of Mg-4Y, AZ31, and pure Mg(97). The authors found that *E. coli* viable colonies were reduced for all the Mg alloys, compared with conventional polyurethane(97). Zhang *et al*. studied the corrosion and biocompatibility of pure Mg and ZK60 in artificial urine and inside rat's bladder(79). The results showed that both biodegradable metals were not toxic and ZK60 degraded faster than pure Mg(79). In another work, Tie *et al*. described the behavior of Mg alloys in large animals(80). It was found that ZJ31 alloy had an homogeneous corrosion rate, was biocompatible and showed antibacterial activity, when compared with stainless steel(80). All these studies provided important findings about the biodegradable metals performance *in vivo* or simulated urinary tract conditions. Moreover, the disadvantages discussed above regarding the use of Mg as a biodegradable implant are expected to be less problematic when applied to biodegradable urinary implants. This is because the urinary tract is an excretory system in which released degradation products are likely to be flushed out with urine. In addition, the urinary system is designed to be largely impermeable to unwanted substances excreted by the body; therefore, the released corrosion products are not expected to be absorbed. On the other side, the development of biodegradable implants for the urinary system is very challenging because the urinary environment is very inconsistent, the composition and volume of urine changes a lot in the same individual, and even more from person to person. Also, the urine itself is very hostile which would most likely lead to a faster degradation of the implant. Therefore, it is challenging to develop a biodegradable urinary implant with controllable degradation. The research on biodegradable urinary devices has then been focused on the development of a device with controllable corrosion and some works are very promising, even though most of the investigation has been done using biodegradable polymers. Mg has the problem of fast corrosion and one of the most used approaches to control this is the alloying with other elements, which is a very appealing method to develop a biodegradable metallic ureteral stent(88,90). In the following sections, a detailed explanation of biodegradable Mg-based ureteral stent characteristics is discussed.

I-2.1. Requirements for a ureteral stent

The ideal biodegradable ureteral stent would be easy to insert, meaning it should be compatible with the currently used accessories and techniques for urinary stent placement. Currently, ureteral stent placement is performed through minimally invasive procedures, often using an ureteroscope. The ureteroscope is inserted through the urethra and facilitates the entire stent placement process. The procedure begins with the insertion of a guidewire through the urethra. The guidewire passes sequentially through the bladder, ureter, and finally into the kidney(24). One end of the guidewire remains within the kidney, while the other extends outside the body, serving as a guide for the stent placement. The stent is threaded onto the exterior tip of the guidewire and advanced along its length to the desired location within the ureter(1,98). During this process, the stent must possess sufficient flexibility to navigate through the urethra, bladder, and ureter without causing damage to the urothelium. Additionally, a smooth surface is critical for facilitating easy passage through these tissues. To assist in stent placement, a pusher (a rigid tube-like instrument) is used to push the stent along the guidewire. Once the stent is positioned correctly, the guidewire and pusher are carefully removed(1).

The most widely used ureteral stent design is the double pigtail model, characterized by coiled ends that help secure the stent in place within the kidney and bladder. During insertion, these stents are temporarily straightened by the guidewire. After the guidewire is removed, the stent regains its original pigtail shape due to the shape-memory materials used, which are essential for this design(28).

Given the above, a ureteral stent must meet the following essential requirements:

- Standard dimensions to be compatible with the currently used accessories,
- Smooth surface to minimize trauma during placement,
- Flexibility for an easy passage though anatomical contours, and
- Shape memory to recover its original shape after placement.

For biodegradable ureteral stents, additional specific requirements must be met. The stent material and its degradation products must be non-toxic and easily excreted in the urine. Furthermore, the degradation rate should align with the healing process of the ureter, ensuring patency until recovery is complete and the stent is no longer needed. The stent should degrade completely without forming large fragments that could injure tissue or cause obstruction, necessitating surgical removal(3,99).

In summary, in addition to the general characteristics of ureteral stents mentioned above, a biodegradable stent must:

- Exhibit an adequate degradation rate,
- Release non-toxic degradation products, and
- Degrade homogeneously without forming harmful fragments.

The selection of suitable materials and manufacturing techniques is therefore a challenge for the successful development of biodegradable metallic ureteral stents.

I-2.2. Methods for the development of a Mg based ureteral stent

The stent fabrication method will have a significant impact on the stent geometry characteristics, microstructure, corrosion behavior, surface quality and mechanical properties. The selection of suitable materials and manufacturing techniques is therefore a challenge for the successful development of biodegradable metallic ureteral stents(100,101). For example, laser cutting has been used for fabricating cardiovascular stents owing to its high fabrication speed and precision. AM is a more economic method than laser cutting, and it is also possible to construct intricate designs with precision. The extrusion of wires is another method for stent development. The wires can be produced at a desired diameter and then coiled into tube, braided or knitted(102). In the present work, AM and coiled extruded wires were the methods explored, so the following sub-sections will be focused on those methods.

I-2.2.1. Additive manufacturing

Powder bed fusion laser beam (PBF-LB) is an AM technique used to produce intricate, thin and detailed structures with high precision. This makes it particularly valuable in the biomedical field, where high accuracy and complexity are often required(88). During PBF-LB process, the laser selectively melts the fine layers (which thickness can be customized) of metal powder according to the predefined computer-aided design (CAD), printing the parts layer by layer(88,103). The laser is commonly operated in continuous wave (CW) mode, where the laser continuously exposes the selected areas of the powder bed. The input energy from the laser will melt the powder particles of the current layer, as well as the material above, from the previous layers, forming a melt pool. The laser movements along the hatch line will lead to the formation of a melt track(88) (**Figure I 2**). During this process, the heat affected zone will form, which consists of the material in the close proximity with the moving melt pool that is affected by the high temperatures(88). Therefore, the PBF-LB is characterized by this cyclic melting and heating.

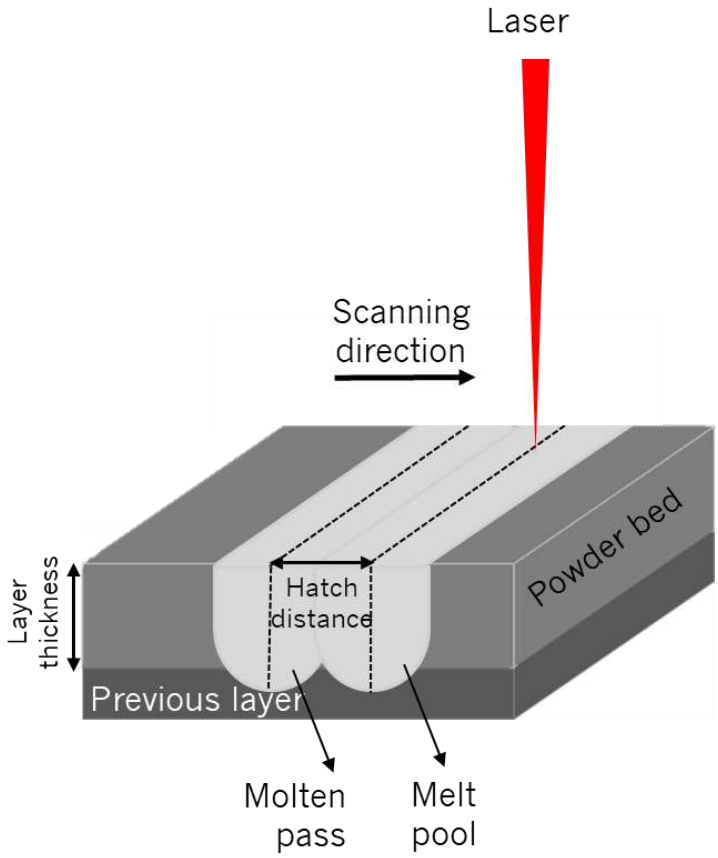


Figure I 2 Printing parameters on PBF-LB. Scheme of the printing process and respective printing parameters in PBF-LB.

The distance between two individual scan lines is called hatch distance. The hatch distance will determine the degree of overlap of two consecutive melt tracks, being one of the main parameters of the PBF-LB process (**Figure I 2**). Together with the hatch distance, the scan speed, laser power and powder layer thickness constitute three of the main process parameters in PBF-LB(88,104). From these parameters, the total energy input to the material can be determined by the volumetric energy density (ED), following Equation 1:

$$ED = \frac{P}{v * h * d} \ (Equation\ 1)$$

Where P is the laser power, v is the scanning speed, h the hatch distance and d the layer thickness(88).

The precision and versatility provided by this technique is especially important for the development of small and thin-walled structures such as stents. Moreover, the production of small

samples maximizes the efficiency of the build plate space, enabling the simultaneous production of a high number of samples in only one print(100). This is particularly beneficial during the optimization phase where different printing parameters - such as combinations of laser power, scan speed and hatch distance - can be varied across the build plate. This flexibility accelerates the research and development by allowing multiple configurations to be tested in parallel. Another key advantage is the material versatility. It can be used for different materials, from non-degradable titanium to biodegradable Mg. Since the feedstock for this technique is metal powder, it is possible to customize powder compositions with varying metal ratios. This capability is crucial for the research and development phase of new devices since it allows extensive material testing and fine-tuning to meet specific design and/or performance requirements. However, the widespread of PBF-LB is hindered by problems regarding structure consistency and quality, which is related with the rapid heating and solidification during printing, leading to structural defects. The most common defect encountered is porosity(104). The porosity can arise due to the lack of fusion, which happens in cases of too low laser power or too fast scan speed, which results on an inefficient fusion, leading to insufficient melting(105). The pores related to the lack of fusion are usually large and can feature unmolten powder particles inside. Another common type of porosity is related to the keyhole. In this one, the pore formation is usually related with too high energy input that creates localized vaporization of the metal leading to the formation of a deep and narrow cavity (the keyhole) inside the melt pool. These defects can, however, be controlled by a correct combination of process parameters(104,105).

In summary, the PBF-LB process provides a highly efficient and versatile platform for manufacturing small, thin-walled structures like stents. Its ability to produce high volumes of samples, enable rapid parameter optimization, and the possibility to use biocompatible and biodegradable materials such as Mg makes it significant for biomedical innovation, allowing for advances in patient care and the development of cutting-edge medical devices.

I-2.2.2. Extruded wire, coiled

Wire extrusion followed by coiling is a traditional and effective method for fabricating stents. This approach involves the extrusion of a metal wire that is subsequently shaped into helical configuration.

Severe plastic deformation of metals encompasses a variety of methods to refine grains through the application of significant plastic deformation(106). In this work, the method used was direct extrusion, where the metal billets are forced through a die cavity under high temperature to produce wires of uniform diameter (**Figure I 3**). This thermomechanical treatment allows the tailoring of the microstructure of the

resulting wire for a targeted performance(107). This is a single-step, simple and effective forming method to produce metal wires. The angle of the die, the reduction in the cross section, extrusion speed and billet temperature, are all very important factors in the extrusion process and will significantly impact the resulting wires' microstructure and resultant mechanical properties(107,108). For biodegradable metals, one important characteristic is the wire surface, which has a profound impact on corrosion. Actually, the extrusion parameters used will also influence the quality of the surface, thus it is very important to optimize the processing parameters in order to obtain wires with smooth surface, avoiding surface defects, in order to prevent localized corrosion(109,110). In the case of Mg, the plastic deformation is more complicated due to the hexagonal lattice structure, but the wrought of Mg with alloying elements, especially rare-earth (RE) elements, leads to the formation of precipitates that results on the improvement of mechanical properties and creep resistance(106). Therefore, direct extrusion of Mg is an efficient technique to produce Mg wires for biomedical applications. The wire coiling is a very useful technique to design ureteral stents since it is a simple method and provides high flexibility, important property for ureteral stent placement. However, this method has a very limited design flexibility compared with the AM technique and the stents formed through coiling have usually lower radial strength(102,111,112).

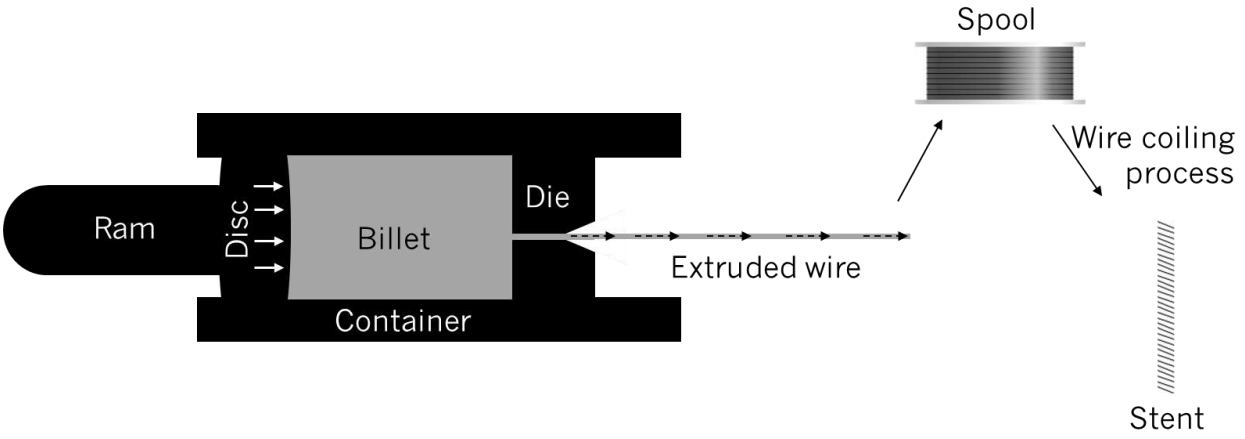


Figure I 3 Wires extrusion and coiling process. Scheme of the wire extrusion and wire coiling processes.

I-3. CONCLUSIONS AND FUTURE PERSPECTIVES

Ureteral stents are indispensable tools in modern urology, widely used in clinical practice. They are typically placed to restore urine flow from the kidney to the bladder in cases of obstruction or as a preventive measure following surgery to mitigate the risk of future ureteral obstructions. Despite their

critical role, ureteral stents are frequently associated with secondary effects, including pain, encrustation, and USAUTIs. Research on ureteral stents has focused on enhancing their performance through improved materials, advanced coatings, new designs, and other strategies aimed at reducing stent-associated complications. These efforts have led to the development of high-quality stents, and today, a wide variety of ureteral stents are available on the market, made from diverse materials and with various shapes to suit individual patient needs and clinical scenarios. However, the ideal ureteral stent still doesn't exist. Encrustation and bacterial infections are the most significant concerns. Biofilm formation on stent surfaces is still very frequent and a main problem because the conventional antibiotic treatments are not efficient. One of the most promising recent strategies involves the use of biodegradable materials, which have a dynamic surface that reduces the likelihood of encrustation and bacterial adhesion. Additionally, biodegradable stents eliminate the need for secondary surgery, enhancing patient comfort and reducing healthcare costs.

Among biodegradable materials, biodegradable metals are particularly attractive for prolonged treatments due to their extended degradation times. Mg, in particular, has emerged as a leading candidate due to its excellent biocompatibility and low density, which is especially advantageous for bone implants. However, research on Mg-based biodegradable ureteral stents remains limited. The primary challenge lies in Mg's rapid corrosion in biological environments, which can be intensified by the harsh conditions of the urinary tract.

For ureteral stent development, specific characteristics are essential, including a smooth surface, flexibility, and shape memory. Magnesium's mechanical properties, corrosion behaviour, and even antibacterial activity can be controlled and optimized through various strategies, such as alloying with other elements or by using different manufacturing techniques. Thus, Mg presents a highly appealing material for the development of next-generation ureteral stents. However, its properties must be precisely tailored to meet the requirements for biodegradable ureteral stents, ensuring safety, efficacy, and long-term performance.

I-4. BIBLIOGRAPHY

1. Zimskind PD, Fetter TR, Wilkerson JL. Clinical Use of Long-Term Indwelling Silicone Rubber Ureteral Splints Inserted Cystoscopically. J Urol. 1967 May;97(5):840–4.

2. Finney RP. Experience with New Double J Ureteral Catheter Stent. J Urol. 1978 Dec;120(6):678–81.

3. Lange D, Bidnur S, Hoag N, Chew BH. Ureteral stent-associated complications —where we are and where we are going. Nat Rev Urol. 2014;12(1).

4. De Grazia A, Somani BK, Soria F, Carugo D, Mosayyebi A. Latest advancements in ureteral stent technology. Transl Androl Urol. 2019 Sep;8(S4):S436–41.

5. Mosayyebi A, Manes C, Carugo D, Somani BK. Advances in Ureteral Stent Design and Materials. Curr Urol Rep. 2018 May 10;19(5):35.

6. Corrales M, Doizi S, Barghouthy Y, Kamkoum H, Somani B, Traxer O. A systematic review of long-duration stents for ureteral stricture: which one to choose? World J Urol. 2021 Sep 2;39(9):3197–205.

7. Domingues B, Pacheco M, de la Cruz JE, Carmagnola I, Teixeira-Santos R, Laurenti M, et al. Future Directions for Ureteral Stent Technology: From Bench to the Market. Adv Ther. 2022 Jan 17;5(1).

8. Christman MS, L'Esperance JO, Choe CH, Stroup SP, Auge BK. Analysis of Ureteral Stent Compression Force and its Role in Malignant Obstruction. J Urol . 2009 Jan;181(1):392–6

9. Wang H, Man L, Li G, Huang G, Liu N, Wang J. Meta-Analysis of Stenting versus Non-Stenting for the Treatment of Ureteral Stones. PLoS One. 2017;12(1).

10.Haleblian G, Kijvikai K, Rosette J de la, Preminger G. Ureteral Stenting and Urinary Stone Management: A Systematic Review. J Urol. 2008;179(2).

11. Miyaoka R, Monga M. Ureteral stent discomfort: Etiology and management. Indian J Urol. 2009;25(4):455.

12. Farsi HMA, Mosli HA, Al-Zemaity MF, Bahnassy AA, Alvarez M. Bacteriuria and Colonization of Double-Pigtail Ureteral Stents: Long-Term Experience with 237 Patients. J Endourol. 1995 Dec;9(6):469–72.

13. Tenke P, Köves B, Nagy K, Hultgren SJ, Mendling W, Wullt B, et al. Update on biofilm infections in the urinary tract. World J Urol. 2012 Feb 18;30(1):51–7.

14. Vallée M, Bey E, Bouiller K, le Goux C, Pimpie R, Tourret-Arnaud J, et al. Epidemiology and risk factors for ureteral stent-associated urinary tract infections in non-transplanted renal patients: a systematic review of the literature. World J Urol. 2021 Oct 15;39(10):3845–60.

15. Pérez-Fentes D, Aranda-Pérez J, de la Cruz JE, Soria F. Indications, Complications and Side Effects of Ureteral Stents. In: Urinary Stents. Cham: Springer International Publishing; 2022. p. 5–20.

16. Beysens M, Tailly TO. Ureteral stents in urolithiasis. Asian J Urol. 2018 Oct;5(4):274–86.

17. Cornette J, Lange D, Chew BH, Tailly T. Bridging the knowledge gap: past, present and future of antibiotic use for ureteral stents. BJU Int. 2024 Dec 4;134(6):858–68.

18.Kim JY, Yeo JK, Park MG, Sung LH, Cho DY, Yu JH. Determination of microbiological characteristics and risk factors associated with bacteriuria and symptomatic urinary tract infection in patients with retained ureteral stents: an observational study. Transl Androl Urol. 2023 Jan;12(1):19–32.

19. Souhail B, Charlot P, Deroudilhe G, Coblentz Y, Pierquet G, Gimel P, et al. Urinary tract infection and antibiotic use around ureteral stent insertion for urolithiasis. Eur J Clin Microbiol Infect Dis. 2020 Nov 26;39(11):2077–83.

20. Tomer N, Garden E, Small A, Palese M. Ureteral Stent Encrustation: Epidemiology, Pathophysiology, Management and Current Technology. J Urol. 2021 Jan;205(1):68–77.

21. Bibby LM, Wiseman OJ. Double JJ Ureteral Stenting: Encrustation and Tolerability. Eur Urol Focus. 2021 Jan;7(1):7–8.

22. Bhardwaj M, Ingole N. Application, Advancement, and Complication of Ureteral Stent and Encrustation: A Major Complication. Cureus. 2022 Aug 31;

23. Guo H, Yuan J-B. New insights into the prevention of ureteral stents encrustation. Open Med. 2023 Dec 6;18(1).

24. Amado P, Zheng S, Lange D, Carugo D, Waters SL, Obrist D, et al. The interplay between bacterial biofilms, encrustation, and wall shear stress in ureteral stents: a review across scales. Front Urol. 2024 Jan 16;3.

25. Skolarikos A, Jung H, Neisius A, Petřík A, Somani B, Tailly T, et al. EAU Guidelines on Urolithiasis. Eur Assoc Urol. 2024;

26. Nestler S, Witte B, Schilchegger L, Jones J. Size does matter: ureteral stents with a smaller diameter show advantages regarding urinary symptoms, pain levels and general health. World J Urol. 2020 Apr;38(4):1059–63.

27. Lee J, Katz M, Shah O. Developments in Ureteral Stent Technology. Front Surg. 2021 Nov 17;8.

28. Bernasconi V, Tozzi M, Pietropaolo A, Coninck V De, Somani BK, Tailly T, et al. Comprehensive overview of ureteral stents based on clinical aspects, material and design. Cent Eur J Urol. 2023;

29. Lange D, Bidnur S, Hoag N, Chew BH. Ureteral stent-associated complications—where we are and where we are going. Nat Rev Urol. 2015 Jan 23;12(1):17–25.

30. Ramachandra M, Mosayyebi A, Carugo D, Somani BK. Strategies to Improve Patient Outcomes and QOL: Current Complications of the Design and Placements of Ureteric Stents. Res Reports Urol. 2020 Jul;Volume 12:303–14.

31. Zhang K, Cui H, Jiang H, Hao Y, Long R, Ma Q, et al. The current status and applications of ureteral stents. Int J Clin Exp Med. 2020;13(4):2122–33.

32. Herdman JP. Polythene tubing in the experimental surgery of the ureter. Br J Surg. 1949 Jul;37(145):105–6.

33. Williams KG, Blacker AJ, Kumar P. Ureteric stents: The past, present and future. J Clin Urol. 2018 Jul 31;11(4):280–4.

34. Tunney M. Comparative assessment of ureteral stent biomaterial encrustation. Biomaterials. 1996;17(15):1541–6.

35. Khandwekar AP, Doble M. Physicochemical characterisation and biological evaluation of polyvinylpyrrolidone-iodine engineered polyurethane (Tecoflex®). J Mater Sci Mater Med. 2011 May 25;22(5):1231–46.

36. Forbes C, Scotland KB, Lange D, Chew BH. Innovations in Ureteral Stent Technology. Urol Clin North Am. 2019 May;46(2):245–55.

37. Stoller ML, Meng M V., editors. Urinary Stone Disease The Practical Guide to Medical and Surgical Management. In: Illustrate. Springer Science & Business Media,; 2007. p. 694.

38. Gadzhiev N, Gorelov D, Malkhasyan V, Akopyan G, Harchelava R, Mazurenko D, et al. Comparison of silicone versus polyurethane ureteral stents: a prospective controlled study. BMC Urol. 2020 Dec 3;20(1):10.

39. Krasovskaya SM, Uzhinova LD, Andrianova MY, Prischenko AA, Livantsov MV, Lomonosov MV. Biochemical and physico-chemical aspects of biomaterials calcification. Biomaterials. 1991 Nov;12(9):817–20.

40. Chew BH, Denstedt JD. Technology Insight: novel ureteral stent materials and designs. Nat Clin Pract Urol. 2004 Nov;1(1):44–8.

41. Rebl H, Renner J, Kram W, Springer A, Fritsch N, Hansmann H, et al. Prevention of Encrustation on Ureteral Stents: Which Surface Parameters Provide Guidance for the Development of Novel Stent Materials? Polymers (Basel). 2020 Mar 3;12(3):558.

42. Liatsikos EN, Karnabatidis D, Katsanos K, Kallidonis P, Katsakiori P, Kagadis GC, et al. Ureteral Metal Stents: 10-Year Experience With Malignant Ureteral Obstruction Treatment. J Urol. 2009 Dec;182(6):2613–8.

43. Rosman BM, Barbosa JABA, Passerotti CP, Cendron M, Nguyen HT. Evaluation of a novel gel-based ureteral stent with biofilm-resistant characteristics. Int Urol Nephrol. 2014 Jun 24;46(6):1053–8.

44. Ganatra AM, Loughlin KR. The Management of Malignant Ureteral Obstruction Treated with Ureteral Stents. J Urol. 2005 Dec;174(6):2125–8.

45. Asakawa J, Iguchi T, Tamada S, Ninomiya N, Kato M, Yamasaki T, et al. Outcomes of indwelling metallic stents for malignant extrinsic ureteral obstruction. Int J Urol. 2018 Mar;25(3):258–62.

46. Elsamra SE, Leavitt DA, Motato HA, Friedlander JI, Siev M, Keheila M, et al. Stenting for malignant ureteral obstruction: Tandem, metal or metal-mesh stents. Int J Urol. 2015 Jul;22(7):629–36.

47. Barros AA, Oliveira C, Lima E, Duarte ARC, Healy K, Reis RL. 7.41 Ureteral Stents Technology: Biodegradable and Drug-Eluting Perspective. In: Comprehensive Biomaterials II. Elsevier; 2017. p. 793–812.

48. Chen Y, Liu C, Zhang Z, Xu P, Chen D, Fan X, et al. Malignant ureteral obstruction: experience and comparative analysis of metallic versus ordinary polymer ureteral stents. World J Surg Oncol. 2019 Dec 30;17(1):74.

49. Modi AP, Ritch CR, Arend D, Walsh RM, Ordonez M, Landman J, et al. Multicenter Experience with Metallic Ureteral Stents for Malignant and Chronic Benign Ureteral Obstruction. J Endourol. 2010 Jul;24(7):1189–93.

50. Buchholz N, Hakenberg O, Bach C, Masood J. Handbook of Urinary Stents: Basic Science and Clinical Applications. Buchholz N, Hakenberg O, Bach C, Masood J, editors. JP Medical Ltd; 2016. 345 p.

51. Turk T, Rao M, Polcari A. Updates on the use of ureteral stents: focus on the Resonance® stent. Med Devices Evid Res. 2010 Dec;11.

52. Blaschko SD, Deane LA, Krebs A, Abdelshehid CS, Khan F, Borin J, et al. In-Vivo Evaluation of Flow Characteristics of Novel Metal Ureteral Stent. J Endourol. 2007 Jul;21(7):780–3.

53. Miyazaki J, Onozawa M, Takahashi S, Maekawa Y, Yasuda M, Wada K, et al. The resonance® metallic ureteral stent in the treatment of malignant ureteral obstruction: a prospective observational study. BMC Urol. 2019 Dec 27;19(1):137.

54. Pedro RN, Hendlin K, Kriedberg C, Monga M. Wire-Based Ureteral Stents: Impact on Tensile Strength and Compression. Urology. 2007 Dec;70(6):1057–9.

55. Agrawal S, Brown CT, Bellamy EA, Kulkarni R. The thermo-expandable metallic ureteric stent: an 11-year follow-up. BJU Int. 2009 Feb;103(3):372–6.

56. Kallidonis P, Kotsiris D, Sanguedolce F, Ntasiotis P, Liatsikos E, Papatsoris A. The effectiveness of ureteric metal stents in malignant ureteric obstructions: A systematic review. Arab J Urol. 2017 Dec 18;15(4):280–8.

57. Chung KJ, Park BH, Park B, Lee JH, Kim WJ, Baek M, et al. Efficacy and Safety of a Novel, Double-Layered, Coated, Self-Expandable Metallic Mesh Stent (Uventa TM) in Malignant Ureteral Obstructions. J Endourol. 2013 Jul;27(7):930–5.

58. Pollak JS, Rosenblatt MM, Egglin TK, Dickey KW, Glickman M. Treatment of Ureteral Obstructions with the Wallstent Endoprosthesis: Preliminary Results. J Vasc Interv Radiol. 1995 May;6(3):417–25.

59. Bahouth Z, Moskovitz B, Halachmi S, Nativ O. Allium Stents: A Novel Solution for the Management of Upper and Lower Urinary Tract Strictures. Rambam Maimonides Med J. 2017 Oct 16;8(4):e0043.

60. Hendlin K, Korman E, Monga M. New Metallic Ureteral Stents: Improved Tensile Strength and Resistance to Extrinsic Compression. J Endourol. 2012 Mar;26(3):271–4.

61. Wang L, Yang G, Xie H, Chen F. Prospects for the research and application of biodegradable ureteral stents: from bench to bedside. J Biomater Sci Polym Ed. 2018 Sep 22;29(14):1657–66.

62. Schlick RW, Planz K. Potentially useful materials for biodegradable ureteric stents. BJU Int. 1997 Dec;80(6):908–10.

63. Olweny EO, Landman J, Andreoni C, Collyer W, Kerbl K, Onciu M, et al. Evaluation of the Use of a Biodegradable Ureteral Stent After Retrograde Endopyelotomy in a Porcine Model. J Urol. 2002 May;167(5):2198–202.

64. Lumiaho J, Heino A, Tunninen V, Ala-Opas M, Talja M, Valinaa T, et al. New Bioabsorbable Polylactide Ureteral Stent in the Treatment of Ureteral Lesions: An Experimental Study. J Endourol. 1999 Mar;13(2):107–12.

65. Li G, Wang Z-X, Fu W-J, Hong B-F, Wang X-X, Cao L, et al. Introduction to biodegradable polylactic acid ureteral stent application for treatment of ureteral war injury. BJU Int. 2011 Feb

66. Lumiaho J, Heino A, Pietiläinen T, Ala-Opas M, Talja M, Välimaa T, et al. The morphological, in situ effects of a self-reinforced bioabsorbable polylactide (SR-PLA 96) ureteric stent; an experimental study. J Urol. 2000 Oct;164(4):1360–3.

67. Yang G, Xie H, Huang Y, Lv Y, Zhang M, Shang Y, et al. Immersed multilayer biodegradable ureteral stent with reformed biodegradation: An in vitro experiment. J Biomater Appl. 2017 Mar 8;31(8):1235–44.

68. Zhang Y, He J, Chen H, Xiong C. A new hydrophilic biodegradable ureteral stent restrain encrustation both in vitro and in vivo. J Biomater Appl. 2020 Aug 16;088532822094937.

69. Soria F, de la Cruz JE, Budia A, Serrano A, Galan-Llopis JA, Sanchez-Margallo FM. Experimental Assessment of New Generation of Ureteral Stents: Biodegradable and Antireflux Properties. J Endourol. 2020 Mar 1;34(3):359–65.

70. Hadaschik BA, Paterson RF, Fazli L, Clinkscales KW, Shalaby SW, Chew BH. Investigation of a Novel Degradable Ureteral Stent in a Porcine Model. J Urol. 2008 Sep;180(3):1161–6.

71. Chew BH, Paterson RF, Clinkscales KW, Levine BS, Shalaby SW, Lange D. In Vivo Evaluation of the Third Generation Biodegradable Stent: A Novel Approach to Avoiding the Forgotten Stent Syndrome. J Urol. 2013 Feb;189(2):719–25.

72. Lingeman JE, Preminger GM, Berger Y, Denstedt JD, Goldstone L, Segura JW, et al. Use of a Temporary Ureteral Drainage Stent After Uncomplicated Ureteroscopy: Results From a Phase II Clinical Trial. J Urol. 2003 May;169(5):1682–8.

73. Lingeman JE, Schulsinger DA, Kuo RL. Phase I Trial of a Temporary Ureteral Drainage Stent. J Endourol. 2003 Apr;17(3):169–71.

74. Barros AA, Rita A, Duarte C, Pires RA, Sampaio-Marques B, Ludovico P, et al. Bioresorbable ureteral stents from natural origin polymers. J Biomed Mater Res Part B Appl Biomater. 2015 Apr 26;103(3):608–17.

75. Barros AA, Oliveira C, Lima E, Duarte ARC, Reis RL. Gelatin-based biodegradable ureteral stents with enhanced mechanical properties. Appl Mater Today. 2016 Dec;5:9–18.

76. Barros AA, Oliveira C, Ribeiro AJ, Autorino R, Reis RL, Duarte ARC, et al. In vivo assessment of a novel biodegradable ureteral stent. World J Urol. 2018 Feb 11;36(2):277–83.

77. Reis R, Duarte AR, Barros A, Lima E, Oliveira C, Pinto J. An ureteral stent, methods and uses thereof. WO2016181371A1, 2016.

78. Lock JY, Wyatt E, Upadhyayula S, Whall A, Nuñez V, Vullev VI, et al. Degradation and antibacterial properties of magnesium alloys in artificial urine for potential resorbable ureteral stent applications. J Biomed Mater Res Part A. 2014 Mar;102(3):781–92.

79. Zhang S, Bi Y, Li J, Wang Z, Yan J, Song J, et al. Biodegradation behavior of magnesium and ZK60 alloy in artificial urine and rat models. Bioact Mater [Internet]. 2017 Jun;2(2):53–62.

80. Tie D, Liu H, Guan R, Holt-Torres P, Liu Y, Wang Y, et al. In vivo assessment of biodegradable magnesium alloy ureteral stents in a pig model. Acta Biomater. 2020 Oct;116:415–25

81. Jin L, Yao L, Yuan F, Dai G, Xue B. Evaluation of a novel biodegradable ureteral stent produced from polyurethane and magnesium alloys. J Biomed Mater Res Part B Appl Biomater. 2020 Sep 14;jbm.b.34730.

82. Aljihmani L, Alic L, Boudjemline Y, Hijazi ZM, Mansoor B, Serpedin E, et al. Magnesium-Based Bioresorbable Stent Materials: Review of Reviews. J Bio- Tribo-Corrosion. 2019 Mar 16;5(1):26.

83. Mostaed E, Sikora-Jasinska M, Drelich JW, Vedani M. Zinc-based alloys for degradable vascular stent applications. Acta Biomater. 2018 Apr;71:1–23.

84. Zheng YF, Gu XN, Witte F. Biodegradable metals. Mater Sci Eng R Reports. 2014 Mar;77:1–34.

85. Hernández-Escobar D, Champagne S, Yilmazer H, Dikici B, Boehlert CJ, Hermawan H. Current status and perspectives of zinc-based absorbable alloys for biomedical applications. Acta Biomater. 2019 Oct;97:1–22.

86. Liu Q, Li A, Liu S, Fu Q, Xu Y, Dai J, et al. Cytotoxicity of Biodegradable Zinc and Its Alloys: A Systematic Review. J Funct Biomater. 2023 Apr 7;14(4):206.

87. Seitz J, Durisin M, Goldman J, Drelich JW. Recent Advances in Biodegradable Metals for Medical Sutures: A Critical Review. Adv Healthc Mater. 2015 Sep 14;4(13):1915–36.

88. Chowdhury S, Yadaiah N, Prakash C, Ramakrishna S, Dixit S, Gupta LR, et al. Laser powder bed fusion: a state-of-the-art review of the technology, materials, properties & defects, and numerical modelling. J Mater Res Technol. 2022 Sep;20:2109–72.

89. Mei D, Wang C, Nienaber M, Pacheco M, Barros A, Neves S, et al. Corrosion behavior of Mg wires for ureteral stent in artificial urine solution. Corros Sci. 2021 Aug;189:109567

90. Niu J, Huang H, Pei J, Jin Z, Guan S, Yuan G. Research and development strategy for biodegradable magnesium-based vascular stents: a review. Biomater Transl. 2021;2(3):236–247.

91. Witte F. The history of biodegradable magnesium implants: A review☆. Acta Biomater. 2010 May;6(5):1680–92.

92. Rola P, Włodarczak S, Doroszko A, Lesiak M, Włodarczak A. The bioresorbable magnesium scaffold (Magmaris)—State of the art: From basic concept to clinical application. Catheter Cardiovasc Interv. 2022 Nov 13;100(6):1051–8.

93. Seitz J-M, Lucas A, Kirschner M. Magnesium-Based Compression Screws: A Novelty in the Clinical Use of Implants. JOM. 2016 Apr 7;68(4):1177–82.

94. Windhagen H, Radtke K, Weizbauer A, Diekmann J, Noll Y, Kreimeyer U, et al. Biodegradable magnesium-based screw clinically equivalent to titanium screw in hallux valgus surgery: short term results of the first prospective, randomized, controlled clinical pilot study. Biomed Eng Online. 2013 Dec 3;12(1):62.

95. Waizy H, Diekmann J, Weizbauer A, Reifenrath J, Bartsch I, Neubert V, et al. In vivo study of a biodegradable orthopedic screw (MgYREZr-alloy) in a rabbit model for up to 12 months. J Biomater Appl. 2014 Jan 3;28(5):667–75.

96. shin WJ, Chung YW, Kim S Do, An K-Y. Additional fixation using a metal plate with bioresorbable screws and wires for robinson type 2B clavicle fracture. Clin Shoulder Elb. 2020 Dec 1;23(4):205–9.

97. Lock JY, Draganov M, Whall A, Dhillon S, Upadhyayula S, Vullev VI, et al. Antimicrobial properties of biodegradable magnesium for next generation ureteral stent applications. In: 2012 Annual International Conference of the IEEE Engineering in Medicine and Biology Society. IEEE; 2012. p. 1378–81.

98. Mcfarlane JP, Cowan C, Holt SJ, Cowan MJ. Outpatient ureteric procedures: a new method for retrograde ureteropyelography and ureteric stent placement. BJU Int. 2001 Feb 16;87(3):172–6.

99. Lingeman JE, Preminger GM, Berger Y, Denstedt JD, Goldstone L, Segura JW, et al. Use of a Temporary Ureteral Drainage Stent After Uncomplicated Ureteroscopy: Results From a Phase II Clinical Trial. J Urol. 2003 May;169(5):1682–8.

100. Ren Z, Fu G, Liu F, Mao S, Gao R, Jiang J, et al. Elucidation of laser irradiation behaviors associated with the keyhole dynamics during laser powder bed fusion. J Mater Res Technol. 2024 Sep;32:1672–82.

101. Julmi S, Abel A, Gerdes N, Hoff C, Hermsdorf J, Overmeyer L, et al. Development of a Laser Powder Bed Fusion Process Tailored for the Additive Manufacturing of High-Quality Components Made of the Commercial Magnesium Alloy WE43. Materials (Basel). 2021 Feb 13;14(4):887.

102. Korei N, Solouk A, Haghbin Nazarpak M, Nouri A. A review on design characteristics and fabrication methods of metallic cardiovascular stents. Mater Today Commun. 2022 Jun;31:103467.

103. Dev Singh D, Mahender T, Raji Reddy A. Powder bed fusion process: A brief review. Mater Today Proc. 2021;46:350–5.

104. Martin AA, Calta NP, Khairallah SA, Wang J, Depond PJ, Fong AY, et al. Dynamics of pore formation during laser powder bed fusion additive manufacturing. Nat Commun. 2019 Apr 30;10(1):1987.

105. Oliveira JP, LaLonde AD, Ma J. Processing parameters in laser powder bed fusion metal additive manufacturing. Mater Des. 2020 Aug;193:108762.

106. Leśniak D, Zasadziński J, Libura W, Gronostajski Z, Śliwa R, Leszczyńska-Madej B, et al. Latest advances in extrusion processes of light metals. Arch Civ Mech Eng. 2024 Jun 20;24(3):184.

107. Nienaber M, Bramkamp S, Ben Khalifa N, Bohlen J. How alloying and processing effects can influence the microstructure and mechanical properties of directly extruded thin zinc wires. Mater Sci Eng A. 2024 Jul;905:146720.

108. Yadav RR, Dewang Y, Raghuvanshi J. A study on metal extrusion process. Int J LNCT. 2018;2(6).

109. Nienaber M, Yi S, Kainer KU, Letzig D, Bohlen J. On the Direct Extrusion of Magnesium Wires from Mg-Al-Zn Series Alloys. Metals (Basel). 2020 Sep 9;10(9):1208.

110. Nienaber M, Braatz M, Ben Khalifa N, Bohlen J. Property profile development during wire extrusion and wire drawing of magnesium alloys AZ31 and ZX10. Mater Des. 2022 Dec;224:111355.

111. Pan C, Han Y, Lu J. Structural Design of Vascular Stents: A Review. Micromachines. 2021 Jun 29;12(7):770.

112. Vanaei S, Hashemi M, Solouk A, Asghari Ilani M, Amili O, Hefzy MS, et al. Manufacturing, Processing, and Characterization of Self-Expanding Metallic Stents: A Comprehensive Review. Bioengineering. 2024 Sep 29;11(10):983.

SECTION 2

EXPERIMENTAL SECTION

CHAPTER II

MATERIALS AND METHODS

OVERVIEW

In this chapter it is described the specifications of the materials and methodology used to the development and characterization of the biodegradable metal samples and stent prototypes. Five extruded Mg-based extruded wires (AZ31, Mg-1Zn, Mg-1Y, pure Mg and Mg-4Ag) were studied in terms of corrosion in urinary tract environment in order to select the best performed one. Then two different ureteral stent processing techniques, coiled, extruded wire and additive manufactured (AM, through powder bed fusion laser beam (PBF-LB)), were used to produce Mg-based biodegradable ureteral stent prototypes. The entire process of optimization and production of these devices is explained, as well as respective corrosion characterization and biological activity, the biocompatibility and antibacterial potential.

II-1. MATERIALS

II-1.1. Extruded Mg-based wires

In the first part of this study, chapter III, five different extruded wires were tested in static and dynamic conditions using artificial urine solution (AUS). AZ31 is a widely used magnesium alloy composed primarily of aluminum (3%), zinc (1%), and magnesium. It is valued for its good mechanical properties, biocompatibility, and ease of processing(1). The addition of aluminum improves strength and ductility, while zinc enhances corrosion resistance(2–4). Mg-1Zn is a magnesium alloy containing 1% zinc by weight. Zinc serves as an alloying element to refine the microstructure, improve mechanical strength, and provide moderate corrosion resistance(4). Its simple composition minimizes potential toxicity, making it suitable for biomedical applications(5). Mg-1Y contains 1% yttrium, a rare earth element that enhances the alloy's mechanical properties and corrosion resistance(6). The addition of yttrium refines the grain structure and promotes the formation of stable oxide layers, resulting in a controlled degradation profile(7). Additionally, Mg-1Y contributes to antibacterial activity(8). Pure Mg is known for its high biocompatibility and simple degradation behavior, making it a baseline material for evaluating the performance of magnesium alloys(9). Its primary limitation is its rapid corrosion rate, which can lead to premature degradation in biological environment(6). Mg-4Ag is an alloy containing 4% silver, designed to combine the mechanical benefits of magnesium with the antibacterial properties of silver, which makes Mg-Ag particularly advantageous for biomedical applications in infection-prone environments such as the urinary tract(10–12).

II-1.2. Additive Manufactured (AM) samples

WE43

WE43 is a magnesium alloy containing yttrium (Y), Neodymium (Nd), and a small amount of zirconium (Zr), known for its excellent combination of biodegradability, biocompatibility, and mechanical properties. WE43 is widely considered a leading material for use in biodegradable implants(13,14). The alloying elements significantly enhance the WE43 corrosion resistance and mechanical stability, addressing the challenges associated with pure magnesium's rapid degradation in physiological environments. These properties make WE43 of particular interest for applications as temporary implants. WE43 has been used for producing complex and patient-specific geometries through AM, including PBF-LB(15–17). The rapid solidification during PBF-LB further refines the alloy's microstructure, expected to enhance its mechanical performance and corrosion resistance. These attributes make WE43 an ideal material for creating complex, biodegradable medical devices such as stents, scaffolds, and other load-bearing implants.

Mg1Y

Mg-1Y, processed using PBF-LB, combines the inherent properties of magnesium with the structural and functional advantages of additive manufacturing(15). PBF-LB technique allows for the creation of highly intricate geometries and controlled microstructures and the addition of yttrium enhances the alloy's grain refinement, mechanical properties, and corrosion resistance(18). The rapid solidification during PBF-LB further improves the alloy's microstructure, which is expected to result in a more uniform degradation behaviour(19). These improvements make additively manufactured Mg-1Y particularly suitable for biomedical applications, such as stents, where precise control over design and degradation rates is critical.

II-2. METHODS

II-2.1. Wire extrusion and coiling

The extrusion process is a widely used technique in the manufacturing of metallic wires due to its ability to produce components with precise dimensions, great surface quality, and refined microstructure. The wire extrusion process ensures consistent wire diameter and is a cost-effective and scalable method, suitable for industrial production. During the extrusion process, a ram pushes the billet

through the die, that has the desired cross-sectional shape. The extrusion is a versatile technique that enables the tailoring of the billet's material properties to achieve specific mechanical characteristics, given the possibility to change the processing parameters, which influence the extruded material's microstructure permitting its refinement(3). The temperature, extrusion rate and extrusion ratio (the ratio of the billet's initial cross-sectional area to its final cross-sectional area) are the parameters that are usually changed to optimize the microstructural characteristics of the metals(3,20).

The extruded magnesium (Mg) wires were subsequently shaped into a helical configuration using a Simplex Rapid dual-point spring coiler. The resulting coiled tubes had an external diameter of 2.33 mm, with the coils tightly wound to ensure no spacing between them.

II-2.1.1. Mg wires extrusion

Pure Mg and 4 Mg alloys (AZ31, Mg-1Zn, Mg-1Y, and Mg-4Ag), used during this work, were cast from the original alloying elements and machined into billets for wire extrusion. The chemical composition of the wires was determined through different techniques, namely, X-ray micro fluorescence (μXRF), used to detect Y, Mn, Al, and Zn; atomic absorption spectrometer (AAS), used to detect Ag and trace elements Fe, Cu, and Ni; and inductively coupled plasma optical emission spectrometry (ICP-OES), used to measure Si. The wires were produced by direct extrusion with 1- or 0.6-mm diameter. Pre-heated cast billets of the materials were used for the extrusion in a 2.5 MN automatic extrusion press and an associated coupled coiler. The extrusion was performed using a die with four nozzles of 0.6 or 1 mm diameter equidistant from the center position, corresponding to an extrusion ratio of 1:625. Extrusion parameters were set to 0.15-0.2 $mm \cdot s^{-1}$ ram speed and 350 ºC for the container as well as the billets. The microstructure of the wires was assessed by optical microscopy (OM) observation. The samples were prepared by grinding with 1200 and 4000 grit silicon carbide papers followed by polishing with water-free oxide polishing suspension (OPS) and 0.15 μm diamond suspension. The polished samples were etched for 10 seconds in standard picric acid solution of 5 ml H2O, 7 ml acetic acid, 200 ml ethanol, and 10 g of picric acid.

II-2.2. Additive manufacturing

Additive manufacturing (AM) represents a versatile technique for fabricating complex, high-precision structures layer-by-layer, directly from digital models. AM is a cutting-edge technology where the parts are constructed based on a 3D computer-aided design (CAD) model via layer-by-layer building. PBF-LB is the most popular AM process, it is very suitable for small volume and fine detail structures,

and offers distinctive characteristics for processing metallic materials(21–23). The building process takes place in a closed chamber with a controlled environment. During the printing, a powder layer is spread in the building plate, and the high-energy laser beam (energy source) selectively melts the freshly deposited powder layer, fusing the powder particles together in specific areas based on the 2D layer cross-section of the 3D CAD model previously prepared. The building plate then lowers at a distance equal to the layer thickness established, and a new layer is deposited for a new laser action. This sequence repeats until the printing is finished(22). The constructs' microstructure, mechanical performance, and corrosion behavior can be controlled by adjusting the scanning path to ensure a stable melting pool. The melt pool's characteristics are influenced by several parameters, such as laser power, hatch distance, layer thickness, laser spot size, and scanning speed(24). These parameters influence the melt pool's cooling rate, shape, spacing, and overlapping(25). The entire process is carried out in an argon-filled chamber to minimize oxidation of the magnesium powder and improve the quality of the fabricated parts. Understanding and optimizing these processes is fundamental to obtaining the desired part's characteristics. One of the main advantages of PBF-LB is the possibility of producing highly precise thin structures often unattainable with traditional manufacturing techniques. For this reason, AM has revolutionized various industries, including biomedical engineering(23). Thin-walled biomedical implants, such as stents, are used daily in the hospital for many different pathologies, so the research for improving these devices is crucial.

In this study, magnesium-based powders, specifically WE43 (a magnesium alloy containing rare-earth elements) and Mg-1Y (a magnesium alloy with 1% yttrium), were processed using PBF-LB technique. This approach enabled the fabrication of thin walls, tubes, wires, and meshed tubular structures, which were further evaluated for their potential application in ureteral stents.

II-2.2.1. AM samples production

WE43-based constructs produced for this work were printed using gas-atomized powder of a WE43 alloy of particle size of 25-67 μm. The powder processing through PBF-LB was performed with an EOS M100 printer under argon atmosphere (O2<0.1%). The samples produced were wires with a diameter of 1 mm and 30 mm height and tubes with an internal diameter of ca. 1.57 mm, external diameter of ca. 2.33 mm, and height of 22 mm. The scan pattern was 67º rotation between each layer, the layer thickness was set to 0.03 mm, and the laser spot diameter was 0.08 mm, for all the samples,

as previously optimized(16,17). The hatch distance was varied between 0.04-0.06 mm, to maintain the values optimized in previous works and maintain low energy density values.

For Mg-1Y-based structures, the Mg-1Y powder was produced by gas atomization, acquired from Nanoval GmbH & CO with a d50 of 39.4 µm. The thin-walled samples (5 x 10 mm) were built using Aconity™ MIDI. The work started by an optimization process where several single tracks per print were produced by combining different values of scanning speed, laser modulation width, laser power and laser modulation frequency, for modulated wave (MW) mode, and combining values of scanning speed and laser power for continuous wave (CW) mode. To produce the single tracks, the hatch distance was set to 1 mm, so the walls are produced by one single scan line. Each track had a length of 10 mm. The layer thickness was 20 µm, the spot size 80 µm and the gas flow was set to 1 m/s for all the prints.

For the meshed tubes, the same Mg-1Y powder was used. The tubes' meshed wall shape was prepared on Autodesk Fusion 360, using a standard meshed tube model, and printed using the Aconity™ MIDI 3D printer. The dimensions of the samples were in accordance with standard internal and external diameters of ureteral stents. The printing parameters were the ones optimized in the Mg-1Y-based thin-walled samples, namely, MW, 50 mm/s speed, 50 W laser power, 0.01 MHz laser modulation frequency, 75 µs laser modulation width and 1 m/s gas flow, 20 µm layer thickness and 80 µm spot size diameter under an argon gas atmosphere.

II-2.3. *In vitro* simulated urinary tract conditions – dynamic system

The corrosion experiments were carried out in dynamic conditions using artificial urine solution (AUS). The AUS composition is in accordance with the ASTM F 1828 – 97, with the following chemical composition: 3 g/L ammonium chloride (NH_4Cl), 2 g/L creatinine ($C_4H_7N_3O$), 2.5 g/L disodium hydrogen orthophosphate anhydrous (Na_2HPO_4), 2.5 g/L potassium dihydrogen orthophosphate (KH_2PO_4), 9 g/L sodium chloride (NaCl), 2.620 g/L sodium sulfite (Na_2SO_3) and 25 g/L urea (CH_4N_2O). A small amount of 0.015 g/L of sodium azide (NaN_3) was added to avoid bacterial contamination during experiments. Before starting the experiments, the samples were cleaned by immersion in pure ethanol and sonicated for 5 minutes to remove any contaminant or dirt. The experimental setup used for the corrosion tests is presented in **Figure II 1**. This dynamic system allows for the independent evaluation of up to 12 samples. The samples were placed inside 3.18 mm diameter plastic tubes, which were positioned inside a holder equipped with a water-recirculating system for thermal control, with the thermostat set to 37 ºC. Each sample support was connected to a common AUS reservoir (10L) and its dedicated pumping

channel. The AUS flow for in vitro studies of urinary devices is not well defined so we can find various flow rates in the literature (26–29). In the experiments conducted for this study, the AUS flow rate was set at 0.25 ml/min for wire samples and 0.5 ml/min for stent prototypes. This adjustment was based on sample size and design considerations: the lower flow rate was applied to wires due to their thinner geometry and to the fact that these samples are far for representing a stent, while the higher flow rate was used for stent prototypes as they more closely resembled actual ureteral stents. The samples were collected and reserved for analysis after defined time points that ranged from 30 minutes to 4 weeks.

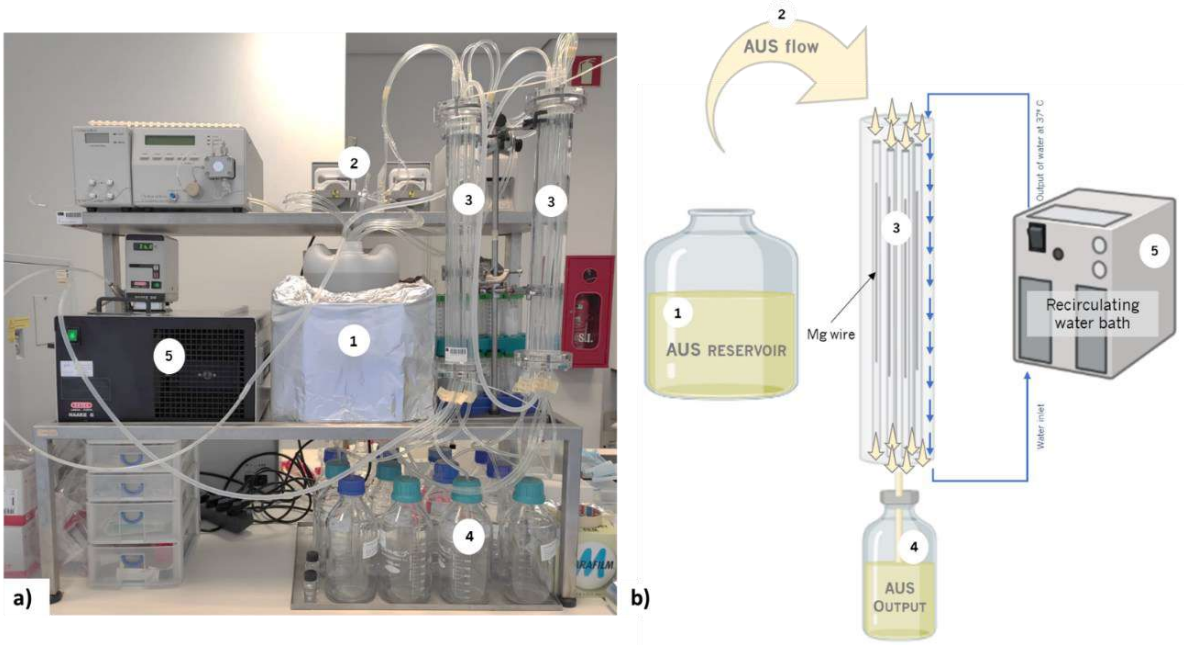


Figure II 1 Dynamic experimental setup. a) Photo, b) schematic. 1. Artificial urine reservoir; 2. Peristaltic pumps; 3. vessel with the tubes containing each sample; 4. Flasks collecting the artificial urine solution (AUS) after passing through the samples; 5. Thermostat to maintain 37 ºC in the vessel containing the samples.

II-2.3.1. AUS at different pH

The influence of pathological AUS with acidic or alkaline pH on corrosion behavior of Mg-based samples was studied in some experiments in order to evaluate if the pH changes induced by Mg alloys would be different for different initial AUS pHs. To that end, the initial pH was adjusted to 4.13 and 7.97 for acidic and alkaline conditions, by adding HCl and NaOH, respectively, and the pH was monitored after 2h, 24h and 48h.

II-2.4. Samples' microstructure and powder analysis

Understanding the microstructure of materials is essential for evaluating their corrosion behavior. For extruded and AM samples, microstructure analysis provides critical insights into the material's grain size, shape, phase distribution, melt pools' shape and the presence of defects such as porosity or secondary phases. These characteristics are essential to understand important features such as the degradation rate and uniformity of corrosion(3,30,31).

The microstructure of the extruded wires was assessed by light optical microscopy (LOM) observation. The samples were prepared by grinding with 1200 and 4000 grit silicon carbide papers followed by polishing with water-free oxide polishing suspension (OPS) and 0.15 µm diamond suspension. The polished samples were etched for 10 seconds in standard picric acid solution of 5 ml H2O, 7 ml acetic acid, 200 ml ethanol, and 10 g of picric acid.

To study the WE43-based AM samples' microstructure, the samples were mounted in conductive resin with carbon fiber and ground with silicone carbide papers (P320 and P800) for 1 min, followed by polishing using diamond suspension (1µm) for 12 minutes. Finally, the samples were etched with 2% Nital solution (2% nitric acid in ethanol) for 5 seconds before microstructural analysis using LOM.

Mg1Y powder surface morphology and cross section, and the as-built Mg-1Y-based constructs were characterized by scanning electron microscopy - energy dispersive spectroscopy (SEM-EDS). To prepare for SEM analysis, the samples (Mg-1Y-based powder or constructs) were embedded in resin, in a polyethylene mounting mold and left do dry. After drying, the samples were removed from the mold and grinded with SiC foil 320 grit for 1 minute in water, followed by a polishing sequence starting with MD-largo foil with DiaPro Allegro/Largo 9 µm for 5 min, MD—Dac foil with DiaPro Dac 3 µm for 4 min, MD-Nap with DiaPro Nap B 1 µm for 3 min and finalized with OP-Chem with OP-U NonDry for 1.5 minutes. After polishing, the samples were rinsed with pure ethanol. Before SEM analysis, the samples were sputtered with gold platinum for improved visualization.

II-2.5. Corrosion layer – chemical characterization

The corrosion layer developed on the samples' surface after exposed to AUS, during the experiments was accessed through different chemical characterization techniques and imaging. The following subsections will detail the techniques used.

II-2.5.1. X-ray photoelectron spectroscopy (XPS)

XPS works by irradiating the sample with X-rays, leading to the emission of photoelectrons from the surface. By measuring the kinetic energy and number of these emitted electrons, XPS is able to identify the elements present on the sample surface and their relative concentrations, as well as their chemical bonding(32). For the characterization works performed, the analysis were conducted using an XPS instrument with an Al Kα X-ray source (1486.6 eV). Survey scans were initially performed to identify the elements present on the surface, followed by high-resolution scans of specific peaks to investigate the chemical states of the elements.

In the works performed, the elemental analysis of the layer formed on the metal's surface after incubation in AUS was analyzed using an XPS equipped with a non-monochromated Mg Kα (hν=1253.6 eV) operated at 300W and monochromated and non-monochromated Al Kα (hν=1486.68 eV) sources, operated at 220W. Some of the measurements were done using Kratos Axis-Supra instrument equipped with a monochromatic X-ray Al Ka (1486.6 eV) source operated at 225 W. Al Kα sources were used to record Mg1s spectra. XPS spectra were collected at pass energies of 200 eV and 50 eV for survey spectra and individual elements, respectively, or 160 eV for survey spectra and 20 eV for individual elements. The energy step for individual elements was 0.1eV. The XPS spectra were peak-fitted using Avantage data processing software. For peak fitting, the Shirley-type background subtraction was used. Quantification has been done using sensitivity factors provided by the Avantage library.

II-2.5.2. Raman spectroscopy

Raman spectroscopy measures the scattering of light by the sample, providing information about the vibrational modes of the molecules in the material. A laser beam is focused on the sample, and the scattered light is collected and analyzed. A small fraction of the scattered light will have a different frequency than the incident laser light, due to interactions with the molecular vibrations in the sample. These frequency shifts are characteristic of the material and can be used to identify its components(33).

Raman spectroscopy measurements were carried out at room temperature in a back scattering geometry on an alpha300 R confocal Raman microscope (WITec) or LabRam Soleil from Horiba Scientific using a 532 nm Nd:YAG laser for excitation. The laser beam (laser spot 1 μm^2) with P=15 mW was focused on the sample by a ×50 lens (Zeiss), and the spectra were collected with a 600 groove/mm grating using 10 acquisitions with a 2 s acquisition time. Some of the samples were analyzed.

II-2.5.3. Fourier transform infrared spectroscopy (FTIR)

FTIR is a technique that analyses the absorption of infrared light by a material to identify its chemical components and study their interactions. A beam of infrared light is passed through the sample, and the instrument measures the amount of light absorbed at each wavelength. The resulting spectrum is a unique fingerprint of the material, reflecting its molecular composition and structure(34).

For the FTIR analysis, the corrosion layer on the sample's surface was scraped and the whitish corrosion layer powder was analyzed in a Shimadzu-IR Prestige 21 spectrometer. The spectral region analyzed was 600 - 4000 cm^{-1} with a resolution of 4.0 for 32 number of scans. The analysis was done at least 3 times for the same sample.

II-2.5.4. X-ray Diffraction (XRD)

XRD is technique used to characterize the crystalline structure of materials. A beam of X-rays is targeted at the sample, and the scattered X-rays are detected. When the X-rays interact with the ordered arrangement of atoms in a crystalline material, they diffract in specific directions, creating a diffraction pattern. This pattern is unique to the crystal structure of the material and can be used to identify the phases present.

XRD was employed as one of the methods to evaluate the chemical composition of the samples' corrosion layer. It was used the high-resolution Bragg-Brentano (Bruker D8 Advance DaVinci(35)) equipped with Cu Kα radiation (λ = 1.506 Å), produced at 40 kV and 40 mA. Data were collected in the 2θ range of 5-70° and 1 s per step.

II-2.5.5. Scanning electron microscopy - energy dispersive spectroscopy (SEM-EDS)

Scanning Electron Microscopy (SEM) provides high-resolution imaging by scanning the sample with a focused electron beam, which interacts with the surface to produce secondary electrons, resulting in detailed surface topography images. Energy Dispersive Spectroscopy (EDS) was used for elemental analysis. When the electron beam interacts with the sample, it induces the emission of characteristic X-rays from elements present on the surface. The EDS detector collects these X-rays, and their energy is analyzed to identify the elemental composition of the sample's surface. This allows for qualitative and semi-quantitative analysis of the elements present(36).

The surface morphology of the samples, with and without corrosion products, was observed using SEM equipped with EDS for corrosion layer chemical characterization. The accelerating voltages

used were 10 and 15 eV. The samples with the corrosion layer were sputtered before SEM with a gold layer for better conductivity and to avoid the charge effect. SEM-EDS was also used for microstructure analysis and Mg-1Y powder characterization (see **section II-2.4**. for the sample's preparation). Before SEM analysis, the samples were sputtered with gold platinum for improved visualization. The accelerating voltages used were 10 and 15 eV.

II-2.6. Corrosion

The corrosion rate was calculated according to ASTM G1-03 using the following equation:

$$Corrosion\ rate = (K \times W)(A \times T \times D),$$

where K is a constant that is defined depending on the corrosion rate units defined, which in this case is millimeters per year (mm/y); thus $K = 8.76 \times 10^4$;

T is the time of exposure in hours

A is the area of the specimen in cm^2

W is the mass loss in grams

D is the density in g/cm^3, which is 1.74 g/cm^3 for pure Mg. Minor deviation of alloys density from this value was neglected.

The mass loss was calculated from the difference between the initial mass of the sample and after collection from AUS, after removing all the residues from the surface through a cleaning process. The cleaning step consisted of the immersion of the metallic samples in a solution composed of 200 g/L chromium (VI) oxide, 10 g/L silver nitrate, and 20 g/L barium nitrate, following ASTM G1-03, until the corrosion layer disappears. Then the samples were immersed in water followed by ethanol for a few seconds and left to air dry before weighting.

II-2.6.1. Profilometry

Profilometry is a surface characterization technique used to measure the topography and roughness of materials with high precision. In this work, a focus variation system was employed, which combines optical microscopy and focus detection to create 3D surface maps. This technique works by capturing images at various focal depths as the system scans across the surface. The sharpest focus points at each location are used to reconstruct the sample's topography, providing accurate

measurements of surface features without physically contacting the material. Focus variation profilometry is particularly useful for analysing complex surfaces, for example, caused by processes like corrosion.

In this study, 3D Focus Variation Optical Profilometry was used to evaluate the surface roughness of as-printed Mg-1Y-based thin walls and corrosion of magnesium alloy-based extruded wires, after removal of corrosion layer. The samples were washed by immersion in absolute ethanol under sonication (35 KHz) for 5 minutes and left to dry before measurements. For corrosion analysis, the surface of each sample was initially observed using a 10 x lens, providing a field of view of 1 x 2 mm^2. For roughness calculations, the image size was reduced to a final area of 0.5 x 2 mm^2. For the printed samples, six individual images were taken with 50 x lens, which provided a field of view of 400x400 μm^2. These images were used to calculate the roughness parameters. To obtain an overview of the surface, the samples were also imaged with the 10 x objective lens that provides an image of 2x2 mm^2.

II-2.6.2. Inductively coupled plasma optical emission spectroscopy (ICP-OES)

ICP-OES is an analytical technique used to measure the concentration of elements in liquid samples with high sensitivity and precision. During the analysis, the sample is carried into an inductively coupled plasma (a high-temperature ionized gas) that excites the atoms and ions of the elements present. As the excited atoms return to their ground state, they emit light at characteristic wavelengths specific to each element. The emitted light is dispersed and detected by an optical spectrometer, which quantifies the concentration of each element based on the intensity of the emitted light. In this work, ICP-OES was used to quantify the release of magnesium and alloying element ions from the AUS samples collected along the experiment. The AUS samples collected were filtered with a 0.22 μm filter and diluted in a 1:10 ratio with deionized water. Finally, a mixture with 90% nitric acid and 10% AUS solution was prepared before the ICP analysis. The nitric acid solution comprised 5% nitric acid (69%) and deionized water.

II-2.6.3. Micro-Computed Tomography (Micro-CT)

Micro-Computed Tomography (Micro-CT) is a non-destructive imaging technique that provides high-resolution, 3D visualization of the internal structure of samples. It uses X-rays to capture detailed cross-sectional images, which are then reconstructed into 3D models. Micro-CT allows for the analysis of both the external and internal features of materials, including porosity, cracks, and surface changes(37). In this study, micro-CT was used to monitor the corrosion of the Mg-based samples over time. The technique enabled the observation of corrosion progression and volume loss.

The 3D reconstruction of the samples in the different time points was accessed using a high - resolution Micro-CT, with a pixel size of 15 μm and voltage range of 50 kV current source 200 μA. App 250 projections were obtained over a rotation angle of 360°, rotation step of 0.3°. Data sets were reconstructed using standardized cone-beam reconstruction software (NRecon 1.6.10.2, Bruker). A representative dataset of the slices was segmented into binary images with a dynamic threshold of 48-250. The binary images were used for the morphometric analysis (CT Analyser, v1.15.4.0, Bruker, USA). The percentage of object volume was accessed.

II-2.7. Interaction of Mg-based samples with cells

II-2.7.1. Cell lines

Cell lines are populations of immortalized cells that can be cultured and propagated in vitro over extended periods. These models provide standardized and reproducible methods for studying cellular responses to materials by evaluating, for example, the cytotoxicity. By maintaining consistent characteristics across experiments, cell lines are widely used in biomedical research as reliable representations of specific tissue types or biological systems.

II-2.7.1.1. L929

The L929 cell line, derived from mouse fibroblasts, is a well-established model for cytotoxicity testing. It is commonly used to assess the biocompatibility of biomaterials. This cell line is referred in international standards such as ISO 10993-5. Therefore this cell line was used in this work for a firs biocompatibility.

II-2.7.1.2. G/G cell line

The G/G cell line (ACC 224) is derived from the urinary bladder of mouse. These cells are a great model for studying interactions of materials in the urinary tract environment. In this work this cell line was used to understand if urinary tract-derived cells would behave differently from the standardized L929.

II-2.7.2. Cytotoxicity assay

The cytotoxicity of metal extracts was performed using mouse fibroblast L929 cell line and G/G cell line as models. L929 cells were cultured in Dulbecco's modified eagle medium (DMEM) with 10% fetal bovine serum (FBS) and 1% antibiotic/antimycotic and G/G in 45% Ham's F10 and 45% DMEM with 10% FBS, 5 μg/ml human insulin, 5 μg/ml human transferrin, 50 nM hydrocortisone, 5 ng/ml selenite

and 1% antibiotic/antimycotic. The samples were sterilized by UV exposure for 30 min, after washing them with absolute ethanol and sonication. To prepare the extracts, each metal was incubated with cell culture media for 24h in a humidified incubator at 37°C with 5% CO_2 and an area/volume ratio of 300 mm^2/ml, or was incubated with the respective cell culture media for 24 h at 37 °C with constant agitation and an area/volume ratio of 27.5 mm^2/ml and 300 mm^2/ml, according to the ISO 10993-12. Nitinol wire was used as a control, given its wide use in biomedical devices. The extracts were applied to cells as direct, 100% extract, and lower concentrations, 50%, 25%, and 12.5%, prepared by diluting the original extract in cell culture media. Nitinol control's extract was used only as direct (100% extract). A positive control (C^+), containing only cells with culture media, and a negative control (C^-), with 25% DMSO, were also applied. The cells were seeded in 96 well plates with a cell density of 1×10^4 for L929 and 0.8×10^4 cells *per* well for 24h in a humidified incubator at 37°C with 5% CO_2. The cell media in each well was replaced by the Mg alloys' extracts at different concentrations and controls. After incubation for 24 h in a humidified incubator at 37°C with 5% CO_2, the cell viability was determined by incubation (3 - 4h) with 3-(4,5-dimethylthiazol-2-yl)-5-(3-carboxymethoxyphenyl)-2-(4-sulfophenyl)-2H-tetrazolium, inner salt – MTS. This method is based on the capacity of metabolically active cells to reduce MTS into a colored formazan. The amount of formazan produced is then quantified by measuring the absorbance at 490 nm, which is proportional to the metabolic active (living) cells. The results were represented as percentage of living cells, taking the C^+ as the reference of maximum viability (100%). To complement the MTS assay, the Live/Dead cell viability assay was performed to observe the viable and dead cells, after contacting with the metals' extracts. This is a color-based method to determine viable and non-viable cells, simultaneously, based on the membrane integrity. The procedure to obtain the metal extracts and the exposure of the cells to the extracts was the same as the one described before for MTS assay. After the 24h incubation with the extracts, the cell layer was washed with phosphate-buffered saline (PBS) and DMEM supplemented with 2 µL/ml Calcein-AM and 1µg/ml Propidium Iodide (PI) was added in each well. The cells were incubated for 10 minutes in the dark at 37°C with 5% CO_2 and then the media with the dyes was removed. The cell layers were washed again, and then new PBS was added in each well. The cells were observed in the fluorescence microscope (Microscope DM6 B, Leica), where the living cells were fluorescent green and the dead cells fluorescent red. This method is based on the cell membrane integrity. The cell membrane is permeable to calcein-AM, which will be converted in a fluorescent green calcein by the esterase activity of living cells. The PI becomes fluorescent when binds

to double stranded DNA, but this compound is membrane impermeant of live cells, thus, it is used to identify non-viable cells.

II-2.8. Antibacterial activity

Magnesium alloys, including Mg-1Y, have gained attention for their intrinsic antibacterial properties, which are particularly valuable in biomedical applications. The antibacterial activity of Mg alloys arises primarily from their corrosion products, specifically, OH^- and Mg^{2+}(38,39). The constantly corrosion surface and the released products create an environment that is unfavorable for bacterial adhesion to the surface and growth. Stent-associated urinary tract infections are among the most prevalent stent-related symptoms reported and *Escherichia coli (E. coli)* and *Staphylococcus aureus (S. aureus)* are the most common strains found(40–42).

To evaluate the antibacterial potential of AM samples, both by avoiding surface bacteria attachment or by the release of corrosion products to the surrounding media, Gram-positive and Gram-negative strains were used, *S. aureus* ATCC 25923 (American Type Culture Collection, Manassas, VA, USA) and *E. coli* ATCC 25922 (Microbiologics, Inc., Saint Cloud, MN, USA). The AM samples, exposed surface area/bacterial suspension volume of 27.5 mm^2/ml, were cleaned by immersion in absolute ethanol and sonicated for 5 minutes and then sterilized by exposition to UV light for 30 minutes. Nitinol was used as control and it was prepared the same way as the AM samples. C^+ was the positive control, which were the bacteria suspension without any sample. The bacteria strains were inoculated using tryptic soy broth (TSB) and incubated overnight under constant agitation at 150 rpm at 37°C. The optical density (O.D.) of the culture was then adjusted to an O.D. of 0.08-0.1 at 600 nm, using TSB to dilute accordingly. Two serial dilutions of the prepared inoculum were done in order to obtain a final concentration of 1-2 x 10^6 cloning forming units (CFUs)/ml. The AM and nitinol samples were placed inside the wells of a 12-well plate and 2 ml of the prepared bacteria suspension was placed afterwards. The plates were incubated at 37°C under constant agitation at 150 rpm for 24 h. To access the amount of bacteria attached to the samples' surface, the metals were removed from the wells using a sterile clamp, washed by immersion in PBS, to remove the non-adherent bacteria, and placed inside a tube with 1 ml PBS. Two cycles of 30 s. of vortexing were applied with a cycle of sonication (5 min, 3500 Hz) between the vortexing cycles. Then serial dilutions were performed and the suspensions were spread into TSB/agar petri dishes for CFU counting. The petri dishes were incubated at 37°C for 24h. To access the amount of bacteria in suspension, 100 µL of suspension was collected from each well and serial

dilutions were performed. The diluted suspensions were spread in petri dishes and incubated at 37°C for 24h as well. After the 24h incubation, the CFU number was accessed.

II-3. Statistical analysis

All quantitative data are presented as mean ± standard deviation (SD). The data and respective statistical analysis were treated on GraphPad Prism 9 software. Statistical significances ($*p \leq 0.05$, $**p \leq 0.01$ and $***p \leq 0.001$) were determined using specific statistical tests described in the subsection of materials and methods in the different chapters, where three to five replicates were used.

II-4. References

1. Song Y, Shan D, Chen R, Zhang F, Han E-H. Biodegradable behaviors of AZ31 magnesium alloy in simulated body fluid. Mater Sci Eng C. 2009;29(3).

2. Song Y, Shan D, Chen R, Zhang F, Han E-H. Biodegradable behaviors of AZ31 magnesium alloy in simulated body fluid. Mater Sci Eng C. 2009 Apr;29(3):1039–45.

3. M. R, P. S. Review on the effect of different processing techniques on the microstructure and mechanical behaviour of AZ31 Magnesium alloy. J Magnes Alloy. 2021 Sep;9(5):1692–714.

4. Jiang P, Blawert C, Zheludkevich ML. The Corrosion Performance and Mechanical Properties of Mg-Zn Based Alloys—A Review. Corros Mater Degrad. 2020 Apr 23;1(1):92–158.

5. Cai S, Lei T, Li N, Feng F. Effects of Zn on microstructure, mechanical properties and corrosion behavior of Mg–Zn alloys. Mater Sci Eng C. 2012 Dec;32(8):2570–7.

6. Johnson I, Liu H. A Study on Factors Affecting the Degradation of Magnesium and a Magnesium-Yttrium Alloy for Biomedical Applications. Zheng J, editor. PLoS One. 2013 Jun 14;8(6):e65603.

7. Sudholz AD, Gusieva K, Chen XB, Muddle BC, Gibson MA, Birbilis N. Electrochemical behaviour and corrosion of Mg–Y alloys. Corros Sci. 2011 Jun;53(6):2277–82.

8. Lock JY, Wyatt E, Upadhyayula S, Whall A, Nuñez V, Vullev VI, et al. Degradation and antibacterial properties of magnesium alloys in artificial urine for potential resorbable ureteral stent applications. J Biomed Mater Res Part A. 2014 Mar;102(3):781–92.

9. Gao J-C, Qiao L-Y, Xin R-L. Effect of Mg2+ concentration on biocompatibility of pure magnesium. Front Mater Sci China. 2010 Jun 4;4(2):126–31.

10. Nomier Y, Meiβner J, Kietzmann M. Novel Study Antimicrobial and Biocompatibility Effect of Magnesium Silver Alloys 1% on Bovine Bacterial Species. Mestorino N, editor. Vet Med Int. 2023 Jan 27;2023(1).

11. Tie D, Feyerabend F, Müller W-D, Schade R, Liefeith K, Kainer K, et al. Antibacterial biodegradable Mg-Ag alloys. Eur Cells Mater. 2013 Jun 16;25:284–98.

12. Liu Z, Schade R, Luthringer B, Hort N, Rothe H, Müller S, et al. Influence of the Microstructure and Silver Content on Degradation, Cytocompatibility, and Antibacterial Properties of Magnesium ‐ Silver Alloys In Vitro. Kolisek M, editor. Oxid Med Cell Longev. 2017 Jan 22;2017(1).

13. Dvorský D, Kubásek J, Vojtěch D. AZ31 and WE43 Alloys for Biomedical Applications. Solid State Phenom. 2017 Nov 27;270:205–11.

14. Byun S, Lim H, Cheon K, Lee S, Kim H, Lee J. Biodegradable magnesium alloy (WE43) in bone ‐ fixation plate and screw. J Biomed Mater Res Part B Appl Biomater. 2020 Aug 12;108(6):2505 – 12.

15. Hyer H, Zhou L, Benson G, McWilliams B, Cho K, Sohn Y. Additive manufacturing of dense WE43 Mg alloy by laser powder bed fusion. Addit Manuf. 2020 May;33:101123.

16. Åhman HN, D'Elia F, Mellin P, Persson C. Microstructural Origins of the Corrosion Resistance of a Mg-Y-Nd-Zr Alloy Processed by Powder Bed Fusion - Laser Beam. Front Bioeng Biotechnol. 2022;10(917812).

17. Nilsson Åhman H, Thorsson L, Mellin P, Lindwall G, Persson C. An Enhanced Understanding of the Powder Bed Fusion–Laser Beam Processing of Mg-Y3.9wt%-Nd3wt%-Zr0.5wt% (WE43) Alloy through Thermodynamic Modeling and Experimental Characterization. Materials (Basel). 2022 Jan 6;15(2):417.

18. Chen C, Ling C, Shao Y, Yang Y, Wang D, Shuai C. Quasicrystal-strengthened biomedical magnesium alloy fabricated by laser additive manufacturing. J Alloys Compd. 2023 Jun;947:169555.

19. Julmi S, Abel A, Gerdes N, Hoff C, Hermsdorf J, Overmeyer L, et al. Development of a Laser Powder Bed Fusion Process Tailored for the Additive Manufacturing of High-Quality Components Made of the Commercial Magnesium Alloy WE43. Materials (Basel). 2021 Feb 13;14(4):887.

20. Nienaber M, Bohlen J, Yi S, Kurz G, Kainer KU, Letzig D. Influence of Ca addition on the dynamic and static recrystallization behavior of direct extruded flat profiles of Mg-Y-Zn alloy. J Magnes Alloy. 2023 Oct;11(10):3736–48.

21. Wu Z, Narra SP, Rollett A. Exploring the fabrication limits of thin-wall structures in a laser powder bed fusion process. Int J Adv Manuf Technol. 2020 Sep 11;110(1–2):191–207.

22. Singh R, Gupta A, Tripathi O, Srivastava S, Singh B, Awasthi A, et al. Powder bed fusion process in additive manufacturing: An overview. Mater Today Proc. 2020;26:3058–70.

23. Liu J, Liu B, Min S, Yin B, Peng B, Yu Z, et al. Biodegradable magnesium alloy WE43 porous scaffolds fabricated by laser powder bed fusion for orthopedic applications: Process optimization, in vitro and in vivo investigation. Bioact Mater. 2022 Oct;16:301–19.

24. Li Z, Xu R, Zhang Z, Kucukkoc I. The influence of scan length on fabricating thin-walled components in selective laser melting. Int J Mach Tools Manuf. 2018 Mar;126:1–12.

25. Abdelmoula M, Musinski W. Predicting and correlating melt pool characteristics with processing parameters in IN625 powder bed fusion additive manufacturing. J Manuf Process. 2024 Jul;121:427–45.

26. Kazmierska KA, Thompson R, Morris N, Long A, Ciach T. In Vitro Multicompartmental Bladder Model for Assessing Blockage of Urinary Catheters: Effect of Hydrogel Coating on Dynamics of Proteus mirabilis Growth. Urology. 2010 Aug;76(2):515.e15-515.e20.

27. Azevedo AS, Almeida C, Gomes LC, Ferreira C, Mergulhão FJ, Melo LF, et al. An in vitro model of catheter-associated urinary tract infections to investigate the role of uncommon bacteria on the Escherichia coli microbial consortium. Biochem Eng J. 2017 Feb;118:64–9.

28. Tian Y, Cai X, Wazir R, Wang K, Li H. Water consumption and urinary tract infections: an in vitro study. Int Urol Nephrol. 2016 Jun 18;48(6):949–54.

29. Kim K-W, Choi YH, Lee SB, Baba Y, Kim H-H, Suh S-H. Analysis of Urine Flow in Three Different Ureter Models. Comput Math Methods Med. 2017;2017:1–11.

30. Feng J, Zhang D, Hu H, Zhao Y, Chen X, Jiang B, et al. Improved microstructures of AZ31 magnesium alloy by semi-solid extrusion. Mater Sci Eng A. 2021 Jan;800:140204.

31. Nilsson Åhman H, D'Elia F, Mellin P, Persson C. Microstructural Origins of the Corrosion Resistance of a Mg-Y-Nd-Zr Alloy Processed by Powder Bed Fusion – Laser Beam. Front Bioeng Biotechnol. 2022 Jul 1;10.

32. Isaacs MA, Davies-Jones J, Davies PR, Guan S, Lee R, Morgan DJ, et al. Advanced XPS characterization: XPS-based multi-technique analyses for comprehensive understanding of functional materials. Mater Chem Front. 2021;5(22):7931–63.

33. Cialla-May D, Schmitt M, Popp J. Theoretical principles of Raman spectroscopy. Phys Sci Rev. 2019 May 27;4(6).

34. Guerrero‐Pérez MO, Patience GS. Experimental methods in chemical engineering: Fourier transform infrared spectroscopy—FTIR. Can J Chem Eng. 2020 Jan 3;98(1):25–33.

35. Khan H, Yerramilli AS, D'Oliveira A, Alford TL, Boffito DC, Patience GS. Experimental methods in chemical engineering: X‐ray diffraction spectroscopy— XRD. Can J Chem Eng. 2020 Jun 3;98(6):1255–66.

36. Girão AV, Caputo G, Ferro MC. Application of Scanning Electron Microscopy–Energy Dispersive X-Ray Spectroscopy (SEM-EDS). In 2017. p. 153–68.

37. Keklikoglou K, Arvanitidis C, Chatzigeorgiou G, Chatzinikolaou E, Karagiannidis E, Koletsa T, et al. Micro-CT for Biological and Biomedical Studies: A Comparison of Imaging Techniques. J Imaging. 2021 Sep 1;7(9):172.

38. Lin Z, Sun X, Yang H. The Role of Antibacterial Metallic Elements in Simultaneously Improving the Corrosion Resistance and Antibacterial Activity of Magnesium Alloys. Mater Des . 2021 Jan;198:109350.

39. Feng H, Wang G, Jin W, Zhang X, Huang Y, Gao A, et al. Systematic Study of Inherent Antibacterial Properties of Magnesium-based Biomaterials. ACS Appl Mater Interfaces. 2016 Apr 20;8(15):9662–73.

40. Domingues B, Pacheco M, Cruz JE, Carmagnola I, Teixeira‐Santos R, Laurenti M, et al. Future Directions for Ureteral Stent Technology: From Bench to the Market. Adv Ther. 2022 Jan 17;5(1):2100158.

41. Pérez-Fentes D, Aranda-Pérez J, de la Cruz JE, Soria F. Indications, Complications and Side Effects of Ureteral Stents. In: Urinary Stents. Cham: Springer International Publishing; 2022. p. 5–20. 42. Vallée M, Bey E, Bouiller K, le Goux C, Pimpie R, Tourret-Arnaud J, et al. Epidemiology and risk factors for ureteral stent-associated urinary tract infections in non-transplanted renal patients: a systematic review of the literature. World J Urol. 2021 Oct 15;39(10):3845–60.

SECTION 3

EXPERIMENTAL STUDIES

CHAPTER III

UNDERSTANDING THE CORROSION OF MG ALLOYS IN *IN VITRO* URINARY TRACT CONDITIONS: A STEP FORWARD TOWARDS A BIODEGRADABLE METALLIC URETERAL STENT.

UNDERSTANDING THE CORROSION OF MG ALLOYS IN *IN VITRO* URINARY TRACT CONDITIONS: A STEP FORWARD TOWARDS A BIODEGRADABLE METALLIC URETERAL STENT.

ABSTRACT

Ureteral stents play a fundamental role in modern time urology. However, following the deployment, stent-related symptoms are frequent and affect patient health and quality of life. Using biodegradable metals as ureteral stent materials have emerged as a promising strategy, mainly due to the improved radial force and slower degradation rate expected. Therefore, this study aimed to characterize different biodegradable metals in urinary tract environment to understand their propensity for future utilization as base materials for ureteral stents. The corrosion of 5 Mg alloys – AZ31, Mg-1Zn, Mg-1Y, pure Mg, and Mg-4Ag – under simulated urinary tract conditions was accessed. The corrosion layer of the different alloys presented common elements, such as $Mg(OH)_2$, MgO, and phosphate-containing products, but slight variations in their chemical compositions were detected. The corrosion rate of the different metals varied, which was expected given the differences in the corrosion layers. On top of this, the findings of this study highlighted the significant differences in the samples' corrosion and corrosion layers when in stagnant and flowing conditions. With the results of this study, we concluded that Mg-1Zn and Mg-4Ag presented a higher propensity for localized corrosion, probably due to a less protective corrosion layer; Mg-4Ag corroded faster than all the other four alloys, and Mg-1Y stood out due to its distinct corrosion pattern, that showed to be more homogeneous than all the other four samples, making this one more attractive for the future studies on biodegradable metals.

Keywords: Biodegradable metals; magnesium alloys; localized corrosion; biodegradable metallic ureteral stent.

This chapter is based on the following pu blication: **Margarida Pacheco**, Ivo M. Aroso, Joana M. Silva, Sviatlana V. Lamaka, Jan Bohlen, Maria Nienaber, Dietmar Letzig, Estêvão Lima, Alexandre A. Barros, Rui L. Reis. Understanding the corrosion of Mg alloys in in vitro urinary tract conditions: A step forward towards a biodegradable metallic ureteral stent. J Magnes Alloys. 2023 Dec; DOI: 10.1016/j.jma.2023.10.002

III-1. Introduction

Ureteral stenting is a daily practice and a fundamental indwelling procedure in modern urology. Since its first description in 1949(1), the use of ureteral stents has broadened to various urological conditions where the normal urine flow from the kidney to the bladder is compromised or is predicted to become compromised (e.g., after surgery)(2,3). Initially, polyethylene(1,4) and silicone(5) were preferred as stent materials, but the polymer qualities improved over time, and currently, both traditional materials, such as silicone, and more recent polymers, such as polyurethane and polyurethane-based proprietary formulations developed by companies are used(2,3,6,7). Metallic-based stents are also currently used, usually made of nitinol(8,9) or nickel–cobalt–chromium–molybdenum alloy(10). These are preferable in benign or malign ureteric obstructions, given the increased radial force that makes them more resistant to high compression, compared with the polymeric counterparts(8–11).

Despite the obvious essential role in urology, ureteral stents are associated with severe adverse events, namely stent encrustation(12,13), bacterial colonization(14,15), stent migration(14), need for a second surgery for stent removal(16), the forgotten stent problem(16–18), among others(2,15). The problems associated with ureteral stents are recognized as severe challenges in urology, given the impact on the patient's health and the increased treatment cost. Therefore, the research community has focused on strategies to circumvent these issues by optimizing the stent design, application of drug-eluting technology, and surface modifications, which have efficiently reduced encrustation and biofilm formation(2,19–22). Despite these significant advancements, stent-related complications persist; hence, continuing the investigations and upgrading these devices is of utmost importance. The use of biodegradable materials for ureteral stents is the most recent approach, and this proposal has been gaining popularity given the expected lower propensity for bacteria and encrustation attachment and the elimination of the second surgery for the stent removal, standing out from non-degradable materials in this point(2,21,23). These features will diminish hospitalizations, reduce associated costs, and decrease patient pain and discomfort. Barros et al. have explored the potential of natural origin polymers – gelatin and alginate – as base materials for biodegradable ureteral stents(24–27), and these investigations lead to the development of HydrUStent®, the first biodegradable ureteral stent, presently in clinical trials(28). Another important work was reported by Soria *et al.*, where a biodegradable anti-reflux ureteral stent, BraidStent®, was shown to have adequate degradation – without formation of obstructive fragments – and avoid vesicoureteral reflux. The efficiency of BraidStent® was also shown to be similar to conventional stents(29,30). Apart from the promising works on biodegradable polymers, investigations

on biodegradable metals emerged. Zn, Fe, and Mg alloys are widely studied for biomedical applications, especially for cardiovascular stents and temporary bone-fixation implants, but for urology in particular, the studies available are scarce. Hence, it is essential to fill this gap, mainly because a biodegradable metallic ureteral stent is expected to have a high radial force and prolonged degradation time, compared with biodegradable polymers, expanding the utilization of biodegradable ureteral stents in endourology. Lock et al. explored the suitability of biodegradable metals for ureteral stents by investigating the antibacterial activity of Mg-4%Y (%wt), AZ31, and pure Mg(31). The authors confirmed that the *Escherichia coli* viable colonies diminished for all the Mg alloys, compared with conventional polyurethane(31). Zhang *et al.* studied the corrosion behavior and biocompatibility of pure Mg and ZK60 in artificial urine and rat's bladder(32). The results revealed that both metals were biocompatible and ZK60 degraded faster than pure Mg(32). Tie *et al.* described the behavior of Mg alloys in large animals(33). It was found that ZJ31 alloy had an homogeneous corrosion rate, was biocompatible and showed antibacterial activity, when compared with stainless steel(33). All these studies provided important findings about the biodegradable metal performance in urinary tract conditions, yet a standard method to carry out these experiments is missing, making the comparisons between different works more difficult. A recent paper published by our collaborating groups consisted on the study of pure Mg and Mg-1%(wt%)Zn for 72h in static conditions in artificial urine solution (AUS), according to the ASTM F1828-97(34). It was found that Mg-1Zn corrodes faster than pure Mg, and both materials are prone to localized corrosion(34). Moreover, encrustation risk is pointed as a factor to focus in further studies(34). Herein, the objective is to expand the amount of tested alloys to five, comparing their corrosion profile and propensity for encrustation. This complements the previous results especially due to following the established methods such as the use of standardized AUS, thus, enabling comparisons between different studies. In this work, five Mg alloys were studied under static and dynamic conditions, mimicking the urinary tract, with the objective to provide a more detailed understanding of the corrosion pattern and trend to form encrustation for a future utilization of Mg alloys as biodegradable ureteral stent materials.

III-2. MATERIALS AND METHODS

III-2.1. Preparation of samples – wire extrusion

Pure Mg and 4 Mg alloys (AZ31, Mg-1Zn, Mg-1Y, and Mg-4Ag) were cast from the original alloying elements and machined into billets for wire extrusion. The chemical composition of the wires was accessed through different techniques (**Table III 1**). X-ray micro fluorescence (μXRF, M4 Tornado,

Bruker) was used to detect Y, Mn, Al, and Zn. The elements Ag and trace elements Fe, Cu, and Ni were determined by atomic absorption spectrometer (AAS, 240FS AA, Agilent). Si was measured by inductively coupled plasma optical emission spectrometry (ICP-OES, Acros II FHX22, Spectro Ametek). Wires were produced by direct extrusion with ca. 1 mm diameter. Pre-heated cast billets of the materials were used for the extrusion in a 2.5 MN automatic extrusion press (Müller Engineering GmbH & Co. KG, Todtenweis/Sand, Germany) and an associated coupled coiler. The extrusion was performed with a die with four nozzles of 1 mm diameter equidistant from the center position, corresponding to an extrusion ratio of 1:625. Extrusion parameters were set to 0.15-0.2 $mm \cdot s^{-1}$ ram speed and 350 ºC for the container as well as the billets. A detailed description of the wire manufacturing procedure can be found elsewhere(35). The microstructure of the wires was assessed by optical microscopy (OM) observation. The samples were prepared by grinding with 1200 and 4000 grit silicon carbide papers followed by polishing with water-free oxide polishing suspension (OPS) and 0.15 µm diamond suspension. The polished samples were etched for 10 seconds in standard picric acid solution of 5 ml H_2O, 7 ml acetic acid, 200 ml ethanol, and 10 g of picric acid.

Table III 1 Chemical composition, in wt%, of the extruded Mg-based wires used in this work.

	X-ray micro fluorescence (µXRF)				**Atomic absorption spectrometer (AAS)**				**Inductively coupled plasma – optical emission spectrometry**
	Y	**Mn**	**Al**	**Zn**	**Ag**	**Fe**	**Cu**	**Ni**	**Si**
AZ31		0.23 wt%	2.79 wt%	0.99 wt%		0.0028 wt%	0.0031 wt%	0.0003	0.0157
Mg-1Zn				1.15 wt%		0.0018 wt%	0.0002 wt%	<0.0001	0.0041
Mg-1Y	0.79 wt%					0.0038 wt%	0.0003 wt%	<0.0001	0.0053
Pure Mg						0.0016 wt%	0.0008 wt%	<0.0001	0.0129
Mg-4Ag					4.01 wt%	0.0009 wt%	0.0002 wt%	<0.0001	0.4800

III-2.2. Experimental setup

The degradation/corrosion experiments were carried out in static and dynamic conditions using AUS. The AUS composition is in accordance with the ASTM F 1828 – 97 – see the composition in **Table III 2**. Following one of the standard's AUS compositions, a small amount of 0.015 g/L of sodium azide (NaN_3) and 2.62 g/L of sodium sulfite (Na_2SO_3), an efficient oxygen scavenger were added to avoid bacterial contamination during the experiments. Before starting the experiments, the samples were

cleaned by immersion in pure ethanol and sonicated for 5 minutes to remove any contaminant or dirt. For the static conditions, the samples (surface area of 3.79 cm^2, equal to ca. 7.57 $mm^2 \cdot ml$) were immersed in AUS for defined time points and maintained in a water bath at 37 ºC. The AUS was changed daily. An experimental setup was used for the dynamic conditions, allowing for the independent evaluation of up to 12 samples. The metallic wires (surface area of ca. 11 cm^2) were placed inside 3.18 mm diameter plastic tubes, which were positioned inside a holder equipped with a water-recirculating system for thermal control, with the thermostat set to 37 ºC. Each sample support was connected to a common AUS reservoir (10L) and its dedicated pumping channel. After passing through the samples, the AUS was collected in individual flasks. The AUS flow for in vitro studies of urinary devices is not well defined so we can find various flow rates in the literature (36–39). Herein, since we are working with thin devices (wires instead of a whole stent), the AUS flow was set to 0.25 ml/min, which is one of the lowest values used in other works. The AUS pH was measured at the beginning of the experiment, 6.89 (**Table III 2**), and after 2, 24, and 48h in contact with the alloys (static conditions). The influence of the AUS of pathological composition with acidic or alkaline pH on corrosion behavior of Mg alloys was also assessed in order to evaluate if the pH changes induced by Mg alloys would be different in different urine pHs. To that end, the initial pH was adjusted to 4.13 and 7.97 for acidic and alkaline conditions, by adding HCl and NaOH, respectively (**Table III 2**). The pH was monitored after 2h, 24h and 48h as well. However, since the neutral pH is the most representative for the urine, most of the degradation and surface characterization experiments were done at pH 6.89 (40).

The metallic samples were collected and reserved for analysis after one, two, and four weeks in contact with AUS (both in static and dynamic conditions). An optical photograph and a schematic of the dynamic system are presented in **Figure III 1.**

Table III 2 Chemical composition of the artificial urine solution (AUS) used in this study and respective concentration in g/L and mol/L, and the AUS pH in acidic, neutral and alkaline conditions.

Component	Amount (g) *per* L			Molar concentration (mol/L)
Ammonium chloride (NH_4Cl)	3.000			0.05600
Creatinine ($C_4H_7N_3O$)	2.000			0.01800
Disodium hydrogen orthophosphate, anhydrous (Na_2HPO_4)	2.500			0.01800
Potassium dihydrogen orthophosphate (potassium phosphate monobasic (KH_2PO_4))	2.500			0.01800
Sodium azide (NaN_3)	0.015			0.00023
Sodium chloride (NaCl)	9.000			0.15000
Sodium sulfite (Na_2SO_3)	2.620			0.02100
Urea (CH_4N_2O)	25.000			0.42000
$pH_{initial}$	**Acidic**	**Neutral**	**Alkaline**	
	4.13	6.89	7.97	

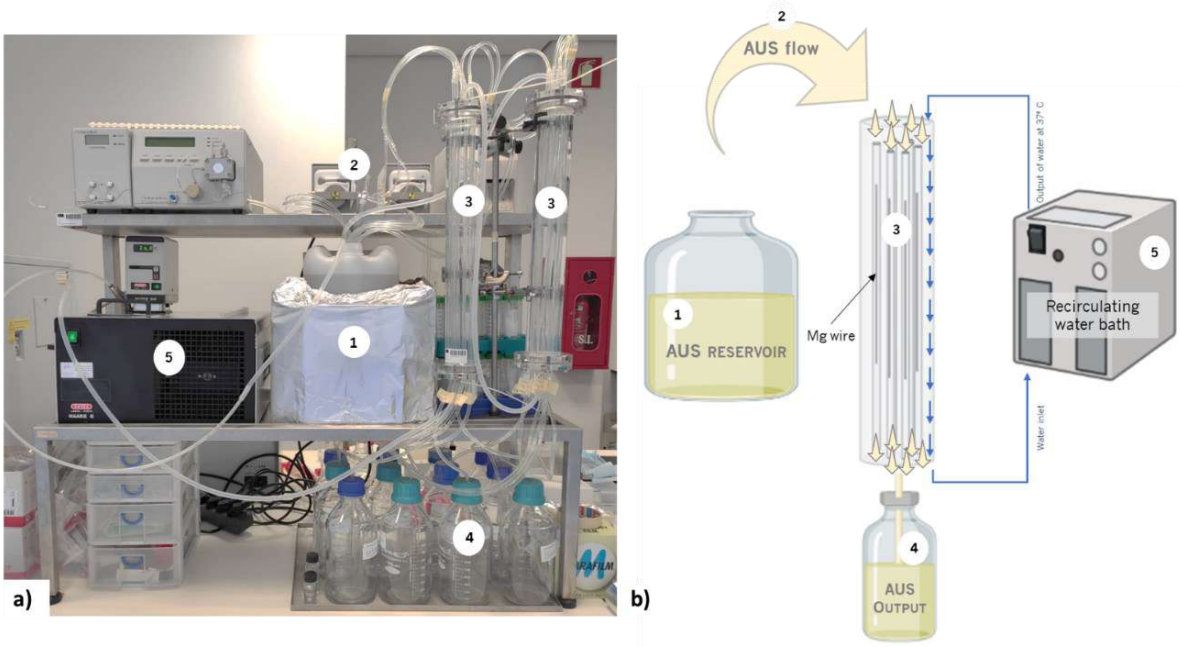


Figure III 1 Dynamic experimental setup. a) Photo, b) schematic. 1. Artificial urine reservoir; 2. Peristaltic pumps; 3. vessel with the tubes containing each sample; 4. Flasks collecting the artificial urine solution (AUS) after passing through the samples; 5. Thermostat to maintain 37 ºC in the vessel containing the samples.

III-2.3. Corrosion rate

The corrosion rate was calculated according to ASTM G1-03 using the following equation:

$$Corrosion\ rate = (K \times W)(A \times T \times D),$$

where K is a constant that is defined depending on the corrosion rate units defined, which in this case is millimeters per year (mm/y); thus $K = 8.76 \times 10^4$;

T is the time of exposure in hours

A is the area of the specimen in cm^2

W is the mass loss in grams

D is the density in g/cm^3, which is 1.74 g/cm^3 for pure Mg. Minor deviation of alloys density from this value was neglected.

The mass loss was calculated from the difference between the initial mass of the sample and after collection from AUS, after removing all the residues from the surface through a cleaning process. The cleaning step consisted of the immersion of the metallic samples in a solution composed of 200 g/L chromium (VI) oxide (Laborspirit), 10 g/L silver nitrate (Laborspirit), and 20 g/L barium nitrate (Laborspirit), following ASTM G1-03, until the corrosion layer disappears. Then the samples are immersed in water for a few seconds and left to air dry before weighting.

III-2.4. Profilometry

The surface profile was assessed using the 3D Focus Variation Optical Profilometry (InfiniteFocus, BRUKER-Alicona) technique after removing the layer of corrosion products, as described above (section 2.3). Each sample was initially observed employing a 10X lens, providing a field of view of 1x2 mm^2. The image size was reduced to 0.5x2 mm^2 final area for the roughness calculations.

III-2.5. X-ray photoelectron spectroscopy (XPS)

The elemental analysis of the layer formed on the metal's surface after incubation in AUS was analyzed using an X-ray inducted photoelectron spectroscopy (XPS, ESCALAB250Xi (ThermoFisherScientific)) equipped with a non-monochromated Mg Kα (hν=1253.6 eV) operated at 300W and monochromated and non-monochromated Al Kα (hν=1486.68 eV) sources, operated at 220W. Al Kα sources were used to record Mg1s spectra. XPS spectra were collected at pass energies of 200 eV and 50 eV for survey spectra and individual elements, respectively. The energy step for individual elements was 0.1eV. The XPS spectra were peak-fitted using Avantage data processing software. For

peak fitting, the Shirley-type background subtraction was used. Quantification has been done using sensitivity factors provided by the Avantage library.

III-2.6. Raman spectroscopy

Raman spectroscopy measurements were carried out at room temperature in a back scattering geometry on an alpha300 R confocal Raman microscope (WITec) using a 532 nm Nd:YAG laser for excitation. The laser beam (laser spot 1μm^2) with P=15 mW was focused on the sample by a ×50 lens (Zeiss), and the spectra were collected with a 600 groove/mm grating using 10 acquisitions with a 2 s acquisition time.

III-2.7. Scanning electron microscopy - energy dispersive spectroscopy (SEM/EDS)

The surface morphology of the metallic wires, with and without corrosion products, was observed using an analytical scanning electron microscope (SEM, JEOL JSM-6010LV) equipped with an energy dispersive X-ray spectroscopy (EDS, INCAx-Act, PentaFET Precision, Oxford Instruments). The accelerating voltages used were 10 and 15 eV. The samples with the corrosion layer were sputtered before SEM with a gold layer for better conductivity and to avoid the charge effect.

III-2.8. ICP-OES

The amount of cations released from the metallic wires to the AUS was accessed by analyzing the collected AUS aliquots through ICP-OES analysis (JY 2000 2, HORIBA JOBIN YVON). The AUS samples collected were filtered with a 0.22 µm filter and diluted in a 1:10 ratio with deionized water. Finally, a mixture with 90% nitric acid and 10% AUS solution was prepared before the ICP analysis. The nitric acid solution comprised 5% nitric acid (69%) and deionized water.

III- 2.9. Cytotoxicity

Mouse fibroblast L929 cell line was the model used to evaluate the cytotoxicity of the Mg alloys' extracts. The cells were cultured in Dulbecco's modified eagle medium (DMEM, Laborspirit) with 10% fetal bovine serum (FBS, ALFAGENE) and 1% antibiotic/antimycotic (ALFAGENE). To prepare the extracts, each metal was incubated with cell culture media for 24h in a humidified incubator at 37°C with 5% CO_2 and an area/volume ratio of 3 cm^2/ml, according to the ISO 10993-12. Nitinol wire (3 cm^2/ml) was used as a control, given its wide use in biomedical devices [1]. The extracts were applied to cells as direct, 100% extract (E100), and lower concentrations, 50% (E50), 25% (E25), and 12.5% (E12.5), prepared by diluting the original extract in cell culture media. Nitinol control (CTR_Nit)'s extract was used only as

direct (100% extract). A positive control (C^+), containing only cells with culture media, and a negative control (C^-), with 25% DMSO, were also applied. The L929 cells were seeded in 96 well plates with a cell density of 1×10^4 cells per well for 24h in a humidified incubator at 37°C with 5% CO_2. The cell media in each well was replaced by the Mg alloys' extracts at different concentrations and the controls. After incubation for 24h in a humidified incubator at 37°C with 5% CO_2, the cell viability was determined by incubation (3 - 4h) with 3-(4,5-dimethylthiazol-2-yl)-5-(3-carboxymethoxyphenyl)-2-(4-sulfophenyl)-2H-tetrazolium, inner salt – MTS. This method is based on the capacity of metabolically active cells to reduce MTS into a colored formazan. The amount of formazan produced is then quantified by measuring the absorbance at 490 nm, which is proportional to the metabolic active (living) cells. The results were represented as percentage of living cells, taking the positive control (C^+) as the reference of maximum viability (100%). To complement the MTS assay, the Live/Dead cell viability assay was performed to observe the viable and dead cells, after contacting with the metals' extracts. This is a color-based method to determine viable and non-viable cells, simultaneaously, based on the membrane integrity. The procedure to obtain the metal extracts and the exposure of the cells to the extracts was the same as the one described before for MTS assay. After the 24h incubation with the extracts, the cell layer was washed with phosphate-buffered saline (PBS) and DMEM supplemented with 2 µL/ml Calcein-AM (Biotium) and 1ug/ml Propidium Iodide (PI, Biotium) was added in each well. The cells were incubated for 10 minutes in the dark at 37°C with 5% CO_2 and then the media with the dyes was removed. The cell layers were washed again, and then new PBS was added in each well. The cells were observed in the fluorescence microscope (Microscope DM6 B, Leica), where the living cells were fluorescent green and the dead cells fluorescent red. This method is based on the cell mebrane integrity. The cell mebrane is permeable to calcein-AM, which will be converted in a fluorescent green calcein by the esterase activity of living cells. The PI becomes fluorescent when binds to double stranded DNA, but this compound is membrane impermeant of live cells, thus, it is used to identify non-viable cells.

III-2.10. Statistical analysis

In this work, the repeated measurements were represented as mean ± standard deviation. Statistically significant data was estimated through one-way analysis of variance (ANOVA). A statistically significant difference was considered at $p < 0.05$.

III-3. RESULTS AND DISCUSSION

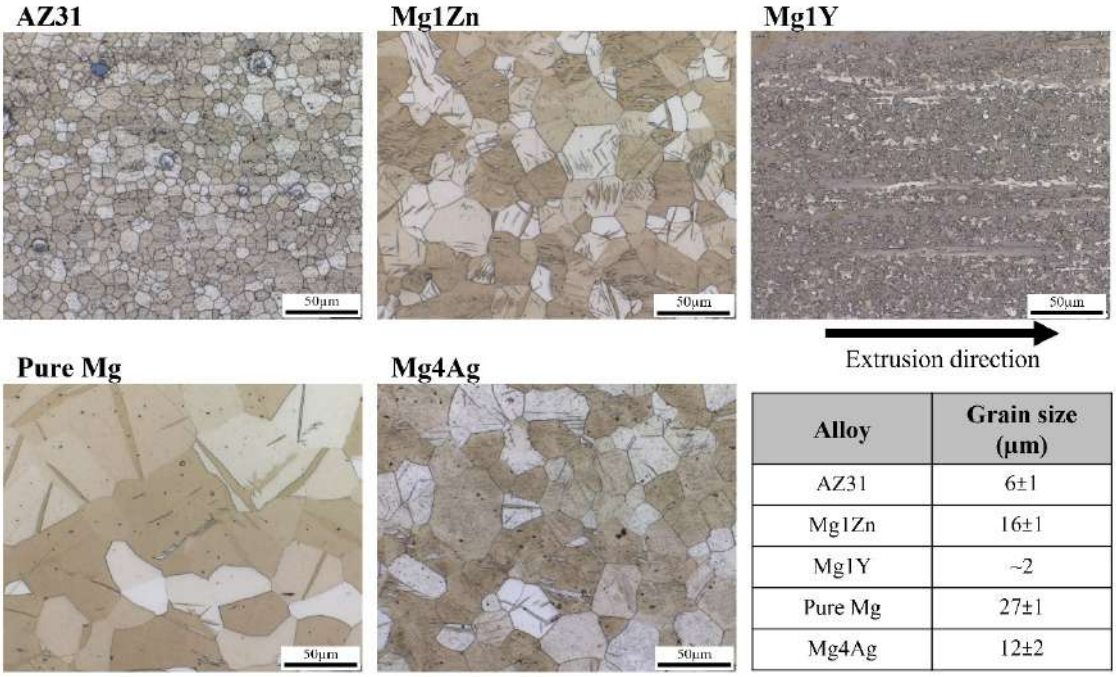
After incubation in AUS, a layer of corrosion products was visually observed in static and dynamic conditions. Once the corrosion products were removed, the corrosion impact was also seen on the magnesium wires at the naked eye. It was noticed at first sight that with time the corrosion increased, and some wires presented non-uniform corrosion. In the following sections, the chemical characterization of the corrosion layer, the corrosion, and its relation with each alloy's microstructure are discussed in detail.

III-3.1. Microstructure

Figure III 2 shows the microstructure of the Mg-wires in the extrusion direction obtained by OM. The visible elongated intragranular substructure (twins) in the microstructure are not related to the manufacturing process. The deformation twins are remnants of sample preparation, which is sometimes difficult to avoid, especially in coarse-grained microstructures (Pure Mg, Mg-1Zn, Mg-4Ag).

All of the microstructures, with the exception of Mg-1Y, show a fully recrystallized globular microstructure. Mg-1Y exhibit an inhomogeneous bimodal microstructure with non-recrystallized grains elongated parallel to extrusion direction. Very small grains surround these non-recrystallized grains.

Pure magnesium has the coarsest grain structure with an average grain size of 27 µm. The alloying elements cause grain refinement and, in the case of Mg-1Y, even a significant delay in recrystallization. With an average grain size of 2 µm, Mg-1Y is the finest grained, followed by AZ31 with 6 µm. There is only a minor difference in grain size between Mg-4Ag (12 µm) and Mg-1Zn (16 µm), although the Ag containing alloy has a more homogeneous grain structure. The grain structure of Mg-Zn alloy is clearly more inhomogeneous.



Alloy	Grain size (µm)
AZ31	6±1
Mg1Zn	16±1
Mg1Y	~2
Pure Mg	27±1
Mg4Ag	12±2

Figure III 2 Microstructure of the five extruded alloys studied in this work, obtained by optical microscopy, and respective grain size.

III-3.2. Corrosion layer – SEM analysis

All the samples submitted to static conditions, after 1 week, showed a corrosion layer characterized by the presence of geometrically defined fragments, resembling crystals. The corrosion layers presented a more amorphous structure for longer time points, characterized by a smoother aspect and cracks (**Figure III 3**). In dynamic conditions, the formation of crystal-like precipitates is not so evident as in static conditions, nor present for all samples (**Figure III 4**). This behavior might be related to the constant flow of AUS, which may force the more loosely attached agglomerates to be washed away, or the formation of smaller crystals is favored owing to the lower local concentration of the corresponding ionic constituents. The behavior of the different alloys is further discussed in detail below.

AZ31 and Mg-1Zn's corrosion layers have similar aspects in both static and dynamic conditions. The corrosion layers in dynamic conditions are smoother and present irregularly distributed cracks, even though, in some cases, it is possible to see defined crystal-like structures similar to the ones formed in static conditions. A point of localized corrosion is also evident for Mg-1Zn (arrow in **Figure III 3**), corroborating the results obtained by a previous work published by our collaborating groups, showing this process already occurring at 72h(34). Mg-1Y's corrosion layer presented smaller fragments in the first 2 weeks of dynamic conditions, whereas after that, both defined crystal-like structures and smooth

surfaces with cracks were formed (**Figure III 4**). On pure Mg, the corrosion layer is mostly smooth with some cracks, even with some exceptions, such as at 4 weeks, for dynamic conditions. Similar results were observed by Champagne *et al.*, although with slightly different conditions, where the formation of surface cracks on Mg corrosion layer was observed as well (41). On Mg-4Ag, defined crystal structures were only observed for static conditions after 1 week of the experiment (**Figure III 3**); the remaining cases were characterized by non-defined structures (**Figures III 3** and **III 4**). In dynamic conditions, pronounced corrosion occurred, as clearly visible after 2 weeks and 4 weeks of experiment (**Figure III 4**).

The formation of a corrosion layer on Mg alloys surface was expected, and its formation process is well-known and characterized(42). Upon contact with physiological fluids, Mg is attacked by the surrounding fluid, which leads to Mg consumption (oxidation), hydrogen gas production, and pH increase. The Mg sample gradually degrades during this process, and a layer of corrosion products is continuously formed. These processes are highly dependent on the composition of the physiological fluid, since each component has a different impact on the Mg corrosion, and on the experimental conditions(43,44). In this work, the same AUS was used for static and dynamic, to address the differences between the two conditions. It is expected that they would impact the corrosion of the samples differently since the continuous flow of fresh AUS and the continuous movement of the fluid through the surface would attack the metal more efficiently than a static solution(42). These two situations lead to different appearances of the corrosion layers formed on the same metal exposed to different experimental conditions. Another factor influencing the corrosion layer is, of course, the sample composition. The different components in the Mg matrix will release different cations, affecting the hydrolysis reaction and the composition of the corrosion layer formed. As expected, this can also influence the corrosion layers aspect, even though the alloying elements exist in low amount in all samples. For urinary tract applications, the corrosion layer can be a problem if it becomes thick enough to cause an obstruction of the stent. However, given that here we are focused on primary studies on the Mg alloys behaviors under urinary tract conditions and using wires (not stent prototypes), it is not possible to design conclusions regarding that part. The following sections address the chemical composition of the corrosion layer in detail and allowed us to understand better the nature of the different corrosion layer formed.

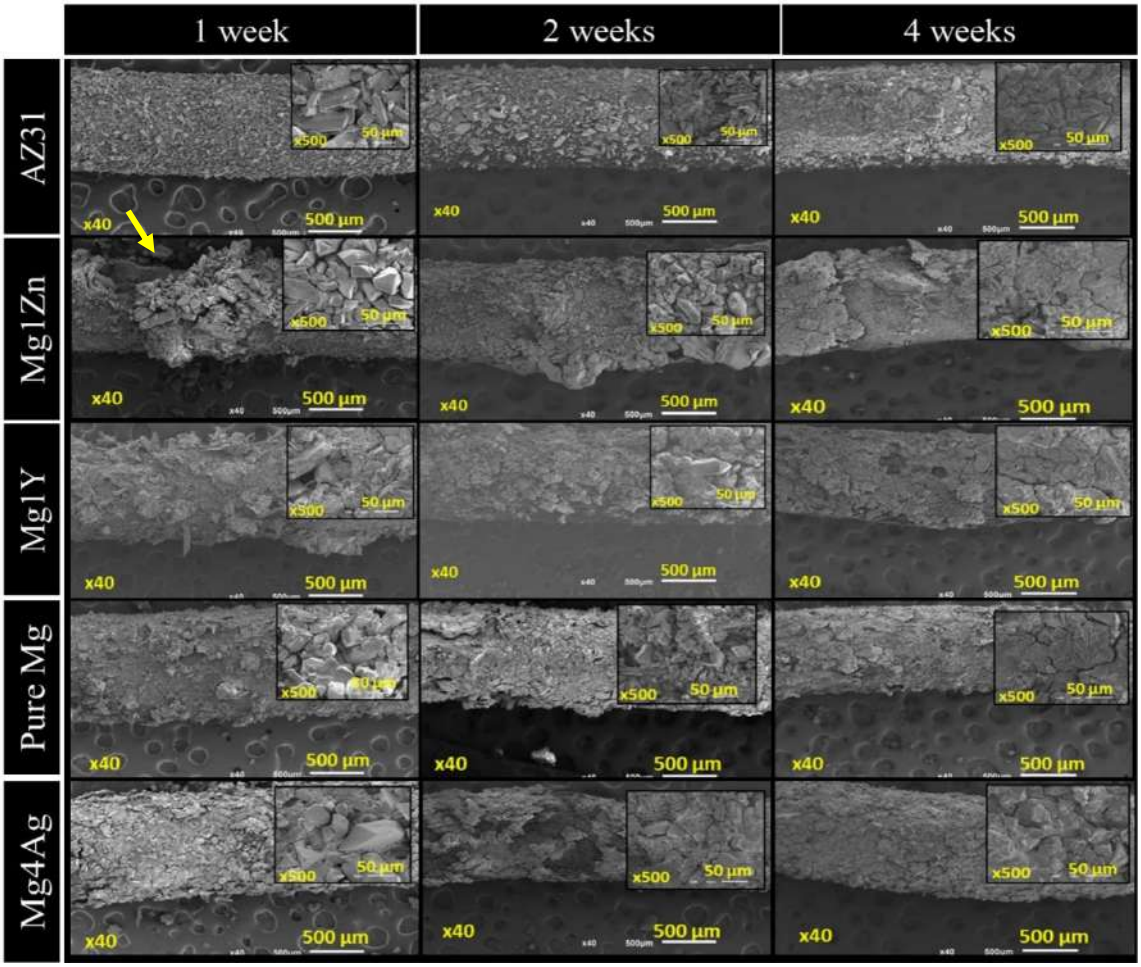


Figure III 3 Representative SEM images of the sample's corrosion layers after 1, 2, and 4 weeks of incubation with artificial urine solution (AUS), pH 6.89, in static conditions. Condition before removing the corrosion products with chromic acid.

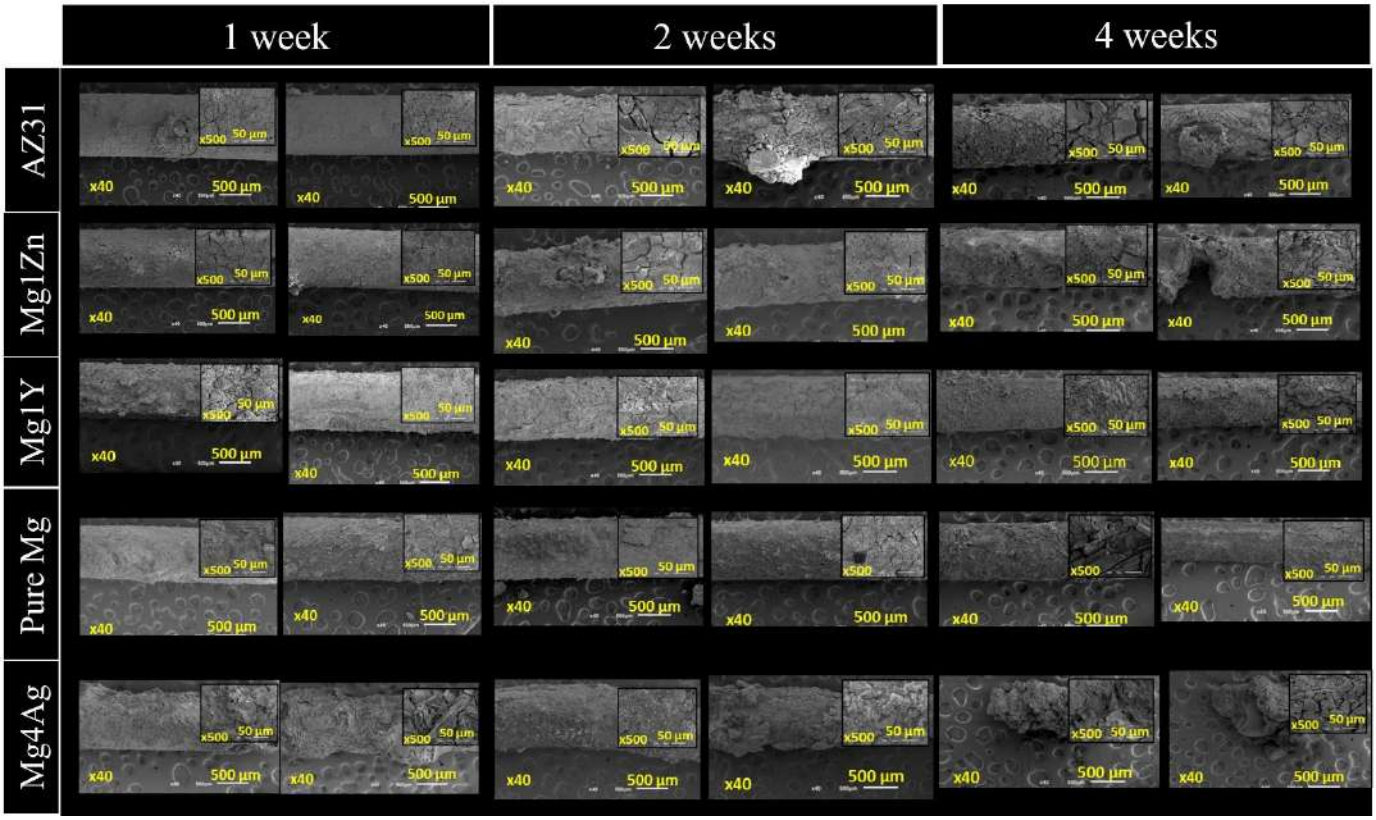


Figure III 4 Representative SEM images of the sample's corrosion layers after 1, 2 and 4 weeks incubation with artificial urine solution (AUS), pH 6.89, in dynamic conditions. Condition before removing the corrosion products with chromic acid.

III-3.4. Corrosion layer – Chemical characterization

III-3.3.1. XPS

The chemical composition of the corrosion layers of the five alloys was investigated through XPS (**Figure III 5** and Supplementary Material) after incubation with AUS for 4 weeks in static conditions. The spectra pattern is very similar for all the samples, evidencing the presence of the same elements arranged in similar chemical groups. As shown in the survey spectrum obtained (**Figure III 5**), the peaks O1s, N1s, C1s, P2s, P2p, and Mg2s were detected for all the samples. In **Table III 3**, we can find the peaks associated with the high-resolution spectra of O1s (545-525 eV), C1s (298-279 eV), and P2p (144-124 eV), as well as the associated chemical elements (see Supplementary Material for the high-resolution spectra). As previously reported, the peaks of O1s high-resolution spectra in the values 530.38-531.09 eV and 532.0-532.25 eV (**Table III** 3 and Supplementary Material) correspond to oxide and hydroxide in MgO and $Mg(OH)_2$, respectively(45,46). These components are common and present even on freshly prepared Mg surface(45,46). Upon contact with aqueous solutions, the layer formation on Mg consists

of the fast thickening of an external porous layer of hydroxide, $Mg(OH)_2$, on the native MgO layer covering the Mg surface that undergoes dynamic growth during immersion (**Figure III 6**). The thickness of the oxide layer is typically counted in nanometers, while the hydroxide layer thickness often reaches above tens of microns(47,48). A layer composed of MgO and $Mg(OH)_2$ grows during immersion in AUS(49–52). From **Table III 3** and **Supplementary Material**, we can see that the $Mg(OH)_2$ signal is stronger than that of MgO for all the samples. This corroborates the expected behavior mentioned above: the $Mg(OH)_2$ layer considerably thickens during immersion in physiological fluids. The fact that the MgO layer is still detected may be related to the $Mg(OH)_2$ layer's porosity, which exposes the MgO layer underneath. Interestingly, on Mg-4Ag's O1s high-resolution spectra, the peak corresponding to MgO was not detected, which suggests that the $Mg(OH)_2$ layer is sufficiently thick to cover all the MgO layer underneath. In fact, the signal corresponding to $Mg(OH)_2$ for Mg-4Ag is the strongest (**Table III 3** and **Supplementary Material**). The peaks present on the O1s high-resolution spectra between 533.60-533.81 eV (**Table III 3** and **Supplementary Material**) are ascribed to $MgCO_3$, a compound that is also commonly found in the Mg corrosion layer after immersion in aqueous solutions(45,52,53).

Regarding the C1s high-resolution spectra (**Table III 3** and **Supplementary Material**), the peaks between 284.84-285.21 eV are related to the C-C covalent link, the peaks between 285.61-286.45 eV are associated with the C-OH covalent link and the peaks between 288.93-290.05 eV with CO_3, as suggested in other works(43,44). In the high-resolution spectra of P2p, the peaks encountered on all the samples of this XPS analysis were between 133.99-134.46 eV, previously reported by other authors to be associated with the Mg_3HPO_4 and HPO_4^{2-}(41,49). Previous works have reported the formation of the same phosphate-containing elements as the ones encountered here, on Mg alloys, after incubation on biological fluids such as SBF, AUS, NaCl, and Ringer's physiological solution, corroborating the obtained results(32,34,51,55).

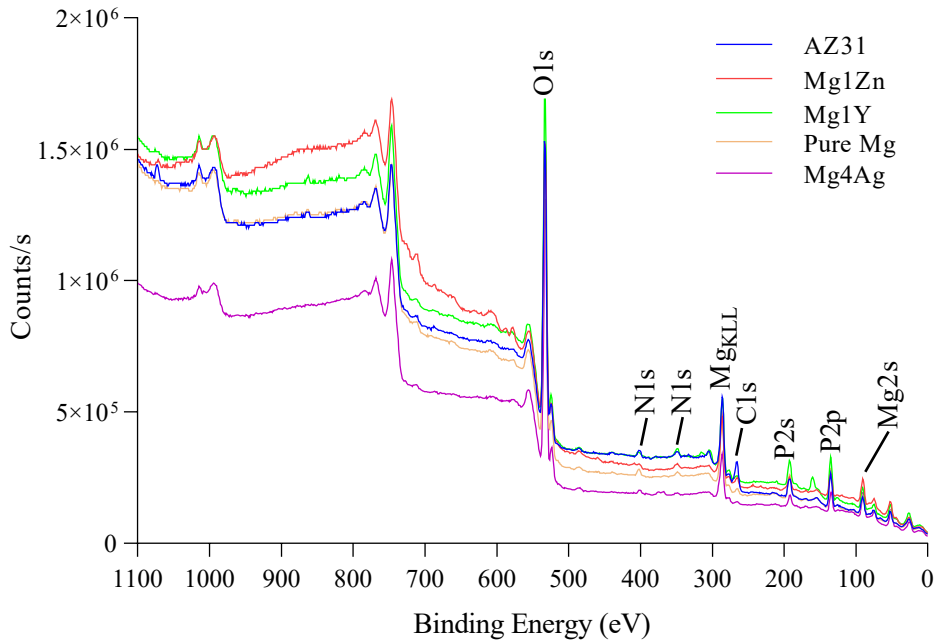


Figure III 5 Survey spectrum of all the sample's corrosion layers obtained by X-ray inducted photoelectron spectroscopy (XPS) after 4 weeks incubation in artificial urine solution (AUS), pH 6.89, in static conditions.

Table III 3 Binding energies (eV) and atomic concentrations (%at) associated with the peaks detected in the XPS high-resolution spectra of O1s, C1s, and P2p obtained for all the alloys after 4 weeks immersed in artificial urine solution (AUS), pH 6.89, in static conditions.

	O1s O^{2-} in MgO (eV) (1)		**O1s** OH^- in $MgO/Mg(OH)_2$ (eV)(1,2)		**O1s** CO_3 in $MgCO_3$ (eV)(1,2)		**C1s** C-C (eV)(3)		**C1s** C-OH (eV)(3)		**C1s** CO_3 in $MgCO_3$ (eV)(1–3)		**P2p** HPO_4^{2-} and/or $MgHPO_4$ (eV)(3,4)	
	eV	At%	eV	At%	eV	At%	eV	At%	eV	At%	eV	At%	eV	At%
AZ31	531.09	8.8	532.22	29.68	533.70	7.94	285.02	15.5	285.84	13.34	289.18	3.14	134.05	9.46
Mg-1Zn	530.38	6.22	532.25	39.13	533.69	6.3	285.14	12.42	286.05	9.67	290.05	3.65	134.46	6.67
Mg-1Y	530.98	6.28	532.20	35.12	533.72	8.43	284.84	10.29	285.61	14.68	288.94	2.46	134.19	11.02
Pure Mg	530.88	6.56	532.03	34.07	533.6	11.00	284.91	8.58	285.83	13.46	288.93	2.56	133.99	12.17
Mg-4Ag			532.00	46.36	533.81	5.09	285.21	10.74	286.45	8.46	289.93	5.8	134.07	6.63

The findings for XPS are in accordance with the ones obtained by EDS for the same samples – static conditions after 4 weeks of incubation - (**Table III 4**). Interestingly, Mg-1Zn and Mg-4Ag had the lowest P concentration and higher Mg amount on the surface, as shown by the EDS results in **Table III 4**. It is known that the different components present in the surrounding media will influence differently the Mg corrosion and respective corrosion layer, the reaction of Mg with phosphates and carbonates, for

example, lead to the formation of stable compounds on the corrosion layer. In this case, the corrosion layer will have a protective role against corrosion. On the other side, other elements, such as Cl^- ions have the reverse effect, Cl^- ions are known for being highly aggressive for Mg since they promote localized corrosion by disturbing the $Mg(OH)_2$ corrosion layer(56). Given the poor phosphate content and presence of Cl on the corrosion layers of Mg-1Zn and Mg-4Ag, comparing to the other alloys, these metals may have a more unstable corrosion layer, making them more susceptible to corrosion attack by AUS aggressive components. These findings can be the reason for the severe corrosion taking place on Mg-1Zn' and Mg-4Ag's surfaces, as discussed later in this paper.

Table III 4 Chemical elements (%wt) detected on the sample's corrosion layers through EDS analysis after 4 weeks in contact with artificial urine solution (AUS), pH 6.89.

	Elements (%wt) EDS analysis									
	O	**P**	**Mg**	**N**	**C**	**Al**	**K**	**Zn**	**Cl**	**S**
AZ31	64.7±0.4	14.6±0.1	10.01±0.1	6.4±0.3	3.6±0.4	0.3	0.2	0.2		
Mg-1Zn	54.1±0.3	4.7±0.1	19.8±0.1	6.1±0.2	9.9±0.4		0.6	3.3±0.1	0.9	0.6
Mg-1Y	64±0.4	13.2±0.1	10.6±0.1	7.8±0.3	4.2±0.5		0.2			
Pure Mg	56.4±0.4	15.3±0.1	14.5±0.1	4.9±0.3	8.1±0.5		0.3	0.2		0.2
Mg-4Ag	59.3±0.4	6.3±0.1	18.9±0.2	5.6±0.3	8.6±0.4		0.3	0.6	0.2	0.1

III-3.3.2. Raman spectroscopy

Raman was employed to complement and confirm the results obtained by the other chemical characterization techniques. Each sample was submitted to more than one analysis on different sites, randomly selected, until three or more similar spectra were obtained to access the homogeneity of the Raman spectra generated by each corrosion layer. Except for pure Mg in dynamic conditions, the Raman spectra were similar in different spots of the same sample for all the samples, so a representative spectrum was selected (**Figures III 6** and **III 7**). Pure Mg, in dynamic conditions (**Figure III 6**), showed different Raman spectra at different surface points, indicating non-homogeneity of the corrosion layer's composition. Three representative spectra were selected in this case (**Figure III 6a, b, c, and d**). Regarding the results obtained in dynamic conditions after 4 weeks (**Figure III 6**), there is a close similarity of the Raman spectra of AZ31, Mg-1Zn, and Mg-1Y with the 3 from pure Mg. The spectra of AZ31 are from the amorphous type and do not present much information, but it is possible to see

similarities with one of the spectra of pure Mg (sample pure Mg c, see **Figure III 6a**). AZ31 and the sample pure Mg c present a peak around 1000 cm^{-1}, in AZ31 at 1008 cm^{-1} and in pure Mg c at 985 cm^{-1}. According to the literature, the 989 cm^{-1} peak is associated with the $\upsilon 1$ PO_4^{3-} symmetric stretching vibration, while the band in AZ31 spectra, at 1008 $cm^{-1,}$ is assigned to the $\upsilon 3$ antisymmetric stretching vibrations of the HPO_4^{2-} and PO_4^{3-} antisymmetric stretching vibrations(57,58). The Raman spectra of Mg-1Zn is also similar to one of the three of pure Mg (see pure Mg b in **Figure III 6b**) and show a typical spectrum of struvite ($NH_4MgPO_4 \cdot 6H_2O$), as we can see by comparing the results obtained elsewhere, in the interval 100-1000 cm^{-1}(59). The spectrum from Mg-1Y shows some similarity with one of the spectra of pure Mg as well (sample pure Mg a in **Figure III 6c**), and the pattern of the peaks, even though associated with amorphous structure and slightly deviated, seem to be associated with newberyite ($Mg(PO_3OH) \cdot 3H_2O$) Raman spectra, as published by Frost *et al.*(60). The peaks at 915 and 997 cm^{-1} are assigned to the $\upsilon 1$ symmetric stretching mode of the HPO_4^{2-} units and PO_4^{3-} $\upsilon 1$ symmetric stretching mode, respectively, which are common bands in many phosphate minerals(60). The bands observed at 420 and 560 cm^{-1} are ascribed to the PO_4^{3-} antisymmetric bending mode $\upsilon 4$(59,60). Finally, Mg-1Y Raman spectra present a band in the region of 3200 cm^{-1}, which is a characteristic of newberyite and is absent in struvite(60). The spectrum of Mg-4Ag is clearly different from any of pure Mg samples (**Figure II 6d**), in contrast to the other samples. Still, it is important to highlight the peak at 3654 cm^{-1}, which corresponds to O-H stretching vibrations in $Mg(OH)_2$ crystals (**Figure III 6d**) (61). The peaks at 285 and 482 cm^{-1} are related to lattice vibrations. The Raman spectra present in **Figure III 6e** shows the difference in the peak pattern of the samples (except for pure Mg), which permits better analysis of the discrepancies of the layers formed by the different alloys. In **Figure III 7**, one can analyze the Raman spectra obtained for the samples tested in static conditions for 4 weeks, and, despite slight deviations in the peaks, it is clear that the Raman pattern is similar in both static and dynamic conditions for almost all the samples, indicating that, in general, the same components are formed. The determinant factors leading to their development are the AUS and the composition of the metal itself, which were the common factors in the two experiments. The composition of the corrosion layer developed by Mg-4Ag seems to be the only one affected by fresh AUS flow (**Figures III 6 and III 7**). Interestingly, in static conditions, the pattern shown for Mg-4Ag is very similar with the ones of Mg-1Zn, thus can be also associated with the formation of struvite, besides, the corrosion layer of Mg-4Ag in static conditions presents an individual feature, identical to the Mg-4Ag's corrosion layer in dynamic conditions, which is the peak at 3662 cm^{-1}, ascribed $Mg(OH)_2$ (61). This is in accordance with the aforementioned XPS data, where the corrosion

layer of Mg-4Ag seems to present a higher amount of $Mg(OH)_2$ than the other samples. Moreover, considering the EDS data, a relation between Mg-1Zn and Mg-4Ag can be seen since the two have the lowest phosphate content and higher Mg concentration (**Table III 4**), which suggests that this can be a characteristic of struvite. In the previous paper by our collaborating groups, it was found for Mg-1Zn and pure Mg that the samples present an outer layer of struvite and an inner one composed of $Mg(OH)_2$(34). Herein, since in Mg-4Ag for static conditions presents Raman spectra associated with both struvite and $Mg(OH)_2$, an external layer of struvite may exist, which is suggested to be less compact given the presence of cracks (**Figure III 3**), justifying the exposure of $Mg(OH)_2$(34). Overall, all the samples present peaks associated with phosphates, which is expected considering the conditions that were tested – simulated urinary tract conditions – but the different samples present different phosphate bending modes, indicating that each alloy promotes the formation of varying ratios of several phosphate species. **Figure III 8** highlights the main differences found in the corrosion layers developed on each alloy, in terms of chemical composition. The formation of these complexes is because of the pH increase at the sample's surface due to the release of OH^- ions, leading to the precipitation of phosphates in AUS and the formation of a dense protective layer (**Figure III 8**). Phosphate and dihydrogen phosphate ions can benefit Mg corrosion by protecting the metal surface from further attack by AUS components.

Phosphate-based crystals such as struvite and newberyite are commonly encountered in urinary encrustation, as well as other phosphate compounds (34). Ureteral stent encrustation is one of the most frequent problems in stented patients. Heavy encrustation is associated with severe problems such as obstruction and challenging stent removal (2,15). In addition to encrustation problems, bacterial infection is also a main concern, specially biofilm formation on the stent surface, that leads to complicated infections(15). In the case of biodegradable metals, the phosphate containing products have one relevant benefit, the protective role against corrosion, so this characteristic can be used as an advantage over the other bad aspects if the phosphate containing products are controlled, i.e., the phosphate products are not significant to create the other problems and sufficient to provide corrosion protection. Regarding the accumulation of phosphate containing products, and subsequent obstruction/problems with the stent removal, we expect that by using a biodegradable material this can be prevented. The constant dynamics of the surface (constantly degrading), will probably lead to a more unstable encrustation layer which, with the urine flow and peristaltic movements of the ureter can be constantly deteriorated at the same time as it is being produced. Still, this hypothesis can only be efficiently studied and proved in a later phase of this project when we have the ureteral stents prototypes (so that we can evaluate the accumulation of

the encrustation inside the stent), and in a future *in vivo* experiment. Furthermore, the problem of stent removal is obviously avoided with a biodegradable ureteral stent, which is expected to degrade by itself along the time. Regarding the bacteria attachment, we also believe that the degrading metal and dynamic corrosion layer (i.e. encrustation) will hamper the bacteria contamination, first because if the surface is dynamic, it will be more difficult for the bacteria to attach and form a biofilm, second, in this case that we are working with Mg alloys, it is already verified that Mg has antibacterial activity against specific bacterial strains that are common in urinary tract infections, such as *E. coli, P. aeruginosa* and *S. aureus*(33,62–65). In conclusion, we can expect that in the future studies, the formation of a phosphate containing corrosion layer can be mostly beneficial for biodegradable Mg-based ureteral stent.

Herein, the identification of the specific phosphate containing components indicates that these crystals probably exist in higher amounts than others. Still, it does not discard the probability of existing other crystals/components, which can be present in lower amounts(66–68). Considering the composition of the AUS and the tested samples, we can conclude that both the corrosion of the metal and the AUS precipitates contribute to the formation of the surface layers, as verified in other work(63). Curiously, in the previously published work from this group, the compounds detected in the corrosion layer were the same as the ones found here, struvite and $Mg(OH)_2$, but the corrosion layers do not present the same aspect (as observed by comparing the SEM images of the two works(34). Besides, in the previous work, Mg-1Zn presented an inhomogeneous corrosion layer, and pure Mg showed a homogeneous corrosion layer. Herein, pure Mg had a homogeneous corrosion layer only in static conditions, and the corrosion layer of Mg-1Zn appears homogeneous in both situations. These differences can be due to the different electrolyte flow patterns, measurements performed at 23 ºC vs. 37ºC in this work, and time points analyzed since the corrosion layer is developing over time, and it is believed that the composition of precipitated products is dynamic(32,63). In fact, in this work, the corrosion layer formed after 4 weeks is analyzed, and in the previous work, after 72h, which is a considerable difference. This highlights the importance of studying the development of the corrosion layer at several time points during the immersion and should be considered as future work.

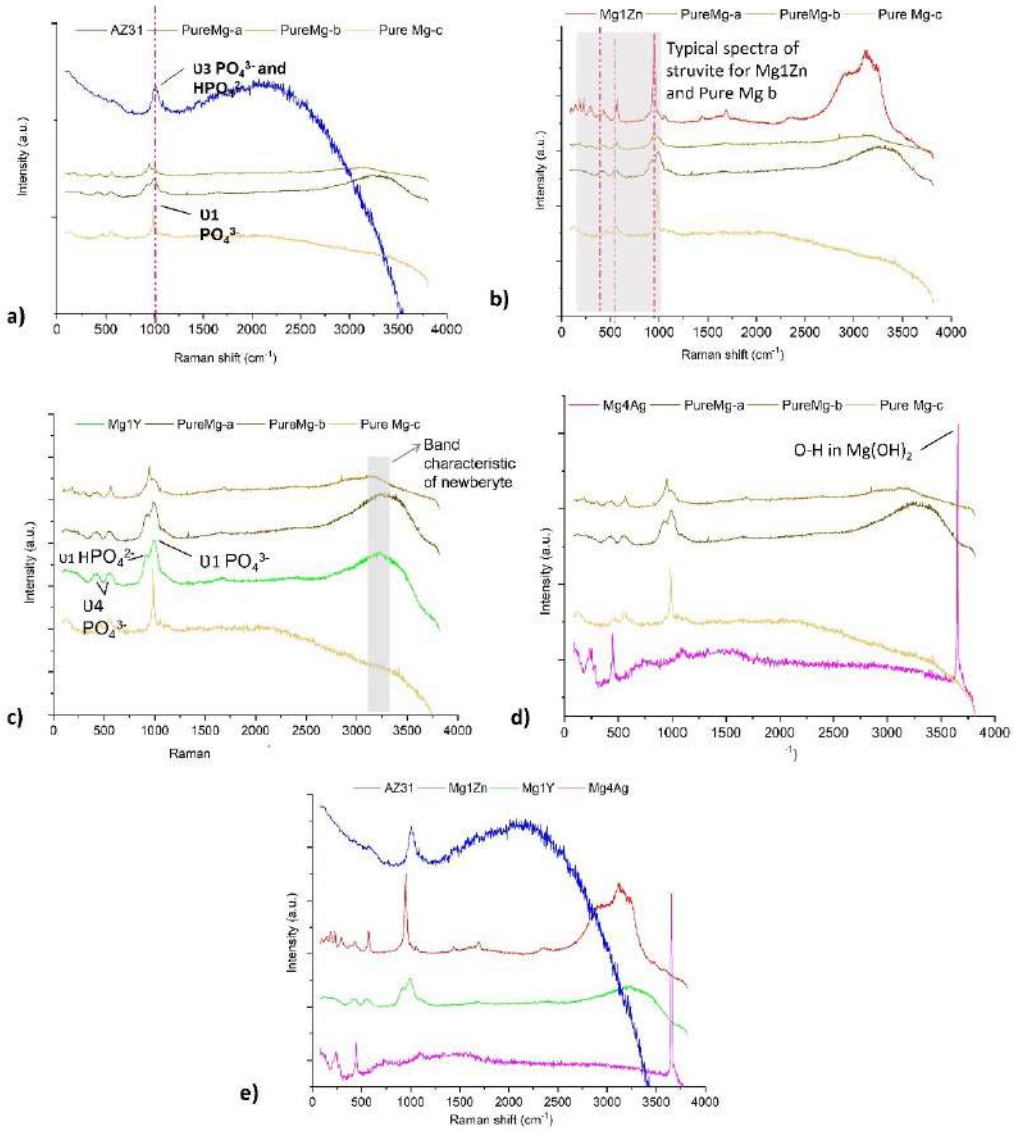


Figure III 6 Raman spectra obtained for the corrosion layers of all the samples after 4 weeks incubation with artificial urine solution (AUS), pH 6.89, in dynamic conditions. Pure Mg's corrosion layer presented different Raman spectra for different sites on the surface and 3 representative Raman spectra are presented for this sample, Pure Mg a, Pure Mg b, and Pure Mg c.

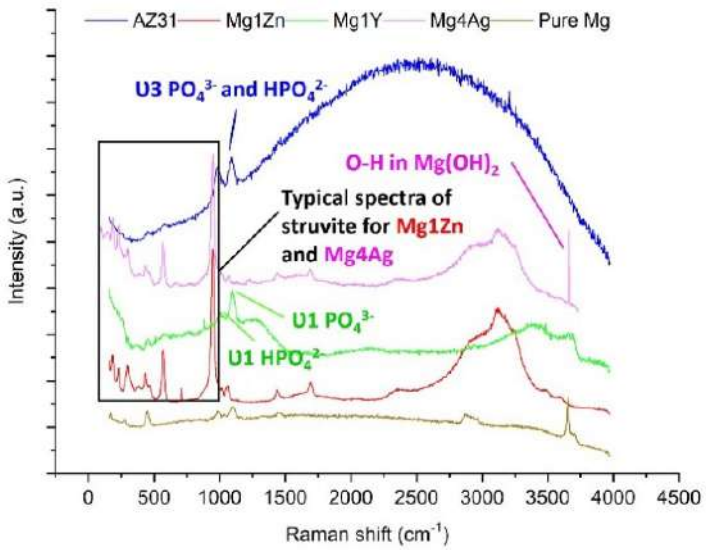


Figure III 7 Representation of all the Raman spectra obtained for the corrosion layers of all the samples after incubation with artificial urine solution (AUS), pH 6.89, for 4 weeks in static conditions.

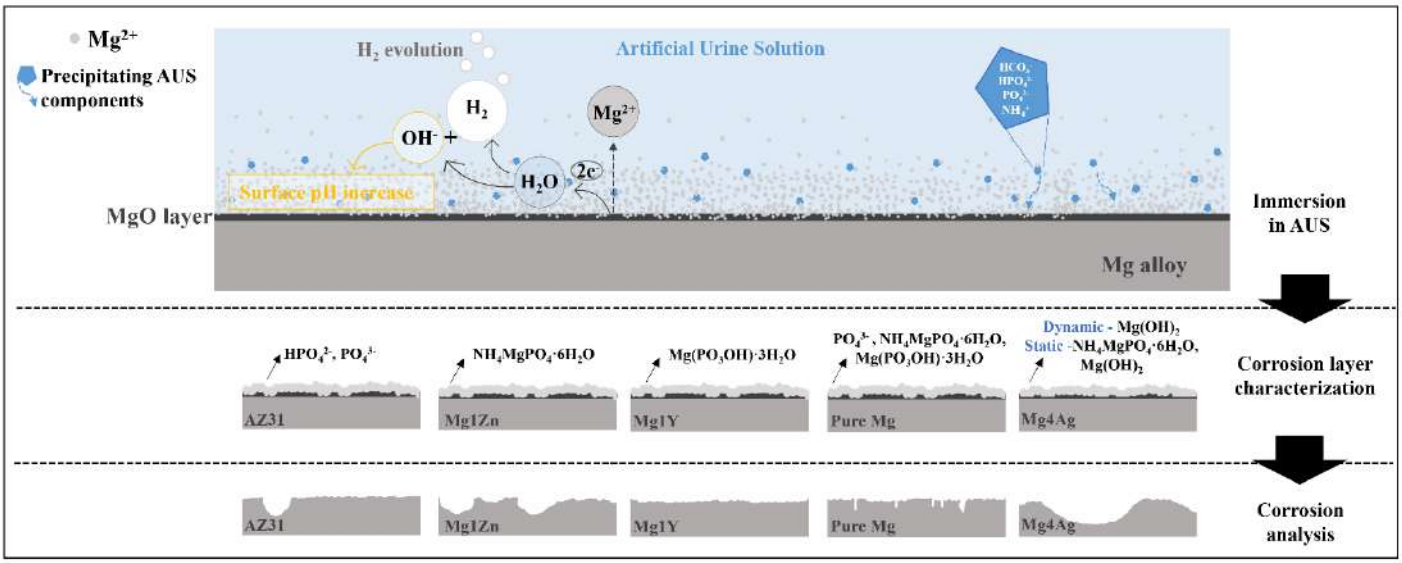


Figure III 8 Schematic illustration representing the reactions of Mg alloys when immersed in AUS.

The study of the chemical composition of the corrosion layers formed on the different alloys' surfaces in simulated urinary tract conditions explored in this study provides essential data for future studies on biodegradable metals for urinary tract applications. The results proved that the different alloys respond differently to the surrounding fluid, possibly because of the different arrangement of the intermetallic phase of their microstructure, which can be observed in **Figure III 2**. We have seen that the aspects of the corrosion layers formed were different, and the investigation of their chemical composition revealed that the same chemical elements were formed for all the corrosion layers of the different samples (according to the results from XPS), even though the compounds formed were different, as revealed by Raman analysis. We can conclude that the different composition of the Mg alloys determines the tendency of the sample to form specific compounds in their corrosion layer, even with the same base elements. This will allow us to select the most suited alloys for urinary application more effectively in future studies. For example, pure Mg is more likely to form a nonhomogeneous corrosion layer, leading to uneven corrosion – e.g., localized corrosion. For ureteral stents application, this can be problematic since the uneven corrosion may lead to the break of the stent and the creation of big fragments. Besides, the composition of the corrosion layer will be closely related to the corrosion pattern since the different components provide different protection against the surrounding media. In the following sections, the corrosion of each metal is explored, which will complement the results obtained for the corrosion layer analysis.

III-3.4. Corrosion – Corrosion rate

The corrosion process of the metal samples was further assessed by calculating the corrosion rates, by profilometry, and SEM images observation to analyze the roughness and complemented by ICP-OES for quantifying the amount of cationic species released in AUS during degradation.

The corrosion rate was calculated according to the procedure described in the Materials and Methods section, and the results are presented in **Figure III 9**. The corrosion rate varied over time for all the samples for static and dynamic conditions (**Figures III 9a and III 9c**). In most cases, the corrosion rate decreased with immersion time, which is typically observed for Mg alloys. In static conditions, comparing the variation of each metal separately (**Figure III 9a**), it was observed that AZ31 had a higher corrosion rate in the first week, which then decreased with time, only evidencing a statistically significant difference between 1 week and 4 weeks (**Figure III 9a**). Similarly, Mg-4Ag had a decrease in the corrosion rate value along the time of immersion, with a significant difference for all the

time points tested, suggesting a faster degradation of this metal compared to AZ31 (**Figure III 9a**). For Mg-1Zn and Mg-1Y, the corrosion rate was more intense at 2 weeks immersion time, and pure Mg was the only metal where the corrosion rate value seems to be constant (**Figure III 9a**). Zuo *et al.* published an interesting work where the corrosion of pure Mg in 3 physiological fluids, including AUS, in static conditions was studied(69). The authors reported that pure Mg had a higher degradation in the first days of incubation and decreased over time, contrary to what was observed in our work. The authors ascribed this behavior to the initial lower AUS pH value, which was found to abruptly increase in the first 72h and stabilize after 1 week. The AUS used in this work maintains the pH in the initial phase of the experiment (**Figure III 10b**), which is replaced regularly in static conditions, guaranteeing a stable pH for the time between replacements. This pH stability was achieved by using a large volume of electrolytes and control of microbial life via NaN_3 and Na_2SO_3 for both conditions. The AUS used in the Zuo *et al.*'s work presented a different composition and had a significant pH alteration. This AUS did not show an antibacterial agent, which could be a reason for the pH increase. The reason for different results may be related to the composition and pH changes of the immersion solution, which can be determinant in the corrosion of the metal and hampers comparisons between different works(51,69). In this work we also submitted the alloys to acidic, neutral and alkaline AUS to evaluate the influence of pathologic urine compositions on several Mg alloys. When in acidic AUS, pH 4.13 (**Table III 2**), after 2h, the increase of pH is already significant for all the alloys, and even higher after 24h immersion. Between 24 and 48h, the pH seems to stabilize around 6 (**Figure III 10a**). For neutral and alkaline conditions, the pH seems to be stable over a 48h time period (**Figure III 10b and c**). The results indicate that with this AUS the pH tends to be more stable in the range between 6 to 8. At these values the phosphate containing products are less soluble, thus prone to precipitate, which is in accordance with the obtained results(40). Besides the influence of the surrounding solution, the degradation behavior of pure Mg varies in a wide range, depending on the amount and distribution of impurities (Fe, Si, Ni, Cu, Al, Zr, etc.). For example, it was shown that high-purity Mg containing 50 ppm Fe corroded ca. 50 times faster than high-purity Mg containing 51 ppm Fe owing to different compositions and distribution of noble impurities in the magnesium matrix; thus, the differences in the pure Mg composition used in the different works may as well be an influencing factor. Comparing the metals among each other at the same time point, significant differences were detected (**Figure III 9b**). After 1 week, Mg-4Ag is distinct from all the other 4 metals, and for the second week, the corrosion rate of Mg-1Zn, Mg-1Y, and pure Mg increased, becoming closer

to Mg-4Ag (**Figure III 9b**). At 4 weeks, pure Mg stands out, and the corrosion rate was significantly higher when compared with AZ31, Mg-1Y, and Mg-4Ag (**Figure III 9b**).

Regarding the corrosion rate for the dynamic assay and focusing on the corrosion of each metal separately, a decrease in the corrosion rate of Mg-1Zn along the time was observed, which didn't happen in static conditions (**Figure III 9c**). Mg-4Ag also presented a reduction in the corrosion rate over time, corroborating the data from the static assay (**Figures III 9a and III 9c**). Significant differences between the different metals were noticed for 1 week and 2 weeks, for dynamic conditions (**Figure III 9d**). For 1 week, Mg-4Ag was the metal with the highest corrosion rate value, while for 2 weeks, Mg-4Ag stood out and had a significantly higher corrosion rate value than all the other four metals (**Figure III 9d**).

Overall, it is evident that the corrosion is more substantial in dynamic conditions (**Figure III 9e**), which is typically observed for most metals. Besides the influence on the corrosion rate speed, the flow conditions also affect the corrosion pattern. Only AZ31 and Mg-4Ag presented a similar corrosion pattern for both static and dynamic, as the corrosion rate values decreased over time (**Figure III 9a and III 9b**). Mg-1Zn, Mg-1Y, and pure Mg corrosion patterns are slightly affected.

Several previous studies evaluate the corrosion of Mg and Mg alloys in different physiological fluids, under static or dynamic conditions, and various time points, making the literature broad and rich in information(54,70–72). However, it is difficult to compare different works (71,72). In the present study, our main aim was to approach the human body conditions through *in vitro* and to evaluate whether the use of a dynamic system is significantly different (from the static conditions) to make its use worthwhile for future experiments. Essential conclusions were described in this sense: we have verified that using static and dynamic conditions lead to different results, which can determine the outcomes of a study. Therefore, it is highly recommended to consider using flow conditions for studies related with the implementation of biodegradable metals in the urinary tract. The corrosion rate findings of this work will also be a strong base for the future investigations on the project, aiming to develop a biodegradable metallic ureteral stent. Since this consisted of a preliminary screening study, it is difficult to correlate these corrosion rate values with the ones intended in the final biodegradable metallic ureteral stent prototype since the design, strut thickness and the amount of metal will be different. We can, however, focus on the degradation pattern of the alloys. Mg-4Ag for example, has a fast degradation at the beginning, which may not be a good indication for ureteral stent application, since this can be translated in a stent weakness and associated failure at an early stage of the treatment, and the same happens

with Mg-1Zn even though at lower corrosion rate values. On top of these conclusions, a significant change on the corrosion rate along the time could lead to unwanted severe clinical situations. For instance, an abrupt material loss can generate an excess of loose particles/fragments on the ureter, which may cause occlusion. AZ31, Mg-1Y and pure Mg degraded at similar rate during 4 weeks testing period, which can be an interesting feature since the time of stent failure can be predicted with higher precision in this case.

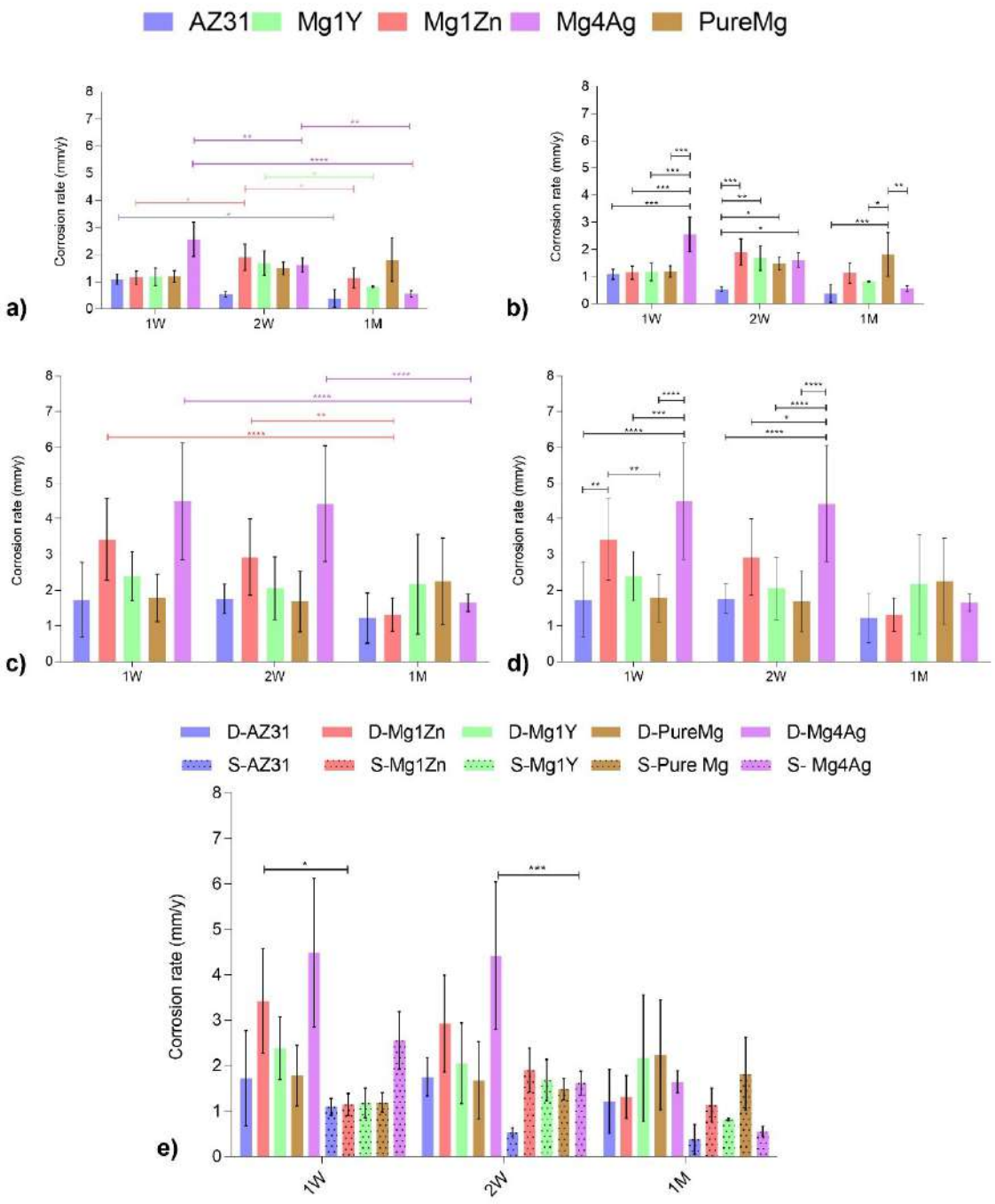


Figure III 9 Corrosion rate (mm/y) of all the samples at different time points in static conditions representing the corrosion rate difference along the time (a), in static conditions representing the corrosion rate differences of the different alloys (b), in dynamic conditions representing the corrosion rate variation along the time (c) and in dynamic conditions representing the corrosion rate differences of the different alloys. A comparison between the static and dynamic conditions is also represented (e). The artificial urine solution (AUS) used had a pH of 6.89.

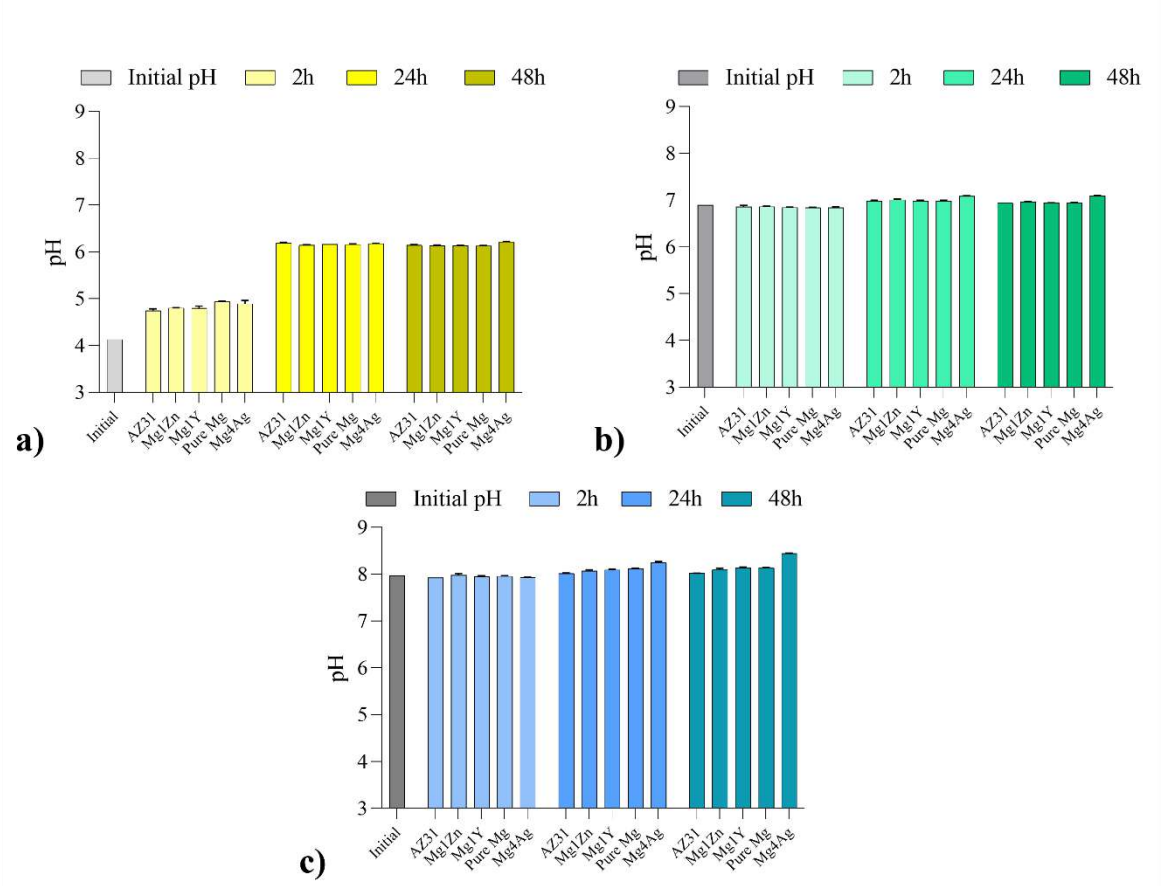


Figure III 10 pH evolution over 48h exposure to Mg alloys in a) acidic, b) basic and c) alkaline conditions.

III-3.5. Corrosion - Profilometry

After removing the layer of corrosion products, profilometry was performed to assess how uniform the corrosion was throughout the length of the wires. Samples from the static assay after 4 weeks of incubation were used for this analysis. **Figure III 11** shows a large representative fraction of wire surfaces, identifying localized corrosion in most of the alloys. **Figure III 12** presents the 3D optical images of the samples - surface area 1x2 mm^2 and 0.5x2 mm^2- and the topography map - in a 0.5x2 mm^2 area - for all the samples and respective triplicates. For Mg-1Zn, the higher values are around -20 and -30 µm, indicating the presence of deep holes, in accordance with the heavy corrosion observed in **Figure III 11**. AZ31 and Mg-4Ag had values around -10 and -20 µm, so they have shallower holes compared with Mg-1Zn (**Figure III 12**). On the other hand, AZ31's, Mg-1Zn's, and Mg-4Ag's corrosion holes are differently distributed along the surface of each sample, and the corrosion patterns seem also to vary from sample to sample. This uneven corrosion will not be a good characteristic for a biodegradable

ureteral stent; the localized corrosion spots will be the targets of increased degradation over time and will become weak structural points, eventually leading to stent break and generation of fragments that can cause ureter obstruction. Regarding Mg-1Y, the situation seems different; the corrosion holes are in the values of -10 and -30 µm (**Figure III12**), but, interestingly, the corrosion pattern shows consistency along the surface, corroborating the photos in **Figure III 11**. Finally, pure Mg shows regions of very deep holes (around -50 and -60 µm deep), and those are randomly spread on the surface, clearly representing zones of higher corrosion attack. These differences on the corrosion profile exhibited by the different alloys may also be related with their different microstructures (**Figure III 2**). **Figure III 8** summarizes the different corrosion patterns presented by each alloy. Mg-1Y had the finest grain structure and pure Mg had the coarsest. Correlating this with the profilometry data (**Figures III 11 and III 12**), relationships can be seen. It seems that the finer the microstructure, the more homogeneous the corrosion behavior (less pitting). The literature also reflects a similar behavior(73–76). It is suggested by other authors that the smaller grain size is related with a slower and even corrosion and coarse grain are more prone to crack formation, which may lead to the formation of localized corrosion and big corrosion holes(42,77). It can therefore be assumed that the microstructure, in addition to other effects such as precipitation, also has an influence on the corrosion behavior.



Figure III 11 Optical images of all the metals, in triplicate, after 4 weeks immersion in artificial urine solution (AUS), pH 6.89, in static conditions. Corrosion products were removed by chromic acid before taking these images.

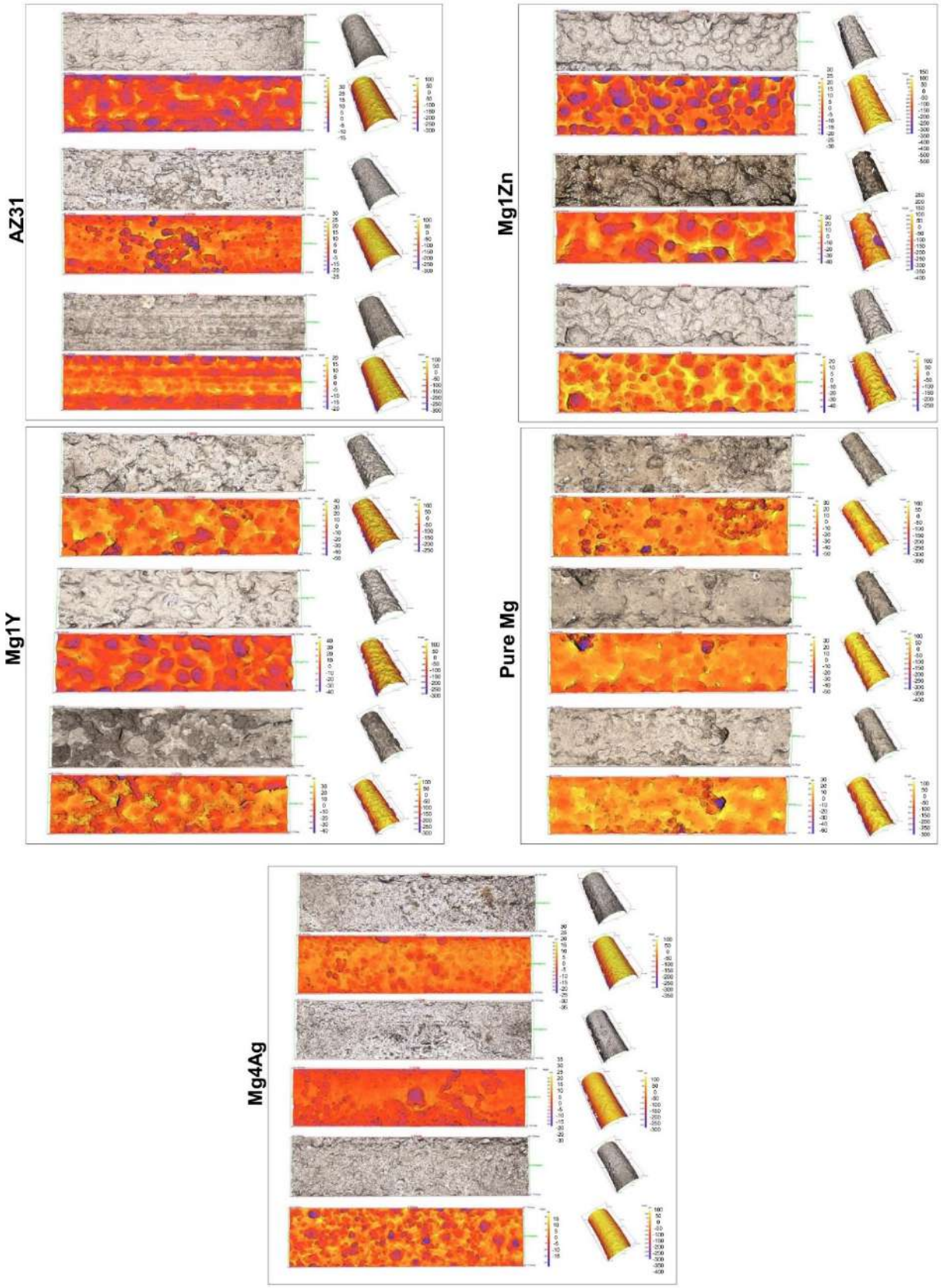


Figure III 12 3D optical images of all the samples (surface area of 1x2 mm^2 and 0.5x2 mm^2) after 4 weeks immersion in artificial urine solution (AUS), pH 6.89, in static conditions. The field of view of each optical image and the profilometric map is 0.5x2 mm^2.

III-3.6. Corrosion - SEM

The SEM images in **Figure III 13** were taken after removing corrosion products by chromic acid solution from the wires exposed to AUS in static conditions for 1, 2, and 4 weeks. Only metallic magnesium gets passivated by chromic acid treatment, while the degradation products are removed, and corrosion-affected areas become visible. Focusing on the 4 weeks time point, it is possible to see large and deep corrosion cavities on the surface of the Mg-1Zn sample, in agreement with the previous results. A great extent of localized corrosion is also observed for pure Mg, even though different from Mg-1Zn. Mg-4Ag has mostly a smooth surface (especially compared with pure Mg); however, single events of strong corrosion were identified, corroborating the results from profilometry. Lastly, Mg-1Y and AZ31 present a corroded surface characterized by most shallow cavities homogeneously distributed along the whole surface, evidencing homogeneous corrosion of tested wires. Considering all the time points, for Mg-1Zn and pure Mg, it is evident the increase in the corrosion along the time, and for Mg-1Zn, a high corrosion degree is observed as early as after 1 week, where various large dimples were formed (**Figure III 13**). Similar results were obtained in the previous work published by our collaborating groups, where severe localized corrosion was detected in Mg-1Zn and not for pure Mg(34). In the present work, for pure Mg, after 1 week, the extent of localized corrosion is significant, considering the depth of the cavities and groups of small pits (**Figure III 13**). In the second week, intense corrosion was already evident. AZ31 presented severe corrosion in defined spots dispersed on the surface, and the same happened with Mg-4Ag (**Figure III 13**). Mg-1Y does not present deep or large corrosion dimples but still presents groups of small pits (**Figure III 13**). From a general point of view, except for Mg-1Y, all the metals seem to have some degree of non-homogeneity characterized by the dispersed cavities on the surface, even if these are rare, as in the case of AZ31. Mg-1Y presents signs of corrosion, given the irregular surface and groups

of shallow cavities. Still, these corrosion signs are consistent through the surface, indicating more uniform corrosion, which is a main requirement for a biodegradable metallic ureteral stent.

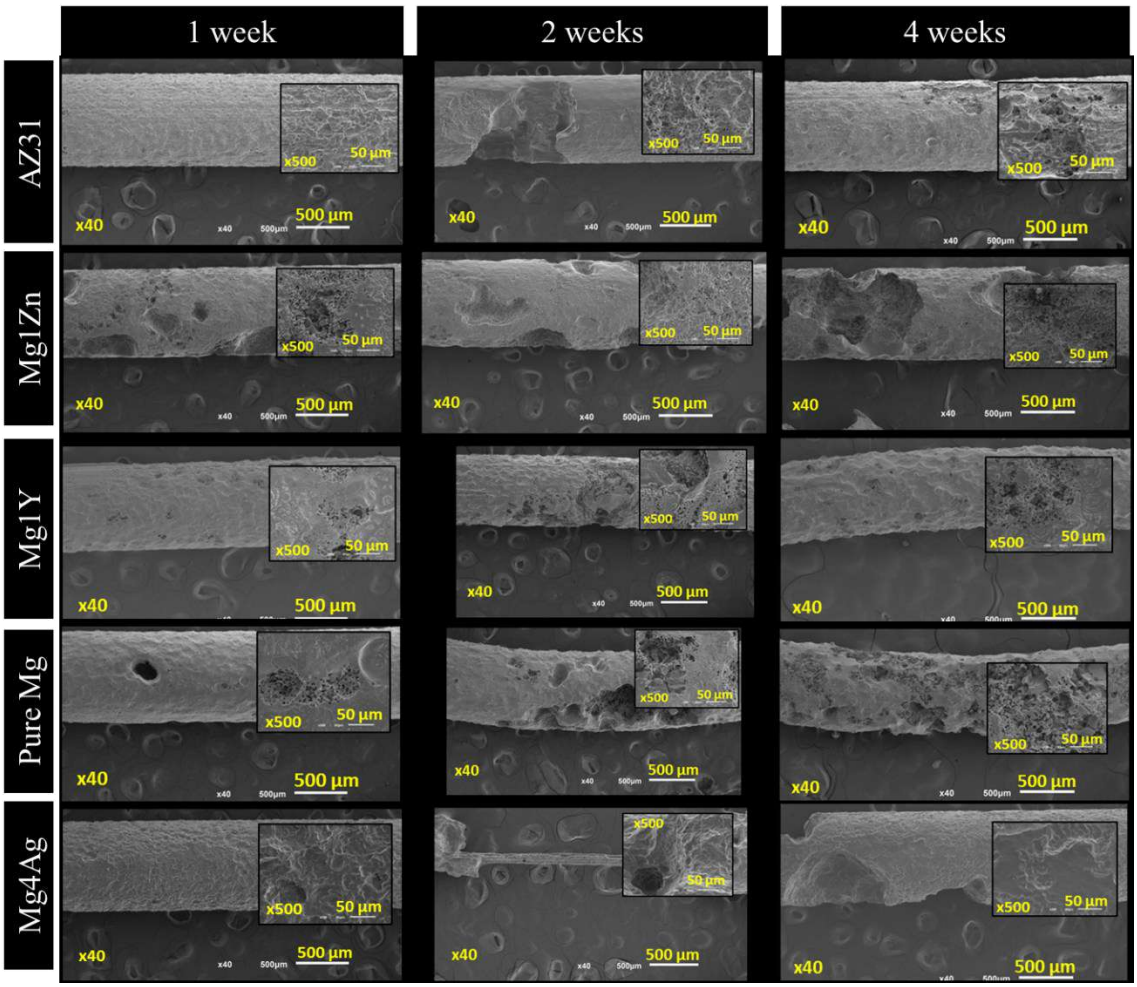


Figure III 13 SEM images of the corroded samples after removing the corrosion layer at 1, 2 and 4 weeks incubation with artificial urine solution (AUS), pH 6.89, in static conditions

Figure III 14 represents the SEM images for the dynamic conditions at different time points. After 1 week, the corrosion is heavier for all the alloys, compared with the static conditions (**Figure III 13**), and Mg-1Zn and Mg-4Ag are the most affected ones. After 2 weeks of incubation, strong corrosion occurs, and large corrosion dimples appeared in AZ31, Mg-1Zn, and Mg-4Ag, even though regions of lighter corrosion also exist for these three alloys. Mg-1Y and pure Mg presented a smoother surface, which differs from the corrosion pattern observed in the static assay (**Figure III 13**). After 4 weeks (**Figure III 14**), a smooth surface for all the samples was seen when compared with static conditions

(**Figure III 13**), but large corrosion holes appeared in AZ31, Mg-1Zn, and Mg-4Ag, while Mg-1Y seems to have a surface free of those. Pure Mg corrosion is mainly characterized by the presence of groups of small pitting, as seen in static conditions (**Figure III 13**).

As a general conclusion obtained from SEM analysis for static and dynamic conditions, the extent of localized corrosion is similar for AZ31, Mg-1Zn, and Mg-4Ag wires. Localized corrosion was stronger in dynamic conditions for AZ31 alloy and in static conditions for pure Mg (**Figures III 13 and III 14**). However, this does not correlate with the weight loss results (**Figure III 9**) referring to the total loss of material, where dynamic conditions consistently led to faster degradation. Thus, even though the metal loss is lower in static conditions, micro-confined environments may occur locally, leading to various types of localized corrosion and forming shallow or deep cavities. Importantly, Mg-1Y alloy demonstrated a lesser extent of localized corrosion in static and dynamic electrolyte conditions, which is one of the major indications that makes this alloy adequate for prototyping the ureteral stents. The extent of localized corrosion can be related to the nature of alloying elements, formed secondary phases and cathodic impurities, their Volta potential difference with the matrix and distribution with regards to grain boundaries, hydrolysis susceptibility of formed cations Me^{n+}, insulating property and coverage by the native oxide layer, the density of formed corrosion products and other factors, e.g., the porous nature of the $–Mg(OH)_2$ layer allows penetration of AUS to the oxide layer and corrosion attack by aggressive chlorides that leads to the corrosion of the metallic substrate in that area(32,52). Correlating the results obtained here for the corrosion with the ones obtained in the last sections for the corrosion layer composition, we can see that Mg-1Zn and Mg-4Ag seem to be the most affected by corrosion, compared to the other samples (**Figures III 12 and III 13**). They also have lower amounts of phosphate-containing species and the ones presenting Cl on the corrosion layer composition (**section III 3.3.1 XPS**). These results emphasize the role of the alloy composition on metal corrosion protection. In this specific case, Mg-1Zn and Mg-4Ag, when immersed in AUS, have less propensity to form the protective phosphate-containing layer, so the metal surface is more exposed to the aggressive components of AUS, such as Cl^- ions. This may be the main reason for the aggressive corrosion in these alloys, making them less suitable for urinary applications.

From a general point of view, the dynamic conditions lead to faster corrosion, which may be related to the constant fresh AUS flow at the samples' surface that removes the corrosion products being formed and neutralizes the surface pH. Given that the alkaline environment potentiates the formation of

a protective layer that becomes thicker and more protective of the metal underneath, in dynamic conditions, this effect is difficulted by the fresh fluid flow.

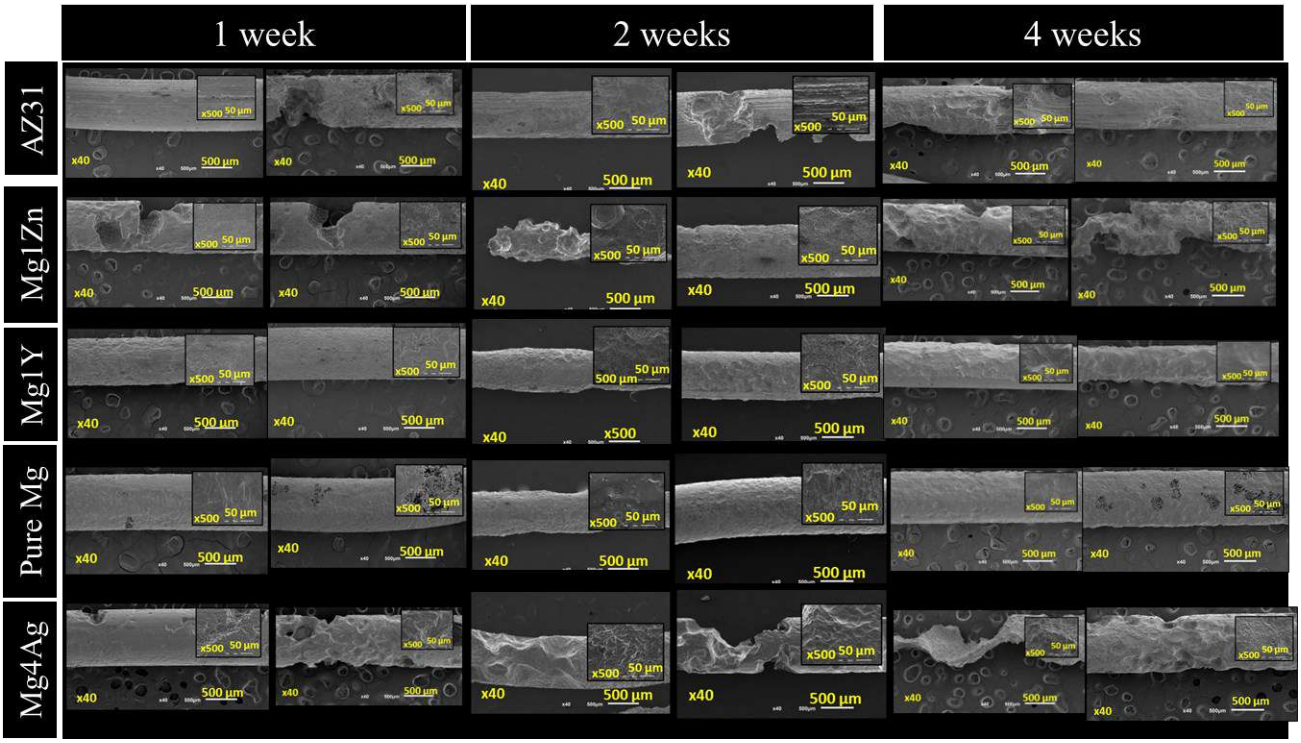


Figure III 14 SEM images of the corroded samples after removing the corrosion layer at 1, 2, and 4 weeks of incubation with artificial urine solution (AUS), pH 6.89, in dynamic conditions.

III-3.7. Corrosion – ICP-OES analysis

The ICP-OES analysis assessed the amount of material eroded from the samples. **Figure III 15** shows the amount of each metal dissolved in the AUS by a specific time point. According to the results, the metal with higher concentration was Mg for all the samples in both static and dynamic conditions, which was expected given that Mg is the major component in all the samples. Comparing the two graphs, it is evident that the Mg values are higher for the first week for the dynamic conditions, which suggests that a constant flow accelerates the corrosion in the first week of the assay (**Figure III 14**). This was expected, given the output of the weight loss measurements (**Figure III 9**). On the other hand, from the second week until the fourth, the Mg concentration in AUS is between 40 and 100 mg/L for static conditions and between 10 and 80 mg/L for dynamic conditions. Indeed, in this last case, the concentration of Mg from Mg-4Ag samples stands out from the other samples, indicating higher corrosion of Mg-4Ag for this period. However, if we account for all the samples except for Mg-4Ag, the Mg

concentration in AUS in dynamic conditions is between 10 and 40 mg/L, which means that from the first week forward, there is a higher material loss for static conditions. We can conclude from these results that there is a large corrosion in the first week for dynamic conditions, while for static conditions, this happens later, from the first week forward. Considering the weight loss analysis results, these ICP-OES data were not expected. However, it is important to consider the influence of the formation of the corrosion layer, which is known to confine the liberation of metal residues from the surface and, for the weight loss assay, the cleaning of the corrosion layer can also wash away the loosely attached metal grains, known as "chunk effect". Knowing the concentrations of released cations may not directly correlate with the other results presented. Still, it is important to understand their accumulation and influence on surrounding cells, tissues, and organs, and it requires deeper and more focused studies(78–80).

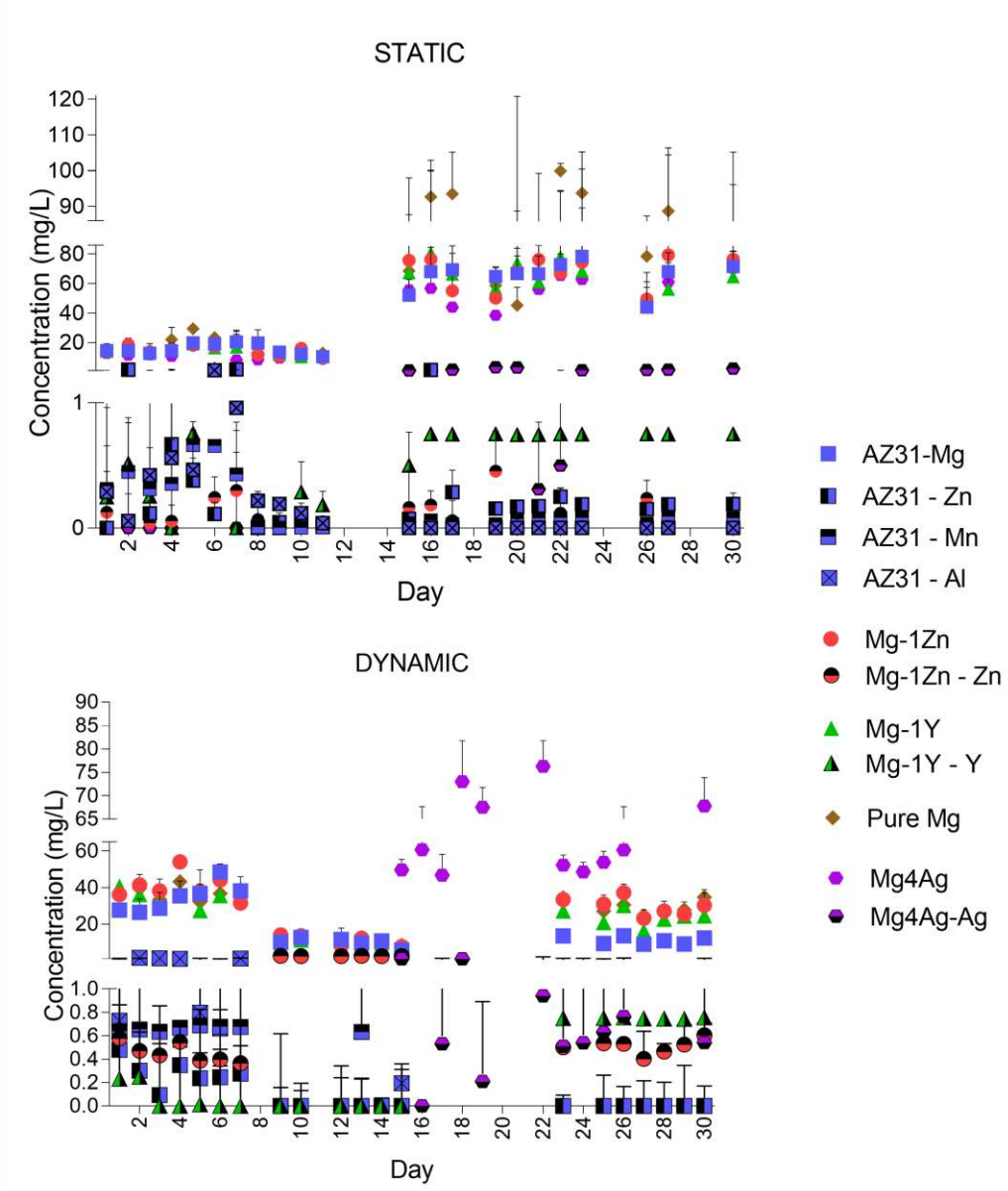


Figure III 15 The concentration of the different metals (mg/L) in artificial urine solution (AUS), pH 6.89, on different days of the experiment at both static and dynamic conditions for all the alloys.

III-3.8. Cytotoxicity

The cytotoxicity of the wires was evaluated by exposing L929 cells to the metals' extracts (ISO 10993-12) using two techniques, MTS and Live/Dead, as explained on **section III 2.9.Cytotoxicity.** The graph below (**Figure III 16**) shows the cell viability, obtained by MTS assay, upon contact with each metal's extract. None of the Mg alloys' extract seems toxic to cells, even at higher concentrations (E100). However, the fluorescence images obtained with the Live/Dead assay (**Figure III 17**) indicate that with the highest concentration of extract (E100), the cells seem to be affected. This is not in agreement with

the MTS results. **Figure III 17** shows that, for all the alloys, when exposed to media with the highest concentration of extract, the cell density is much lower and they present a more rounded shape, which indicate that they are not healthy. However, the images do not present dead cells (which should be represented in red, as in C-). One of the hypotheses that can explain this phenomenon is that the cells indeed are affected with the highest Mg concentration, but they are not completely dead (given the green color). It may happen that some of their functions are affected by the high Mg content of the media, such as the capacity to adhere on the well's bottom. So, when we perform the Live/Dead assay, which implies more washing steps than the MTS, the weakened cells have more tendency to detach from the well's bottom, therefore when observed on the microscope only some of them remain. The ones that remain are affected but still alive. In the MTS assay, it is possible that more cells stay attached to the bottom and since they are alive, they still have the capacity to metabolize MTS. Therefore, we can conclude that L929 cells are sensitive to high concentrations of Mg, even though they don't die.

Mg-based devices are known for their biocompatibility, given that Mg^{2+} is the main compound released by Mg-based materials, and this ion is the fourth most abundant in the human body, being fundamental for many enzymatic reactions(81). This is one of the several advantages of Mg-based biomedical devices. However, Mg-based implants can be toxic due to the hydrogen release (hydrogen bubbles) and the alkalinization of the surrounding media (**Figure III 8**), both caused by the dynamic reaction of Mg with the surrounding fluid. The toxicity caused by these events will depend on the Mg alloy and respective immersion media. In the conditions tested herein, the alloys' extracts seem to cause some toxicity to L929 cells when at high concentrations. Still, we need to be aware that this kind of test represent the extreme situation. It is known that urothelial cells are impermeable to urine's components since their job is to protect and serve as a barrier to the tissues underneath. On top of this, when the stent is inserted in the patient's ureter, the urine will constantly flow and neutralize the surface pH and drag away the released products (including hydrogen bubbles). Further studies with ureter cells in dynamic conditions and *in vivo* studies should be performed to validate the safety of these Mg alloys. Given this, we believe that the metals explored in this work can still be safe and can be used for future investigations on biodegradable urinary devices.

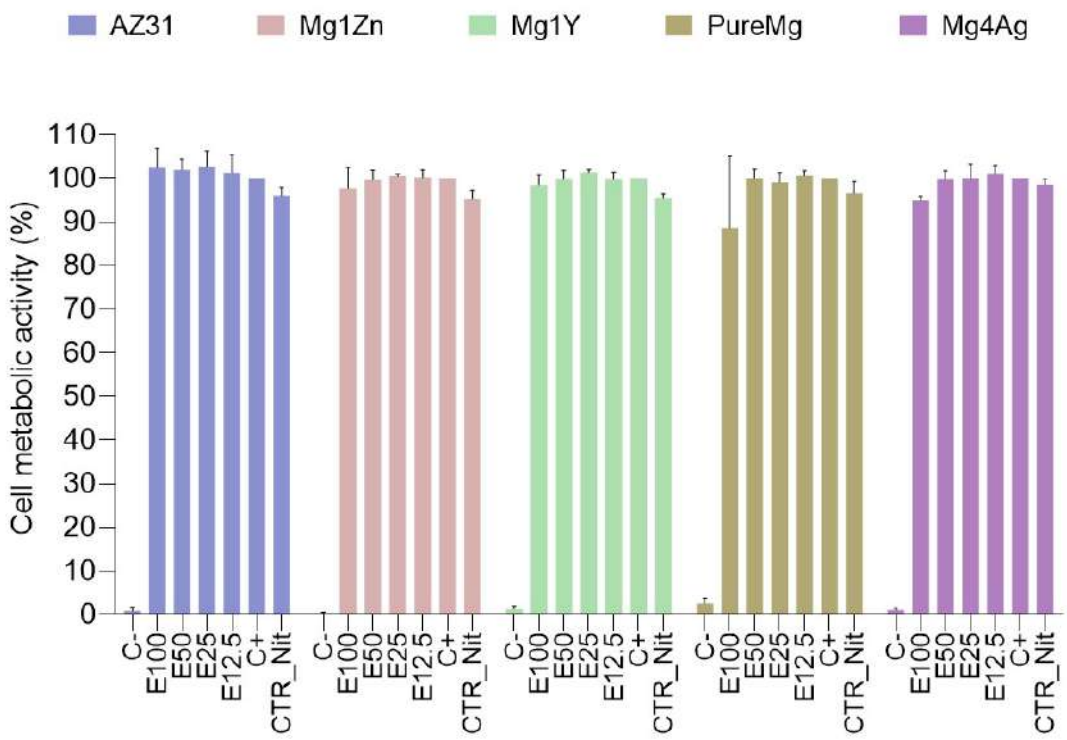


Figure III 16 Cytotoxicity, measured by the metabolic activity of the living cells, of L929 cells after 24h exposure to Mg alloys' extracts. C- represents the negative control, 25% DMSO, C+ represents the positive control, cells with cell culture media, CTR_Nit is the condition of exposure to nitinol extract and E100, E50, E25 and E12.5 represent the different concentrations of samples' extracts exposed to cells, 100%, 50%, 25% and 12.5%, respectively.

The utilization of Mg/Mg alloys-based devices for ureteral stents development would bring several advantages, such as good biocompatibility, degradation in the biological environment by corrosion, and, since Mg is one of the most abundant elements in the human body, toxicity caused by Mg may not be a problem. Besides, since it will be applied in an excretory system, some common problems associated with Mg corrosion, such as hydrogen liberation, shouldn't be problematic since the hydrogen bubbles are expected to be dragged away with urine(82). Also, the urine pH may not be significantly altered since new urine is constantly being produced, neutralizing the metal's alkaline surface pH more rapidly.

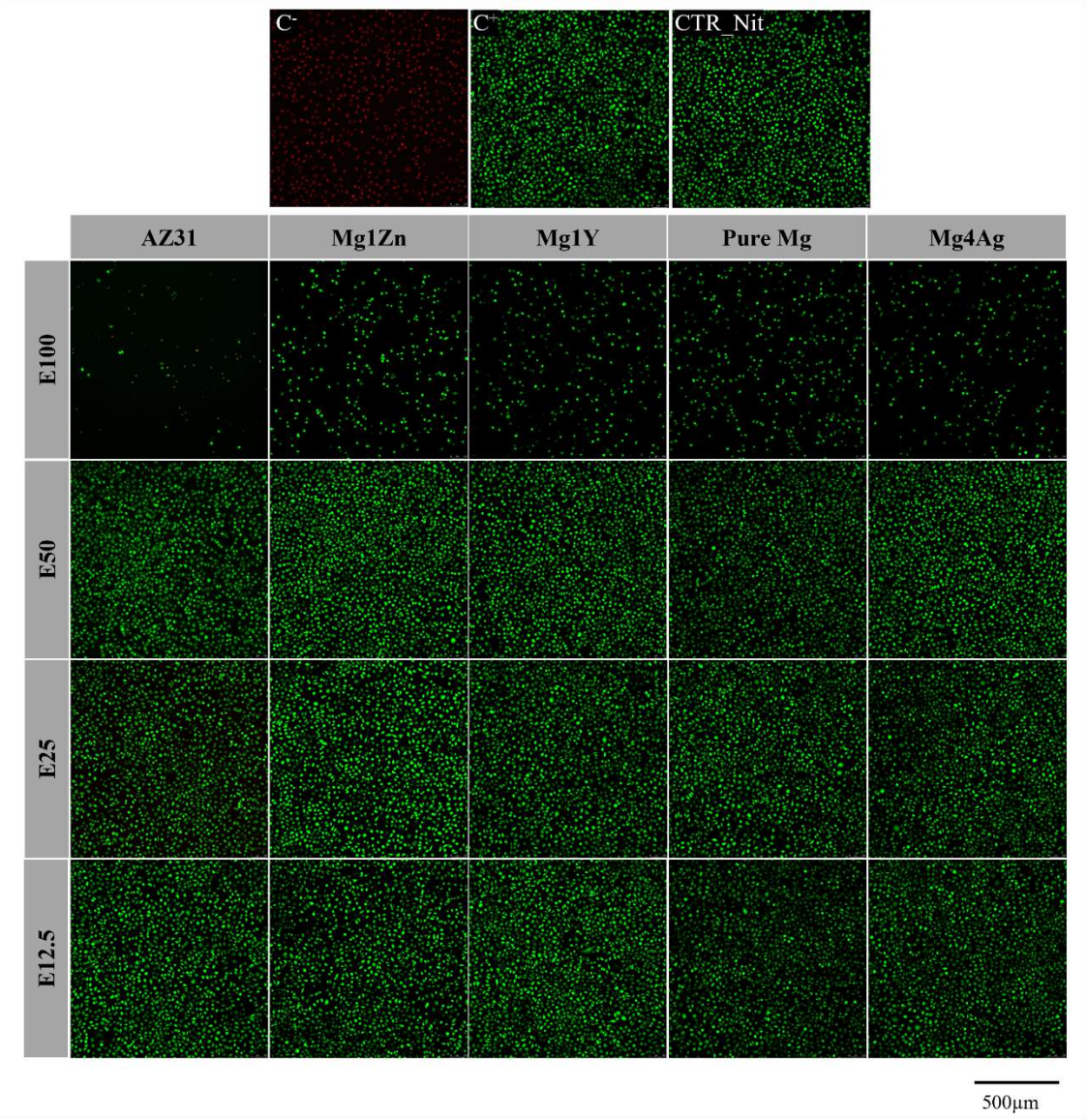


Figure III 17 Microscopic images of L929 cells after exposed to Mg alloys extracts for 24h, at different concentrations, obtained by Live/Dead assay. The controls, C+ and C- as well as a reference material, Nitinol (CTR_Nit) are also represented.

Regardless of the interesting findings of this work, it is important to consider the limitations of the study. Human urine is very difficult to mimic, especially in terms of composition, pH, and flow rate, because it is not a stable fluid, and its characteristics will depend on food and liquid intake and health status of the person, for example, beside the fact that it is different in each person. In this work we used AUS (with a defined chemical composition) at a stablished pH, and flow rate, in order to have control over the experiment and better interpretate the results. However, this does not completely mimic the reality. The dynamic system that we developed is clearly better than static conditions – as we can see by the different results obtained in these two situations – but it is still far from the complexity of the ureter

environment, where there are cells surrounding the stent, peristaltic movements, among others. All these considerations influence the metal behavior and if we use different conditions, different results may be obtained, so future *in vitro* studies using real urine and then *in vivo* studies for validation are required.

This work is a starting point for future exploration and optimization of Mg alloys for urinary applications since it provides essential features on corrosion and encrustation. From here, the production characteristics of the alloys can be tailored and optimized towards adequate corrosion that should occur homogeneously and have a lower propensity for encrustation.

III-4. Conclusion

This study deciphers the corrosion layer composition and corrosion profile of pure Mg and four Mg alloys extruded wires under a simulated urinary tract environment. The layer of corrosion products formed after immersion in AUS, in both dynamic and static conditions, is composed predominantly of $Mg(OH)_2$, MgO, and phosphate-containing species, including struvite ($NH_4MgPO_4 \cdot 6H_2O$) and newberyite ($Mg(PO_3OH) \cdot 3H_2O$). The phosphate-containing products can be advantageous because they protect the metal from corrosion. Still, they can also be a concern since they are associated with urinary calculi formation. However, further and focused studies should be conducted, i.e., the evolution of the corrosion layer thickness along the time in biodegradable ureteral stents prototypes, to determine if they are unfavorable. The corrosion rate results indicate that dynamic conditions accelerate the metal's corrosion. For static and dynamic conditions, Mg-4Ag was the most affected in average corrosion rate at 1, 2, and 4 weeks of immersion. The analysis of the corrosion pattern showed that AZ31, Mg-1Zn, pure Mg, and Mg-4Ag are notoriously prone to site-directed corrosion – large corrosion dimples were formed -, thus more susceptible to uneven corrosion, and Mg-1Y degraded most homogeneously both in static and dynamic conditions.

Altogether, the results outlined in this research indicate that Mg-1Y could be a potential candidate as a future base material for a biodegradable metallic ureteral stent, given its distinct homogeneous corrosion compared with other Mg alloys tested in this work.

III- References

1. Herdman JP. Polythene tubing in the experimental surgery of the ureter. Br J Surg. 2005 Dec 6;37(145):105–6.

2. Beysens M, Tailly TO. Ureteral stents in urolithiasis. Asian J Urol. 2018 Oct;5(4):274–86.

3. Auge BK, Preminger GM. Ureteral stents and their use in endourology. Curr Opin Urol. 2002 May;12(3):217–22.

4. Tulloch WS. Restoration of the continuity of the ureter by means of polythene tubing. Br J Urol. 1952 Mar;24(1):42–5.

5. Zimskind PD, Fetter TR, Wilkerson JL. Clinical Use of Long-Term Indwelling Silicone Rubber Ureteral Splints Inserted Cystoscopically. J Urol. 1967 May;97(5):840–4.

6. Gadzhiev N, Gorelov D, Malkhasyan V, Akopyan G, Harchelava R, Mazurenko D, et al. Comparison of silicone versus polyurethane ureteral stents: a prospective controlled study. BMC Urol. 2020 Dec 3;20(1):10.

7. Chew BH, Denstedt JD. Technology Insight: novel ureteral stent materials and designs. Nat Clin Pract Urol. 2004 Nov;1(1):44–8.

8. Corrales M, Doizi S, Barghouthy Y, Kamkoum H, Somani B, Traxer O. A systematic review of long-duration stents for ureteral stricture: which one to choose? World J Urol. 2021 Sep 2;39(9):3197–205.

9. Elsamra SE, Leavitt DA, Motato HA, Friedlander JI, Siev M, Keheila M, et al. Stenting for malignant ureteral obstruction: Tandem, metal or metal-mesh stents. Int J Urol. 2015 Jul;22(7):629–36.

10. Asakawa J, Iguchi T, Tamada S, Ninomiya N, Kato M, Yamasaki T, et al. Outcomes of indwelling metallic stents for malignant extrinsic ureteral obstruction. Int J Urol. 2018 Mar;25(3):258–62.

11. Chen Y, Liu C, Zhang Z, Xu P, Chen D, Fan X, et al. Malignant ureteral obstruction: experience and comparative analysis of metallic versus ordinary polymer ureteral stents. World J Surg Oncol. 2019 Dec 30;17(1):74.

12. Yoshida T, Takemoto K, Sakata Y, Matsuzaki T, Koito Y, Yamashita S, et al. A randomized clinical trial evaluating the short-term results of ureteral stent encrustation in urolithiasis patients undergoing ureteroscopy: micro-computed tomography evaluation. Sci Rep. 2021 Dec 14;11(1):10337.

13. Tomer N, Garden E, Small A, Palese and M, Information VAA. Ureteral Stent Encrustation: Epidemiology, Pathophysiology, Management and Current Technology. J Urol. 2021;205(1):68–77.

14. S R E-F, Shamsuddin A, SC H, R A, A H K, M K O, et al. Polyurethane internal ureteral stents in treatment of stone patients: morbidity related to indwelling times. J Urol. 1991;146(6):1487–91.

15. Zumstein V, Betschart P, Albrich WC, Buhmann MT, Ren Q, Schmid H-P, et al. Biofilm formation on ureteral stents - Incidence, clinical impact, and prevention. Swiss Med Wkly. 2017 Feb 3;3(147):w14408.

16. Monga M, Klein E, Castaneda-Zuniga WR, Thomas R. The Forgotten Indwelling Ureteral Stent: A Urological Dilemma. J Urol. 1995 Jun;153(6):1817–9.

17. Singh V, Srinivastava A, Kapoor R, Kumar A. Can the Complicated Forgotten Indwelling Ureteric Stents be Lethal? Int Urol Nephrol. 2005 Sep;37(3):541–6.

18. Abdelaziz AY, Fouda WB, Mosharafa AA, Abelrasoul MA, Fayyad A, Fawzi K. Forgotten ureteral stents: Risk factors, complications and management. African J Urol. 2018 Mar;24(1):28–33.

19. Finney RP. Experience with New Double J Ureteral Catheter Stent. J Urol. 1978 Dec;120(6):678–81.

20. Mosayyebi A, Manes C, Carugo D, Somani BK. Advances in Ureteral Stent Design and Materials. Curr Urol Rep. 2018 May 10;19(5):35.

21. Barros AA, Oliveira C, Lima E, Duarte ARC, Healy K, Reis RL. 7.41 Ureteral Stents Technology: Biodegradable and Drug-Eluting Perspective. In: Comprehensive Biomaterials II. Elsevier; 2017. p. 793–812.

22. Barros AA, Oliveira C, Reis RL, Lima E, Duarte ARC. Ketoprofen-eluting biodegradable ureteral stents by CO2 impregnation: In vitro study. Int J Pharm. 2015 Nov;495(2):651–9.

23. Zhang K, Cui H, Jiang H, Hao Y, Long R, Ma Q, et al. The current status and applications of ureteral stents. Int J Clin Exp Med. 2020;13(4):2122–33.

24. Barros AA, Browne S, Oliveira C, Lima E, Duarte ARC, Healy KE, et al. Drug-eluting biodegradable ureteral stent: New approach for urothelial tumors of upper urinary tract cancer. Int J Pharm. 2016 Nov;513(1–2):227–37.

25. Barros AA, Rita A, Duarte C, Pires RA, Sampaio-Marques B, Ludovico P, et al. Bioresorbable ureteral stents from natural origin polymers. J Biomed Mater Res Part B Appl Biomater. 2015 Apr;103(3):608–17.

26. Barros AA, Oliveira C, Ribeiro AJ, Autorino R, Reis RL, Duarte ARC, et al. In vivo assessment of a novel biodegradable ureteral stent. World J Urol. 2018 Feb 11;36(2):277–83

27. Barros AA, Oliveira C, Lima E, Duarte ARC, Reis RL. Gelatin-based biodegradable ureteral stents with enhanced mechanical properties. Appl Mater Today. 2016 Dec;5:9–18.

28. Barros A, Oliveira C, Correia-Pinto J, Lima E, Reis RL, Duarte AR. AN URETERAL STENT, METHODS AND USES THEREOF. WO2016181371A1, 2016.

29. Soria F, Morcillo E, Serrano A, Budia A, Fernández I, Fernández-Aparicio T, et al. Evaluation of a New Design of Antireflux-biodegradable Ureteral Stent in Animal Model. Urology. 2018 May;115:59–64.

30. Soria F, de la Cruz JE, Budia A, Serrano A, Galan-Llopis JA, Sanchez-Margallo FM. Experimental Assessment of New Generation of Ureteral Stents: Biodegradable and Antireflux Properties. J Endourol. 2020 Mar 1;34(3):359–65.

31. Lock JY, Draganov M, Whall A, Dhillon S, Upadhyayula S, Vullev VI, et al. Antimicrobial properties of biodegradable magnesium for next generation ureteral stent applications. In: 2012 Annual International Conference of the IEEE Engineering in Medicine and Biology Society. IEEE; 2012. p. 1378–81.

32. Zhang S, Bi Y, Li J, Wang Z, Yan J, Song J, et al. Biodegradation behavior of magnesium and ZK60 alloy in artificial urine and rat models. Bioact Mater. 2017 Jun;2(2):53–62.

33. Tie D, Liu H, Guan R, Holt-Torres P, Liu Y, Wang Y, et al. In vivo assessment of biodegradable magnesium alloy ureteral stents in a pig model. Acta Biomater. 2020 Oct;116:415–25.

34. Mei D, Wang C, Nienaber M, Pacheco M, Barros A, Neves S, et al. Corrosion behavior of Mg wires for ureteral stent in artificial urine solution. Corros Sci. 2021 Aug;189:109567.

35. Nienaber M, Yi S, Kainer KU, Letzig D, Bohlen J. On the Direct Extrusion of Magnesium Wires from Mg-Al-Zn Series Alloys. Metals (Basel). 2020 Sep 9;10(9):1208.

36. Kazmierska KA, Thompson R, Morris N, Long A, Ciach T. In Vitro Multicompartmental Bladder Model for Assessing Blockage of Urinary Catheters: Effect of Hydrogel Coating on Dynamics of Proteus mirabilis Growth. Urology. 2010 Aug;76(2):515.e15-515.e20.

37. Azevedo AS, Almeida C, Gomes LC, Ferreira C, Mergulhão FJ, Melo LF, et al. An in vitro model of catheter-associated urinary tract infections to investigate the role of uncommon bacteria on the Escherichia coli microbial consortium. Biochem Eng J. 2017 Feb;118:64–9.

38. Tian Y, Cai X, Wazir R, Wang K, Li H. Water consumption and urinary tract infections: an in vitro study. Int Urol Nephrol. 2016 Jun 18;48(6):949–54.

39. Kim K-W, Choi YH, Lee SB, Baba Y, Kim H-H, Suh S-H. Analysis of Urine Flow in Three Different Ureter Models. Comput Math Methods Med. 2017;2017:1–11.

40. Worcester EM, Bergsland KJ, Gillen DL, Coe FL. Mechanism for higher urine pH in normal women compared with men. Am J Physiol Physiol. 2018 Apr 1;314(4):F623–9.

41. Champagne S, Mostaed E, Safizadeh F, Ghali E, Vedani M, Hermawan H. In Vitro Degradation of Absorbable Zinc Alloys in Artificial Urine. Materials (Basel). 2019 Jan 18;12(2):295.

42. Esmaily M, Svensson JE, Fajardo S, Birbilis N, Frankel GS, Virtanen S, et al. Fundamentals and advances in magnesium alloy corrosion. Prog Mater Sci. 2017 Aug;89:92–193.

43. Heakal FE-T, Bakry AM. Role of amoxicillin in enhancing AZ31 alloy degradation resistance and its monitoring using nano-Pd electrochemical sensor. Mater Chem Phys. 2019 Aug;234:224–36.

44. Mei D, Lamaka S V., Gonzalez J, Feyerabend F, Willumeit-Römer R, Zheludkevich ML. The role of individual components of simulated body fluid on the corrosion behavior of commercially pure Mg. Corros Sci. 2019 Feb;147:81–93.

45. Liu M, Zanna S, Ardelean H, Frateur I, Schmutz P, Song G, et al. A first quantitative XPS study of the surface films formed, by exposure to water, on Mg and on the Mg–Al intermetallics: Al3Mg2 and Mg17Al12. Corros Sci. 2009 May;51(5):1115–27.

46. Mercier D, Światowska J, Protopopoff E, Zanna S, Seyeux A, Marcus P. Inhibition of Mg Corrosion by Sulfur Blocking of the Hydrogen Evolution Reaction on Iron Impurities. J Electrochem Soc. 2020 Jan 9;167(12):121504.

47. Wang L, Snihirova D, Deng M, Wang C, Vaghefinazari B, Wiese G, et al. Insight into physical interpretation of high frequency time constant in electrochemical impedance spectra of Mg. Corros Sci. 2021 Jul;187:109501.

48. Mercier D, Światowska J, Zanna S, Seyeux A, Marcus P. Role of Segregated Iron at Grain Boundaries on Mg Corrosion. J Electrochem Soc. 2018 Jan 13;165(2):C42–9.

49. Wu L, Zhao L, Dong J, Ke W, Chen N. Potentiostatic Conversion of Phosphate Mineral Coating on AZ31 Magnesium Alloy in 0.1 M K2HPO4 Solution. Electrochim Acta. 2014;145:71–80.

50. Zeng R-C, Yin Z-Z, Chen X-B, Xu D-K. Corrosion types of Magnesium Alloys. In: Tański T, Borek W, Król M, editors. Magnesium Alloys. 9th ed. IntechOpen; 2018. p. 29–52.

51. Kieke M, Feyerabend F, Lemaitre J, Behrens P, Willumeit-Römer R. Degradation rates and products of pure magnesium exposed to different aqueous media under physiological conditions. BioNanoMaterials. 2016 Jan 1;17(3–4):131–43.

52. Santamaria M, Di Quarto F, Zanna S, Marcus P. Initial surface film on magnesium metal: A characterization by X-ray photoelectron spectroscopy (XPS) and photocurrent spectroscopy (PCS). Electrochim Acta. 2007;53(3):1314–24.

53. Petrovic DS, Mandrino D, Šarler B, Horky J, Ojdanic A, Zehetbauer MJ, et al. Surface Analysis of Biodegradable Mg-Alloys after Immersion in Simulated Body Fluid. Materials (Basel). 2020;13(7):1740.

54. Gu X, Zheng Y, Cheng Y, Zhong S, Xi T. In vitro corrosion and biocompatibility of binary magnesium alloys. Biomaterials. 2009 Feb;30(4):484–98.

55. Rosalbino F, De Negri S, Saccone A, Angelini E, Delfino S. Bio-corrosion characterization of Mg–Zn–X (X = Ca, Mn, Si) alloys for biomedical applications. J Mater Sci Mater Med. 2010 Apr 18;21(4):1091–8.

56. Xiong Y, Sun T, Zhang A. Corrosion Behavior of Micro-arc Oxidation-Coated AZ80 Magnesium Alloy in Simulated Body Fluid at Different Flow Rates. J Mater Eng Perform. 2023 Apr 3;

57. Frost RL, Xi Y, Scholz R, López A, Belotti FM. Vibrational spectroscopic characterization of the phosphate mineral hureaulite – (Mn, Fe)5(PO4)2(HPO4)2·4(H2O). Vib Spectrosc. 2013 May;66:69–75.

58. Prywer J, Kozanecki M, Mielniczek-Brzóska E, Torzewska A. Solid Phases Precipitating in Artificial Urine in the Absence and Presence of Bacteria Proteus mirabilis—A Contribution to the Understanding of Infectious Urinary Stone Formation. Crystals. 2018 Apr 9;8(4):164.

59. Liao M, Liu Y, Tian E, Ma W, Liu H. Phosphorous removal and high-purity struvite recovery from hydrolyzed urine with spontaneous electricity production in Mg-air fuel cell. Chem Eng J. 2020 Jul;391:123517.

60. Frost RL, Palmer SJ, Pogson RE. Raman spectroscopy of newberyite Mg(PO3OH)·3H2O: A cave mineral. Spectrochim Acta Part A Mol Biomol Spectrosc. 2011 Sep;79(5):1149–53.

61. Maltseva A, Shkirskiy V, Lefèvre G, Volovitch P. Effect of pH on Mg(OH)2 film evolution on corroding Mg by in situ kinetic Raman mapping (KRM). Corros Sci. 2019 Jun;153:272–82.

62. Tie D, Hort N, Chen M, Guan R, Ulasevich S, Skorb E V., et al. In vivo urinary compatibility of Mg-Sr-Ag alloy in swine model. Bioact Mater. 2022 Jan;7:254–62.

63. Lock JY, Wyatt E, Upadhyayula S, Andrew Whall V, Nuñez VI, Vullev HL. Degradation and antibacterial properties of magnesium alloys in artificial urine for potential resorbable ureteral stent applications. J Biomed Mater Res - Part A. 2013;102(3):781–92.

64. Cerqueira L, Oliveira JA, Nicolau A, Azevedo NF, Vieira MJ. Biofilm formation with mixed cultures of Pseudomonas aeruginosa / Escherichia coli on silicone using artificial urine to mimic urinary catheters. Biofouling. 2013 Aug;29(7):829–40.

65. He G, Wu Y, Zhang Y, Zhu Y, Liu Y, Li N, et al. Addition of Zn to the ternary Mg–Ca–Sr alloys significantly improves their antibacterial properties. J Mater Chem B. 2015;3(32):6676–89.

66. Cauda V, Chiodoni A, Laurenti M, Canavese G, Tommasi T. Ureteral double-J stents performances toward encrustation after long-term indwelling in a dynamic in vitro model. J Biomed Mater Res Part B Appl Biomater. 2017 Nov;105(8):2244–53.

67. Gorman SP, Garvin CP, Quigley F, Jones DS. Design and validation of a dynamic flow model simulating encrustation of biomaterials in the urinary tract. J Pharm Pharmacol. 2010 Feb 18;55(4):461–8.

68. L.Prien E, L. Prien Jr. E. Composition and structure of urinary stone. Am J Med. 1968;45(5):654–72.

69. Zuo M, Wang W, Wu H, Yang L, Yan J, Ni J, et al. In vitro degradation and mineralization of high-purity magnesium in three physiological fluids. Mater Lett. 2019;240:279–83.

70. Song Y, Han E-H, Shan D, Yim CD, You BS. The effect of Zn concentration on the corrosion behavior of Mg–xZn alloys. Corros Sci. 2012 Dec;65:322–30.

71. Sanchez AHM, Luthringer BJC, Feyerabend F, Willumeit R. Mg and Mg alloys: How comparable are in vitro and in vivo corrosion rates? A review. Acta Biomater . 2015 Feb;13:16–31

72. Atrens A, Shi Z, Mehreen SU, Johnston S, Song G-L, Chen X, et al. Review of Mg alloy corrosion rates. J Magnes Alloy. 2020 Dec;8(4):989–98.

73. Ralston KD, Birbilis N. Effect of Grain Size on Corrosion: A Review. CORROSION. 2010 Jul;66(7):075005-075005–13.

74. Wang Y, Zhang Y, Jiang H. Effect of grain size uniformity and crystallographic orientation on the corrosion behavior of Mg-2Zn-1Al bar. Mater Charact. 2021 Sep;179:111374.

75. Liu Y, Li H, Zhang Z, Li Y, Jia L, Wang J, et al. Effect of Cu micro-alloying on the microstructure, mechanical and corrosion properties of Mg-Gd-Y-Zn based alloy applied as plugging tools. J Alloys Compd. 2023 Apr;939:168768.

76. Orlov D, Ralston KD, Birbilis N, Estrin Y. Enhanced corrosion resistance of Mg alloy ZK60 after processing by integrated extrusion and equal channel angular pressing. Acta Mater. 2011 Sep;59(15):6176–86.

77. Liao J, Hotta M, Motoda S, Shinohara T. Atmospheric corrosion of two field-exposed AZ31B magnesium alloys with different grain size. Corros Sci. 2013 Jun;71:53–61

78. Lin X, Saijilafu, Wu X, Wu K, Chen J, Tan L, et al. Biodegradable Mg-based alloys: biological implications and restorative opportunities. Int Mater Rev. 2022 Jun 16;1–39.

79. Costantino MD, Schuster A, Helmholz H, Meyer-Rachner A, Willumeit-Römer R, Luthringer-Feyerabend BJC. Inflammatory response to magnesium-based biodegradable implant materials. Acta Biomater. 2020 Jan;101:598–608.

80. Kim Y-K, Lee K-B, Kim S-Y, Bode K, Jang Y-S, Kwon T-Y, et al. Gas formation and biological effects of biodegradable magnesium in a preclinical and clinical observation. Sci Technol Adv Mater. 2018 Dec 31;19(1):324–35.

81. Al Alawi AM, Majoni SW, Falhammar H. Magnesium and Human Health: Perspectives and Research Directions. Int J Endocrinol. 2018;2018:1–17.

82. Berglund IS, Jacobs BY, Allen KD, Kim SE, Pozzi A, Allen JB, et al. Peri-implant tissue response and biodegradation performance of a Mg–1.0Ca–0.5Sr alloy in rat tibia. Mater Sci Eng C. 2016 May;62:79–85.

SUPPLEMENTARY INFORMATION

Understanding the corrosion of Mg alloys in in vitro urinary tract conditions: a step forward towards a biodegradable metallic ureteral stent

Margarida Pacheco[1,2], Ivo M. Aroso[1,2], Joana M. Silva[1,2], Sviatlana V. Lamaka[3], Jan Bohlen[4], Maria Nienaber[4], Dietmar Letzig[4], Estêvão Lima[5], Alexandre A. Barros[1,2], Rui L. Reis[1,2]

[1]3B's Research Group—Research Institute on Biomaterials, Biodegradables and Biomimetics, University of Minho, Guimarães, Portugal. [2]ICVS/3B's-PT Government Associate Laboratory, Braga/Guimarães, Portugal. [3]Institute of Surface Science, Helmholtz-Zentrum hereon GmbH, Germany. [4]Institute of Material and Process Design, Helmholtz-Zentrum hereon GmbH, Germany [5]School of Health Sciences, Life and Health Sciences Research Institute (ICVS), University of Minho, Braga, Portugal

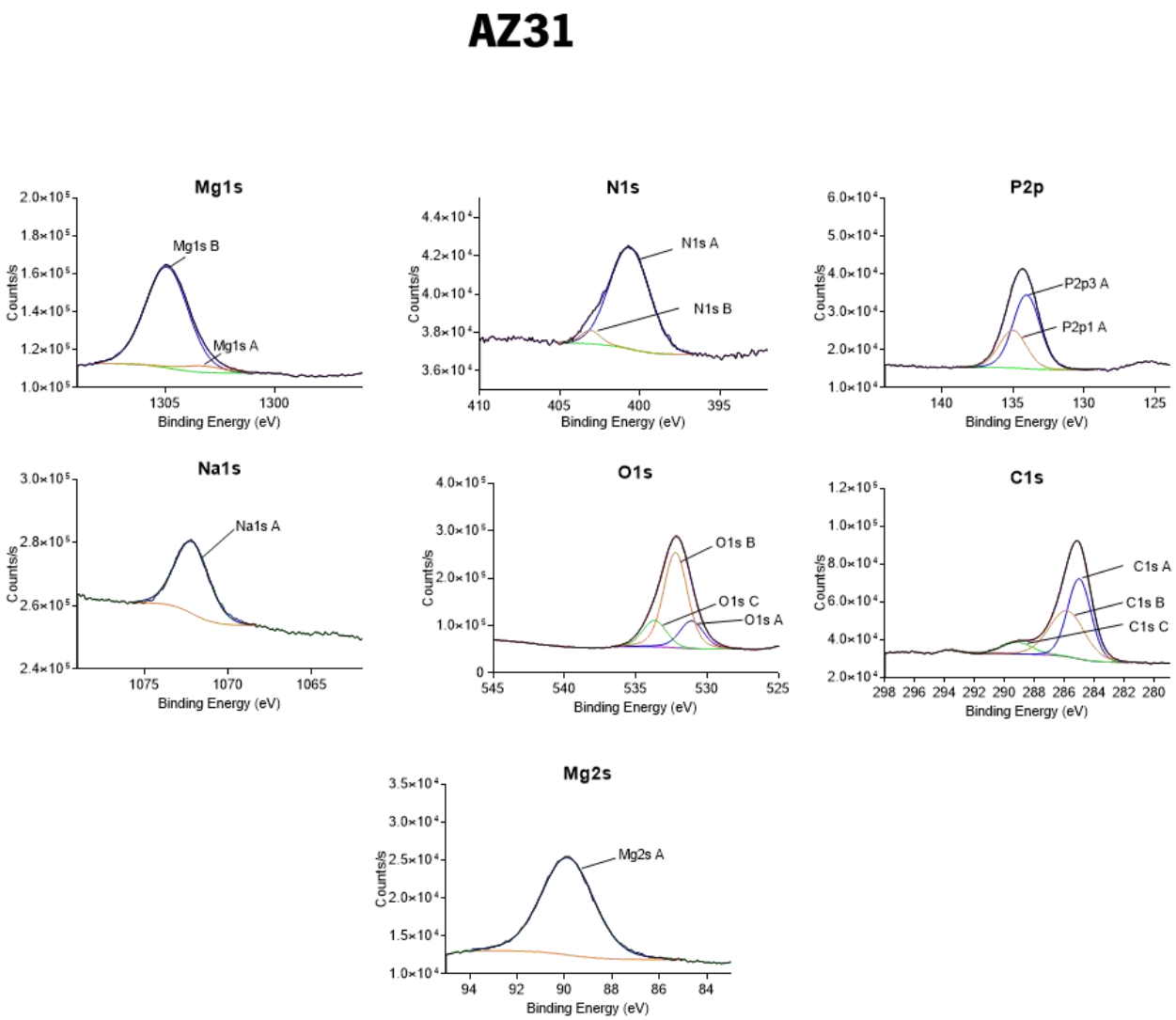


Figure III S 1 High resolution XPS spectra of the corrosion layer of AZ31 after 4 weeks in static conditions with artificial urine solution (AUS).

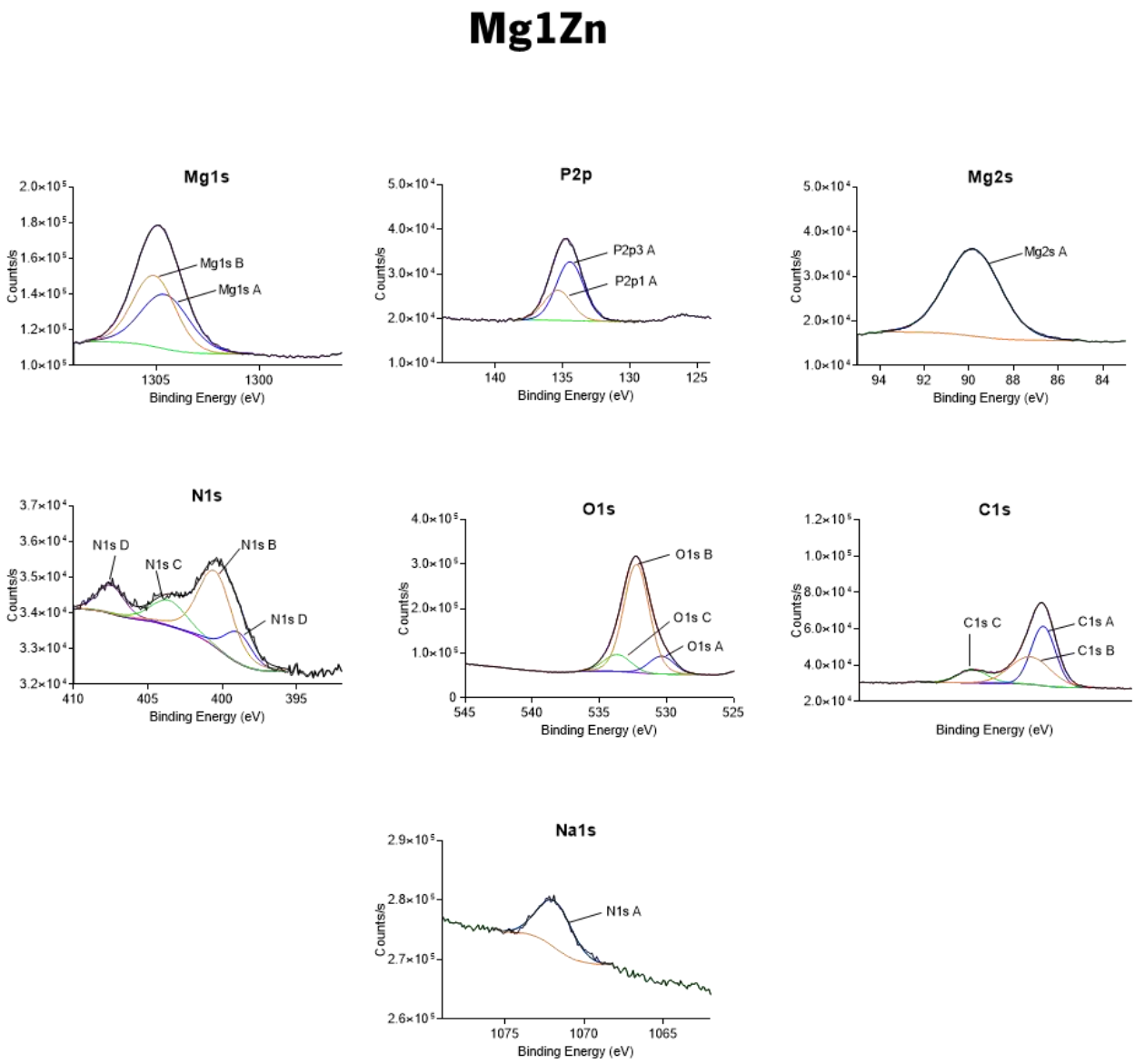


Figure III S 2 High resolution XPS spectra of the corrosion layer of Mg-1Zn after 4 weeks in static conditions with artificial urine solution (AUS).

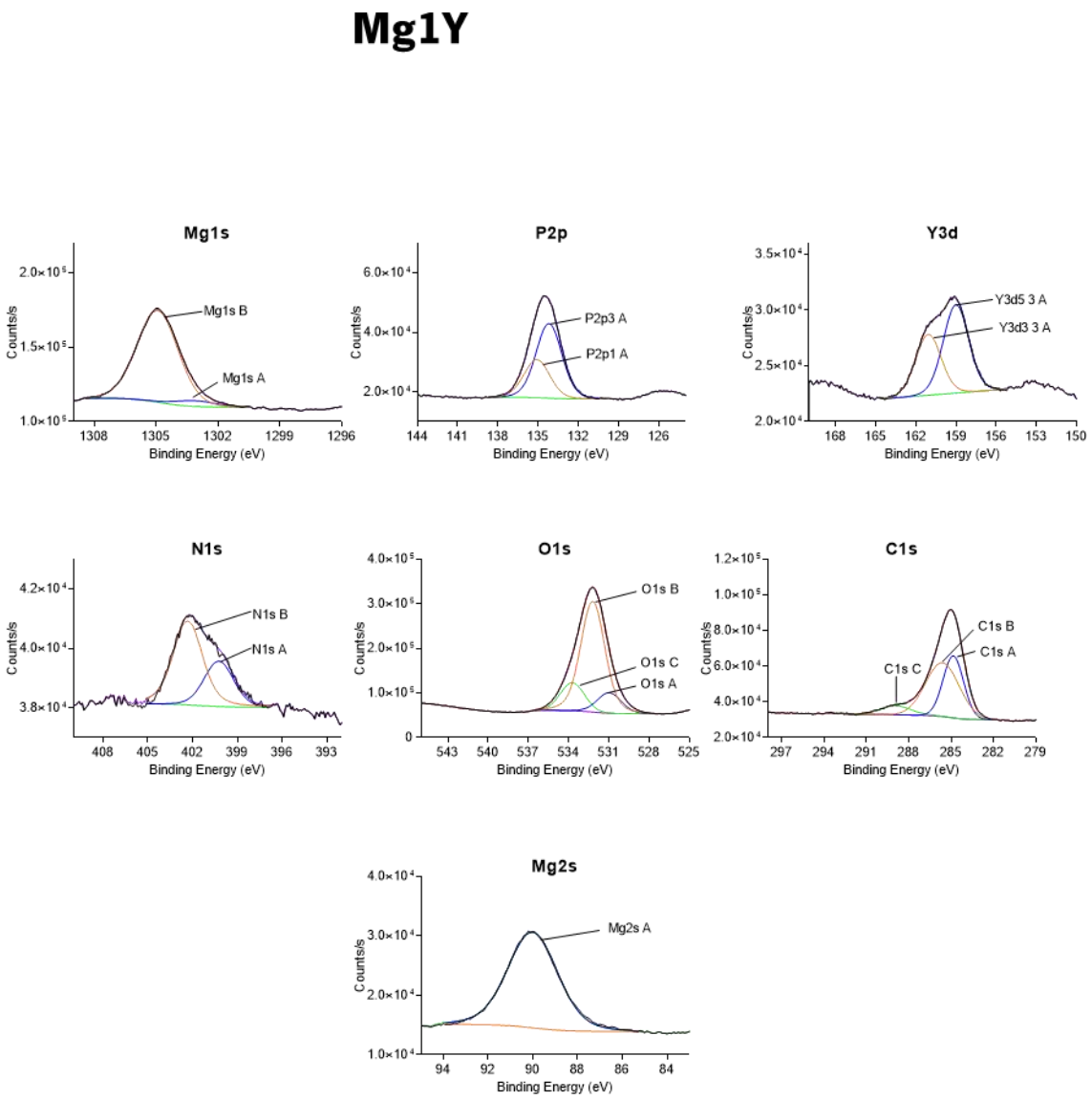


Figure III S 3 High resolution XPS spectra of the corrosion layer of Mg1Y after 4 weeks in static conditions with artificial urine solution (AUS).

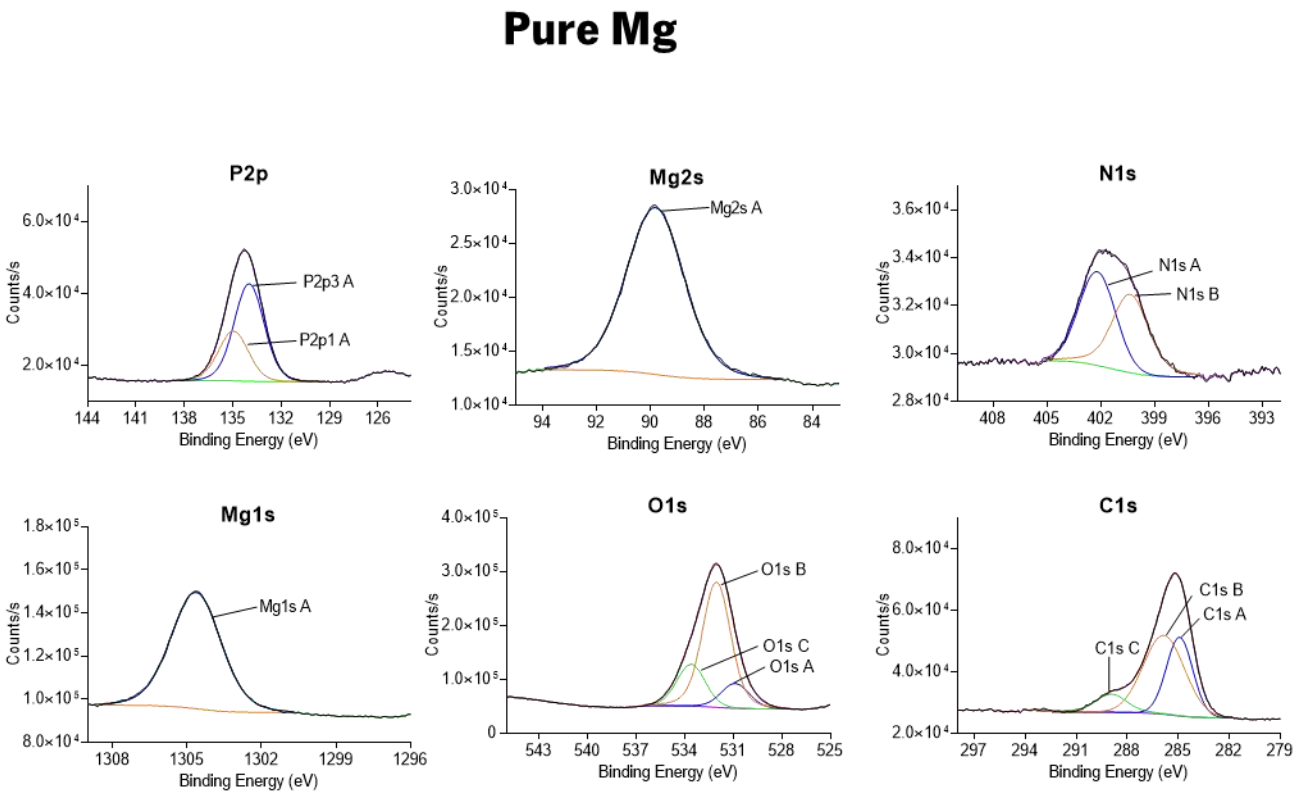


Figure III S 4 High resolution XPS spectra of the corrosion layer of Pure Mg after 4 weeks in static conditions with artificial urine solution (AUS).

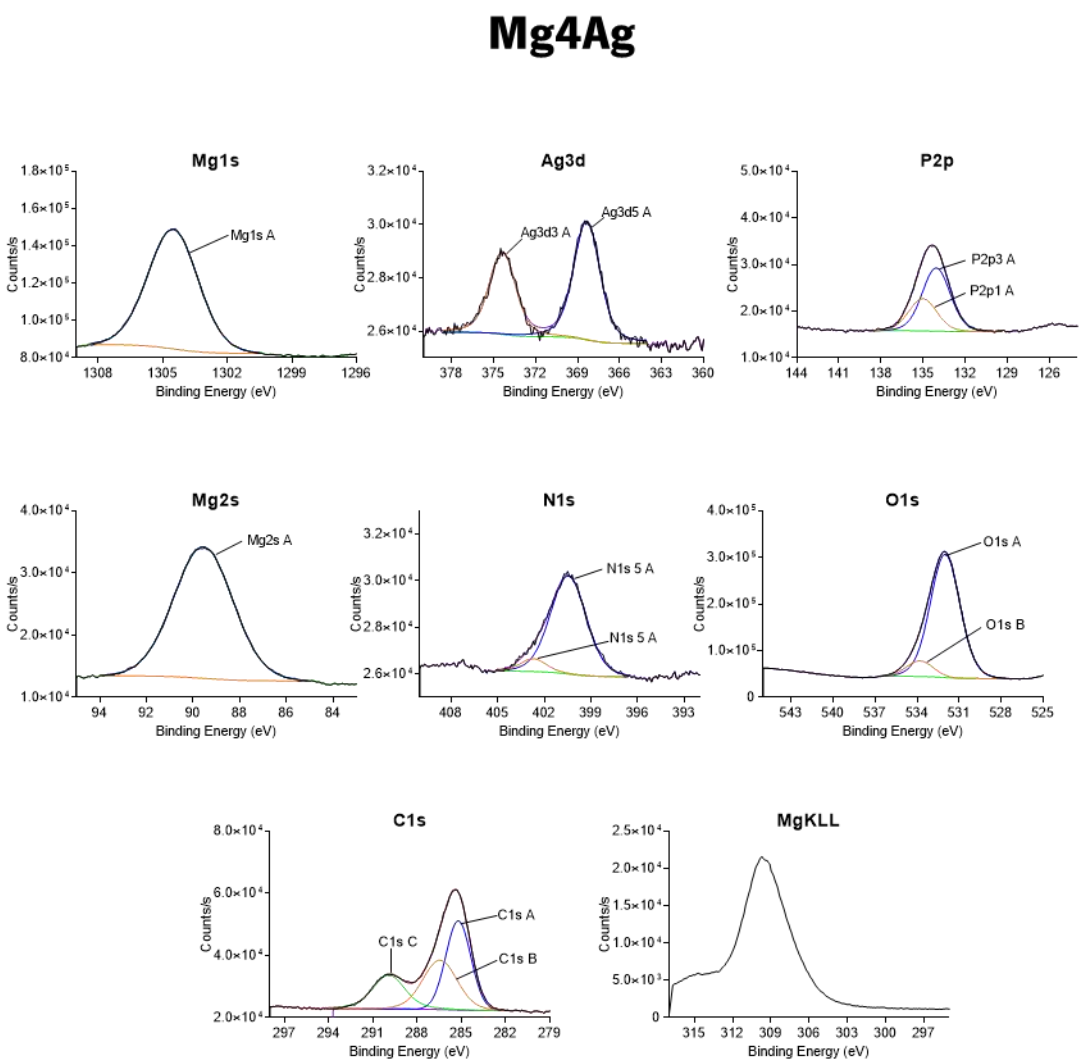


Figure III S 5 High resolution XPS spectra of the corrosion layer of Mg4Ag after 4 weeks in static conditions with artificial urine solution (AUS).

CHAPTER IV

ADDITIVELY MANUFACTURED WE43 FOR BIODEGRADABLE URINARY DEVICES: EXPLORING THE CORROSION PROFILE UNDER *IN VITRO* URINARY TRACT CONDITIONS

ADDITIVELY MANUFACTURED WE43 FOR BIODEGRADABLE URINARY DEVICES: EXPLORING THE CORROSION PROFILE UNDER *IN VITRO* URINARY TRACT CONDITIONS.

ABSTRACT

Urinary stents are widely used medical devices, however, the necessity of a second surgery for the stent removal is a significant drawback. Hence, using biodegradable materials for stent development has been considered a promising approach. Biodegradable Mg alloys have been gaining popularity for biodegradable medical devices due to the recognized biocompatibility and mechanical characteristics. This work explored the suitability of a WE43 alloy for urinary stent applications using additive manufacturing (AM). This manufacturing technique allows the creation of intricate geometries with high resolution, thus presenting a significant potential for stent design development. The corrosion behaviour of WE43-printed tubes and wires, potential precursors for ureteral stents, were investigated under simulated dynamic urinary tract conditions.

While the corrosion pattern was found to be greatly influenced by the different designs and process parameters, where the corrosion rate values along the time varied considerably among the samples, the resulting corrosion layer exhibited similarities, all presenting a non-homogeneous coverage and the same chemical elements. This work highlighted the challenge of obtaining homogeneous corrosion but suggested that this type of design exploration could be a useful approach to optimize and tune the stents' corrosion pattern, given the considerable influence of the design on the corrosion pattern. AM is hence a promising research strategy for the exploration of ureteral stent designs given the possibility to easily print a high amount of samples with different printing parameters.

Keywords: Biodegradable urinary stents; WE43; additive manufacturing; corrosion; dynamic conditions.

This chapter is based on the following publication: **Margarida Pacheco**, Francesco D'Elia, Hanna Nilsson-Åhman, Estêvão Lima, Alexandre Barros, Cecilia Person, Rui L. Reis. Additively manufactured WE43 for biodegradable urinary devices: exploring the corrosion profile under in vitro urinary tract conditions. Applied Materials Today. 2025 Dec; DOI: 10.1016/j.apmt.2025.102975.

IV-1. INTRODUCTION

Ureteral stents are widely used in clinics to allow urine drainage in case of temporary ureteral obstruction, which can occur for e.g. renal calculi, ureteral stricture, external ureteral compression, among others(1,2). After serving their purpose, ureteral stents should be removed from the body through surgery. This procedure implies physical pain to the patient and additional costs both for the patient and for the healthcare system(2-4). On top of this, there are other severe disadvantages associated with ureteral stenting such as frequently-occurring infections and encrustation, which, in more serious clinical scenarios can lead to obstruction and renal failure(5,6). Numerous alternatives to address these problems have been proposed. One of the most recent approaches for ureteral stent improvement is the use of biodegradable materials(7-10). Biodegradable ureteral stents are expected to have lower propensity for bacterial and encrustation attachment, given the dynamic surface during degradation, and will obviously avoid a second surgery for stent removal given its self-degrading property. Magnesium and its alloys are gaining popularity nowadays as base material for temporary implantable devices given their role in many biological functions, biocompatibility, and biodegradability(11-15). A biodegradable metallic ureteral stent, with an adequate corrosion rate, could bring unique advantages, such as lower degradation rate and higher mechanical properties compared with the current polymeric based ones(16), which can expand the utilization of biodegradable ureteral stents to more clinical scenarios, so more patients can benefit from these advantages. Another property that has been associated with Mg alloys, and important for ureteral stents given the frequency of urinary infections related to stenting, is the antibacterial potential. One of the first works reporting this feature was the paper from Lock *et al.*(17). The authors verified an improved antibacterial activity of as-cast Mg4Y (4 wt% yttrium) when compared with a currently used polymer for ureteral stents (polyurethane). Other studies have also demonstrated the potential of Mg-based alloys for biodegradable urinary tract devices. Zhang and co-workers investigated the corrosion of pure Mg and ZK60 (Mg-5.6 wt % Zn-0.5 wt % Zr) *in vitro* (static conditions with artificial urine) and *in vivo* (rat model)(18). The authors reported histocompatibility of both implants, and no harm to the bladder, liver and kidney. Also, ZK60 presented a faster degradation than pure Mg both *in vitro* and *in vivo,* which was due to the faster increase of the pH and the resulting composition of the corrosion layer formed on ZK60 being more soluble, thus having a less protective effect of the metal. In 2020, Tie *et al.* investigated the corrosion and biocompatibility of an extruded ZJ41 (Mg-4.00 wt% Zn-1.00 wt% Sr) wire in porcine ureters for 14 weeks(19). The authors reported no inflammation and higher antibacterial activity of ZJ41 than stainless steel. In a more recent publication, Tie *et al.* presented a Mg-1.00 wt% Sr-0.50 wt% Ag

alloy as ureteral stent material candidate(20). This alloy showed no cytotoxicity, good histocompatibility and distinctive antibacterial activity.

While the above studies show promise for the application of several different Mg alloys, to the best of our knowledge, Mg alloys belonging to the WE43 family (e.g. Mg-Y-Nd-Zr), have not previously been investigated under urinary tract conditions. These are some of the most used and characterized Mg alloys for biomedical implants, and have also reached clinical use as bone repair implants(21). These alloys' rare-earth element (REE) content typically renders them a good corrosion resistance in biological fluids compared with other Mg alloys(22-25). Recently, Wang *et al.* described the impact of torsional and tensile stress on the corrosion of a modified version of WE43 – this modified version had Y, neodymium (Nd), zinc (Zn) and calcium (Ca) in non-specified amounts - in simulated body fluid (SBF)(26). This study indicated that the application of torsion and tensile stresses simultaneously on the implant, representing the complex forces resulting from daily activity, can severely impact the implant corrosion, highlighting the importance of testing under non-static conditions. In another work, Imani *et al.* described the role of glucose and bovine serum on WE43 corrosion mimicking disease stages of hyperglycemia and hyperproteinemia(27). These and other works have contributed to the understanding of WE43 behaviour under biological conditions and confirmed its safety and suitability for implants. Since this alloy was optimized and studied towards improved mechanical performance and corrosion rate, it appears specially promising for ureteral stent applications given the importance of a homogeneous corrosion – the cracking of the stent into big fragments must be avoided – and appropriate strength – it has to be able to endure stent placement and constant peristaltic movements of the ureter.

Another objective of the present work was to explore basic, representative, stent unit designs (i.e. simple thin structures), as a first step towards a future, complex ureteral stent model. Here, we aimed to establish the most suitable process parameters for each kind of structure prior to the exploration of complete ureteral stent designs. In view of the potential complexity of future designs, additive manufacturing (AM), through powder bed fusion laser beam (PBF-LB) was chosen as the manufacturing technique. AM permits design flexibility, which means that in the future we can easily explore different stent designs (including complex structures and different types of meshes). Besides, AM allows the manufacturing of many samples in only one print (considering that we are working with small structures) and the printing of different designs/parameters in one single step, allowing an efficient process and design optimization. Process parameters for this technique are currently under development for biodegradable metals, where WE43 is one of the most reported ones, including process parameter

development for PBF-LB of a WE43 alloy by the co-authors(28,29). Different process parameters were found to influence the grain size and grain size distribution of WE43 constructs. Other groups have reported similar studies on WE43, extensively describing printing process, microstructure, density and mechanical behaviour and the relation of these properties among the same(30-32). Other groups have also found that AM is a suitable technique to produce a dense and homogeneous microstructure for WE43 constructs(24,30,31). The studies performed until now, showed that AM is a very useful technique to produce small and meshed structures(33) (such as stents), therefore, in this work, we explored the suitability of WE43 as base material for ureteral stent development through AM. Thin simple structures – tubes and wires – were printed and their corrosion under ureteral stent environment was investigated. The findings of this study are the first steps towards the employment of a new design technique for ureteral stent development.

IV-2. Materials and Methods

This section describes the fabrication of WE43-based tubes and wires and the respective corrosion characterization under a simulated urinary tract environment. The assessment of the corrosion layer formed on the samples, as well as the corrosion pattern over time is addressed in detail in the following sub-sections.

IV-2.1. Mg alloy WE43 powder and sample preparation

Gas-atomized powder of a WE43 alloy (NMD GmbH, Heemsen Germany) of particle size 25-67 μm was used in the present study for PBF-LB. The powder composition was provided by the manufacturer and is given in **Table IV 1**. Further details on this powder can be found elsewhere(29). Processing through PBF-LB was performed with an EOS M100 printer (EOS GmbH, Krailling, Germany) under argon atmosphere (O2<0.1%). The argon flow across the bed allowed for removal of evaporation products. The print was carried out using a build plate of a commercial Mg-based alloy (KG Fridman AB, Karlstad, Sweden). The parameters used to produce the samples were based on previously optimized parameters from some of the authors and considering the size and geometry of the samples tested herein(29,34). The samples produced were wires (cylinders) with a diameter of 1 mm and 30 mm height and tubes with an internal diameter of ca. 1.57 mm, external diameter of ca. 2.33 mm (i.e. wall thickness of 0.76 mm), and height of 22 mm. Based on the previously optimized parameters(29,34), three groups of tubes and two groups of wires were produced, as presented in **Table IV 2**. The scan pattern was 67° rotation between each layer, the layer thickness was set to 0.02 mm, and the laser spot diameter was 0.04 mm, for all the samples, as previously optimized(29,34). The hatch distance was varied between 0.04-0.06

mm, to maintain proximity to the parameters optimized in previous works while also optimizing for thin structures.

Table IV 1 Chemical composition of the WE43 powder, as provided by the manufacturer (NMD, GmbH, Heemsen, Germany).

Element	Mg	Y	Nd	Zr
Amount (wt%)	Balance	3.9	3.0	0.49

Table IV 2 Group designations and the process parameters used to produce samples from WE43 powder in an EOS M100 PBF-LB machine (EOS GmbH, Krailling, Germany).

Sample	Hatch distance (mm)	Speed (mm/s)	Power (W)	Energy density (J/mm3)
Wire 0.05 hatch distance (W005)	0.05	1100	90	54.55
Wire 0.06 hatch distance (W006)	0.06	1100	90	45.46
Tube 0.04 hatch distance (T004)	0.04	1100	80	60.61
Tube 0.05 hatch distance (T005)	0.05	1100	90	54.55
Tube 0.06 hatch distance (T006)	0.06	1100	90	45.55

IV-2.2. Microstructural analysis

To study the manufactured samples' microstructure in the building direction, the samples were mounted in conductive resin (PolyFast, Struers) and ground with silicone carbide papers (P320 and P800) for 1 min, followed by polishing using diamond suspension (1 µm) for 12 minutes. Finally, the samples were etched with 2% Nital solution (2% nitric acid in ethanol) for 5 seconds before microstructural analysis using light optical microscope (LOM, Olympus AX70 Research Microscope).

IV-2.3. Corrosion test set-up

Corrosion assays were carried out in an in-house built dynamic system specifically developed to test urinary devices (**Figure IV 1**). This dynamic system allows for the simultaneous individual study of up to 12 samples. The samples were placed inside 3.18 mm diameter plastic tubes, positioned inside a holder equipped with a water recirculating system for thermal control. The recirculating water at 37 ^{0}C allows for maintaining that temperature in the artificial urine solution (AUS) reservoir and in the sample's holder. Each sample support tube was connected to a common AUS reservoir (10L) and its own dedicated pumping channel. The AUS was prepared according to the ASTM F 1828 – 97 recommendations, using

3.00 g/L ammonium chloride (NH4Cl), 2.00 g/L creatinine (C4H7N3O), 2.50 g/L disodium hydrogen orthophosphate, anhydrous (Na2HPO4), 2.500 g/L potassium phosphate monobasic (KH2PO4), 9.00 g/L sodium chloride (NaCl), 2.62 g/L sodium sulfite (Na2SO3) and 25.00 g/L urea (CH4N2O). To the standard's AUS composition, sodium azide (NaN3), 0.015 g/L, was added to avoid bacterial contamination during the experiments. The AUS flow rate was set to 0.250 ml/min in the peristaltic pump. This flow rate was selected based on the average urine production per day by humans(35). Since the flow rate is low, the flow will run drop by drop, so, the sample's surface will not be totally completely immersed in AUS all the time. After passing through the samples, the AUS was collected in individual flasks for posterior analysis. The samples were analysed after 24, 48, and 72h for corrosion and corrosion layer analysis.

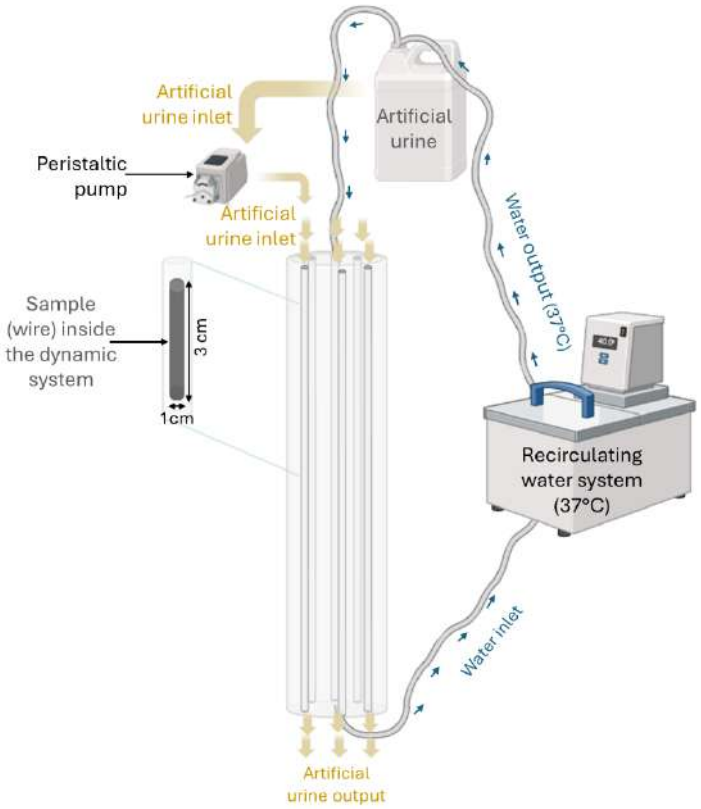


Figure IV 1 Schematic representation of the dynamic system used in this study.

IV-2.4. Corrosion layer analysis

IV-2.4.1. Scanning electron microscopy - energy dispersive spectroscopy (SEM-EDS)

After each time point, the samples' surface was analysed by scanning electron microscopy (SEM, JEOL JSM-6010LV) equipped with an energy dispersive X-ray spectroscopy (EDS, INCAx-Act, PentaFET Precision, Oxford Instruments). EDS was used to investigate the corrosion layers' composition, and SEM was carried out to observe both the corrosion layer and the corrosion process, i.e., after removing the corrosion layer. The protocol used for removing the corrosion layer is described in the following sections.

IV-2.4.2. Fourier transform infrared spectroscopy (FTIR)

For the FTIR analysis, the corrosion layer on the sample's surface was scraped and the whitish corrosion layer powder was analysed in a Shimadzu-IR Prestige 21 spectrometer. The spectral region analysed was 600 - 4000 cm-1 with a resolution of 4.0 for 32 number of scans. The analysis was done at least 3 times for the same sample.

IV-2.4.3. X-ray photoelectron spectroscopy (XPS)

Elemental analysis of the corrosion layers on the samples' surface, formed during the first 24h of contact with AUS, was done using X-ray photoelectron spectroscopy (XPS Kratos Axis-Supra instrument) equipped with a monochromatic X-ray Al Ka (1486.6 eV) source operated at 225 W. XPS spectra were collected at pass energy of 160 eV for survey spectra and 20 eV for individual elements. Binding energy of C1s photopeak at 285.0 eV (C1s hydrocarbon peak) was set for charge referencing.

IV-2.5. Corrosion rate – mass loss and ion release measurements

To analyse the corrosion rate, the samples collected at the different time points of the experiment were subjected to a cleaning process to remove the corrosion layer so that the corroded surface would be exposed and possible to study. For that, the samples were immersed in a solution containing 200g/L Chromium (VI) oxide (Laborspirit), 10 g/L silver nitrate (Laborspirit), and 20 g/L barium nitrate (Laborspirit), as described in ASTM G1-03, for approximately 5 min, until the corrosion layer disappeared(36). After that, the samples were immersed in deionized water for a few seconds (to remove any trace of the cleaning solution) and finally left to air dry.

The corrosion rate of each sample over time was calculated using the following equation, (suggested in the ASTM G1-03(36)):

$$\boldsymbol{Corrosion\ rate} = (\boldsymbol{K} \times \boldsymbol{W}) \div (\boldsymbol{A} \times \boldsymbol{T} \times \boldsymbol{D})$$

where K is a constant that is defined depending on the corrosion rate units defined, which in this case is millimeters per year (mm/y); thus $K = 8.76 \times 10^4$;

T is the time of exposure in hours

A is the area of the specimen in cm^2

W is the mass loss in grams

D is the density in g/cm^3, which in this case is $1.74\ g/cm^3$ for pure Mg. Minor deviation of the alloy density from this value was neglected.

The mass loss was calculated by the difference between the initial and final masses of the sample, at each time point, after removing the corrosion layer.

To follow the alloys' corrosion over time, AUS samples were collected every 24 hours and analysed through inductively coupled plasma optical emission spectrometry (ICP-OES, JY 2000 2, HORIBA JOBIN YVON) to assess the amount of cations released over time in AUS.

IV-2.6. Statistical analysis

The repeated measurements in this work were presented as mean ± standard deviation. Statistically significant differences between groups at each time point were estimated through a two-way analysis of variance (ANOVA). The normality of data was assessed through the Shapiro-Wilk test. A statistically significant difference was considered at $p<0.05$.

IV-3. Results

This work focused on understanding the suitability of a WE43 alloy, and in particular an additively manufactured such, for ureteral stent applications. Thin structures - thin-walled tubes and wires – were printed (**Figure IV 2**) using previously optimized parameters for WE43 and the first days of corrosion were investigated under simulated urinary tract environment. The corrosion layer and the corrosion pattern of the samples were assessed, and the results and respective interpretation are presented in the following sections.

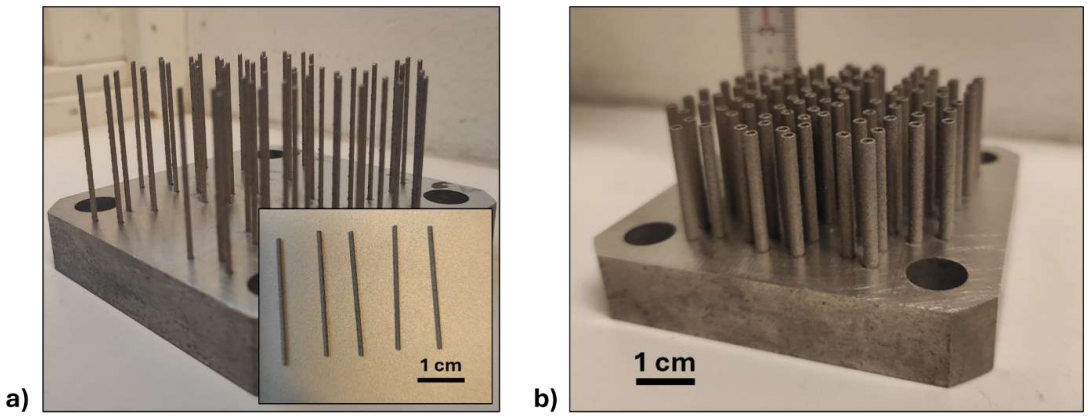


Figure IV 2 As printed WE43-based thin structures, a) wires and b) thin-walled tubes.

IV-3.1. Microstructural characterization

Figure IV 3 shows the cross-sections of the as-built WE43 samples having different printing parameters (**Table IV 2**), both parallel and perpendicular to the building direction. Individual melt pool boundaries are clearly observed in the micrographs. Looking at the plane parallel to the building direction of the tubes (**Figure IV 3 a)**, **b)** and **c)**) and wires (**Figure IV 3 d)** and **e)**), one can see that the shape of the melt pools on the tubes were more heterogeneous, given the different depths and overlapping of the melt pools in the same sample. In the wires, the melt pools seem to be homogeneous. Perpendicular to the building direction, the scan tracks were visible along both the tubes and the wires. For the wires, the tracks were distributed at various angles, consistent with the 67° scan rotation, while this distribution was not noticeable in the tubes, likely due to the thinner walls of the same. All the samples presented porosity having the characteristic round shape typical of keyhole pores or gas entrapment. The porosity appeared to be more frequent in the tubes, which, again, is most likely related to the thinner walled structure, compared to the diameter of the wires. Thinner structures dissipate heat faster, allowing for faster solidification and trapping gas bubbles before they escape the melt pool.

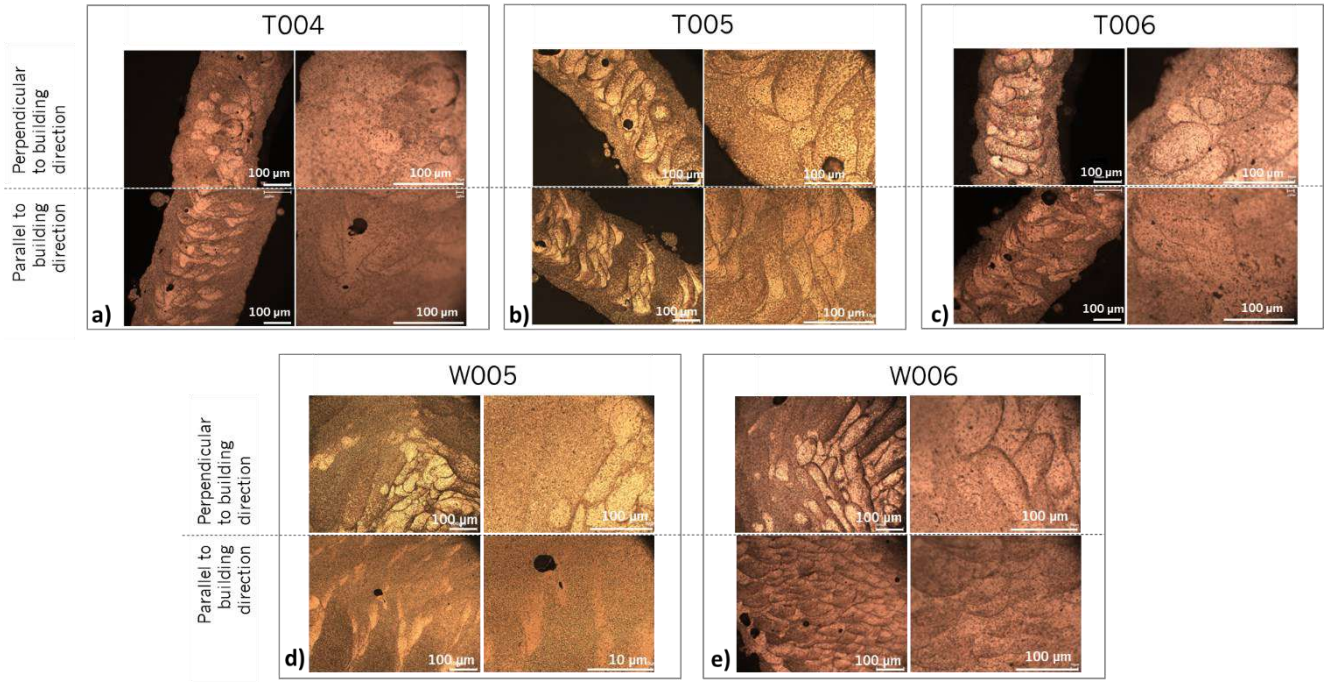


Figure IV 3 LOM images of the samples in the planes perpendicular and parallel to the building direction, after polishing and etching with Nital. a), b) and c) refer to the tubes, printed using hatch distances of 0.04, 0.05 and 0.06 mm, respectively, and d) and e) refer to the wires, printed using a hatch distance of 0.05 and 0.06 mm, respectively.

IV-3.2. Corrosion layer analysis

The corrosion layer morphology is usually related with its capacity to protect the underlying substrate from corrosion and is hence very important to study. **Figure IV 4** shows an overview of the corrosion layer formed on the samples' surface over time. There are differences between the corrosion layers' aspect of the different samples. For example, T004, after 24h, seems to be the tube with the lowest accumulation of corrosion layer, while after 48h, T004 has the thickest coverage. The corrosion layers' aspect was also non-homogeneous, for all the samples, as one can see by the higher accumulation of the whitish corrosion layer product in some places of the same sample's surface. In fact, in certain samples, this inhomogeneity seems to have a pattern, there were elongated marks along some of the sample's corrosion layers, in the AUS flow direction, which may be related to the fluid flow path (T005 and T006 at 72h, **Figure IV 4**). The AUS fluid rate is low (0.250 ml/min), so, since the AUS flows drop-by-drop, the surface of the sample will not be totally immersed in AUS – and the same happens with the ureteral stents when implanted in the body – hence, the fluid flow may have a preferred path along the surface and that can be one of the reasons for an inhomogeneous corrosion layer coverage. Additionally, defined pits are visible in some of the samples, such as in T004 and T006 at 48h and T004 at 72h

(arrows in **Figure IV 4**). Regarding the wires, W006 at 24h seems to have a thicker corrosion layer but after 48 and 72h no considerable increase can be seen, whereas for W005 there is a clear increase in layer content over time.

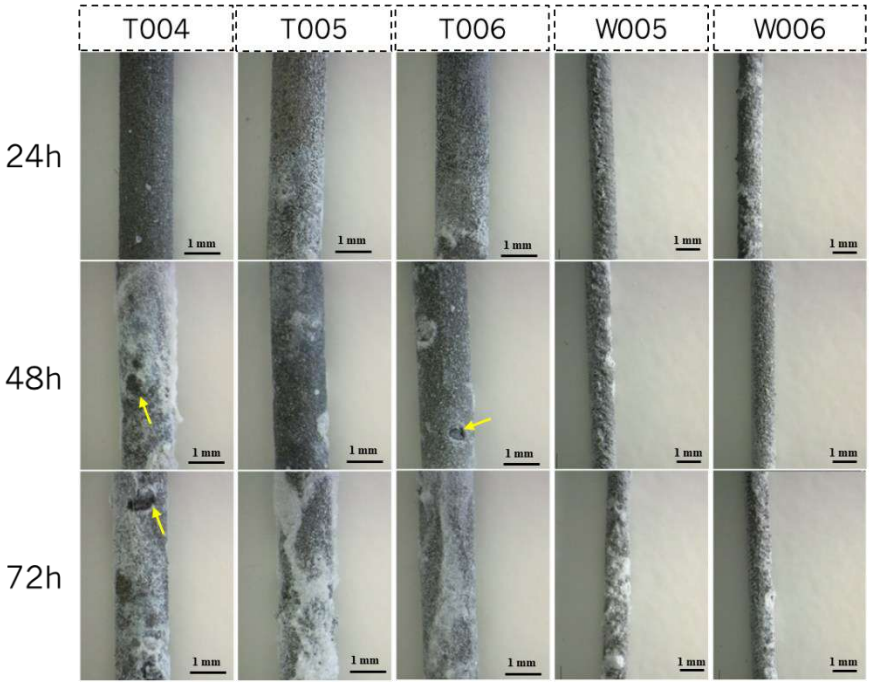


Figure IV 4 Optical images of the samples' corrosion layer development over time.

Figure IV 5 shows a more detailed representation of the corrosion layers. In general, the corrosion layers formed on the tubes were more irregular and characterized by the formation of crystal-shaped structures poorly attached to the surface, making them more rough and uneven. The corrosion layers formed on the wires, were more uniform along the surface and looked more homogeneous and compact despite the presence of cracks.

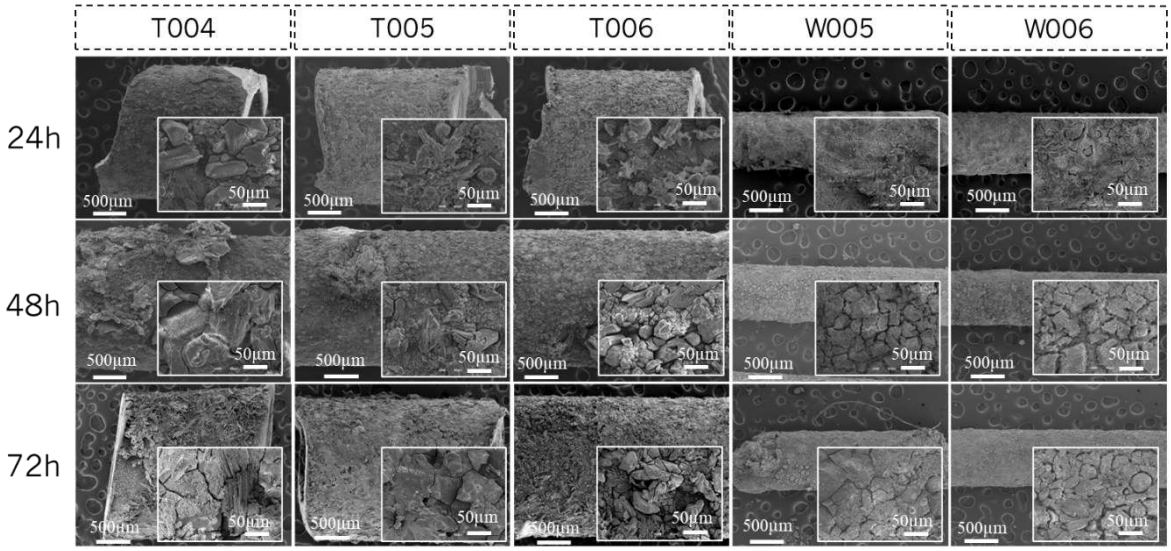


Figure IV 5 SEM images of the samples' corrosion layer development over time.

The chemical composition of the corrosion layer formed on the samples was analysed by EDS (**Table IV 3**). The major component in all the samples was O, followed by Mg, indicating the formation of MgO and $Mg(OH)_2$. P and C were also detected in all the samples except in W006. Interestingly, the alloying elements Y and Nd were found only in the corrosion layer of the wires.

Table IV 3 Chemical composition of the corrosion layer determined by EDS.

Sample:	O	Mg	P	C	Na	S	K	Cl	Y	N	Nd
T004	53.5±0.9	24.7±0.5	13.6±0.4	6.3±1.1	0.8±0.2	0.7±0.2	0.4±0.2	n.d	n.d	n.d	n.d
T005	58.0±0.8	31.6±0.6	0.2±0.2	8.7±1.1	0.6±0.2	0.1±0.1	0.1±0.2	0.7±0.2	n.d	n.d	n.d
T006	55.3±0.9	17.9±0.4	24.0±0.6	2.0±1.2	n.d	n.d	0.8±0.2	n.d	n.d	n.d	n.d
W005	45.1±0.8	12.3±0.3	9.9±0.3	9.3±0.7	0.4±0.1	n.d	0.7±0.1	n.d	8.6±0.5	5.2±0.5	7.8±0.9
W006	47.7±0.8	9.4±0.2	18.2±0.4	n.d	0.5±0.2	n.d	0.5±0.2	n.d	10.1±0.7	3.9±0.4	9.0±1.1

Figure IV 6 presents the FTIR spectra of all the samples' corrosion layers. The same main peaks were detected for all the samples and they correspond mostly to Mg-, O-, C- and P- containing molecules, which is in accordance with the EDS results(37-42). The most intense peaks are highlighted in the spectra (**Figure IV 6**) and the substances associated to it are probably magnesium hydroxide, magnesium carbonates and magnesium phosphates.

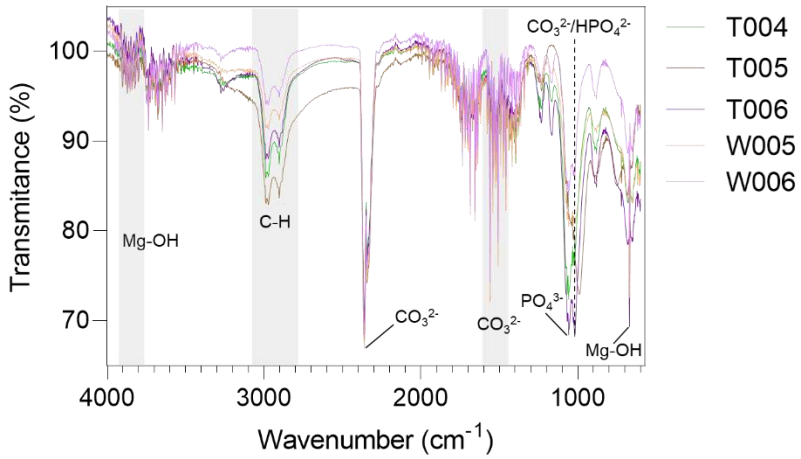


Figure IV 6 FTIR spectra of the corrosion layers of all the samples tested.

Figure IV 7 shows the survey scan obtained by XPS for all the sample's corrosion layers. As expected, and in agreement with the results obtained for FTIR, the composition of the corrosion layers were similar for all the samples (**Figure IV 7 f)**), indicating that the major elements were Mg, O, C and P. Hence, the compounds based on these elements prevail, such as magnesium oxide (MgO) and hydroxide ($Mg(OH)_2$) and magnesium phosphate crystals such as newberyite ($MgHPO_4 \cdot 3H_2O$) and struvite ($MgNH_4PO_4 \cdot 6H_2O$), which are commonly encountered on Mg alloys' corrosion layers after immersion in aqueous solutions(43,44). The amount of signal detected, however, varies, which means that the different geometries and printing parameters can lead to different tendencies in accumulating corrosion layer's elements. For example, T006 had a lower amount of corrosion layer products, while T004 and T005 showed increased amounts (**Figure IV 7**).

In **Figure IV 8** the high-resolution spectra of O1s, Y3d, P2p, Mg2s and Mg2p are presented for each sample, where some of the major components of the corrosion layers are distinguishable, such as $Mg(OH)_2$, MgO, $MgCO_3$, magnesium phosphates and even yttrium oxides for most of the samples(37,45-50). Also, there are indeed different tendencies of the samples to accumulate specific components. For example, for O1s spectra, with the exception of T006, all the samples accumulate higher $Mg(OH)_2$, whereas in T006 the $MgCO_3$ signal prevailed. For Y3d, the tubular samples accumulated more $Y_2O_3/Y(OH)_3$ than other components, while for the wires in W005 Y was not detected, in contrast to what EDS results showed, and in W006 the prevailing component was YCl_3. In P2p high-resolution spectra, $Mg_3(PO_4)_2$, prevailed only in some of the samples, which also happened for Mg2p on the wires. All these characteristics will influence the corrosion protection capacity of the corrosion layer.

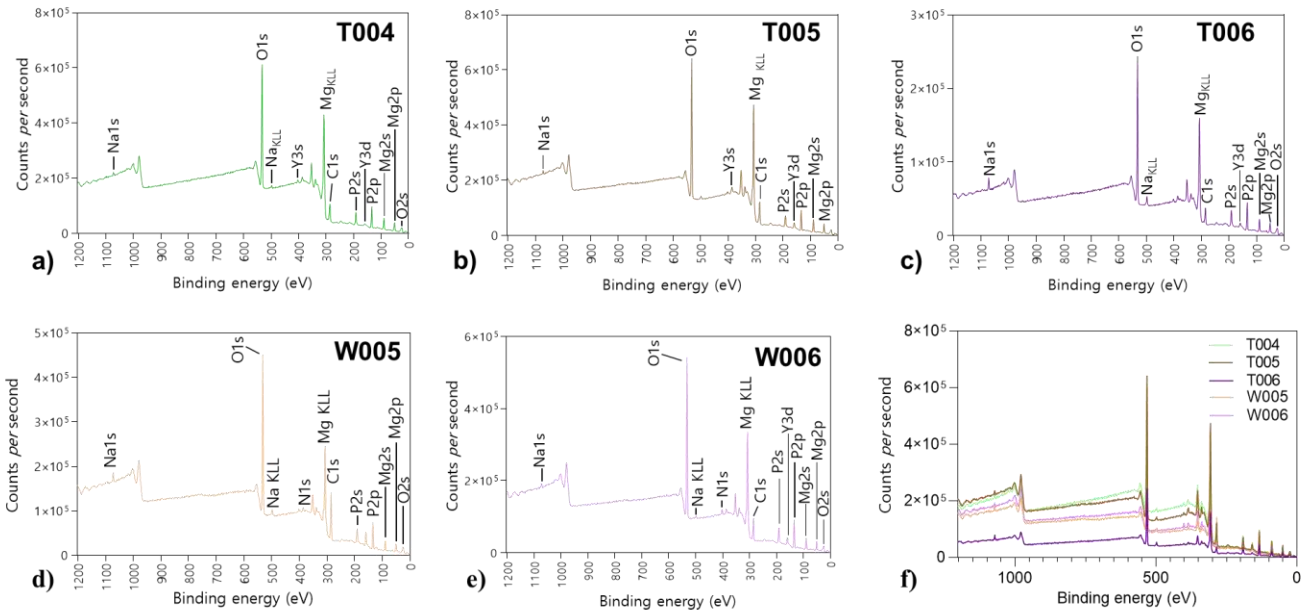


Figure IV 7 XPS spectra obtained for the corrosion layers formed on the samples a) T004, b) T005, c) T006, d) W005, e) W006 and f) all the corrosion layer's spectra represented, after 24h in AUS.

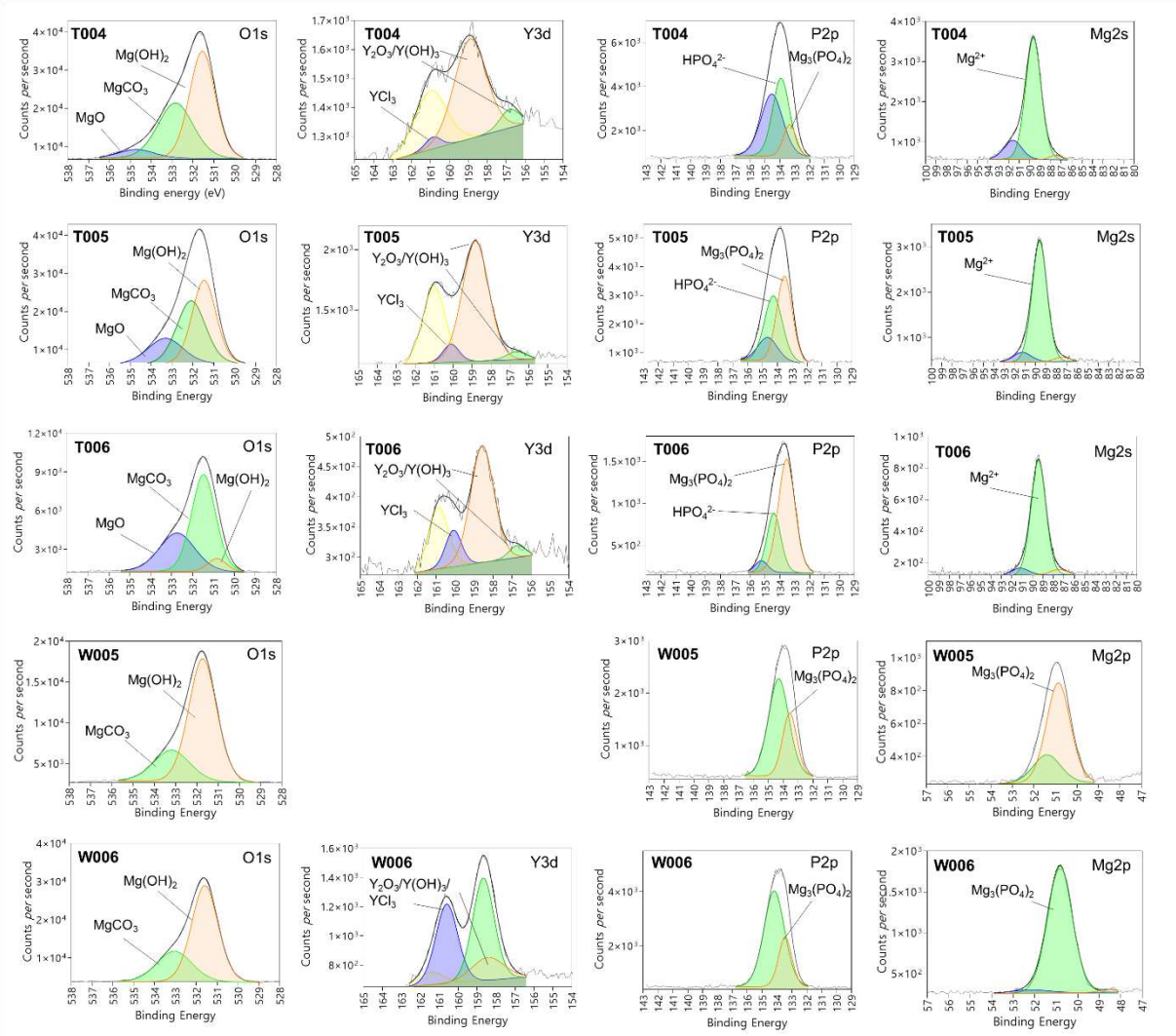


Figure IV 8 XPS high resolution spectra of O1s, Y3d, P2p, Mg2s and Mg2p for all the samples' corrosion layers after 24h in dynamic conditions with AUS.

IV-3.3. Corrosion analysis

To evaluate the corrosion of the different samples over the 72h, the corrosion layer was removed using a chromium oxide solution, as mentioned in the materials and methods section. The corroded surface was analysed by SEM, and the results are shown in **Figure IV 9**. T004 showed substantial signs of corrosion at 48h, characterized by surface pits and the same was true for T005. T006 showed corrosion-derived cavities only at 72h immersion. The surface of the latter is, however slightly different from T004 and T005, presenting small undulations that form a pattern along the surface for all the time points. The wires presented a different corrosion pattern compared with the tubes, i.e., the surface irregularity caused by corrosion looks different. The wires' surface seems smoother, and there are some larger pits that formed. Besides, in several regions, there is a different type of corrosion characterized by the accumulation of small pits.

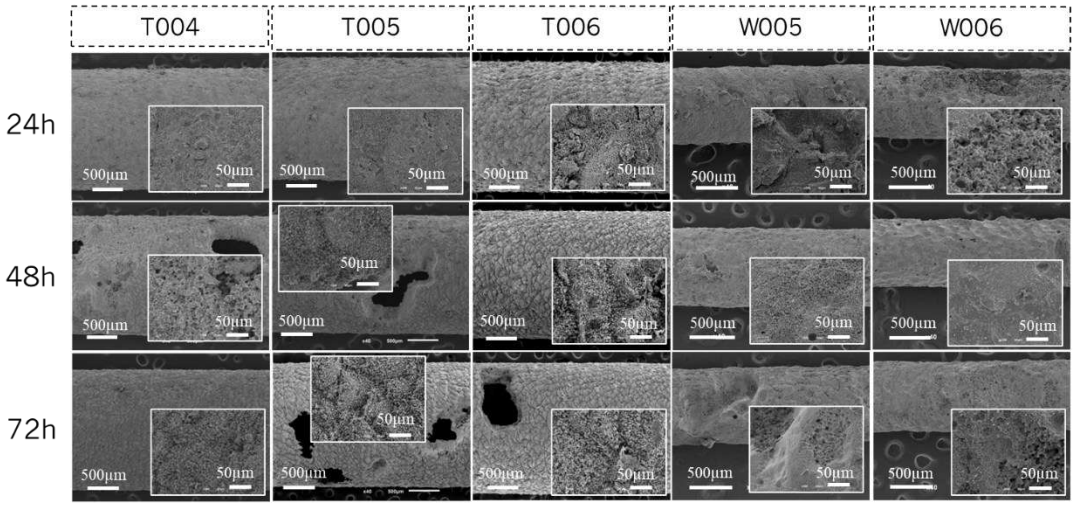


Figure IV 9 SEM images of the sample's surface evolution over time, after removing the corrosion layer with chromium oxide-based solution.

The corrosion rates of the samples along the three days were determined (**Figure IV 10**). The sample's corrosion behaviour varied considerably, independently of using the same parameters for differently shaped samples or the same shape with different printing parameters. The corrosion rate of T004 was the most stable along the 72h, the values were always round 3-4 mm/y. T005 corrosion rate decreased over time, starting with a high value of 10 mm/y, then decreasing to approximately 4 mm/y after 3 days. For T006, the average was always around 5 mm/y but with very large error values, i.e. a high variation over time. Regarding the wires, W005 started at a corrosion rate around 6 mm/y, then had a significant increase at 48h (**Figure IV 10**, in black), to 12 mm/y, which was the highest value achieved and significantly higher than those for the other samples at the same time point (**Figure IV 10** in grey). At 72h the corrosion rate for W005 decreased. W006 had a high corrosion rate at 24h, around 10 mm/y, but then decreased significantly to 4 mm/y, after 48h and then the value didn't change much at 72h.

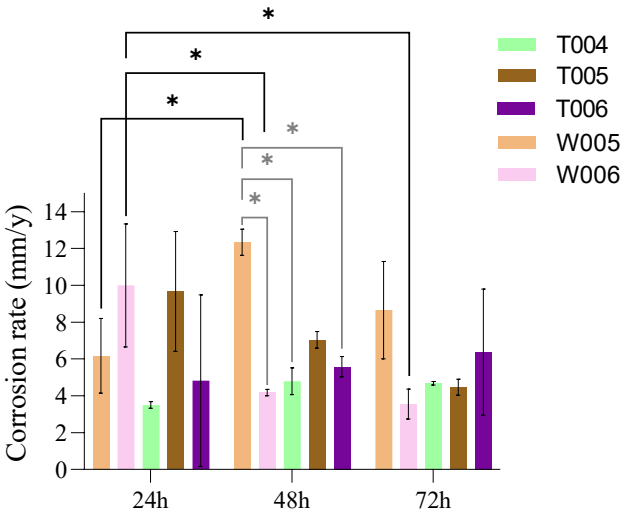


Figure IV 10 Corrosion rate (mm/y) of the WE43-based tubes and wires.

AUS samples were collected daily to monitor the sample's corrosion and complement the corrosion results with ICP-OES analysis. The results are shown in **Figure IV 11**. **Figure IV 11 a)** presents the variation in Mg concentration, the primary component of WE43, along the time for each sample in AUS. There are slight variations between the tubes and the wires. Interestingly, in the tubes, there is a decrease in the Mg content in AUS after 30 min, which indicates that there is a higher release of Mg ions in the first contact of the sample with AUS (T0) and after 30 min, the release slows down and increases again after 1h. From 1h on, the Mg release decreases and stabilizes from 5h, at around 10 mg/L. Between 24 and 48h, the Mg release of the tubes increases slightly, but then different behaviours are noted. T006 presents a slight decrease in Mg release, T005 a more pronounced decrease, and T004 a significant increase.

Regarding the wires, there was a decrease in the first half hour of the experiment, and then the Mg release continued to diminish slightly until 5h after immersion, and from that point on, the release was more stable for both wires. The graphs b), c), and d) in **Figure IV 11** represent the release of the alloying elements Y, Nd, and Zr. In this case, the concentrations were considerably lower compared with Mg, which was expected given the amount of these alloys in the samples. Regarding the release of Y, the tubes were very similar among them, while in the case of the wires, the release was very low for both, but for W005, there was a peak at 3h incubation. Then from 8h until 72h, W005 seemed to release higher quantities of Y compared with W006, but the results show high variation.

Regarding Nd, the release from the tubes appeared to be very variable, showing several peaks over time. The Nd release by the wires was around 0. Zr is the element of lowest amount in the samples and the released quantity was also considerably lower than that of the other elements. In summary, for the alloying elements, the amount of ions released was very low and close to the limits of detection of the equipment, also reflected in the high variations. Thus, the use of this analysis for these elements is limited. However, the Mg released over time was in sufficient amount to follow the sample's degradation along the time.

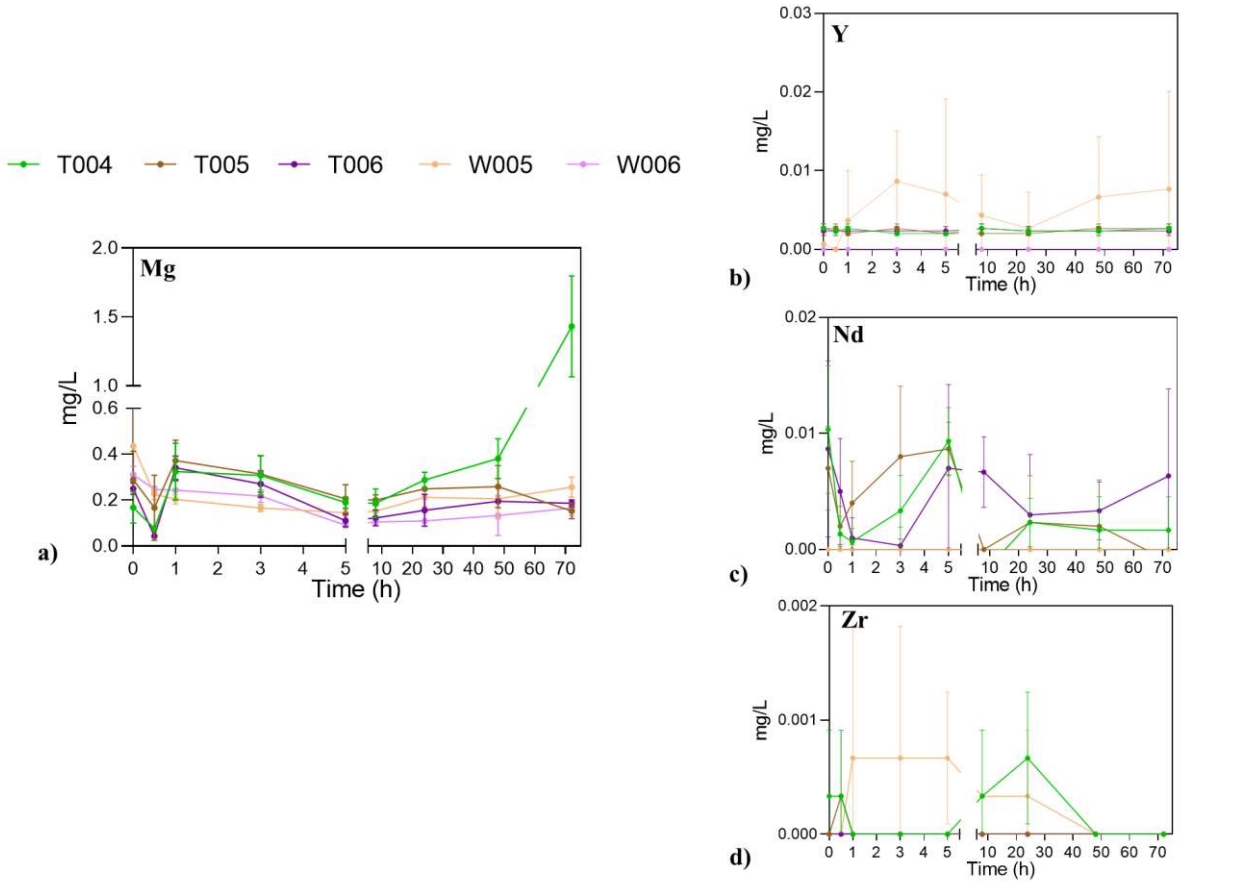


Figure IV 11 Concentration of the metallic ions, Mg in a), Y in b), Nd in c) and Zr in d) in AUS, released along the time by each sample.

IV-4. Discussion

In this work we successfully produced two types of thin structures, wires and thin-walled tubes that are simple representations of ureteral stent designs (**Figure IV 2**). We have characterized the first days of corrosion under simulated dynamic urinary tract conditions and the influence of printing

parameters and different shapes on the corrosion behaviour, which, to our knowledge, represents the first study of AM-WE43 based thin structures' corrosion behaviour in simulated urinary tract conditions. Through this study we were able to describe important characteristics of the corrosion pattern and its relationship with the printing parameters and structures' design, which are crucial inputs for the future development of biodegradable metallic ureteral stents.

Spherical microstructural pores were formed in both types of specimens, mostly typical keyhole pores, resulting from excessive vaporization in unstable meltpools(51). In the tubes, the pores appeared mainly when the melt pools were deep and narrow – for example in T004, parallel to the build direction, the side with more pores is also the one with deeper melt pools (**Figure IV 3**). Indeed, porosity is one very influencing factor on the sample's corrosion performance and it is also very difficult to avoid, especially when printing thin structures using Mg. This happens primarily due to two reasons, first because of the small difference between the melting and boiling point of Mg, which makes its processing through PBF-LB difficult due to the high susceptibility of evaporation(52-54). Second, thinner structures have higher susceptibility to porosity due to the warmer process, and rapid solidification leading to insufficient time for trapped gas bubbles to escape the melt pool(28,53,55). The tubes exhibited more pores likely because of this factor i.e., during the printing there is an increased local heat accumulation in the thinner structures, thus, a higher propensity for keyhole porosity formation. This is in agreement with other works, where a high laser power leads to evaporation and formation of a vapor cavity(28,51,56). In a recent paper from the co-authors of this work, WE43-based structures were produced though PBF-LB and the same type of keyhole associated pores were obtained(28). Besides, it was observed that using laser powers of 90 and 80 W to produce thinner samples, with the same printing parameters, lead to larger keyhole pores, in agreement to the results obtained in the present work.

The corrosion layer's aspect and chemical composition gives information about the corrosion, where for example a non-uniform corrosion layer coverage and/or its non-compactness is linked with an inhomogeneous corrosion(57). The presence of microscopic cracks was found in the corrosion layer of all samples, which indicates that the corrosion layers were not compact. This was detrimental to the corrosion resistance as these cracks typically act as interstitial sites for degradation attack making the substrate more susceptible to localized corrosion(58,60). Among the tubes, the chemical composition of the corrosion layer of T006 stood out due to the lower amount of overall corrosion products, as shown in the XPS spectra (**Figure IV 8**). As such, given the lower amount of corrosion products, this corrosion layer may have been less protective allowing for a higher tendency to rupture, ultimately leading to fluid

attack and enhanced localized corrosion. This may be the reason why the corrosion rate of this sample has higher error values, indicating inhomogeneity. T005 had a higher amount of corrosion products but a lot of corrosion pits were formed at 72h (**Figure IV 9**). In fact, this was the sample where Cl was detected through EDS, which was probably one of the reasons for the localized corrosion since Cl- ions are aggressive and accelerate the corrosion(44,60,61). In aqueous solutions a $Mg(OH)_2$ corrosion layer forms on top of the usual MgO layer present on the surface that forms upon exposition of Mg/Mg alloys to the air, prior to immersion. If the chloride ions are present in the solution, they will disturb the $Mg(OH)_2$ corrosion layer by reacting with it, according to the following equation(58):

$$Mg(OH)_{2(s)} + 2Cl^-_{(aq)} \rightarrow MgCl_{2(aq)} + 2OH^-$$

Therefore, since Cl^- ions were detected in the T005 corrosion layer, it is possible that the main reason for T005 localized corrosion could be related with the Cl^- ions penetration through the corrosion layer. Notwithstanding, the corrosion rate of T005 tends to decrease after the first 24h. This could be due to the corrosion layer becoming thicker and more protective over time, generally avoiding corrosion, even though it can present random points of sensitivity where the AUS (containing Cl^- ions) penetrates, which was in fact expected for T005 given the nonuniform appearance of the corrosion layer. T004 was the sample with the most stable corrosion rate and the smoothest surface (**Figure IV 9**), even though the SEM images demonstrate the occurrence of localized corrosion (at 48h).

Another explanation for the localized corrosion on the tubes can be attributed to the non-uniform distribution and accumulation of second phases along the microstructure (e.g., melt pool boundaries) of AM alloys. As second phases typically have a more positive corrosion potential than the (alpha Mg) matrix, galvanic corrosion is often promoted(28,58,62). Although in the present work we did not focus on the characterization of the second phases, inspection of the surfaces for T005 and T006 (**Figure IV 9**), demonstrate preferred regions of corrosive attack that may be consistent with accumulated second phases. These accumulated regions can be impacted by the AUS' corroding components and trigger the formation of corrosion pits. In contrast, for T004, less localized attack was observed. It is possible that the use of lower laser power reduced the extent of Mg vaporization during processing and thereby promoted less second phase formation. Moreover, the increase in remelting between neighbouring melt pools attributed to the lower hatch distance may have contributed to a more homogeneous phase distribution in this sample. Indeed, future work is warranted to confirmation these hypotheses.

The corrosion layer of the wires was smoother but with cracks. The corrosion rate peak for W005 was at 48h, i.e. most of the corrosion of the sample happened between 24 and 48h, again, probably due to the instability of the corrosion layer. W006 had a corrosion rate peak at 24h and then stabilized, indicating that the first hours were critical for the protective corrosion layer formation but then it probably stabilized being more effective in protecting the sample. Probably the corrosion layer is thicker and even with the cracks, that are critical for corrosion, it's enough to offer more protection compared with W005.

These results show that the corrosion layer morphology can be different even though the constructs have the same base material and the same shape but different processing parameters, which will influence the corrosion behaviour.

In summary, we established a preliminary set of parameters for tube printing, T004, although further optimizations are needed for e.g. porosity. Regarding the wires the best parameters were the ones used for W006. Both T004 (highest energy density) and W006 (lowest energy density, i.e. same as T006 but these parameters were more adequate for wire shape) need further optimizations but this work helped us understand that for the thin structures produced in this work, the hatch distance used is one of the most important factors and will severely influence the samples' corrosion behaviour.

The present study was done under dynamic conditions, which is a more realistic representation of ureteral stent's environment than static conditions and a major influencing parameter on the corrosion behaviour(44,61). However, there were some limitations, including the utilization of AUS, which must be used for standardization but, on the other side, doesn't mimic the natural conditions of high urine variability. Besides, the action of constant mechanical forces that the urinary stents are subjected to, the peristaltic movements, were also not considered. The biodegradable metallic ureteral stent we aim for should have a corrosion rate of around 4 weeks, thus the corrosion rate probably needs to be considerably improved. Besides, in natural conditions, the corrosion may be faster than in vitro, considering the peristaltic movements, the existence of proteins and other biomolecules present in urine that will influence the corrosion(19). The next steps will be to optimize the structure of T004 and W006 and delay the corrosion by an additional technique such as surface treatments, as well as getting closer to the real environment during in vitro evaluations, for example by using real urine.

IV-5. Conclusions

This work was a preliminary study to assess the possible use of WE43 to develop a biodegradable metallic ureteral stent, produced through PBF-LB. Two different thin structure types were built (thin-walled tubes and wires) and the first days of contact with AUS in in vitro dynamic conditions was reported. The main conclusions were that the same printing parameters for two different thin structures would give different corrosion layers, that in turn will confer different degrees of substrate protection and different corrosion behaviours. Hence, each specific structure needs individual optimizations. The thinner the structures the more unstable the melt pools and the more difficult it is to avoid structure porosity. The corrosion under dynamic conditions with AUS was fast and future corrosion improvements will be focused on strategies to delay the corrosion.

IV-6. Bibliography

1. Pérez-Fentes D, Aranda-Pérez J, E. de la Cruz J, Soria F. Indications, Complications and Side Effects of Ureteral Stents. In: Urinary Stents Current State and Future Perspectives. 2022. p. 8–16.

2. Sali GM, Joshi HB. Ureteric stents: Overview of current clinical applications and economic implications. Int J Urol. 2020 Jan 23;27(1):7–15.

3. Staubli SEL, Mordasini L, Engeler DS, Sauter R, Schmid H-P, Abt D. Economic Aspects of Morbidity Caused by Ureteral Stents. Urol Int. 2016;97(1):91–7.

4. Ghani KR, Rojanasarot S, Cutone B, Bhattacharyya SK, Krambeck AE. Economic burden of complicated ureteral stent removal in patients with kidney stone disease in the USA. J Comp Eff Res. 2022 Dec;11(17):1253–61.

5. Soria F, Rako D, de Graaf P, editors. Urinary Stents. Cham: Springer International Publishing; 2022.

6. Domingues B, Pacheco M, Cruz JE, Carmagnola I, Teixeira‐Santos R, Laurenti M, et al. Future Directions for Ureteral Stent Technology: From Bench to the Market. Adv Ther. 2022 Jan 17;5(1):2100158.

7. Barros AA, Oliveira C, Ribeiro AJ, Autorino R, Reis RL, Duarte ARC, et al. In vivo assessment of a novel biodegradable ureteral stent. World J Urol. 2018 Feb 11;36(2):277–83.

8. Pacheco M, Silva JM, Aroso IM, Lima E, Barros AA, Reis RL. Biomaterials for Ureteral Stents: Advances and Future Perspectives. In: Urinary Stents. Cham: Springer International Publishing; 2022. p. 197–208.

9. de la Cruz JE, Soto M, Martínez-Plá L, Galán-Llopis JA, Sánchez-Margallo FM, Soria F. Biodegradable ureteral stents: in vitro assessment of the degradation rates of braided synthetic polymers and copolymers. Am J Clin Exp Urol. 2022 Nov;10(1):1–12.

10. Soria F, de la Cruz JE, Budia A, Serrano A, Galan-Llopis JA, Sanchez-Margallo FM. Experimental Assessment of New Generation of Ureteral Stents: Biodegradable and Antireflux Properties. J Endourol. 2020 Mar 1;34(3):359–65.

11. Chagnon M, Guy L-G, Jackson N. Evaluation of Magnesium-based Medical Devices in Preclinical Studies: Challenges and Points to Consider. Toxicol Pathol. 2019 Apr 3;47(3):390–400.

12. Han H, Jun I, Seok H, Lee K, Lee K, Witte F, et al. Biodegradable Magnesium Alloys Promote Angio - Osteogenesis to Enhance Bone Repair. Adv Sci. 2020 Aug 23;7(15).

13. Mao L, Shen L, Chen J, Zhang X, Kwak M, Wu Y, et al. A promising biodegradable magnesium alloy suitable for clinical vascular stent application. Sci Rep. 2017 Apr 11;7(1):46343.

14. Xu W, Sato K, Koga Y, Sasaki M, Niidome T. Corrosion resistance of HF-treated Mg alloy stent following balloon expansion and its improvement through biodegradable polymer coating. J Coatings Technol Res. 2020 Jul 11;17(4):1023–32.

15. Lukyanova E, Anisimova N, Martynenko N, Kiselevsky M, Dobatkin S, Estrin Y. Features of in vitro and in vivo behaviour of magnesium alloy WE43. Mater Lett. 2018 Mar;215:308–11.

16. Barros AA, Oliveira C, Ribeiro AJ, Autorino R, Reis RL, Duarte ARC, et al. In vivo assessment of a novel biodegradable ureteral stent. World J Urol [Internet]. 2018 Feb 11;36(2):277–83.

17. Lock JY, Tu J, Liu HN. Degradation of Magnesium Alloys in Artificial Urine Solution for Urological Device Applications. Mater Sci Forum. 2014 May;783–786:413–8.

18. Zhang S, Bi Y, Li J, Wang Z, Yan J, Song J, et al. Biodegradation behavior of magnesium and ZK60 alloy in artificial urine and rat models. Bioact Mater. 2017;2(2):53–62.

19. Tie D, Liu H, Guan R, Holt-Torres P, Liu Y, Wang Y, et al. In vivo assessment of biodegradable magnesium alloy ureteral stents in a pig model. Acta Biomater. 2020 Oct;116:415–25.

20. Tie D, Hort N, Chen M, Guan R, Ulasevich S, Skorb E V., et al. In vivo urinary compatibility of Mg-Sr-Ag alloy in swine model. Bioact Mater. 2022 Jan;7:254–62.

21. Tian Y. The Clinical Study of 3D-printed Magnesium Alloy Prosthesis With Controllable Degradation Rate in the Repair of Periarticular Bone Defects.

22. Liu J, Liu B, Min S, Yin B, Peng B, Yu Z, et al. Biodegradable magnesium alloy WE43 porous scaffolds fabricated by laser powder bed fusion for orthopedic applications: Process optimization, in vitro and in vivo investigation. Bioact Mater. 2022 Oct;16:301–19.

23. Plaass C, von Falck C, Ettinger S, Sonnow L, Calderone F, Weizbauer A, et al. Bioabsorbable magnesium versus standard titanium compression screws for fixation of distal metatarsal osteotomies – 3 year results of a randomized clinical trial. J Orthop Sci. 2018 Mar;23(2):321–7.

24. Liu D, Yang D, Li X, Hu S. Mechanical properties, corrosion resistance and biocompatibilities of degradable Mg-RE alloys: A review. J Mater Res Technol. 2019 Jan;8(1):1538–49.

25. Sharma SK, Saxena KK, Malik V, Mohammed KA, Prakash C, Buddhi D, et al. Significance of Alloying Elements on the Mechanical Characteristics of Mg-Based Materials for Biomedical Applications. Crystals. 2022 Aug 12;12(8):1138.

26. Wang B, Gao W, Pan C, Liu D, Sun X. Effect of the Combination of Torsional and Tensile Stress on Corrosion Behaviors of Biodegradable WE43 Alloy in Simulated Body Fluid. J Funct Biomater. 2023 Jan 28;14(2):71.

27. Imani A, Clifford AM, Raman RKS, Asselin E. Insight into synergetic effects of serum albumin and glucose on the biodegradation behavior of WE43 alloy in simulated body fluid. Biomed Mater. 2023 Jan 1;18(1):015011.

28. Åhman HN, Larsson L, Wahman C, Mellin P, D'Elia F, Persson C. Higher laser power improves strength but reduces corrosion resistance of Mg WE43 processed by powder bed fusion. Mater Today Commun. 2024 Jun;39:108979.

29. Nilsson Åhman H, Thorsson L, Mellin P, Lindwall G, Persson C. An Enhanced Understanding of the Powder Bed Fusion–Laser Beam Processing of Mg-Y3.9wt%-Nd3wt%-Zr0.5wt% (WE43) Alloy through Thermodynamic Modeling and Experimental Characterization. Materials (Basel)]. 2022 Jan 6;15(2):417.

30. Soderlind J, Martin AA, Calta NP, DePond PJ, Wang J, Vrancken B, et al. Melt-Pool Dynamics and Microstructure of Mg Alloy WE43 under Laser Powder Bed Fusion Additive Manufacturing Conditions. Crystals. 2022 Oct 12;12(10):1437.

31. Zumdick NA, Jauer L, Kersting LC, Kutz TN, Schleifenbaum JH, Zander D. Additive manufactured WE43 magnesium: A comparative study of the microstructure and mechanical properties with those of powder extruded and as-cast WE43. Mater Charact. 2019 Jan;147:384–97.

32. Hyer H, Zhou L, Liu Q, Wu D, Song S, Bai Y, et al. High strength WE43 microlattice structures additively manufactured by laser powder bed fusion. Materialia. 2021;16(101067).

33. Hyer H, Zhou L, Liu Q, Wu D, Song S, Bai Y, et al. High strength WE43 microlattice structures additively manufactured by laser powder bed fusion. Materialia. 2021;16(101067).

34. Åhman HN, D'Elia F, Mellin P, Persson C. Microstructural Origins of the Corrosion Resistance of a Mg-Y-Nd-Zr Alloy Processed by Powder Bed Fusion - Laser Beam. Front Bioeng Biotechnol. 2022;10(917812).

35. Al-Kazwini H, Simhadri PK. Normal and Abnormal Urine Output and Interpretation. StatPearls. 2024;

36. ASTM G1-03. Standard Practice for Preparing, Cleaning, and Evaluating Corrosion Test Specimens. 2003.

37. Dong H, Lin F, Boccaccini AR, Virtanen S. Corrosion behavior of biodegradable metals in two different simulated physiological solutions: Comparison of Mg, Zn and Fe. Corros Sci. 2021 Apr;182:109278.

38. Rettig R, Virtanen S. Composition of corrosion layers on a magnesium rare ‐ earth alloy in simulated body fluids. J Biomed Mater Res Part A. 2009 Feb 19;88A(2):359 – 69.

39. Wang Y, Ding B-H, Gao S-Y, Chen X-B, Zeng R-C, Cui L-Y, et al. In vitro corrosion of pure Mg in phosphate buffer solution—Influences of isoelectric point and molecular structure of amino acids. Mater Sci Eng C. 2019 Dec;105:110042.

40. Wang X, Jing C, Chen Y, Wang X, Zhao G, Zhang X, et al. Active corrosion protection of super-hydrophobic corrosion inhibitor intercalated Mg–Al layered double hydroxide coating on AZ31 magnesium alloy. J Magnes Alloy. 2020 Mar;8(1):291–300.

41. Mukhametkaliyev TM, Surmeneva MA, Vladescu A, Cotrut CM, Braic M, Dinu M, et al. A biodegradable AZ91 magnesium alloy coated with a thin nanostructured hydroxyapatite for improving the corrosion resistance. Mater Sci Eng C. 2017 Jun;75:95–103.

42. Zeng R, Sun X, Song Y, Zhang F, Li S, Cui H, et al. Influence of solution temperature on corrosion resistance of Zn-Ca phosphate conversion coating on biomedical Mg-Li-Ca alloys. Trans Nonferrous Met Soc China. 2013 Nov;23(11):3293–9.

43. Mei D, Wang C, Nienaber M, Pacheco M, Barros A, Neves S, et al. Corrosion behavior of Mg wires for ureteral stent in artificial urine solution. Corros Sci. 2021 Aug;189:109567.

44. Pacheco M, Aroso IM, Silva JM, Lamaka S V., Bohlen J, Nienaber M, et al. Understanding the corrosion of Mg alloys in in vitro urinary tract conditions: A step forward towards a biodegradable metallic ureteral stent. J Magnes Alloy. 2023 Dec

45. Wang D, Pei S, Wang Y, Ma K, Dai C, Wang J, et al. Effect of magnesium-to-phosphate ratio on the corrosion resistance of magnesium alloy embedded in magnesium potassium phosphate cement. Cem Concr Compos. 2023 Jan;135:104826.

46. Xie J, Zhang J, Zhang Z, Yang Q, Guan K, He Y, et al. New insights on the different corrosion mechanisms of Mg alloys with solute-enriched stacking faults or long period stacking ordered phase. Corros Sci. 2022 Apr;198:110163.

47. Jayaraj J, Kumar SA, Srinivasan A, Raghu KG, Arunchandran C, Rajinikanth V. Corrosion and in vitro characteristics of cerium phosphate based chemical conversion coating on AZ31 magnesium alloy. Appl Surf Sci. 2024 Jan;644:158797.

48. Omar SA, Ballarre J, Schreiner WH, Ceré SM. Micro Raman and XPS surface analysis to understand the electrochemical behaviour of AZ31 and AZ91 magnesium alloys as temporary implant materials. Mater Today Commun. 2022 Jun;31:103557.

49. Jayaraj J, Rajesh KR, Amruth Raj S, Srinivasan A, Ananthakumar S, Dhaipule NGK, et al. Investigation on the corrosion behavior of lanthanum phosphate coatings on AZ31 Mg alloy obtained through chemical conversion technique. J Alloys Compd. 2019 May;784:1162–74.

50. Osipenko MA, Karczewski J, Dominów M, Prześniak-Welenc M, Makarava I V., Kurilo I, et al. Multisine impedimetric monitoring with an in-depth distribution of relaxation times analysis of WE43 and AZ31 magnesium alloys corrosion. Measurement. 2023 Nov;222:113683.

51. Hyer H, Zhou L, Benson G, McWilliams B, Cho K, Sohn Y. Additive manufacturing of dense WE43 Mg alloy by laser powder bed fusion. Addit Manuf. 2020;33.

52. Ng CC, Savalani MM, Man HC, Gibson I. Layer manufacturing of magnesium and its alloy structures for future applications. Virtual Phys Prototyp. 2010 Mar;5(1):13–9.

53. Bär F, Berger L, Jauer L, Kurtuldu G, Schäublin R, Schleifenbaum JH, et al. Laser additive manufacturing of biodegradable magnesium alloy WE43: A detailed microstructure analysis. Acta Biomater. 2019 Oct;98:36–49.

54. Liu J, Liu B, Min S, Yin B, Peng B, Yu Z, et al. Biodegradable magnesium alloy WE43 porous scaffolds fabricated by laser powder bed fusion for orthopedic applications: Process optimization, in vitro and in vivo investigation. Bioact Mater. 2022 Oct;16:301–19.

55. Martin AA, Calta NP, Khairallah SA, Wang J, Depond PJ, Fong AY, et al. Dynamics of pore formation during laser powder bed fusion additive manufacturing. Nat Commun. 2019 Apr 30;10(1):1987.

56. King WE, Barth HD, Castillo VM, Gallegos GF, Gibbs JW, Hahn DE, et al. Observation of keyhole-mode laser melting in laser powder-bed fusion additive manufacturing. J Mater Process Technol. 2024;214:2915–25.

57. Ling C, Li Q, Zhang Z, Yang Y, Zhou W, Chen W, et al. Influence of heat treatment on microstructure, mechanical and corrosion behavior of WE43 alloy fabricated by laser-beam powder bed fusion. Int J Extrem Manuf. 2024 Feb 1;6(1):015001.

58. Li M, Benn F, Derra T, Kröger N, Zinser M, Smeets R, et al. Microstructure, mechanical properties, corrosion resistance and cytocompatibility of WE43 Mg alloy scaffolds fabricated by laser powder bed fusion for biomedical applications. Mater Sci Eng C. 2021;119(111623).

59. Jagadeesh G V, Setti SG. Biodegradation Performance of Ball Burnished Magnesium Alloy in Stimulated Body Fluids for Bioresorbable Implant Applications. Mater Today Commun. 2024 Mar;108525.

60. Yavuzyegit B, Karali A, De Mori A, Smith N, Usov S, Shashkov P, et al. Evaluation of Corrosion Performance of AZ31 Mg Alloy in Physiological and Highly Corrosive Solutions. ACS Appl Bio Mater. 2024 Feb 27;

61. Han L, Li X, Bai J, Xue F, Zheng Y, Chu C. Effects of flow velocity and different corrosion media on the in vitro bio-corrosion behaviors of AZ31 magnesium alloy. Mater Chem Phys. 2018 Sep;217:300–7.

62. Yin B, Liu J, Peng B, Zhou M, Liu B, Ma X, et al. Influence of layer thickness on formation quality, microstructure, mechanical properties, and corrosion resistance of WE43 magnesium alloy fabricated by laser powder bed fusion. J Magnes Alloy. 2022 Oct;

CHAPTER V

IN VITRO CORROSION OF MG1Y-BASED THIN WALLS PRODUCED BY LASER POWDER BED FUSION – INFLUENCE OF CONTINUOUS AND MODULATED LASER MODES.

IN VITRO CORROSION OF MG1Y-BASED THIN WALLS PRODUCED BY LASER POWDER BED FUSION – INFLUENCE OF CONTINUOUS AND MODULATED LASER MODES.

ABSTRACT

This work presents an investigation of the 3D printing of Mg1Y thin walls through powder bed fusion laser beam (PBF-LB) technology, aiming at determining the potential of using Mg-1Y and PBF-LB for the future development of a biodegradable ureteral stent. The samples were fabricated using two laser modes, continuous wave (CW), the most commonly used, and modulated wave (MW), considered to be advantageous for thin structures and for alloys where the melting and evaporation temperature values are close (e.g., Mg). This paper investigated the corrosion behavior of the samples produced by these two laser modes when immersed in artificial urine solution (AUS). The results showed slight differences in the corrosion behavior between the two laser mode and some variations were observed in the surface morphology and structural characteristics. The surface of the MW samples were slightly rougher and presented thinner layer thickness compared with the CW ones. The CW samples' corrosion layer and respective corrosion seemed a bit more inhomogeneous compared with the MW ones. The findings of this work suggest that both laser modes could work for the 3D printing of thin structures from Mg1Y powder, but perhaps using MW mode could offer more accurate corrosion control, a critical aspect for biodegradable medical devices. This work provides interesting insights into the suitability of PBF-LB-based Mg1Y for the production of biodegradable urinary devices.

Keywords: Powder bed fusion laser beam, thin walls, continuous wave, modulated wave, biodegradable.

This chapter is based on the following publication: **Margarida Pacheco**, Carl-Johan Hassila, Francesco D'Elia, Estêvão Lima, Alexandre Barros, Cecilia Persson, Rui L. Reis. *In vitro* corrosion of Mg1Y-based thin walls produced by laser powder bed fusion – influence of continuous and modulated laser modes.

V-1. INTRODUCTION

Additive manufacturing (AM) is a cutting-edge technology where the parts are constructed based on a 3D computer-aided design (CAD) model via layer-by-layer building. PBF-LB is the most popular AM process, is very suitable for small volume and fine detail structures, and offers distinctive characteristics for processing metallic materials(1-4). The building process takes place in a closed chamber with a controlled environment. During the printing, a powder layer is spread in the building plate, and the laser beam (energy source) selectively melts the freshly deposited powder layer, fusing the powder particles together in specific areas based on the 2D layer cross-section of the 3D CAD model previously prepared. The building plate then lowers at a distance equal to the layer thickness established, and a new layer is deposited for a new laser action. This sequence repeats until the printing is finished(2). The constructs' microstructure, mechanical performance, and corrosion behavior can be controlled by adjusting the scanning path to ensure a stable melting pool. The melt pool's characteristics are influenced by several parameters, such as laser power, hatch distance, layer thickness, laser spot size, and scanning speed(5). These parameters influence the melt pool's cooling rate, shape, spacing, and overlapping(6). Understanding and optimizing these processes is fundamental to obtain the desired part's characteristics. One of the main advantages of PBF-LB is the possibility of producing highly precise thin structures that are often unattainable with traditional manufacturing techniques. For this reason, AM has revolutionized various industries, including biomedical engineering(3). Thin-walled biomedical implants, such as stents, are used daily in the hospital for many different pathologies, so the research for improving these devices is crucial. Ureteral stents are tubular-shaped medical devices inserted in the ureter when an obstruction is present or predicted. Traditionally, ureteral stents are made of non-degradable and biocompatible polymers (e.g., silicone and polyurethane) or non-degradable metals (e.g. titanium alloys)(7,8). Since these devices are for temporary use, they require a second surgery for removal, which implies additional economic burdens and patient suffering. Developing biodegradable ureteral stents is attractive since they will degrade gradually and dissolve after fulfilling their function, avoiding the stent removal surgery(9). The research on biodegradable ureteral stents has been gaining popularity and with great success over the past few years, especially using biodegradable polymers(10,14). Mg alloys as biodegradable materials are particularly interesting due to their excellent biocompatibility. They are a natural element in the human body and are vital in many biological functions(9). The combination of AM with degradable Mg alloys for stent development merges the benefits of both. The PBF-LB AM technique allows for controlling specific stent aspects, such as stent architecture, where several detailed meshes, wall thickness, and surface texture can be produced. This level of control allows the fine control of the mechanical properties,

degradation rate, size, and design of the stent, which is especially attractive since it is possible to produce stents with different degradation times – adapted for each treatment-, sizes - adapted to each patient's anatomy - and design(15,17). In the biomedical field, the use of AM for Mg-based biodegradable stents production is in its infancy, but preliminary studies have been promising(18-20). Some studies have been focused on understanding the thin structures printing process by investigating the residual stress generated during printing, which occurs due to the locally concentrated energy input that results from the rapid temperature oscillations; porosity; and the influence of wall thickness and height on the stability of the fabricated part(1,21,22). Understanding the printing process for each material and structural design is the basis for understanding its behavior. Adjusting the characteristics of the energy source is one of the approaches for structure optimization. The heat source used to achieve melting is most commonly operated in the continuous wave exposure mode (CW), where the laser continuously exposes the powder bed while scanning the hatches. However, the laser can also be used in the modulated wave mode (MW). In the MW mode, the laser fires in short sequences at a given length and frequency. The length of the sequences may vary in the micro- to millisecond range, while the frequency is usually in the kHz – MHz range. The two modes of exposure offer different benefits. In MW, due to the sequences to which the laser exposure of the powder bed is limited, the total build-up of heat is reduced due to the limited input and the excess time for heat to dissipate from the melt pool between laser pulses. Consequently, this affects the development of the melt pool, which, in turn, may influence the development of the microstructure(23). This is primarily due to a more rapid cooling than CW, which can be beneficial for certain alloys such as amorphous alloy systems that require a limited heat affected zone, or alloys with an evaporation temperature close to the melting point, e.g., magnesium-based alloys. The smaller melt pools that result from MW compared to CW also improve accuracy and may be beneficial for printing thin geometries such as single tract, struts, and lattice structures(24). Since our objective is to achieve Mg-based thin structures with fine control of microstructure and corrosion, accuracy is one important detail. So, in this study, we evaluated the suitability of MW and CW for the development of Mg1Y-based thin structures for urological applications. The selection of the alloy is another factor that influences corrosion behavior. Regardless of the advantages of Mg for biomedical applications, its spreading is hindered by the associated fast corrosion of Mg implants, that can result in premature implant failure, besides the problems associated with hydrogen gas bubbles released during Mg alloys' corrosion. The scientific community has been proposing efficient strategies to overcome these limitations, including alloying strategies and microstructural modifications that improve structural characteristics and degradation rates(25). This study explores the suitability of 3D printing of thin structures of Mg1Y by two laser modes,

MW and CW, and respective corrosion in artificial urine solution (AUS). In a previous work from our group, we verified that Mg1Y could be a good candidate for ureteral stent development due to its homogeneous corrosion under simulated urinary tract environment(26). Herein, even though we used a different fabrication strategy, Mg1Y was used, also due to its reported antibacterial potential, which is a fundamental characteristic for ureteral stents(27).

With this work, we aimed to evaluate the suitability of Mg1Y as a base material for the future production of a biodegradable metallic ureteral stent through the 3D printing of thin-walled sheets and understanding the influence of printing conditions on the corrosion behavior of the constructs in AUS.

V-2. MATERIALS AND METHODS

V-2.1. Thin walls production

V-2.1.1. Powder

Mg1Y powder was produced by gas atomization, acquired from Nanoval GmbH & CO with a d_{50} of 39.4 µm. X-ray diffraction (XRD, Bruker D8 Advance X-ray diffractometer with a Lynx-eye position-sensitive detector) was employed to characterize the phases in the powder. The data was obtained using Cu Kα radiation (produced at 40 kV and 41 mA) on a zero-background single-crystal Si sample holder. All data were collected in the 2θ range of 10–85° with a step size of 0.021° and 0.3 s *per* step.). The powder morphology and cross section were examined by scanning electron microscopy with energy dispersive x-ray (SEM/EDS) – specifications detailed below.

V-2.1.2. Thin walls printing and sample preparation

The thin-walled samples (5 x 10 mm) were built along the Y-axis, parallel to the moving direction of the recoating blade, using Aconity™ MIDI. This started by an optimization process where several single tracks *per* print were produced by combining different values of scanning speed, laser modulation width, laser power and laser modulation frequency, for MW mode, and combining values of scanning speed and laser power for CW mode. To produce the single tracks, the hatch distance was set to 1 mm, so the walls are produced by one single scan line. Each track had a length of 10 mm. The layer thickness was 20 µm, the spot size 80 µm and the gas flow was set to 1 m/s for all the prints. The figure below (**Figure V 1)** shows the layout used for the optimization phase. The method used was dividing the building plate in 9 groups and each group had a specific laser power and laser modulation frequency value. Each group was then divided in 9 subgroups and each subgroup had the same laser power and laser modulation frequency value but different scanning speed and laser modulation width (**Figure V 1**). Each subgroup

was composed of 10 single tracks with the same printing parameters. The first phase of selection was done by macro visualization of the track's characteristics, especially the surface roughness (i.e. the amount of nonmelted powder attached).

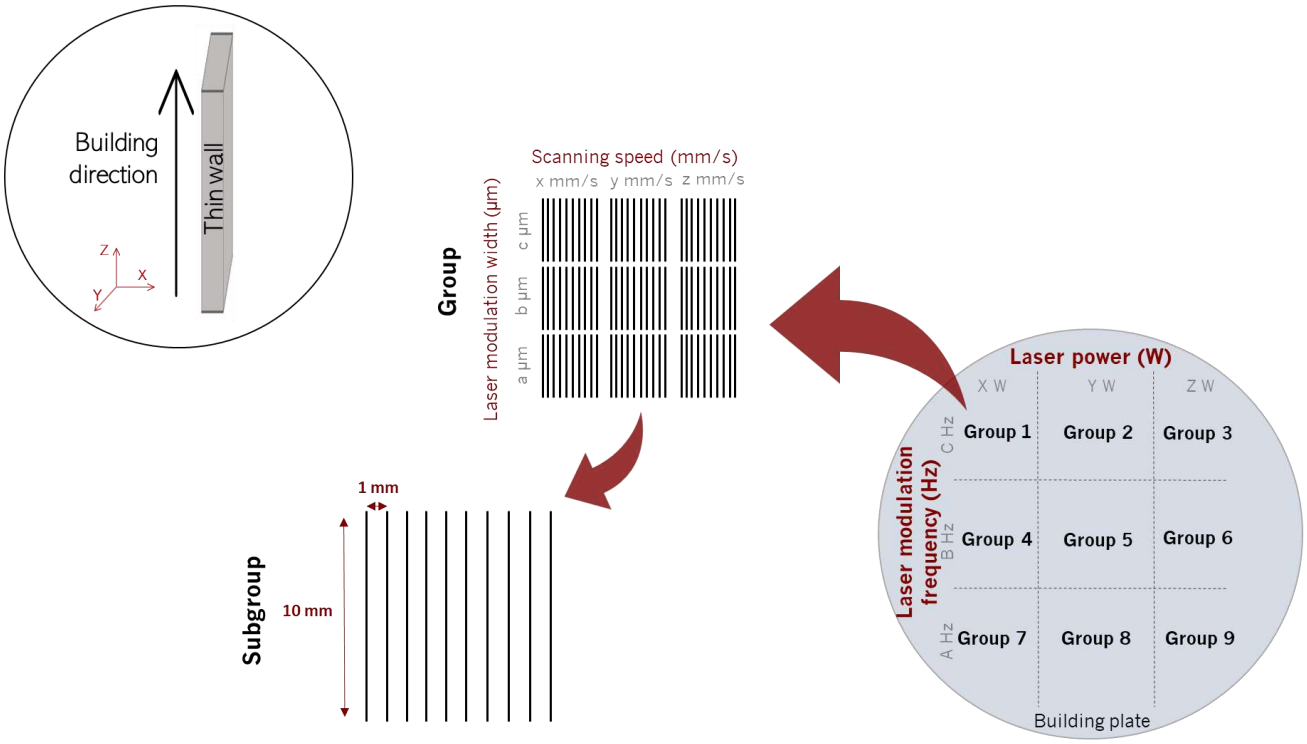


Figure V 1 Scheme of the building plate organization of the parameter's optimization phase.

V-2.1.3. Samples's characterization SEM/EDS

The powder morphology and cross section, and the as built thin walls' cross section (XZ plan, **Figure V 1**) were characterized by SEM/EDS (Zeiss Leo 1530, Carl Zeiss, Germany). To prepare for SEM analysis, the sample (powder or thin wall) was embedded in resin (KM-B RESIN, PRESI) in a polyethylene mounting mold and left do dry. After drying, the samples were removed from the mold and grinded with SiC foil 320 grit for 1 minute in water, followed by a polishing sequence starting with MD-largo foil with DiaPro Allegro/Largo 9 µm for 5 min, MD—Dac foil with DiaPro Dac 3 µm for 4 min, MD-Nap with DiaPro Nap B 1 µm for 3 min and finalized with OP-Chem with OP-U NonDry for 1.5 minutes.

After polishing, the samples were rinsed with pure ethanol. Before SEM analysis, the samples were sputtered with gold platinum for improved visualization.

V-2.1.4. Profilometry

The as-printed samples were washed by immersion in absolute ethanol under sonication (35 KHz) for 5 minutes and left to dry. The samples' surface was analysed by 3D Focus Variation Optical Profilometry (InfiniteFocus, BRUKER-Alicona). In each sample, six individual images were taken with 50 x lens, which provided a field of view of 400x400 μm^2. These images were used to calculate the roughness parameters. To obtain an overview of the sheet surface, the samples were also imaged with the 10 X objective lens that provides an image of 2x2 mm^2.

V-2.2. Samples' corrosion

Before starting the corrosion tests, the samples were washed with ethanol, as explained before (section 2.1.5). For the corrosion tests, the samples were immersed in AUS (**Table V 1**) at a ratio of 27.5 mm^2/ml for 24, 48 and 72h and 7 days. The samples were maintained at 37°C and collected at each time point defined. The AUS composition was based on the ones suggested on ASTM F 1828 – 97 and sodium azide was added to avoid bacterial contamination.

Table V 1 Chemical composition of the artificial urine solution (AUS) used.

Component	Amount (g) *per* L
Ammonium chloride (NH_4Cl)	3.000
Creatinine ($C_4H_7N_3O$)	2.000
Disodium hydrogen orthophosphate, anhydrous (Na_2HPO_4)	2.500
Potassium dihydrogen orthophosphate (KH_2PO_4)	2.500
Sodium azide (NaN_3)	0.015
Sodium chloride (NaCl)	9.000
Sodium sulfite (Na_2SO_3)	2.620
Urea (CH_4N_2O)	25.000

V-2.2.1. Fourier Transform Infrared Spectroscopy (FTIR)

The corrosion layer deposited on the samples' surfaces after immersion in AUS solution was characterized by FTIR. For the analysis, the corrosion layer was removed from the samples' surface by scrapping, and the "powder" obtained was analyzed by FTIR (Shimadzu-IR Prestige 21 spectrometer).

The analyzed spectral region was 600-4000 cm^{-1} with a resolution of 4.0 for 32 number of scans. Each sample was analyzed at least three times to assess possible inhomogeneities.

V-2.2.2. Raman

The corrosion layer was also analyzed by confocal Raman microscopy (LabRam Soleil from Horiba Scientific) equipped with a green laser (λ_{ex} = 532 nm) with a maximum output of 75 mW. The laser beam used was 15 mW using a 50x objective, 2 s acquisition time using 10 acquisitions, in the range of 200-4000 cm^{-1}.

V-2.2.3. Corrosion

The sample's corrosion layer percentage was calculated by weighting the sample before and after corrosion layer removal. The corrosion layer was removed by immersion in a cleaning solution composed of 200 g/L chromium (VI) oxide (Laborspirit), 10 g/L silver nitrate (Laborspirit), and 20 g/L barium nitrate (Laborspirit). Then, the corrosion rate was calculated using the formula suggested in the ASTM G1-03 using the following equation:

$$Corrosion\ rate = \frac{K \times W}{A \times T \times D}$$

where K is a constant that is defined depending on the corrosion rate units defined. In this case we defined it for millimeters per year (mm/y); thus $K = 8.76 \times 10^4$;

- T is the time of exposure in hours
- A is the area of the specimen in cm^2
- W is the mass loss in grams
- D is the density in g/cm^3, which is 1.74 g/cm^3 for pure Mg. Minor deviation of alloys density from this value was neglected.

V-3. Results

V-3.1. Mg1Y powder characterization

The Mg1Y powder used to print the thin structures was characterized by X-ray photoelectron spectroscopy (XPS) and SEM/EDS (**Figure V 2**). According to the XPS spectra peaks, only one phase of

Mg was present, with no signs of the alloying element. However, the EDS analysis of the powder surface showed that the particles are mainly composed of Mg, but Y and oxides were also identified (**Figure V 2 b)**). SEM of the powder was done to evaluate both the particles' surface and cross-section. The powder showed agood spherical morphology, and some particles had satellites (**Figure V 2 c)**). Analyzing the surface of the powder particles, it presented marks of randomly distributed lines all over the surface that might have been formed during the gas atomization process. Amorphous small particles are also present. Regarding the cross-section, it was possible to observe some round particles and a defined network of connected precipitates, probably β phase(3).

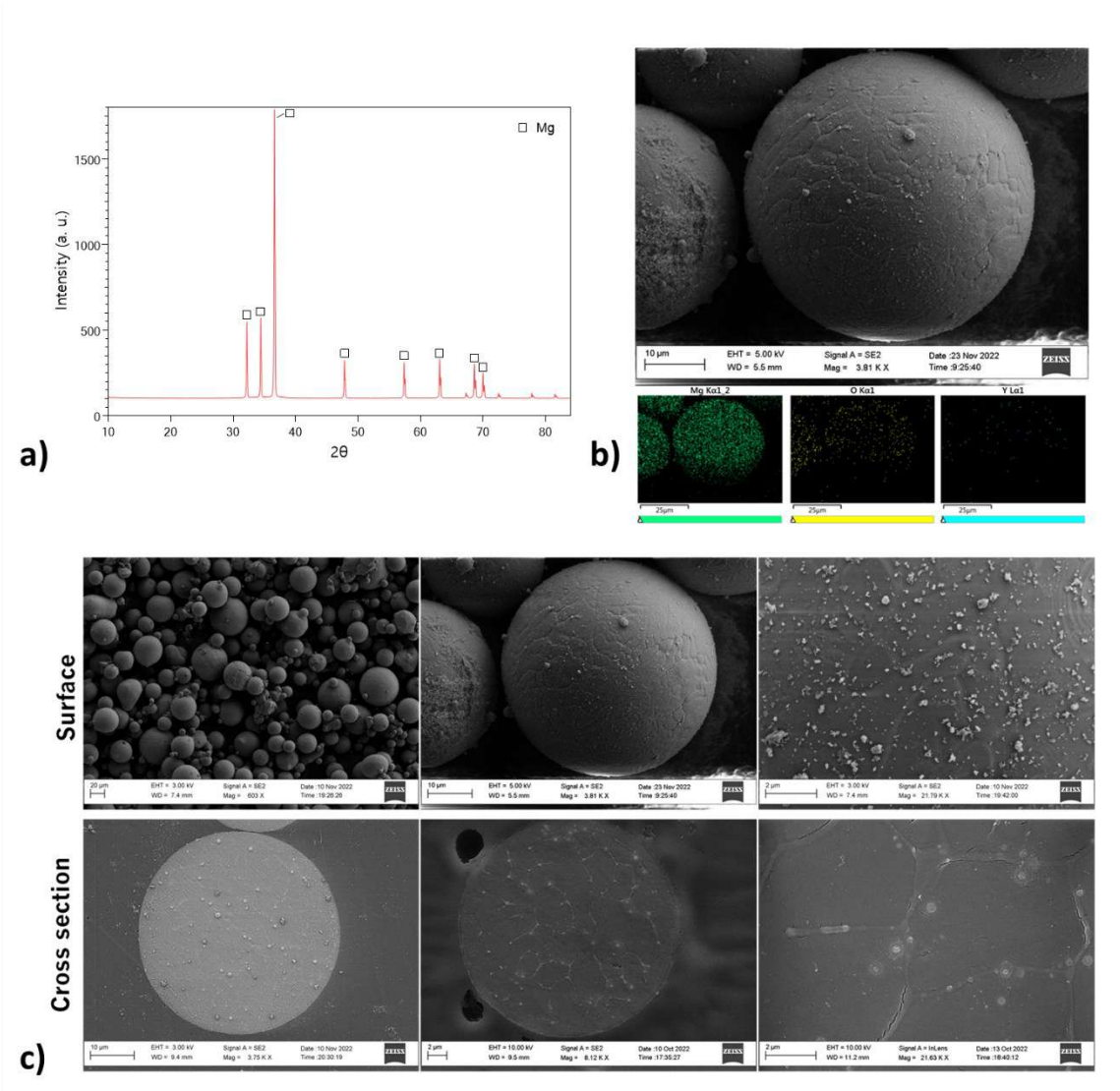


Figure V 2 XPS and SEM/EDS analysis of the Mg1Y powder used for printing.

V-3.2. Thin walls characterization

After an optimization process with continuous and modulated laser, following the strategy described in section 2.1.2. from the Materials and Methods section, the best parameters for each laser mode were:

- Modulated laser: 50 mm/s speed, 50 W laser power, 0.01 MHz laser modulation frequency, 75 µs laser modulation width.
- Continuous laser: 50 mm/s speed and 100 W laser power.

These parameters were employed to fabricate the CW and MW samples used for the subsequent experiments.

The as-printed samples were detached from the building plate, the unattached powder was removed, and the samples dimensions were accessed and presented on **Figure V 3**. The width was 10.05±0.01 mm for CW and 10.11±0.03 mm for MW, the height was 5.33±0.21 mm for CW and 6.08±0.04 mm for MW, and the thickness was 0.29±0.01 mm and 0.35±0.01 mm for CW and MW respectively. The width was very close to the dimensions defined for both samples, while the height was quite different for MW, which was a bit more than the established value (5 mm). Regarding the walls' thickness, higher values were obtained for MW, but both were considerably larger than the spot size defined (0.08 mm). This difference is probably related to the intensity of the laser power that leads to a high melting volume and, thus, larger melting pools and to the partially melted powder particles that attached to the surface.

SEM images of the samples show no porosity on the walls' structure (**Figures V 3 and 4**). We can also see the scanning tracks of adjacent layers formed during the printing process in some of the SEM images as well as un-melted powder particles attached to the surface (**Figure V 3**). The two laser modes produced samples with similar structures, but the layers' thickness seemed to be affected by using CW or MW. For CW, the layer thickness varied between 9.73-14.74 µm and for MW from 7.83 and 9.51 µm (**Figure V 4**). These results suggested that the differences in heat accumulation and dissipation from the two laser modes can indeed influence the layer stacking of the samples, which may influence the structure integrity of the thin walls.

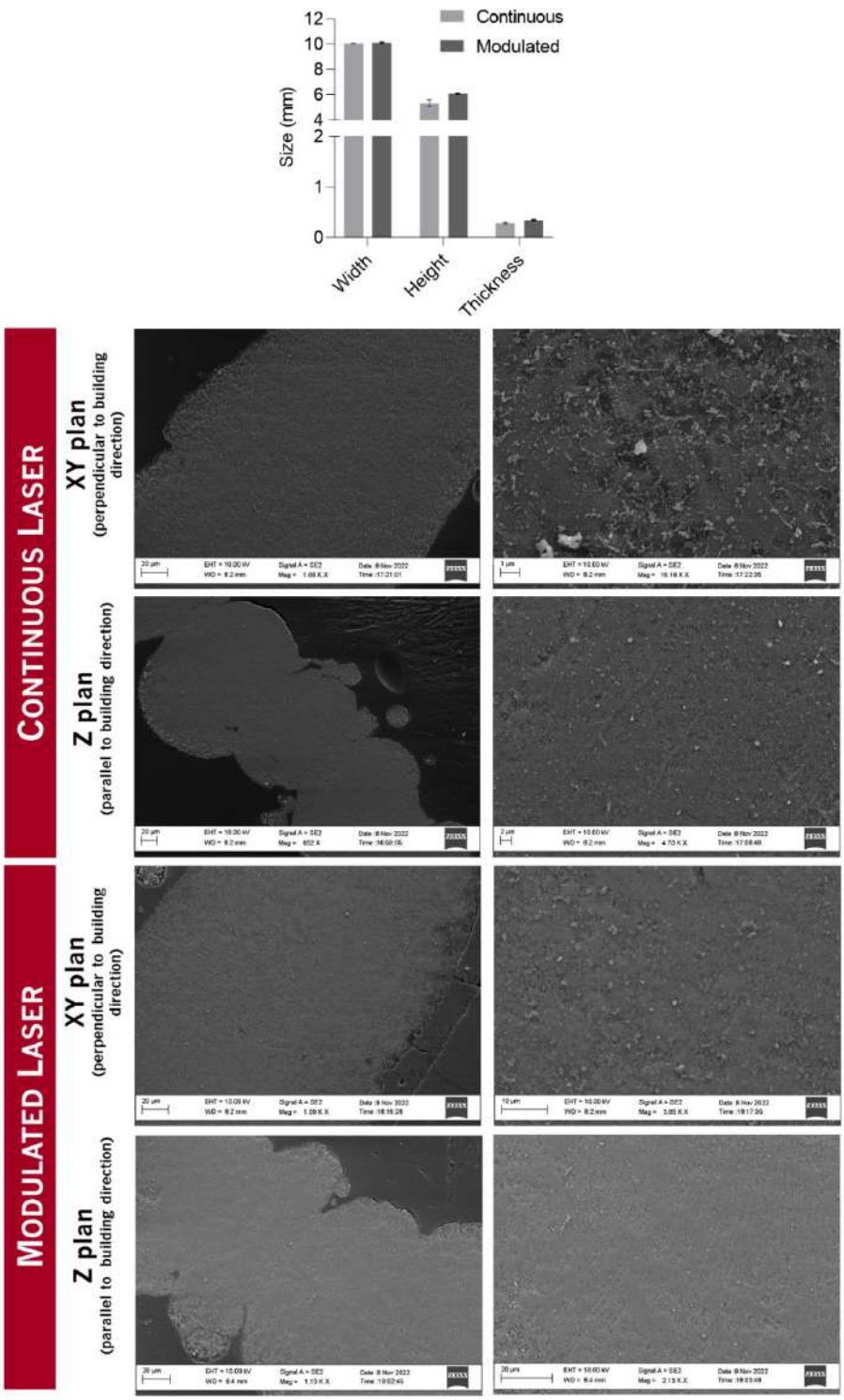


Figure V 3 SEM of the thin walls, parallel and perpendicular to the building direction, built with continuous and modulated laser modes.

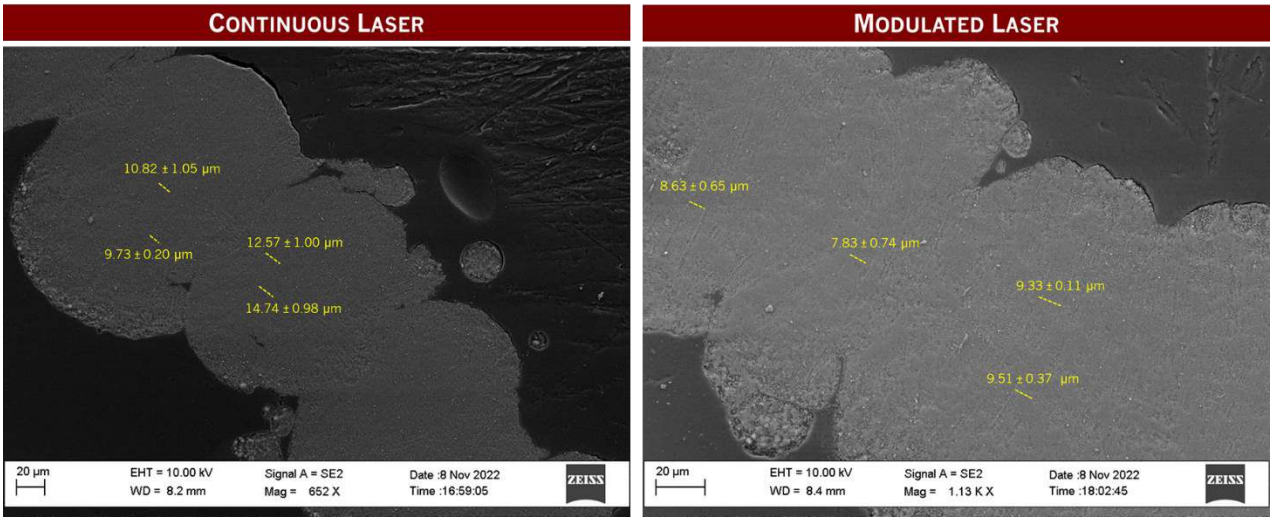


Figure V 4 SEM of the thin walls, parallel to the building direction (XZ plan), built with continuous and modulated laser modes. The width (µm) of four representative layers in each image is presented.

CW and MW samples were analyzed by profilometry to find possible differences in surface roughness between the two laser modes (**Figure V 5**). All the samples seem to have a deeper part on the edges of the melting pools, and some grains are more salient from the surface due to the balling phenomenon. The roughness measurements are shown in **Table V 2** and **Figure V 6**, for a better comparison of the results. The roughness values are very similar for CW and MW-based samples. However, MW-based walls seem to have slightly higher values (**Figure V 6**).

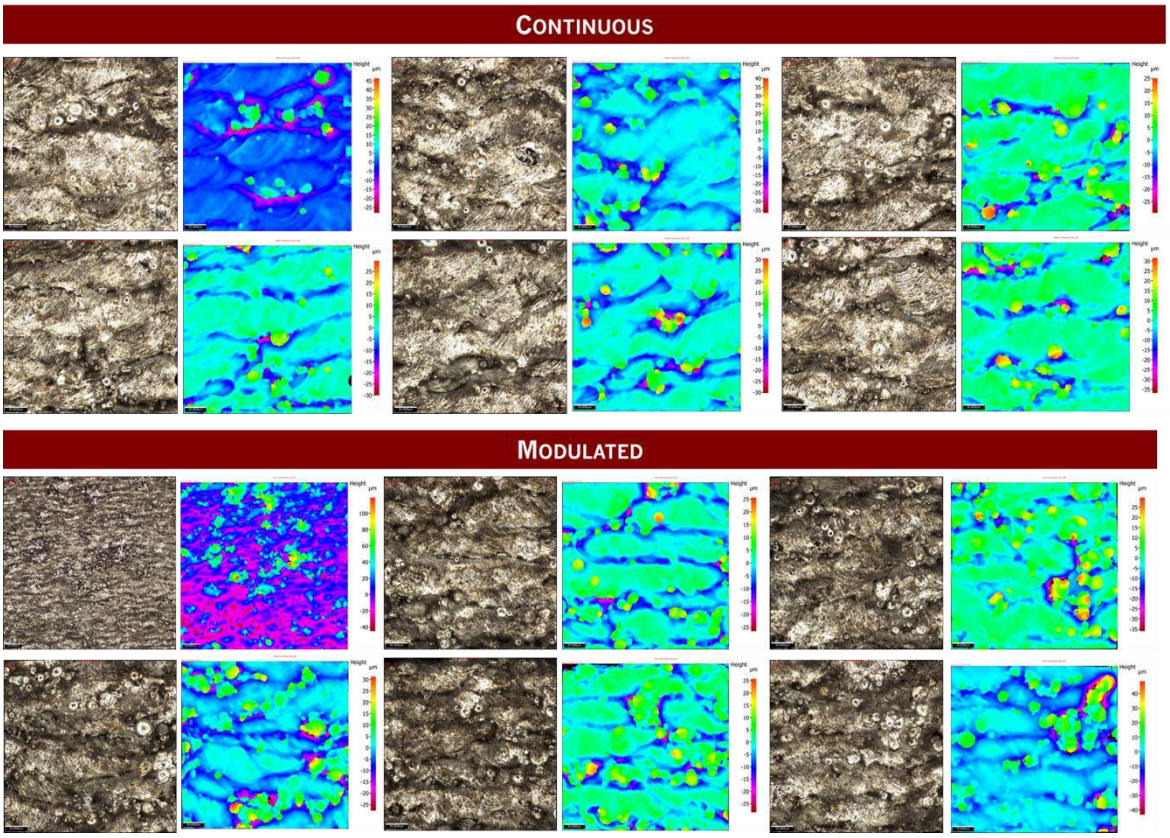


Figure V 5 Profilometry of the surface of the thin walls built with continuous and modulated laser modes.

Table V 2 Profilometry values for the surface of the thin walls built with continuous and modulated laser modes.

	Continuous		Modulated	
Parameter	Average	Std. Dev.	Average	Std. Dev.
Sa (µm)	3.670	0.354	4.662	0.735
Sq (µm)	5.554	0.570	6.733	1.260
Sp (µm)	33.896	7.161	32.783	7.875
Sv (µm)	31.916	3.468	32.490	5.824
Sz (µm)	65.812	8.019	65.273	13.246
S10z (µm)	59.748	4.039	60.593	12.891
Ssk	0.338	0.337	0.402	0.283
Sku	7.117	0.753	5.230	0.686
Sdq	3.364	0.425	4.002	0.960
Sdr (%)	322.952	69.203	486.460	216.397
FLTt (µm)	65.812	8.019	65.273	13.246
Lc (µm)	78.265	0.000	78.265	0.000

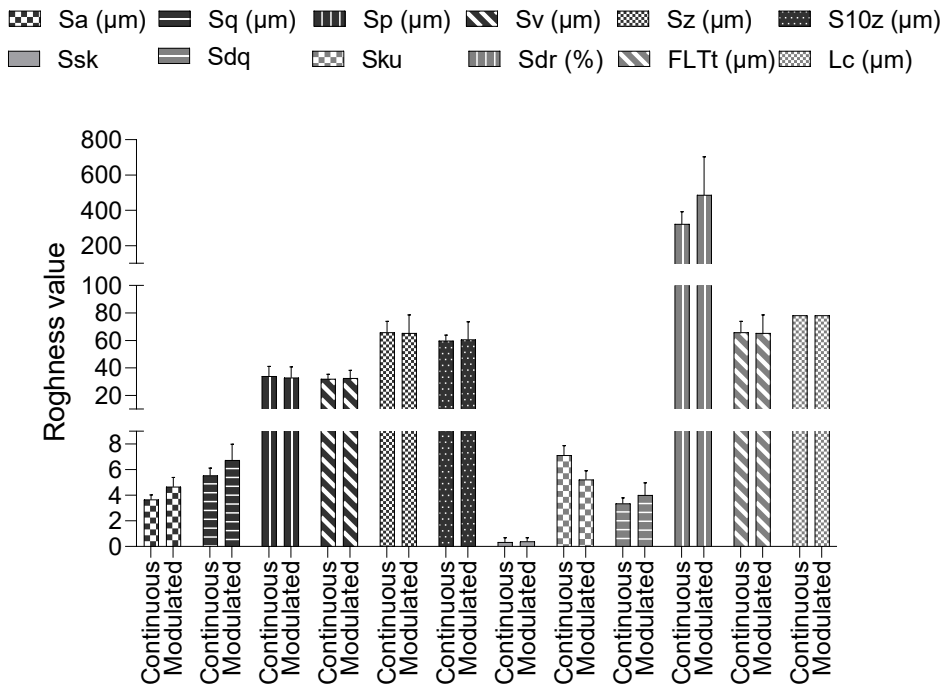


Figure V 6 Profilometry values for the surface of the thin walls built with continuous and modulated laser modes.

V-3.3. Characterization of the sample's corrosion in artificial urine solution

CW and MW-based thin walls were immersed in AUS at 37 ºC for 24, 48, 72h, and 7 days under agitation to evaluate the corrosion behavior of the samples produced by the two different laser modes. At each time point, the respective samples were collected, and the corrosion layer and corrosion were characterized. **Figure V 7** presents the photos of representative samples for each time point. From the macro visualization of the samples, CW-based samples seem to corrode faster than the MW-based ones, especially by observing the samples corresponding to day 7 of incubation. Also, it looks like most of the MW samples start to corrode from the edges, even though not homogeneously, while the CW tends to corrode from random places on the center – localized corrosion.

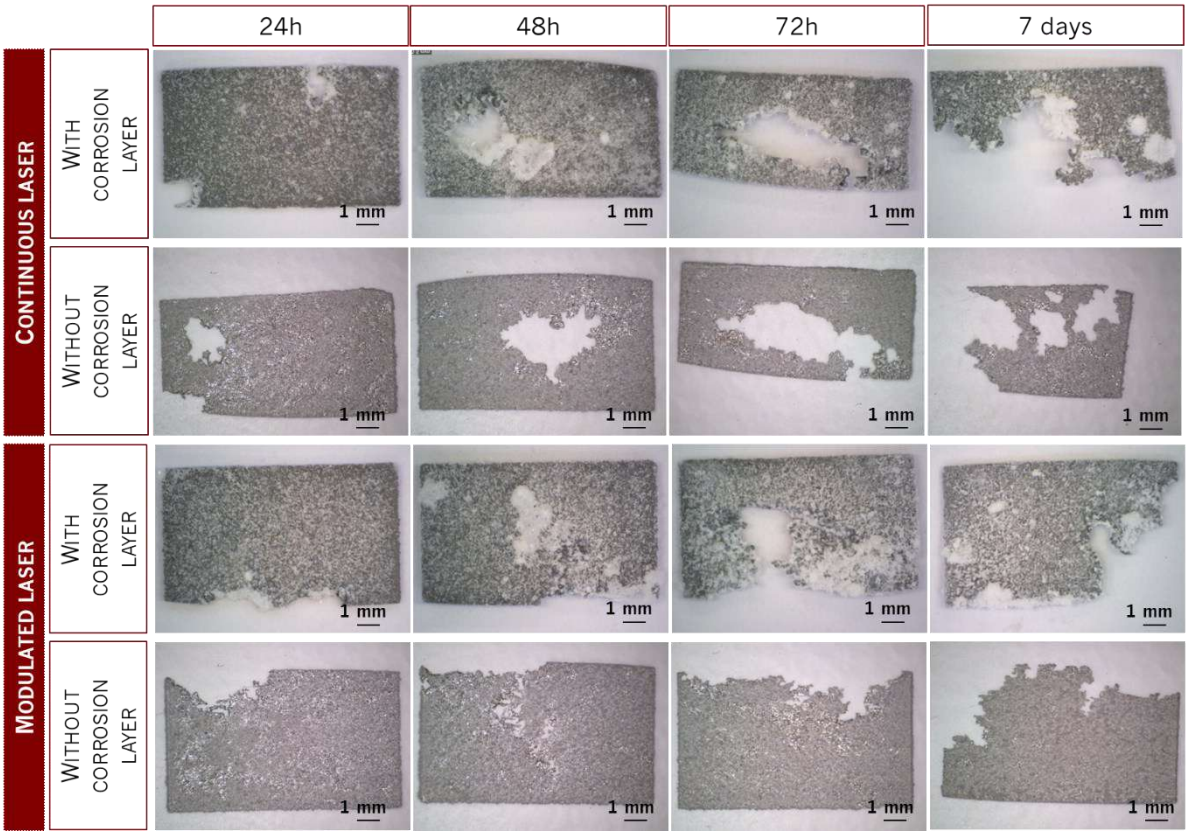


Figure V 7 Photos of the thin walls produced by continuous and modulated laser after 1, 2, 3 and 7 days immersion in artificial urine solution.

The molecular structure and composition of the samples' corrosion layers was characterized by FTIR and Raman. **Figure V 8** presents the FTIR spectra obtained for the corrosion layers of CW (red) and MW (black) laser modes after seven days of incubation. Three measurements were done on the same sample to evaluate the corrosion layer homogeneity. The peaks obtained were the same for all measurements, and they reveal mostly the presence of nitrogen-, carbon- and phosphorous-containing molecules, according to previous studies (**Figure V 8**). Peaks corresponding to struvite (magnesium ammonium phosphate) are the ones around 2362, which correspond to N-H and C-H stretching, around 1469, NH^{3+} symmetrical bending, and around 970, P-O-C (**Figure V 8**)(4,28,29)

These peaks are probably related to precipitated AUS components. Some peaks are associated with -OH (probably from $Mg(OH)_2$) and MgO, common elements resulting from Mg corrosion.

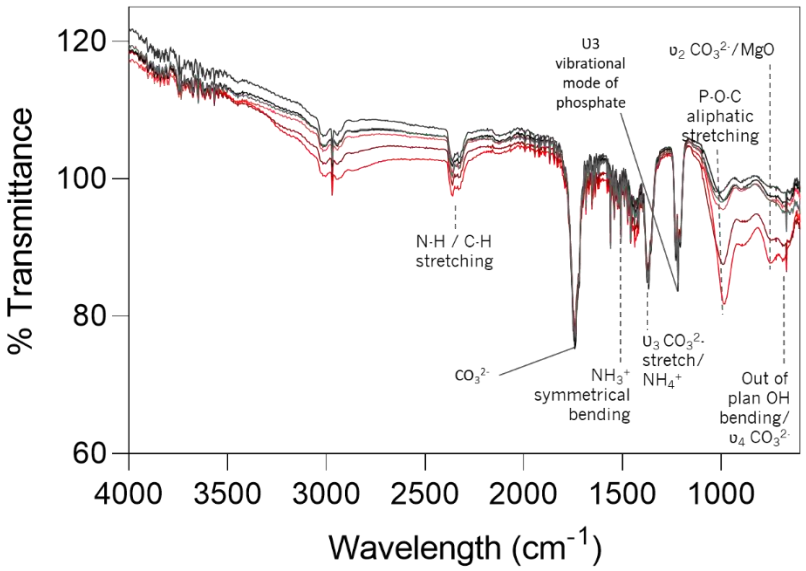


Figure V 8 FTIR spectra of the corrosion layer obtained for both continuous (red) laser- and modulated (black) laser- based thin walls after 7 days incubation in artificial urine under static conditions.

The Raman spectra (**Figure V 9**) show the results for CW-based, in red, and MW-based, in grey, samples' corrosion layers after seven days of incubation in AUS. Like FTIR analysis, at least three measurements were done for each sample. The observed peaks were generally consistent throughout the surface, though their intensities varied, suggesting the presence of the same components in different quantities along the surface. This variability was more pronounced in CW-based thin walls. Regarding the chemical composition, the Raman analysis indicated that the peaks corresponded to the presence of $Mg(OH)_2$ and struvite, despite some slight peak deviations. Struvite, a common component formed on urinary implants, in this case, was formed by a mixture of precipitates from the AUS and Mg corrosion.

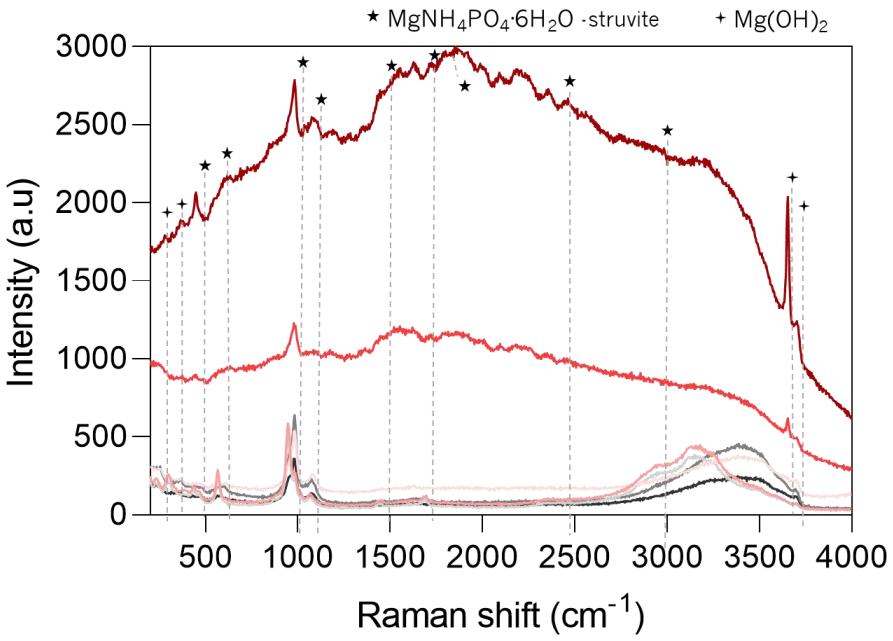


Figure V 9 Raman spectra of the sample's surface, continuous laser- based (red) and modulated laser-based (grey), after 7 days incubation in artificial urine in static conditions.

The percentage of corrosion layer developed on the surface of the samples over time was also accessed. **Figure V 10 a)** illustrates that, after the initial 24h of contact with AUS, the corrosion layer remains relatively stable for both CW- and MW-based samples. This indicates that the corrosion layer forms rapidly in the first 24h, accounting for approximately 40-50% of the sample's weight, and subsequently stabilizes, showing only a 5-10% variation from 24h to 7 days. Samples' weight loss was measured to monitor the metal loss over time (**Figure V 10 b)**). On the first 24h immersion, the samples lost 20-30% of the weight, and from that point until 7 days, the weight loss increases until 40-45%, so, 10-15% increase. In accordance with the results for the corrosion layer development (**Figure V 10 a)**), where most of the corrosion layer developed in the first 24h of immersion, in this case, most of the samples' weight was lost in the first 24h. These two phenomena are related; as the corrosion occurs, the corrosion layer forms, so, the more corrosion takes place, the greater the amount of the corrosion layer that develops. In this case, the first 24h of contact with AUS were more active, i.e., the corrosion occurred faster, so a thick corrosion layer was formed. From 24h further, the corrosion layer stabilized and probably acted as a protective coverage that delayed corrosion. Additionally, we can notice from the results that MW-based samples presented less variation in the weight loss at each time point (revealed by the lower error values), and from 72h, the weight loss values were lower than the CW ones.

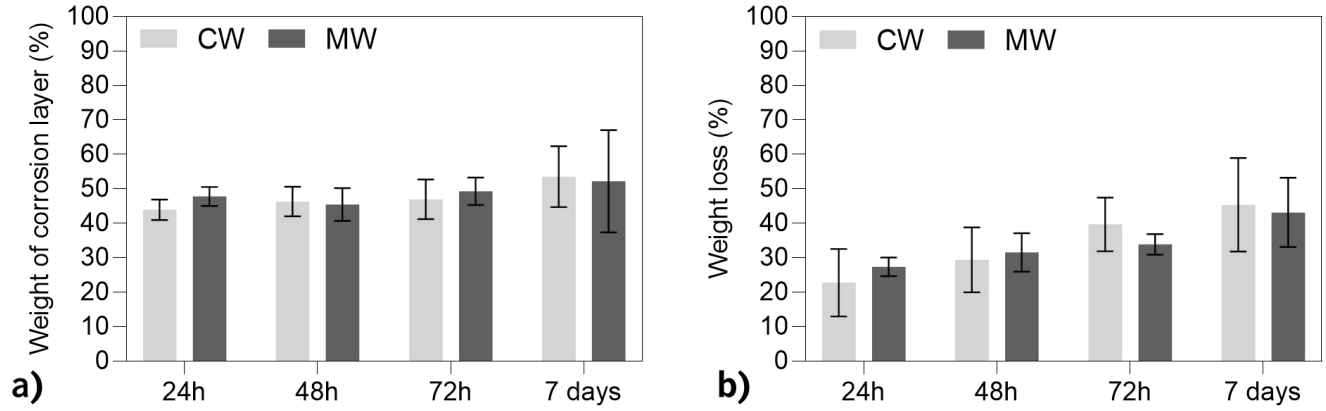


Figure V 10 Corrosion layer percentage (a) and weight loss (b) along the time.

V-4. Discussion

The powder characteristics is a very important part of the 3D printing process since the size, oxidation status, contaminants and shape will significantly influence the final structure, thus helping on interpretation of results. The Mg1Y powder surface analysis, through XRD, showed only one phase, the α phase (**Figure V 2 a)**). In fact, according with previous studies, the Y solubility in Mg can vary depending on the processing conditions and the maximum solubility of Y in the α-Mg matrix can be as high as 4.7 at.% Y(30). The EDS analysis revealed that Y and oxides are also present, probably not in sufficient amount to be detected by XRD. The cross section of the powder particles, on the other hand, showed obvious phase differences, as seen by the dendritic structures presented, which is typic given the process of rapid cooling during gas atomization. These structures correspond to the accumulation of yttrium atoms that are most probably in higher concentrations in those regions. The powder had the round morphology, which leads to a good flowability, that is ideal for PBF-LB processing(31). After characterization, the powder was used for the following step of thin structures optimization. This process involved a comprehensive study of process parameters combinations util the smoothest surface and no structural pores were obtained. The SEM images showed that a continuous line is obtained in the cross section perpendicular to the building direction (XY plan). According to other authors, when the speed and power are not well combined, i.e. high speed and low power or vice versa, the balling phenomenon takes place, which is seen by the wall's aspect that becomes discontinuous and can even present fragmentation(32). In this case, the XY plan was continuous and homogeneous, indicating that the process parameters combined were adequate. The XZ plan (parallel to the building direction), on the other hand, presented the typical waving shape and in some places, partially melted powder particles attached, which confers the surface some roughness. The partially melted powder particles attached to the tracks borders is

common in 3D printing, since the parts are being built "immersed" in powder. Furthermore, in this specific case where the thin walls are being built close to each other, depending on the hatch distance used (that translated on the distance between two consecutive walls), some bigger powder particles can be "stuck" between two walls, so, easily attached to the surface, even though not(32-34) In this work, the hatch distance was chosen to be enough for the powder particles to spread easily between the walls. The hatch distance was set to 1 mm, the laser spot diameter to 0.08 mm and the results showed that the wall thickness for CW was 0.29±0.01 mm and for MW was 0.35±0.01 mm. So, for CW the space available for the powder particles to circulate is about 0.71 mm and for MW around 0.65 mm. Considering the size of the powder particles (d_{50}: 39.4µm, 0.0394 mm), there should be space enough for the particles to pass. So, even though this phenomenon have been minimized and the smoother surface obtained from the process optimization phase, partially melted powder particles were still present, which is indeed difficult to avoid(35). One of the reasons may be the fact that small particles tend to agglomerate to the surface of the bigger ones, making one big piece that can be more easily stuck in the space between two consecutive walls(32).

Regarding the layers thickness, for CW there was a higher variation, and they were in general thicker than the MW ones. Yet, for both, the thickness was thinner than the initially stablished layer thickness for the process - 20 µm. The melt pools' shape were quite shallow, considering to what was expected for thin structures, where the tendency is for the melt pools to be deeper due to the reduced heat dissipation(36). For this reason, the associated keyhole pores were avoided, and the samples were compact and free of pores.

The surface of the samples presented some roughness, mainly due to the partially melted powder particles attached to the surface, which was difficult to avoid, as discussed before. The profilometry results confirmed this, where small bumps were observed as well as what it seems to be solidification defects, that are normal and were also observed in other studies on thin walled structures produced by(1,21,37). The roughness values were higher for MW samples and that may be the reason for the MW wall thickness to be thicker, so, despite the theoretically expected lower heat accumulation for MW, they seem to have slightly higher tendency for partially melted powder particles to attach.

The *in vitro* corrosion tests were done under partially dynamic conditions (with agitation) and using AUS since the intended target of our investigation is to use biodegradable metals, Mg1Y in this case, for biodegradable urological devices. The use of different laser modes leads to some differences on the corrosion pattern. The results indicated that the CW corroded slightly faster than MW-based samples

and the corrosion pattern was more random for CW samples, where it was observed that the corrosion had more tendency to occur from the middle of the samples than from the edges, which reveals some irregularity of corrosion and maybe some instability of the structures. It was also possible to observe on all the samples, that the corrosion propagation path is similar, the corrosion starts in one spot and from there, it propagates in thin lines, randomly, along the wall. This might be related with the different zones formed in the melt pools during the printing process – resulting from different distribution of intermetallics -, that form due to the heat variations and re-melting during the layer stacking. The different zones formed have different corrosion susceptibilities and some regions will be weak points where localized corrosion will take place. From there the corrosion continues along the path where the microstructure is more susceptible, a process that is detailed in a recent paper where similar results were observed(38). Looking for the corrosion layer development and corrosion rate results, we could see that for CW and MW, most of the corrosion layer develops in the first 24h and, consequently, most of the corrosion takes place in the first 24h as well. The slight differences seen on the corrosion were that at higher time points, MW seems to degrade slower, and CW seems to be more inhomogeneous given the high error bars presented. The chemical composition analysis of the corrosion layers showed that the corrosion layer developed on CW- based samples is uneven, i.e. the same elements formed but in different amounts along the surface. Since the elements have different tendencies to protect the sample from corrosion, the uneven coverage leads to an uneven corrosion, which may be the reason of the inhomogeneous corrosion taking place in CW samples. It was seen that the shape of some of the CW samples was not straight, presenting tilted edges due to high heat input, creating distortion of the structure(35). Even though the CW samples' structure analysis doesn't present porosity, which is a great characteristic and contributes to a good structural stability, probably the high heat input was sufficient to cause stacking instability, creating more weak points, which leads to higher tendency to localized corrosion, compared with the MW samples.

Overall, this study was important to elucidate the differences on using continuous and modulated laser modes in the structure and corrosion of thin-walled constructs. The MW laser mode is expected to lead to less heat accumulation during sample printing, thus leading to a more stable structure, especially in the case of Mg printing, given the close value of melting and evaporating temperatures of Mg and associated tendency to evaporate. In this study it was found that the corrosion behaviour of MW samples was more homogeneous, probably due to the improved structural stability, even though a structure free of pores were obtained for CW as well. This study will be the starting point for further studies using Mg1Y for thin-walled biodegradable urological devices, such as stents.

V-5. Conclusion

This study explored the AM of thin structures thorough PBF-LB, using Mg1Y powder and two laser modes, continuous and modulated, and respective structure characterization and corrosion under artificial urinary environment. Samples with great structural integrity and no observable porosity were obtained, wither by using continuous or modulated laser modes. The samples produced by modulated laser mode showed slightly higher roughness even though both (continuous and modulated laser based samples) were rough, primarily due to the partially melted powder particles. The samples' corrosion in artificial urine solution (AUS), in static conditions, showed that most of the corrosion takes place in the first 24h for all the samples and the corrosion layer and corrosion on continuous laser-based samples was more inhomogeneous compared with the modulated laser-based ones.

Overall, both laser modes were effective for the development of high quality Mg1Y thin structures but the modulated laser-based samples offered more stability in terms of corrosion in AUS. Future work is needed to improve the surface quality of the samples, possibly by applying a post-treatment to remove the partially melted powder. Also, the rapid corrosion on the first 24h incubation can be controlled by applying protective surface treatments.

V-5. Bibliography

1. Wu Z, Narra SP, Rollett A. Exploring the fabrication limits of thin-wall structures in a laser powder bed fusion process. Int J Adv Manuf Technol. 2020 Sep 11;110(1–2):191–207

2. Singh R, Gupta A, Tripathi O, Srivastava S, Singh B, Awasthi A, et al. Powder bed fusion process in additive manufacturing: An overview. Mater Today Proc. 2020;26:3058–70.

3. Liu J, Liu B, Min S, Yin B, Peng B, Yu Z, et al. Biodegradable magnesium alloy WE43 porous scaffolds fabricated by laser powder bed fusion for orthopedic applications: Process optimization, in vitro and in vivo investigation. Bioact Mater. 2022 Oct;16:301–19.

4. Li Y, Zhou J, Pavanram P, Leeflang MA, Fockaert LI, Pouran B, et al. Additively manufactured biodegradable porous magnesium. Acta Biomater. 2018 Feb;67:378–92.

5. Li Z, Xu R, Zhang Z, Kucukkoc I. The influence of scan length on fabricating thin-walled components in selective laser melting. Int J Mach Tools Manuf. 2018 Mar;126:1–12.

6. Abdelmoula M, Musinski W. Predicting and correlating melt pool characteristics with processing parameters in IN625 powder bed fusion additive manufacturing. J Manuf Process. 2024 Jul;121:427–45.

7. Domingues B, Pacheco M, de la Cruz JE, Carmagnola I, Teixeira-Santos R, Laurenti M, et al. Future Directions for Ureteral Stent Technology: From Bench to the Market. Adv Ther. 2022 Jan 17;5(1).

8. Pacheco M, Silva JM, Aroso IM, Lima E, Barros AA, Reis RL. Biomaterials for Ureteral Stents: Advances and Future Perspectives. In: Urinary Stents. Cham: Springer International Publishing; 2022. p. 197–208.

9. Wang L, Yang G, Xie H, Chen F. Prospects for the research and application of biodegradable ureteral stents: from bench to bedside. J Biomater Sci Polym Ed. 2018 Sep 22;29(14):1657–66.

10. Li K, Liu X, Di X, Bao Y, Bao Y, Xiong C, et al. A novel biodegradable ureteral stent with antibacterial ability to inhibit biofilm formation. Mater Adv. 2022;3(22):8276–87.

11. Barros AA, Oliveira C, Ribeiro AJ, Autorino R, Reis RL, Duarte ARC, et al. In vivo assessment of a novel biodegradable ureteral stent. World J Urol. 2018 Feb 11;36(2):277–83.

12. Zhang Y, He J, Chen H, Xiong C. A new hydrophilic biodegradable ureteral stent restrain encrustation both in vitro and in vivo. J Biomater Appl. 2021 Jan 16;35(6):720–31.

13. Soria F, Morcillo E, Serrano A, Budia A, Fernández I, Fernández-Aparicio T, et al. Evaluation of a New Design of Antireflux-biodegradable Ureteral Stent in Animal Model. Endourol Stones. 2018;115:59–64.

14. Cui H, Zhang K, Gao C, Kang Y, Jiang H, He Y. Preparing and characterizing biodegradable materials for ureteral stents. Polym Adv Technol. 2021 Nov 20;32(11):4547–55.

15. Liu J, Liu B, Min S, Yin B, Peng B, Yu Z, et al. Biodegradable magnesium alloy WE43 porous scaffolds fabricated by laser powder bed fusion for orthopedic applications: Process optimization, in vitro and in vivo investigation. Bioact Mater. 2022 Oct;16:301–19.

16. Raducanu D, Cojocaru VD, Nocivin A, Drob SI, Hendea RE, Stanciu D, et al. The Characterization of a Biodegradable Mg Alloy after Powder Bed Fusion with Laser Beam/Metal Processing for Custom Shaped Implants. Materials (Basel). 2024 Apr 6;17(7):1682

17. Badkoobeh F, Mostaan H, Rafiei M, Bakhsheshi-Rad HR, RamaKrishna S, Chen X. Additive manufacturing of biodegradable magnesium-based materials: Design strategies, properties, and biomedical applications. J Magnes Alloy [Internet]. 2023 Mar;11(3):801–39.

18. Tie D, Liu H, Guan R, Holt-Torres P, Liu Y, Wang Y, et al. In vivo assessment of biodegradable magnesium alloy ureteral stents in a pig model. Acta Biomater. 2020 Oct;116:415–25.

19. Mei D, Wang C, Nienaber M, Pacheco M, Barros A, Neves S, et al. Corrosion behavior of Mg wires for ureteral stent in artificial urine solution. Corros Sci. 2021 Aug;189:109567.

20. Gomes IV, Pacheco M, Nienaber M, Neves SC, Mei D, Barros A, et al. Shielding AZ91D-1%Ca from corrosion through ultrasound melt treatment: A study for stent design. J Magnes Alloy. 2023 Aug;11(8):2901–15.

21. Chakraborty A, Tangestani R, Batmaz R, Muhammad W, Plamondon P, Wessman A, et al. In-process failure analysis of thin-wall structures made by laser powder bed fusion additive manufacturing. J Mater Sci Technol. 2022 Jan;98:233–43.

22. Constantin L, Wu Z, Li N, Fan L, Silvain J-F, Lu YF. Laser 3D printing of complex copper structures. Addit Manuf [Internet]. 2020 Oct;35:101268.

23. Mezzetta J. Process-Property Relationships of Ti6Al4V Fabricated through Selective Laser Melting Department of Mining and Materials Engineering. 2016;(August).

24. Caprio L, Demir AG, Previtali B. Influence of pulsed and continuous wave emission on melting efficiency in selective laser melting. J Mater Process Tech. 2019;266(November 2018):429–41.

25. Zheng Y, Zhang Y, Tian Y, Chen L. Microstructure characteristics and degradation behaviors of medical rare-earth Mg-10.6Gd-0.3Ag-x(Y/Zn) alloys in vitro. J Alloys Compd. 2024 Aug;997:174967.

26. Pacheco M, Aroso IM, Silva JM, Lamaka S V., Bohlen J, Nienaber M, et al. Understanding the corrosion of Mg alloys in in vitro urinary tract conditions: A step forward towards a biodegradable metallic ureteral stent. J Magnes Alloy. 2023 Dec.

27. Lock JY, Draganov M, Whall A, Dhillon S, Upadhyayula S, Vullev VI, et al. Antimicrobial properties of biodegradable magnesium for next generation ureteral stent applications. In: 2012 Annual International Conference of the IEEE Engineering in Medicine and Biology Society. IEEE; 2012. p. 1378–81.

28. Channa NA, Ghangro AB, Soomro AM, Noorani L. Analysis of kidney stones by FTIR spectroscopy. J Liaquat Univ Med Heal Sci. 2007;6(2):66–73.

29. Krishnamoorthy N, Dey B, Arunachalam T, Paramasivan B. Effect of storage on physicochemical characteristics of urine for phosphate and ammonium recovery as struvite. Int Biodeterior Biodegradation. 2020 Sep;153:105053.

30. Zhao HD, Qin GW, Ren YP, Pei WL, Chen D, Guo Y. The maximum solubility of Y in α-Mg and composition ranges of Mg24Y5−x and Mg2Y1−x intermetallic phases in Mg–Y binary system. J Alloys Compd. 2011 Jan;509(3):627–31.

31. Raducanu D, Cojocaru VD, Nocivin A, Drob SI, Hendea RE, Stanciu D, et al. The Characterization of a Biodegradable Mg Alloy after Powder Bed Fusion with Laser Beam/Metal Processing for Custom Shaped Implants. Materials (Basel). 2024;17(7).

32. Calignano F, Cattano G, Manfredi D. Manufacturing of thin wall structures in AlSi10Mg alloy by laser powder bed fusion through process parameters. J Mater Process Technol. 2018;255:773–83.

33. Abele E, Stoffregen HA, Kniepkamp M, Lang S, Hampe M. Selective laser melting for manufacturing of thin-walled porous elements. J Mater Process Technol. 2015 Jan;215:114–22.

34. Pyka G, Kerckhofs G, Schrooten J, Wevers M. The effect of spatial micro-CT image resolution and surface complexity on the morphological 3D analysis of open porous structures. Mater Charact. 2014 Jan;87:104–15.

35. Mumtaz KA, Hopkinson N. Selective Laser Melting of thin wall parts using pulse shaping. J Mater Process Technol. 2010 Jan;210(2):279–87.

36. Jiang H, Wang X, Xi R, Li G, Wei H, Liu J, et al. Size effect on the microstructure, phase transformation behavior, and mechanical properties of NiTi shape memory alloys fabricated by laser powder bed fusion. J Mater Sci Technol. 2023;157:200–12.

37. Yu W, Sing SL, Chua CK, Tian X. Influence of re-melting on surface roughness and porosity of AlSi10Mg parts fabricated by selective laser melting. J Alloys Compd. 2019;792:574–81.

38. Zhang X, Lv Y, Tan S, Dong Z, Zhou X. Microstructure and corrosion behaviour of wire arc additive manufactured AA2024 alloy thin wall structure. Corros Sci. 2021 Jul;186:109453.

CHAPTER VI

TOWARDS BIODEGRADABLE MG-BASED URETERAL STENTS: A COMPREHENSIVE *IN VITRO* STUDY OF TWO MG-1Y STENT PROTOTYPES.

TOWARDS BIODEGRADABLE MG-BASED URETERAL STENTS: A COMPREHENSIVE IN VITRO STUDY OF TWO MG-1Y STENT PROTOTYPES

ABSTRACT

Ureteral stents are fundamental devices in urology but currently used stents are associated with adverse events such as encrustation and infections. Biodegradable magnesium yttrium (MgY) has shown potential as base material for a next-generation biodegradable ureteral stent due to reported lower corrosion rates than pure Mg, homogeneous corrosion and associated antibacterial activity.

In the present work, meshed tubes produced via additive manufacturing (AM) and extruded, and coiled, wire tubes were produced. The corrosion behavior in dynamic conditions was studied, as well as the cytotoxicity and antibacterial activity. AM samples showed a more uniform but significantly faster corrosion, while the extruded ones showed some localized corrosion points. Additionally, AM samples demonstrated lower toxicity compared with the extruded-coiled ones to urinary tract derived cell lines, at a low metal concentration of 27.5 mm^2/ml. AM samples also showed antibacterial activity against *E.coli*.

This study highlights the potential of MgY for the development of a biodegradable ureteral stent, an innovative concept with expected improved patient outcomes.

Keywords: Biodegradable metallic ureteral stent, powder bed fusion laser beam, corrosion, antibacterial activity.

This chapter is based on the following publication: **Margarida Pacheco**, Francesco D'Elia, Maria Nienaber, Jan Bohlen, Zahra Jafari, Sviatlana V. Lamaka, Estêvão Lima, Alexandre Barros, Rui L. Reis, Cecilia Persson, Towards biodegradable Mg-based ureteral stents: a comprehensive in vitro study of two Mg-1Y stent prototypes. 2026. *Submited.*

VI-1. INTRODUCTION

Ureteral stents are currently indispensable medical devices in urology, playing a crucial role in maintaining patency in an obstructed ureter. Despite their efficiency in treating ureter blockages, ureteral stents are associated with severe problems such as stent encrustation and urinary tract infections(1). In the most critical clinical scenarios, encrustation can obstruct the urine flow leading to stent occlusion and the need for an early removal or stent replacement. Moreover, ureteral stent associated urinary tract infections (USAUTI) require the use of more antibiotics or even stent removal, which increases the burden on the healthcare system and affects the patient's quality of life(2). The incidence of these side effects increases with the stent indwelling time, which varies depending on the treatment, but usually between 2-6 months the stent needs removal or replacing(3,4). In response to these challenges, many strategies have been proposed, including the use of biodegradable materials. A biodegradable ureteral stent eliminates the need of a second surgery for stent removal since they are designed to degrade naturally in the human body while fulfilling their purpose(5).

Biodegradable metals, particularly magnesium (Mg) and its alloys, have shown high potential as biomaterials due to favorable mechanical properties for specific applications (such as bone implants), excellent biocompatibility and the possibility to tune the corrosion(6–9). This has led to various Mg-based biodegradable medical devices currently being available on the market(10–13). These include Magmaris, a biodegradable metallic vascular stent, MAGNEZIX®, a biodegradable metallic screw, the Resomet bioresorbable bone screw and Resomet bioresorbable K-wire and pin(10–14). Mg alloys have, therefore, been evolving well over the past few years, although there are still many challenges related with Mg-based biomedical implants, independently of some referred cases of success. These include rapid corrosion in biological environments, especially in solutions containing chloride ions (many body fluids), and the hydrogen liberation during corrosion, that can delay the tissue healing(15–17). For biomedical applications, corrosion control is an important factor since an excessive corrosion rate will lead to premature implant failure, as well as a high accumulation of corrosion products that can become toxic when released in higher amounts. For example, accumulation of hydroxide ions (OH^-) can lead to a critical alkalinization of the local tissue, excess hydrogen gas liberation results in the formation of gas cavities, and high concentrations of Mg ions can also be prejudicial(6,16,18–20). Thus, Mg corrosion must be carefully studied to enable degradation control in a way that when implanted, the corrosion will be adequate for the tissue healing time and the corrosion products released will be safely managed by the body. Additionally, the mechanical strength of Mg is relatively low, which for some applications is a major

disadvantage. Therefore, research on Mg-based implants has focused on developing Mg alloys with better mechanical and corrosion characteristics(21,22).

Yttrium (Y) is one example of a Mg alloying element that has been widely used for increased corrosion resistance and strengthening purposes(23,24). Alloying Mg with Y has been shown to delay Mg corrosion due to the Y_2O_3 protective corrosion layer forming on the surface(25,26). The improvement of Mg properties conferred by the addition of Y varies depending on the alloy, i.e. amount of Y, processing route and on the corrosion media(27,28). In a previous work from this group, it was found that a Mg-0.79wt%Y alloy, manufactured by wire extrusion, had a homogeneous corrosion rate in in vitro conditions in artificial urine(8). Besides the improvement of mechanical and corrosion properties, Mg-Y has antibacterial properties, which is favorable for ureteral stents applications(29). Antibacterial activity is also seen in other Mg alloys and is attributed to the alkalinity promoted by the OH- release during corrosion as well as the Mg2+ ions themselves(17,30,31). As mentioned, USAUTI is a growing problem, which causes high economic burdens and suffering to patients(32). When bacteria colonize the urinary system, they are able to attach to the stent surface and form a biofilm. The cells in the biofilm microenvironment are protected against stressful factors of the surrounding media, such as host immune system and antibiotics, leading to failed treatments(2,32,33). This results in an overuse of antibiotics and hence, contributes to the development of antibiotic-resistant bacteria, one of the most worrying problems in hospitals these days(34). Therefore, the use of stent materials with incorporated antibacterial activity is a major advantage, since they can promote the treatment success and diminish the use of antibiotics(17). Thus, an ideal material for ureteral stents would be able to reduce the incidence of USAUTI and be able to degrade in the body after fulfilling its role without causing tissue reactions. The research on biodegradable metals for ureteral stent applications is scarce but some works have shown promising results. Tie et al. explored the degradation and biocompatibility in vitro and in vivo (pig model) of ZJ41 [Mg–4 wt% zinc (Zn)–1 wt% strontium (Sr)](7). The results revealed that the stent maintained its shape at 7 weeks – i.e. still being functional- and no adverse reactions were detected. Zhang et al. explored the degradation rates of pure Mg and ZK60 alloy [Mg -5.6 wt% Zn -0.5 wt % zirconium (Zr)] in vitro and in rat bladder(35). The authors found no harm in the urinary system after 3 weeks implantation. These studies highlight the importance of developing a biodegradable ureteral stent with a suitable degradation time and with the capacity to degrade without causing tissue toxicity.

In this paper the corrosion of ureteral stent prototypes is explored in an in-house built dynamic system with a constant flow of fresh artificial urine solution (AUS) for 7 days in order to follow, daily, the samples'

corrosion, thus permitting a focused and detailed exploration of the corrosion pattern over time. Built on a previous work on Mg-alloys for biodegradable ureteral stenting, in the present study, the suitability of a Mg-Y alloy as ureteral stent base material was explored(8). We hypothesized that Mg with low amounts of Y (0.79-1wt%) could give a relevant corrosion and biological behavior for use as ureteral stents(8). Samples with similar composition were produced using two different processing techniques with the objective to explore two different methods to develop ureteral stents: additive manufacturing (AM-meshes) through powder bed fusion laser beam (PBF-LB); and wire extrusion followed by coiling to obtain tube-shaped springs. PBF-LB was selected given its ability to fabricate complex geometries and rapid prototypes, while coiled wire was chosen, as it is a more established process for stent designs(36,37). The analysis of these prototypes involved characterizing the microstructure, corrosion layer development, and overall corrosion behavior, as well as assessing their cytotoxicity and antibacterial activity against common urinary pathogens *Escherichia coli* and *Staphylococcus aureus*(32). The findings of this research provided important insights on the corrosion over 7 days incubation in AUS, biocompatibility and antibacterial activity of Mg-Y stent prototypes, which will be essential for the future development of a next generation biodegradable metallic ureteral stent.

VI-2. MATERIALS AND METHODS

VI-2.1. Samples preparation

The samples used in this work were produced either through additive manufacturing or wire extrusion followed by coiling. After production, the samples were washed by immersion in absolute ethanol and 5-minute sonication at 35 000 Hz (Ultrasonic Water Bath, VWR). The samples' external diameter was selected based on the most common ureteral stents dimensions (7Fr, corresponding to approx. 2.33 mm external diameter(38)) and on the average ureter diameter on adults 1.8±0.9 mm, maximum 3 mm(39). In this optimization phase the full stent length was not used, but rather shorter, representative tubes.

VI-2.1.1. Additive manufactured samples

The Mg-1wt%Y powder used to produce the additively manufactured meshed tubes (AM-meshes) was produced by gas atomization (Nanoval, GmbH, Berlin, Germany) – where the size of 50% of the particles (d50) was equal to or lower than 39.4 µm. PBF-LB processing was carried out using an Aconity™ MIDI (Aconity GmbH, Herzogenrath, Germany). Printing parameter optimization for thin Mg-1Y structures was done in a previous study(40), where it was determined that using a modulated wave (MW) laser mode leads to improved corrosion resistance in AUS compared to the conventional continuous wave (CW)

laser mode, possibly due to the lower heat accumulation during the MW printing. The optimized printing parameters for thin Mg-1Y structures were hence 50 mm/s laser scan speed, 50 W laser power, 0.01 MHz laser modulation frequency, 75 µs laser modulation width and 20 µm layer thickness for 80 µm spot size diameter under an argon gas atmosphere with a flow rate of 1 m/sec. These parameters were also used to produce the thin-walled meshed tubes, AM-meshes, developed in this work for the corrosion studies and the tubes (AM_Mg-1Y_t) used for cytotoxicity and antibacterial studies..

The AM-meshes were prepared on Fusion 360 (Autodesk, 2022), using a standard meshed tube model(41). The diameter of AM-meshes and AM_Mg-1Y_t were based on the most common ureteral stents dimensions and using a single track to obtain very thin-walled samples. The samples' eight was 20 mm.

Additively manufactured WE43 (AM_WE43_t, 3.9 wt%Y, 3.0 wt%Nd, 0.49wt%Zr and Mg balance) tubes were used as reference in the cytotoxicity tests given the alloy's demonstrated biocompatibility, as well as its current use in biomedical implants (although not yet in printed form)(10,42). These samples were produced using an EOS M100 printer (EOS GmbH, Krailling, Germany) under an argon gas atmosphere. The printed tubes had an internal diameter of ca. 1.57 mm, external diameter of ca. 2.33 mm (wall thickness of 0.76 mm), and a height of 22 mm. The samples were printed using previously optimized parameters consisting of continuous laser mode, at 1100 mm/s scan speed, 90 W laser power and with a hatch distance of 0.05 mm. The scan pattern was 67^{0} rotation between each layer, the layer thickness was set to 20 µm, and the laser spot diameter 40 µm(43).

VI-2.1.2. Extruded coiled wires

The Mg-1Y (Mg - 0.79 wt%Y) alloy was cast and machined into billets of 49 mm diameter and a length of 75 mm for extrusion. Prior to extrusion a homogenization solution heat treatment at 450 °C for 16h in an air circulation furnace Nabertherm N120/65SHA (Nabertherm GmbH, Bremen, Germany) was carried out followed by air cooling. The billets were then extruded by direct extrusion to the minimum wire diameter possible, 0.6 mm using a 2.5 MN automatic extrusion press (Müller Engineering GmbH & Co. KG, Todtenweis/Sand, Germany) and associated coupled coiler. For a more comprehensive overview of the wire manufacturing process and the used setup, details can be found elsewhere(44). The extrusion was performed with a die with four nozzles of 0.6 mm diameter equidistant from the center position, corresponding to an extrusion ratio of 1:1736. Extrusion parameters were set to 0.05 mm·s−1 ram speed with container and die temperature of 400 ^{0}C.

For the coiling, the wires were placed in the respective holder on the coiling machine and pushed to the coiling center where it was pulled and machined into coiling shape with the desired diameter (2.33 mm external diameter). The spacing between the coils was minimized to ensure the consecutive turns were in contact with each other. The coiled wires (Extr-coiled) were used for the corrosion studies while the as-extruded wires (non-coiled) were used for the cytotoxicity studies (e_Mg-1Y).

VI-2.2. Microstructure analysis

The microstructure of the wires was assessed by light optical microscopy (LOM) both before and after coiling. The wires and Extr-coiled samples were first fixed with cold embedding compound Demotec 30 (Demotec, Nidderau, Germany) and ground using 2500 and 4000 grit silicon carbide papers, then polished with water-free oxide polishing suspension (OPS) and 0.15 µm diamond suspension. The polished samples were etched for 10 s in standard picric acid solution of 5 ml H2O, 7 ml acetic acid, 200 ml ethanol, and 10 g of picric acid. The AM-meshes were first cold-mounted in resin (KM-B RESIN, PRESI) in a polyethylene mounting mold and left to dry for at least 2 hours. After drying, the mounted samples were removed from the mold and ground with SiC foil 320 grit, and then polished through a sequence starting with MD-largo foil for 5 min, MD—Dac foil 4 min, MD-Nap for 3 min and finalized with OP-Chem with OP-U NonDry for 1.5 minutes. After polishing, the samples were rinsed with pure ethanol and etched with 2% Nital solution (2% nitric acid in ethanol) for 5 seconds.

For the scanning electron microscopy (SEM, Zeiss LEO 1550, Oberkochen, Germany) and energy dispersive X-ray spectroscopy (EDS, INCAx-Act, PentaFET Precision, Oxford Instruments) analysis of the AM-meshes, the preparation was the same, but without etching and the samples were sputtered with gold platinum for improved visualization by SEM. EDS was used to qualitatively evaluate of the elemental composition of the structures in the cross-section of the sample.

VI-2.3. Surface characterization - Profilometry

Profilometry studies were conducted using an InfiniteFocusSL 3D scanner (Bruker Alicona). 3D images were acquired from three different sections of each sample, for reproducibility, using two lenses, 10X and 20X. The images were analyzed using GOM software, to determine the surface area of the outer surface.

VI-2.4. *In vitro* dynamic conditions

For the corrosion studies a dynamic system was used as described in a previous work(8). The samples were placed vertically inside plastic tubes (3.18 mm diameter), which were positioned inside a holder equipped with a water recirculating system for temperature control, with the thermostat set to 37 ^{0}C. The connectors used to fix the plastic tubes in place also secured the samples in place. Each sample tube was connected to a pumping channel and a common artificial urine solution (AUS) reservoir. The AUS used in this work was based on the one proposed in ASTM 1828-97(38) and the composition is provided in **Table VI 1**. To the list of reagents proposed on the standard, we added sodium azide, to avoid bacterial contamination. The pH of the AUS was checked to be between 6 and 7 every time a solution was prepared. The AUS flow was set to 0.5 ml/min, based on the average value of urine production by the human body (1 – 2 L per day)(45). 10L of AUS was prepared each time to guarantee constant fluid flow. Samples were collected from the system for analysis after 30 minutes, 1, 2, 3, 4, 5, 6 and 7 days. These time points were selected based on a previous study with extruded wires in AUS(8) and considering the fast corrosion of AM-Meshes, by visualization, during the experiment, given the lack of other works on additive manufactured Mg-1Y in AUS.

Table VI 1 Composition of the AUS used in this study.

Component	Amount (g) *per* L
Ammonium chloride (NH_4Cl)	3.000
Creatinine ($C_4H_7N_3O$)	2.000
Disodium hydrogen orthophosphate, anhydrous (Na_2HPO_4)	2.500
Potassium dihydrogen orthophosphate (KH_2PO_4)	2.500
Sodium azide (NaN_3)	0.015
Sodium chloride (NaCl)	9.000
Sodium sulfite (Na_2SO_3)	2.620
Urea (CH_4N_2O)	25.000

VI-2.5. Corrosion

The corrosion layer developed on the samples' surface during the 7d in in vitro dynamic conditions was characterized by SEM for morphology and Raman spectroscopy, X-ray diffraction (XRD), Fourier-transform infrared spectroscopy (FTIR) and energy dispersive x-ray spectroscopy (EDS) for composition.

The percentage of corrosion layer accumulation was also quantified by weighing the sample before and after corrosion layer removal. The composition and aspect of the corrosion layer gives important data on the corrosion of the sample, being an important step to better interpretate the corrosion results.

VI-2.5.1. SEM/EDS

The morphology of the corrosion layer covering the samples was observed by SEM (JEOL JSM-6010LV, Osaka, Japan) equipped with an EDS (INCAx-Act, PentaFET Precision, Oxford Instruments, Abingdon, UK) for chemical characterization. The accelerating voltages used were 10 and 15 eV. The samples with the corrosion layer were sputtered before SEM with a gold layer for better conductivity and to avoid charging effects.

VI-2.5.2. Raman spectroscopy

Raman spectroscopy measurements were carried out at room temperature in a LabRAM Soleil™ Raman Microscope (Horiba Scientific, Piscataway, New Jersey, USA) using a 532 nm Nd:YAG laser for excitation. The laser beam (laser spot 1 μm^2) with P = 15 mW was focused on the sample by a × 50 lens (Zeiss), and the spectra were collected with a 600 groove/mm grating using 10 acquisitions with a 2 s acquisition time. At least three measurements per sample were done.

VI-2.5.3. XRD

XRD was employed as one of the methods to evaluate the chemical composition of the samples' corrosion layer. A high-resolution Bragg-Brentano diffractometer (Bruker D8 Advance DaVinci, Karlsruhe, Germany) equipped with Cu Kα radiation (λ = 1.506 Å) was used, at 40 kV and 40 mA. Data were collected in the 2θ range of 5-70° and 1 s per acquisition step.

VI-2.5.4. Fourier transform infrared spectroscopy (FTIR)

A corrosion layer analysis was done through FTIR by collecting part of the corrosion layer from the dried samples' surface. The analysis was performed in an IR Prestige 21 spectrometer (Shimadzu, Kyoto, Japan). The analyzed spectral region was 600 - 4000 cm^{-1} with a resolution of 4.0 for 32 number of scans. At least three analyses per sample were done.

VI-2.6. Corrosion

For the corrosion analysis, the corrosion layer was removed by immersing the samples in an etching solution composed of 200 g/L chromium (VI) oxide (Laborspirit), 10 g/L silver nitrate (Laborspirit), and 20 g/L barium nitrate (Laborspirit) and reagent water to make 1000 ml, for a few

minutes, following ASTM G1–03(46). The samples were then thoroughly washed with deionized water and, finally, rinsed with absolute ethanol and left to air dry. Detailed observation of corrosion damage was then carried out using SEM analysis, following the same methodology as that used for corrosion layer observation (**Section VI-2.5.1.**).

VI-2.6.1. Micro-computed tomography (Micro-CT)

3D visualization of the samples at different time points was done using a high-resolution micro-CT (SkyScan 1272, Bruker, USA), with a pixel size of 15 µm, voltage range of 50 kV, and current source of 200 uA. Approximately 250 projections were obtained over a rotation angle of 360°, and rotation step of 0.3°. Data sets were reconstructed using standardized cone-beam reconstruction software (NRecon 1.6.10.2, Bruker). A representative dataset of the slices was segmented into binary images with a dynamic threshold of 48-250. The binary images were used for the morphometric analysis (CT Analyser, v1.15.4.0, Bruker, USA). The percentage of object volume over time was assessed.

VI-2.6.2. Inductively Coupled Plasma - Optical Emission Spectroscopy (ICP-OES)

The amount of cations released from the samples to the AUS was assessed by analyzing the collected AUS aliquots through ICP-OES analysis (JY 2000 2, HORIBA JOBIN YVON, Inc, Kyoto, Japan). The AUS samples collected were filtered with a 0.22 µm filter and diluted in a 1:10 ratio with deionized water. Finally, a mixture with 90% nitric acid and 10% AUS solution was prepared before the ICP analysis. The nitric acid solution comprised of 5% nitric acid (69%) and deionized water.

VI-2.7. Cytotoxicity

The cytotoxicity of Mg alloy extracts from AM_Mg-1Y_t, e_Mg-1Y and AM_WE43_t samples, was evaluated using a mouse fibroblast L929 cell line (European Collection of Cell Cultures (ECCC), UK) and a G/G cell line (DSMZ, German collection of Microorganisms and Cell Cultures, GmbH, Braunschweig, Germany), a cell line isolated from mouse bladder. Thereby, these cells represented the cells that line the urinary tract, including the bladder and ureters. This latter is a cell line isolated from the mouse bladder. The L929 cells were cultured in Dulbecco's modified eagle medium (DMEM, Laborspirit) with 10 % fetal bovine serum (FBS, ALFAGENE) and 1% antibiotic/antimycotic (ALFAGENE) and G/G in 45 % Ham's F10 (ALFAGENE) and 45 % DMEM (Laborspirit) with 10 % FBS (ALFAGENE), 5 µg/ml human insulin, 5 µg/ml human transferrin, 50 nM hydrocortisone, 5 ng/ml selenite and 1 % antibiotic/antimycotic (ALFAGENE). The samples were sterilized by UV exposure for 30 min, after washing them with absolute ethanol under sonication for 5 min. To prepare the extracts, each metal was incubated with the respective cell culture media for 24 h at 37 °C with constant agitation and an area/volume ratio of 27.5 mm^2/ml, based on

previous studies(18,47,48),and 300 mm^2/ml, according to the ISO 10993-12. Since there is no biodegradable ureteral stent currently in the market, nitinol wire (300 mm^2/ml) was used as a control, given its wide use in biomedical devices. The extracts were applied to cells as direct extracts, i.e. 100% extract (E100), and lower concentrations, 50% (E50), 25% (E25), and 12.5% (E12.5), prepared by diluting the original extract in cell culture media. Nitinol control (CTR_Nit)'s extract was used only as direct extract (100% extract). A positive control (C+), containing only cells with culture media, and a negative control (C−), with 25 % DMSO, were also applied. The cells were seeded in 96 well plates with a cell density of 1×104 per well for L929 cell line and 0.8 × 104 per well for G/G cell line, for 24 h in a humidified incubator at 37 °C with 5 % CO2. The cell media in each well was replaced by the Mg alloys' extracts at different concentrations and/or the controls. After incubation for 24 h, the cell viability was determined by incubation (3-4 h) with 3-(4,5-dimethylthiazol-2-yl)−5-(3-carboxymethoxyphenyl)−2-(4-sulfophenyl)−2H-tetrazolium, inner salt – MTS. This method is based on the capacity of metabolically active cells to reduce MTS into a colored formazan(49). The amount of formazan produced is then quantified by measuring the absorbance at 490 nm, which is proportional to the metabolic active (living) cells.

To complement the MTS assay, a Live/Dead cell viability assay was performed to observe viable and dead cells, after contact with the metals' extracts. This is a color-based method to determine viable and non-viable cells, simultaneously, based on the membrane integrity. The procedure to obtain the metal extracts and the exposure of the cells to the extracts was the same as the one for the MTS assay. After 24 h incubation with the extracts, the cell layer was washed with phosphate-buffered saline (PBS) and cell media supplemented with 2 µl/ml Calcein-AM (Biotium) and 1ug/ml Propidium Iodide (PI, Biotium) was added in each well. The cells were incubated for 10 min in the dark at 37 °C with 5 % CO2 and then the media with the dyes was removed. The cell layers were washed again, and then new PBS was added in each well. The cells were observed in a fluorescence microscope (Microscope DM6 B, Leica), where the living cells were fluorescent green and the dead cells fluorescent red. This method is based on the cell membrane integrity. The cell membrane is permeable to calcein-AM, which will be converted in a fluorescent green calcein by the esterase activity of living cells. The PI becomes fluorescent when it binds to double stranded DNA, but this compound is membrane impermeant of live cells, thus, it is used to identify non-viable cells.

VI-2.8. Antibacterial activity

To evaluate the antibacterial potential of AM_Mg-1Y_t, both by avoiding surface bacteria attachment or by the release of corrosion products to the surrounding media, Gram-positive and Gram-negative strains were used, *S. aureus* ATCC 25923 (American Type Culture Collection, Manassas, VA, USA) and *E. coli* ATCC 25922 (Microbiologics, Inc., Saint Cloud, MN, USA), respectively. The AM_Mg-1Y_t, exposed surface area/bacterial suspension volume of 27.5 mm^2/ml, were cleaned by immersion in absolute ethanol and sonicated for 5 minutes and then sterilized by exposition to UV light for 30 minutes. Nitinol was used as control and was prepared the same way as the AM_Mg-1Y_t. C- was the negative control, i.e. the bacteria suspension without any metal treatment. The bacteria strains were inoculated using tryptic soy broth (TSB, Quimigen Unipessoal LDA) and incubated overnight under constant agitation at 150 rpm at 37°C. The optical density (O.D.) of the culture was then adjusted to value of 0.08-0.1 at 600 nm, using TSB to dilute accordingly. Two serial dilutions of the prepared inoculum were done in order to obtain a final concentration of 1-2 x 10^6 cloning forming units (CFUs)/ml. The AM_Mg-1Y_t and Nitinol samples were placed inside the wells of a 12-well plate and 2 ml of the prepared bacteria suspension was placed afterwards. The plates were incubated at 37°C under constant agitation at 150 rpm for 24 h. To quantify the number of bacteria attached to the samples' surface, the metals were removed from the wells using a sterile clamp, washed by immersion in PBS to remove the non-adherent bacteria, and placed inside a tube with 1 ml PBS. Two cycles of 30 sec. of vortexing were applied with a cycle of sonication (5 min, 3500 Hz) between the vortexing cycles. Then serial dilutions were done, and the suspensions were spread into TSB/agar petri dishes for CFU counting. The petri dishes were incubated at 37°C for 24 h. To quantify the number of bacteria in suspension, 100 µL of suspension was collected from each well and serial dilutions were done. The diluted suspensions were spread in petri dishes and incubated at 37°C for 24 h as well. After the 24 h incubation, the CFU number was determined.

VI-2.9. Statistical analysis

Statistically significant differences between groups were probed through a one-way analysis of variance (ANOVA), followed by a Dunnett's post-hoc test. A statistically significant difference was considered at $p < 0.05$.

VI-3. RESULTS

VI-3.1. Microstructure characterization

Figure VI 1 a) and d) present the macroscopic images of the ureteral stent prototypes studied in this work. The microstructure of the AM-meshes and Extr-coil samples was analyzed by LOM and SEM (**Figure VI 1 b), c), e) and f)**). A representative optical micrograph of the AM-mesh (**Figure VI 1 b)**) shows that the edges of the structure were not completely straight, but rather of a wavy shape. This is typical for thin structures and often due to melt pool instability resulting from variations in heat input. **Figure VI 1 b)** also shows some structural pores resulting from these variations in heat input, whereby evidence of lack of fusion and gas porosity is present, due to both low and high energy input, respectively. A representative SEM image of the AM-meshes is presented in **Figure VI 1 c)**, showing a network of brighter structures, which, according to the EDS analysis (**Figure S VI 1, Supplementary information**), have higher oxygen content (15.5-18 wt%) compared with the darker regions (4.4-8.9 wt%), indicating that the brighter structures are rich in oxides, such as yttrium oxides (Y_2O_3). These are typically present along the surface of powder particles. Given their high melting point (well above the boiling point of Mg), such oxides are not completely melted during PBF-LB of Mg alloys, and often remain within the microstructure as cracked shells. Here, the micrograph suggests that regions of agglomerated oxides were present within the microstructure. This may have been due to low energy input at these regions, which did not enable sufficient cracking of oxide shells, thereby forming a network of such structures.

The Extr-coil samples' microstructural analysis showed the cross section of the wire before (**Figure VI 1 e)**) and after (**Figure VI 1 f)**) coiling. At this scale, no evident defects are noticed on the wires after extrusion or after the coiling process.

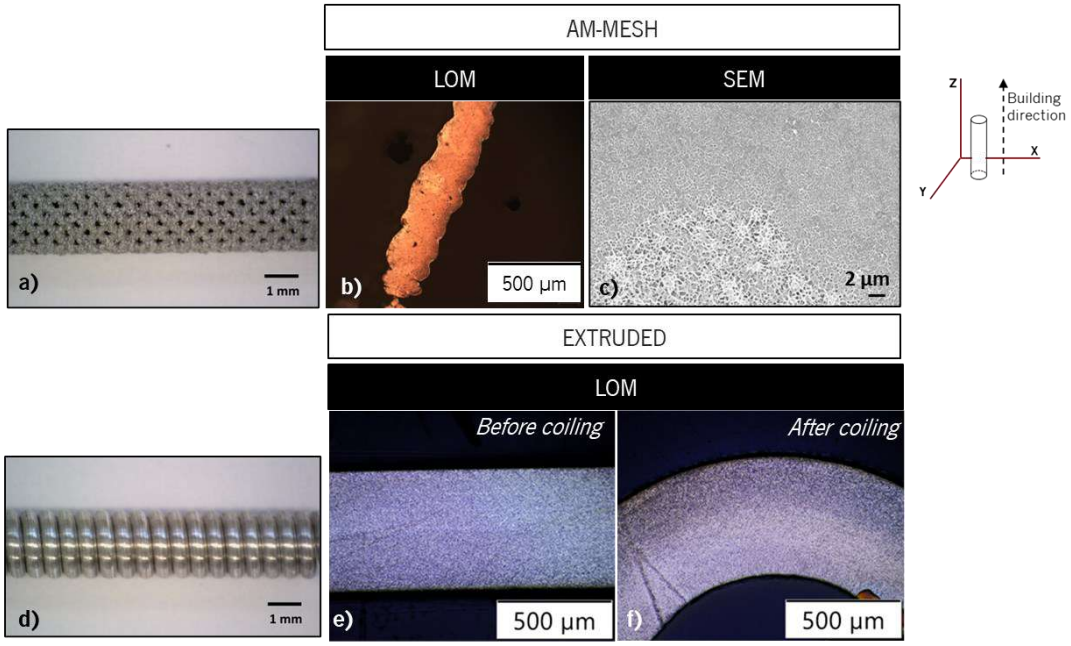


Figure VI 1 Macroscopic image of AM-mesh, a), LOM b) and SEM c) of AM-mesh sample, parallel to the building direction. Macroscopic image of Extr-coiled tubes, d), and longitudinal cross section of the extruded wires before, e), and after, f), coiling.

VI-3.2. Corrosion layer characterization

The corrosion tests were done in an in house built dynamic system, simulating the urinary tract environment, for 7 days. Before contact with AUS, the samples' surface was analyzed. The outer surface area was 11.39±0.22 mm^2 for AM-meshes and 9.31±0.12 mm^2 for Extr-coiled, indicating that AM-meshes have a higher surface area compared with the Extr-coiled ones, which is due to the non-melted powder particles attached to the surface during printing. **Figure VI 2** shows representative 3D images obtained of a) AM-meshes, and b) Extr-coiled samples used for surface area analysis.

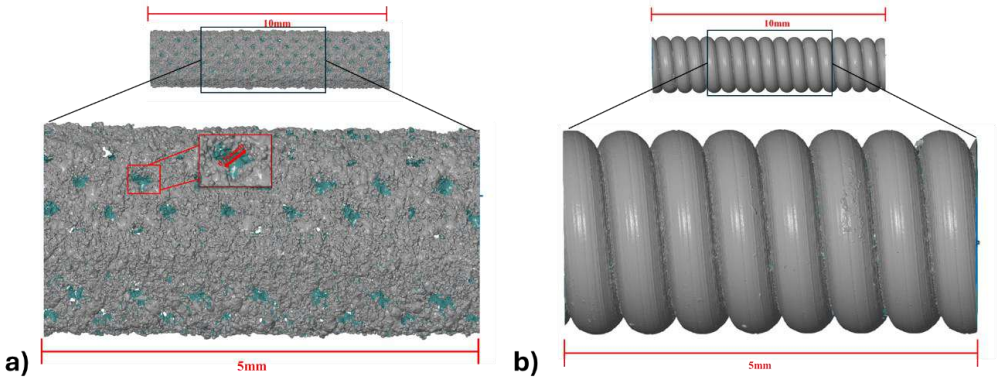


Figure VI 2 3D images of a) the AM-meshed, and b) Extr-coiled samples before immersion in AUS.

Figure VI 3 shows the development of the AM-meshes' corrosion layer over the course of the experiment. After 1 h in the dynamic system, a corrosion layer was already established, characterized by the accumulation of crystal-like structures. From 24 h on, the corrosion layer had a smoother aspect, although with the presence of some cracks. This smoothness could be related with the constant flow of AUS along the surface. It could also be seen that the corrosion layer grew until it accumulated and obstructed the free spaces in the mesh structure, as seen in the 5 days' time point. However, at days 6 and 7, the mesh structure was visible again, even though signs of severe corrosion were noticed. This was possibly because the corrosion layer was not fully dense and as the thickness increased, it detached from the surface and disintegrated.

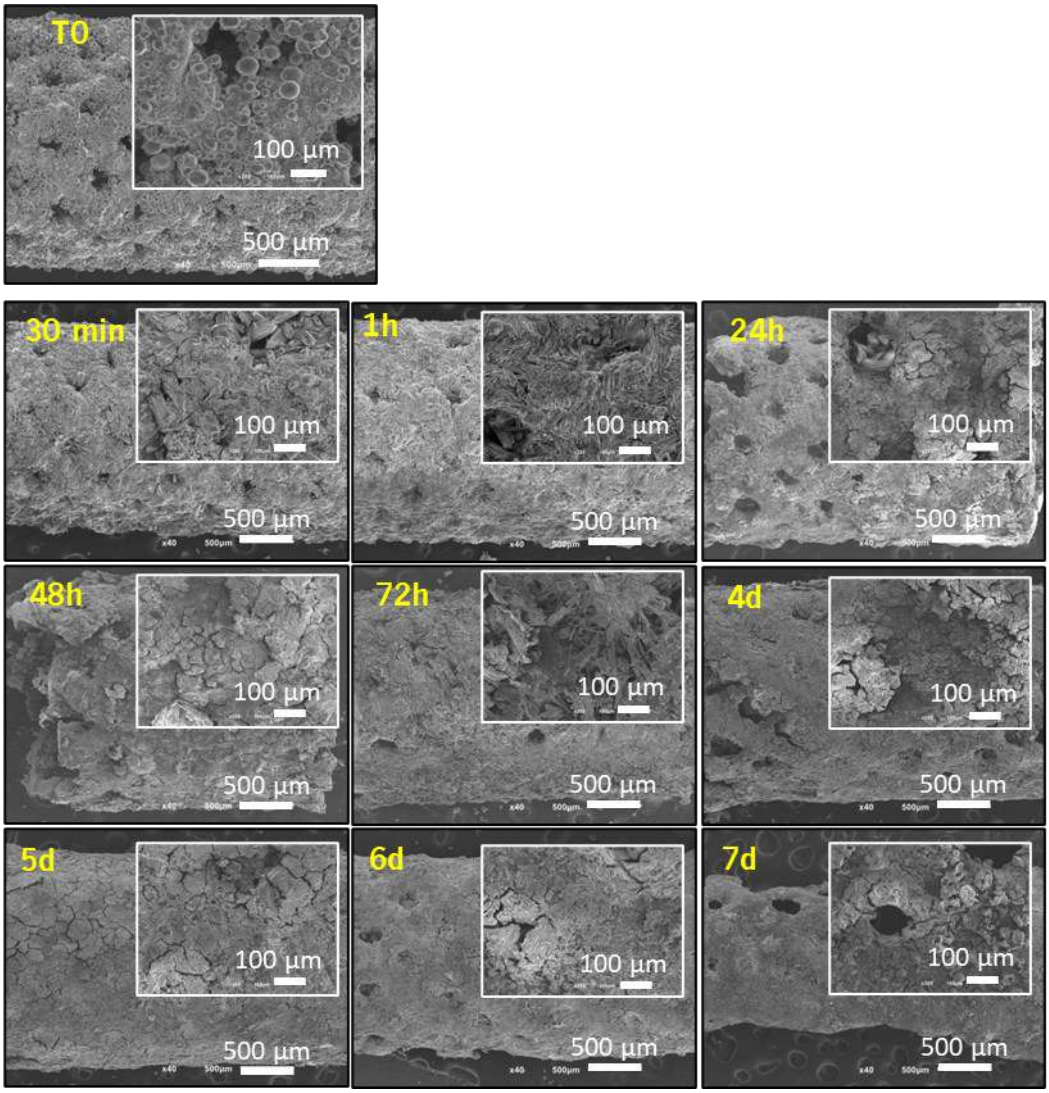


Figure VI 3 SEM of the AM-meshes' corrosion layer after incubation in the dynamic system with constant flow of artificial urine at different time points.

The corrosion layer on the Extr-coil tubes is presented in **Figure VI 4**. After 30 min in the dynamic system, the corrosion layer presented disorganized crystal-like structures and after 1 h it appeared more compact and with cracks. The corrosion layer accumulated preferentially in the spaces between each coil and in some cases, such as at 5 d, it was thick enough to cover the space between two consecutive coils, thereby demonstrating evidence of crevice corrosion.

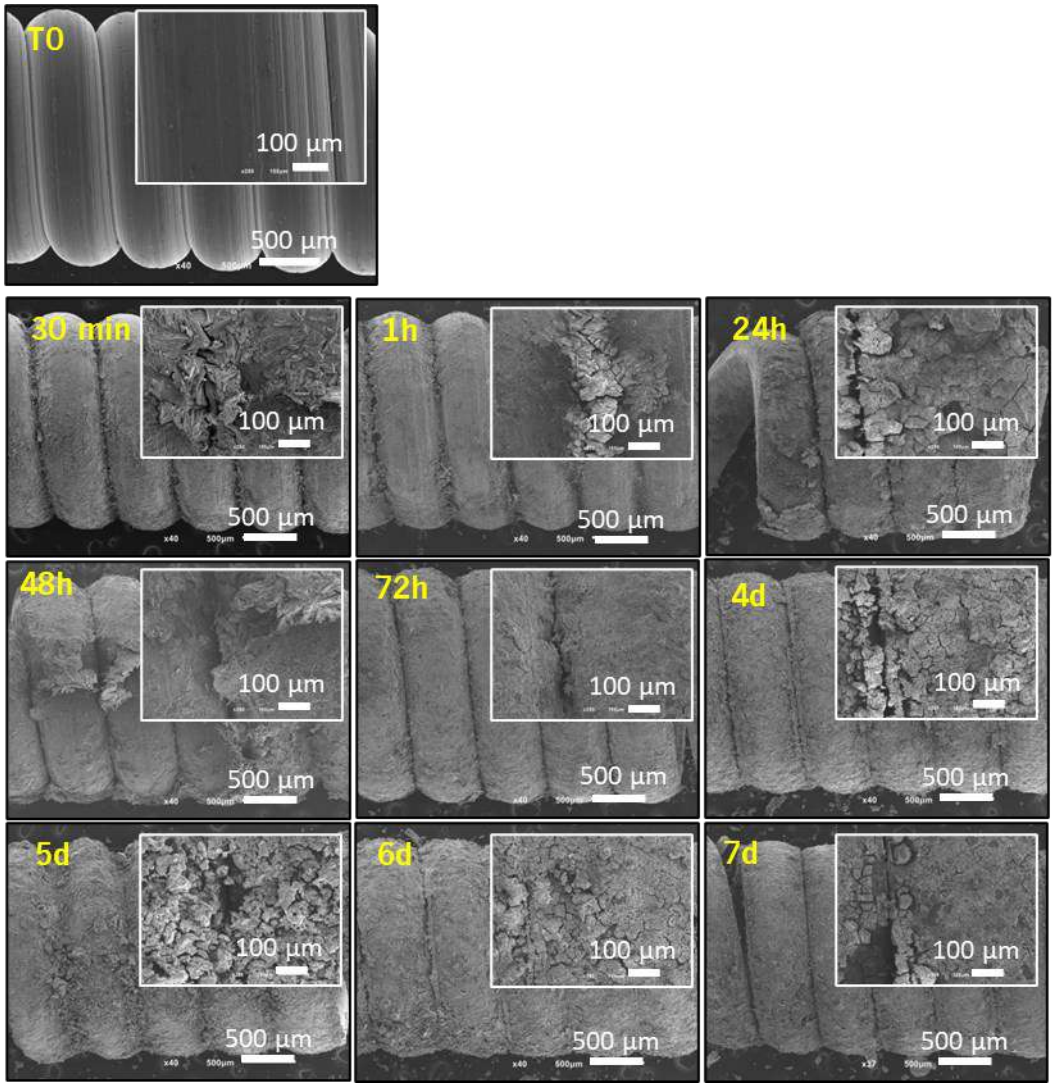


Figure VI 4 SEM of the coiled tubes' corrosion layer after incubation in the dynamic system with constant flow of artificial urine at different time points

Figure VI 5 summarizes the analysis of the chemical composition of the corrosion layer developed on AM-meshes and Extr-coil tubes after 7 d in the dynamic system with AUS. In **Figure VI 5 a), b) and c)**, the grey line represents the data for AM-meshes, while the blue line represents that for the Extr-coil tubes. The Raman spectra in **Figure VI 5 a)** shows no considerable variation in the measurements made within each sample, indicating a homogeneous chemical distribution of the corrosion layer. This analysis also revealed the presence of struvite and the typical $Mg(OH)_2$, on both samples.

In the XRD analysis (**Figure VI 5 b)**), the AM-meshes showed some additional peaks compared to the Extr-coil samples, related to the presence of struvite and $Mg(OH)_2$, which were the same as the ones detected through Raman spectroscopy. In the FTIR spectra both samples had mostly peaks associated with C-, N- and P- containing molecules. The subtle signal for the typical $Mg(OH)_2$ at 3696 cm^{-1} was detected for all the measurements(50). The bands detected around 3163 and 3488 cm^{-1} are attributed to O-H stretching and the peak observed at 867 cm^{-1} is attributed to CO_3^{2-}, associated to the apatite structure(50–52). The signals around 2366-2315 cm^{-1} and 1440-1463 cm^{-1} correspond to N-H stretching and NH^{3+} symmetrical bending, associated with the struvite molecule(53). The peak around 1000 cm^{-1} corresponds to the P-O link and at 760 cm^{-1} is the typical band of MgO(54). Finally, the EDS (**Figure 5 VI d)**) confirmed the previous analysis, O, Mg, P and C being the most abundant elements, and, interestingly, Y being one of the most abundant for AM-meshes but not for Extr-coil tubes. On the other hand, Na and Cl seemed to be present in higher amounts on Extr-coil tubes than on AM-meshes.

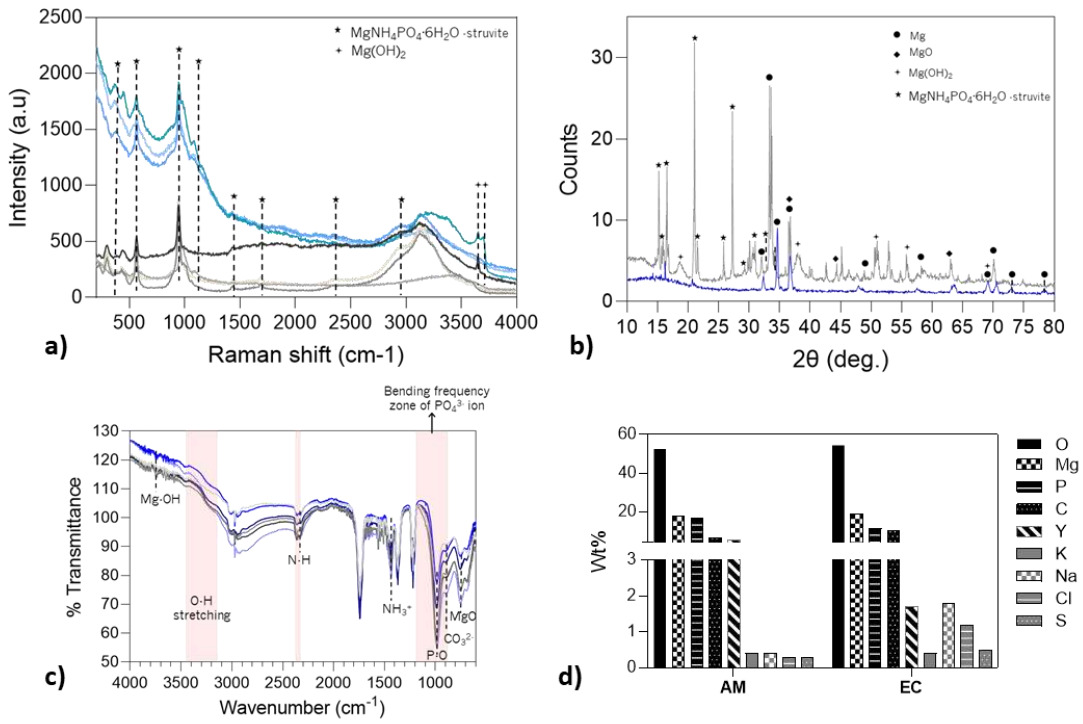


Figure VI 5 Chemical analysis of the corrosion layer developed on the samples surface after 7 days incubation in artificial urine in dynamic conditions. a) Raman, b) XRD, c) FTIR and d) EDS analysis. For a), b) and c), grey represents the AM-meshes and blue the Ext

The percentage of corrosion layer developed on the samples' surface along the time was estimated (**Figure VI 6 a)**). For the AM-meshes, most of the samples' weight after 7 days was corrosion layer, which is expected for a sample with a rapid corrosion.

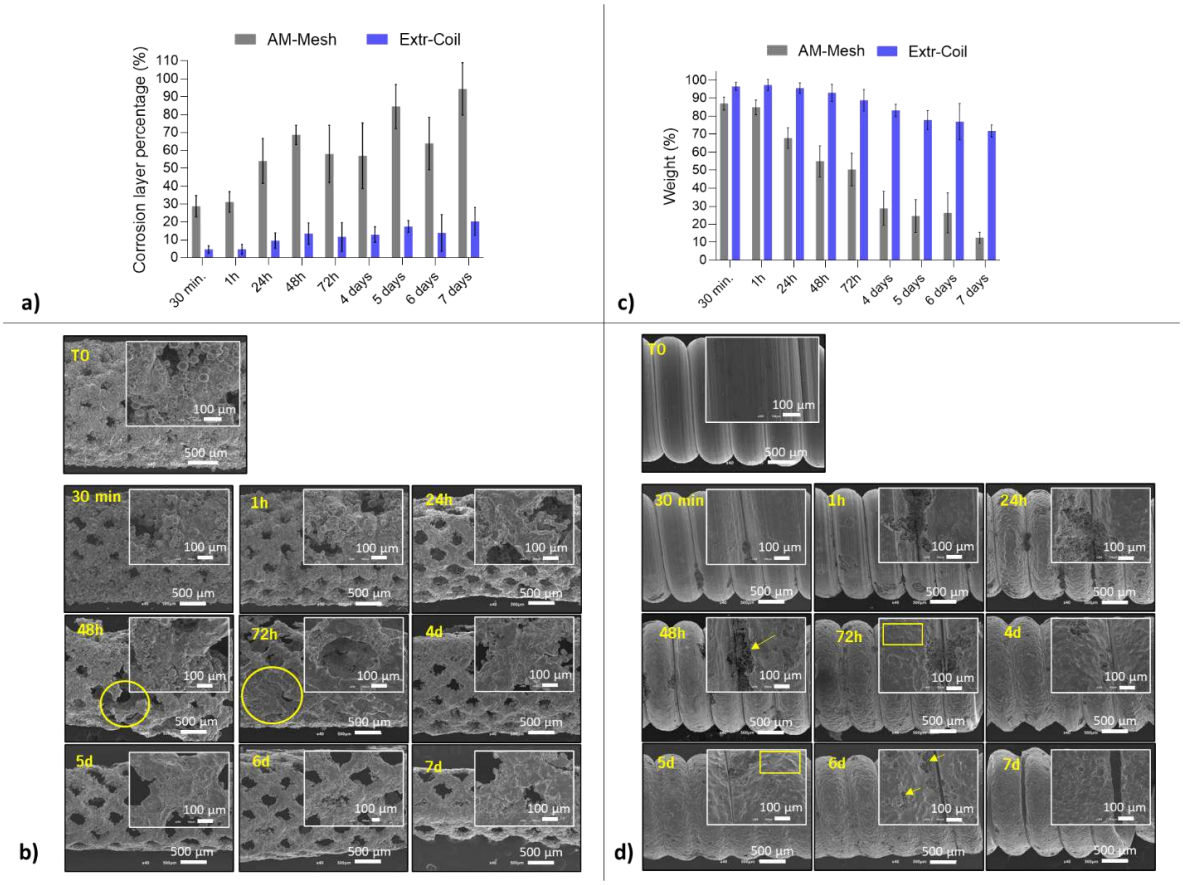


Figure VI 6 Sample's corrosion analysis after being in contact with AUS for 7 days in dynamic conditions. a) corrosion layer accumulated on the samples, in percentage, b) SEM images of the AM-meshes' corroded surfaces over time. The circles highlight material disintegration spots on AM-meshes, c) Relative weight of metallic stent (% of initial) after corrosion exposure and removing the corrosion products and d) SEM images of the Extr-coil samples' corroded surface over time. The rectangles highlight the shallow cavities and the arrows the spots of small corrosion pits accumulation.

VI-3.3. Corrosion characterization

To evaluate the corrosion, the samples' corrosion layer was removed by an etching solution according to ASTM G1-03(55). The exposed corroded surface was evaluated by SEM, and the loss of material was studied by analysis of the AUS samples through ICP-OES, weight loss calculation and µCT analysis.

After removing the corrosion products, the surface of the AM-meshes appeared relatively unaffected for the first hour, according to the electron micrographs in **Figure VI 6 b)**. The weight loss of over 10% within the first hour of exposure (according to **Figure VI 6 c)**) is probably masked by the

high surface roughness of as printed meshes, as evidenced by the partially melted powder particles on the surface (**Figure VI 6 b)**). After 24 h, the corrosion was already noticeable, given the smoother surface. From that time point the corrosion evolution was more prevalent, as extensive material loss occurred along the interconnected meshes, ultimately leading to material disintegration, as indicated (circles) in **Figure VI 6 b)**.

Regarding the Extr-coiled tubes, **Figure VI 6 d)** presents the SEM images of the corrosion over time. In the first hour, as expected, corrosion initiated particularly along crevices between the coils. After 1 h, corrosion marks started to be seen, as revealed by the surface roughness. At this point two types of corrosion were seen, most of the surface presents shallow cavities, characteristic of homogeneous alloy dissolution (**Figure VI 6 d)**, yellow rectangles), which were very similar to the results of a previous study, using the same wire without coiling in the as-extruded condition(8), while in some points localized corrosion took place and these large areas of localized corrosion were characterized by accumulated small corrosion pits (**Figure VI 6 d)**, yellow arrows).

The mass loss of the samples over time is presented in **Figure VI 6 c)**, as a percentage. There was a high loss of material for AM-meshes. After 30 min incubation, the AM samples' weight was already around 85 % of the original and after 3 days around 50 % of the sample was lost. The coiled sample, after 7 days, lost less than 30 %. These results are in agreement with the ones obtained for the percentage of corrosion layer over time (**Figure VI 6 a)**), as the fastest corroded sample develops a thicker corrosion layer.

AUS samples were collected every day of the experiment to assess the Mg and Y release over time (**Figure VI 7**). Confirming the previous results, ICP-OES data showed that AM tubes had a rapid degradation time, given the high release of Mg and Y from these samples. The maximum Mg release of Extr-coiled was right at the first contact of AUS with the metal, 0.196±0.0216 mg/L, and then 0.118±0.018 mg/L at 7d, while the maximum for AM-meshes was after 30 min, 0.398±0.096 mg/L, and 0.266±0.039 mg/L at 7d.

AUS samples were collected every day of the experiment to assess the Mg and Y release over time (**Figure VI 7**). Confirming the previous results, ICP-OES data showed that AM tubes had a rapid degradation time, given the high release of Mg and Y from these samples. The maximum Mg release of Extr-coiled was right at the first contact of AUS with the metal, 0.196±0.0216 mg/L, and then 0.118±0.018 mg/L at 7d, while the maximum for AM-meshes was after 30 min, 0.398±0.096 mg/L, and 0.266±0.039 mg/L at 7d.

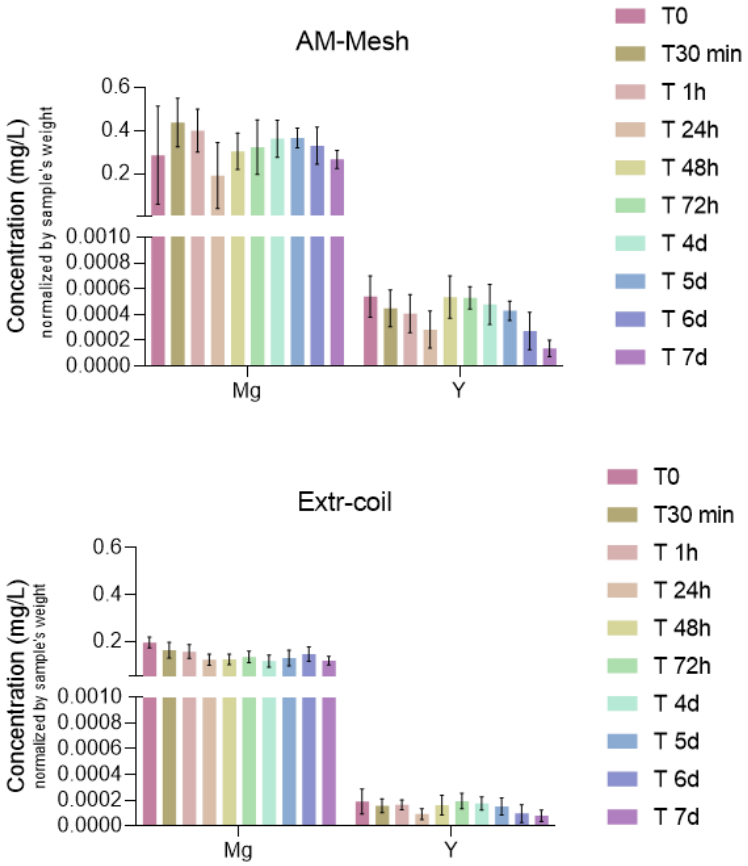


Figure VI 7 Concentrations of Mg and Y uncovered by ICP-OES in the artificial urine samples collected over time for AM-meshed tubes and the extruded coiled tubes.

To complement the corrosion results, µCT was done on the Extr-coil and AM-meshes before the experiment and at each time point (without corrosion layer). Obvious signs of corrosion were found on the AM-mesh at 48 h incubation (**Figure VI 8 e)**), where the wires of the network that form the meshed tube become thinner and in some places of the sample they were already completely degraded (see **Figure VI 8 e)**, yellow circle). In fact, from this time point, the amount of wires of the network that were totally degraded increased, and all from the same side of the tube, which can indicate that the flow of

AUS had a preferential path through the sample. After 7 days (**Figure VI 8 j)**), more than half of the sample was degraded.

It is possible to see that after 1 h, the Extr-coil tube already presented signs of corrosion (**Figure VI 8 m)**), especially between the coils (see the arrows in **Figure VI 8 m)**). After 72 h, we can notice that the Extr-coiled wires started to lose its rounded shape, which was more visible in one of the sides of the tube (**Figure VI 8 p)**). This can be due to the preferential AUS path along the sample. In fact, the way that AUS flows will have a significant impact on the way the samples corrode. Usually, in natural conditions, the flow of urine is not sufficient to cover all the stent surface equally. This was also true for this experiment, as a stream of artificial urine passes through the sample and will maintain that preferential continuous path over time. This causes part of the sample to be more attacked by the AUS flow than others. After 7 days with continuous AUS flow, it is possible to see that in some parts of the Extr-coiled tube, the space between consecutive turns increases.

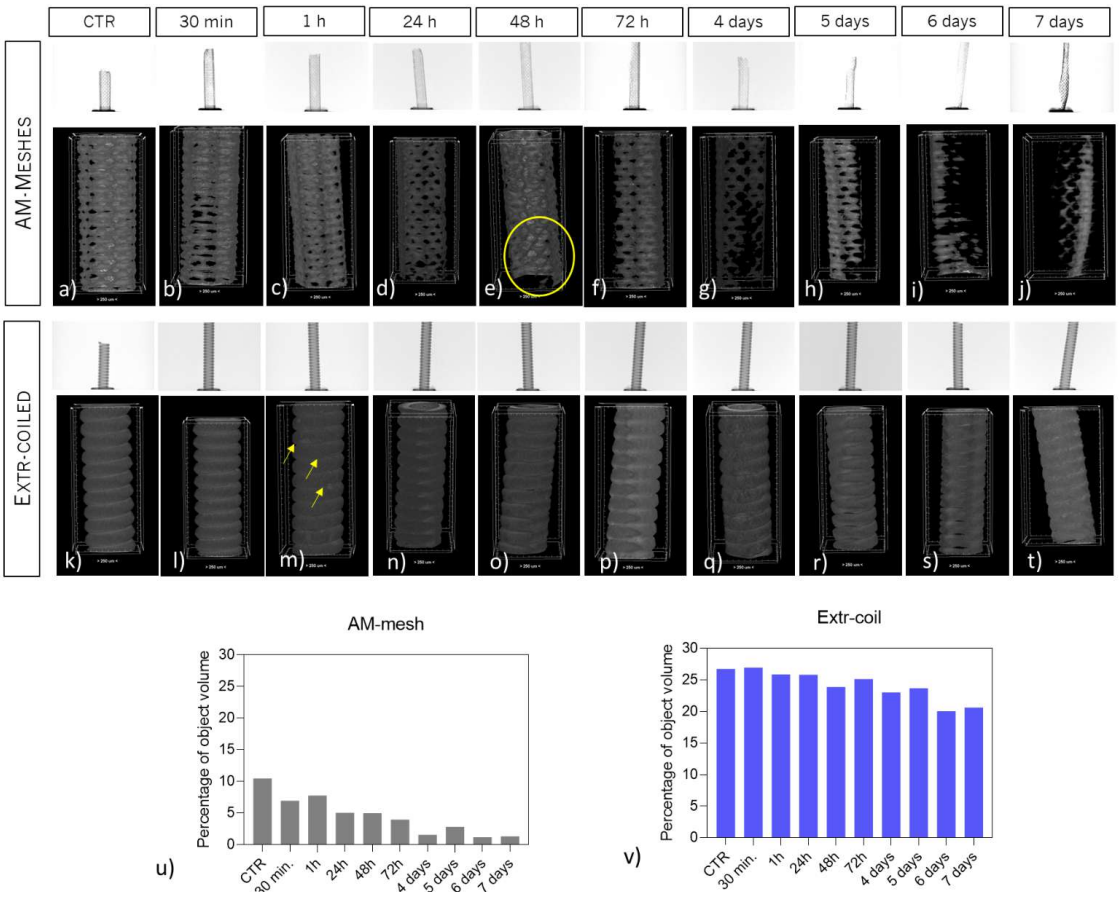


Figure VI 8 MicroCT scans of the AM-mesh and Extr-coil samples and corresponding remaining sample volume before the experiment and after incubation in dynamic conditions in AUS for defined time points (corrosion layer removed by chromic acid etching).

VI-3.4. Cytotoxicity

Figure VI 9 shows the resume of the MTS results and **Figure S VI 2 Supplementary information**, presents all the data obtained. The samples used for biological studies were tubes (not meshes) for AM samples (AM_Mg-1Y_t and AM_WE43_t) and extruded wires (non-coiled, e_Mg-1Y) for the extruded ones. This was done to avoid error associated with the calculation of exposed surface area of more complex geometries. The results are presented as percentage of living cells, taking the positive control (C+) as the reference of maximum viability (100 %). At 27.5 mm^2/ml exposed surface area, L929 cells seem to be more affected by than G/G, as for the former approximately 65% of the cells were alive with the direct extract (E100), whereas for the latter more than 70% of cells were alive with the direct extract (**Figure VI 9 a)**). e_Mg-1Y was more toxic for G/G cell line, compared with AM_Mg-1Y_t, since when in contact with the direct extract (E100) the cell viability was only around 30% (**Figure VI 9 a)**). With 75% extract, the viability of G/G increased to around 70% (**Figure S VI 2 Supplementary information**). AM_WE43_t appeared to be non-toxic for both cell lines (**Figure VI 9**).

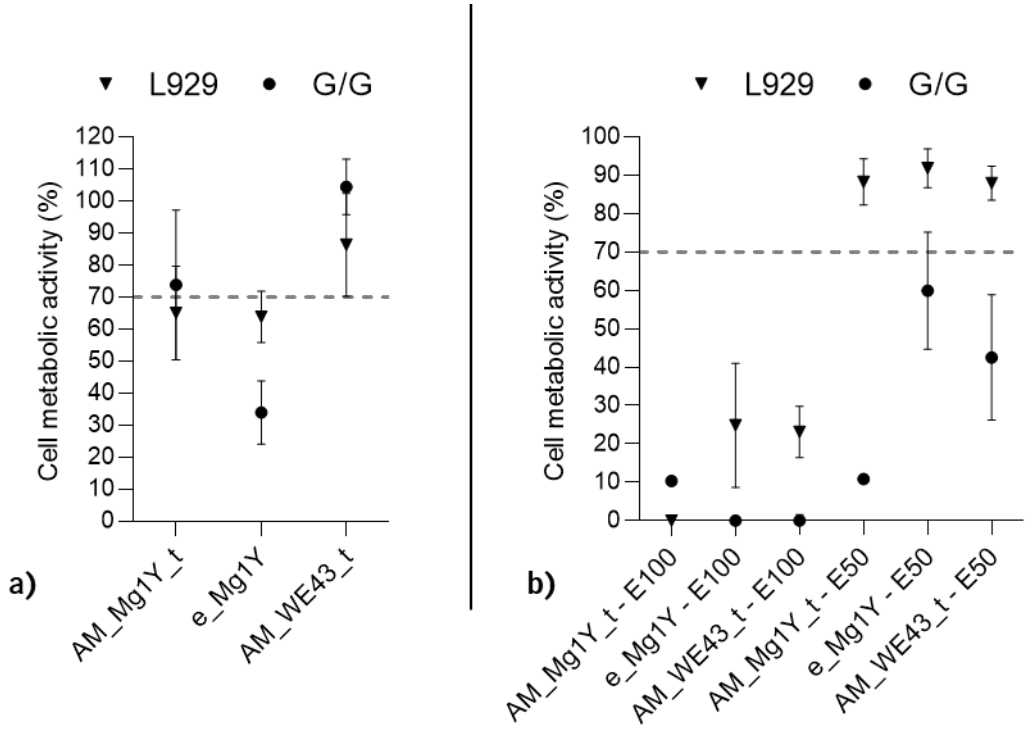


Figure VI 9 Cytotoxicity of AM_Mg-1Y_t, AM_WE43_t and e_Mg-1Y against L929 and G/G cell lines. a) shows the results of the direct extract and with a samples exposed surface area/ media volume ratio of 27.5 mm^2/ml and b) the direct (E100) and 50% (E50) extracts for a samples surface area/ volume ratio of 300 mm^2/ml. For this study the AM samples were in the form of tubes and the extruded ones in the form of extruded wire (not coiled). The standard deviation is presented.

To evaluate cell behavior in more extreme conditions, we followed the recommendation of the standard (ISO 10993-12), where the suggested ratio of exposed surface area/volume is 300 mm^2/ml. This is considered an extreme condition in our case since we have degradable materials, which is not taken into consideration by the standard. In these conditions, AM_Mg-1Y_t was much more toxic to G/G cell line than to L929 (**Supplementary information Figure S VI 2**). The extract was only acceptable for G/G cells when in 12.5 % concentration. e_Mg-1Y was not so toxic for cells as AM_Mg-1Y_t but was still more toxic to G/G cells (**Figure VI 9 b)** and **Supplementary information Figure S VI 2**). AM_WE43_t was also more toxic to G/G cells (**Figure 9 VI b)** and **Supplementary information Figure S VI 2**). Nitinol was used on these tests as control, given its widespread use in stents. This metal was also toxic for cells - with exception of G/G cells with AM-Mg-1Y_t experiments - despite being non-degradable (**Supplementary information Figure S VI 2**). Therefore, indeed the samples were toxic to the cell lines tested but only under extreme conditions, that do not directly translate to reality, where a constant flow of urine would avoid local metal ion accumulation. As a supplement to the MTS-based cytotoxicity test, we performed live/dead assay (see **Supplementary information Figure S VI 3**). The live/dead results were in accordance with the findings for MTS and, even though in some cases MTS test showed almost 0 % viability (translated by the cells metabolic activity), the live /dead test showed that there were some live cells in these conditions, e.g., for L929 E100 with AM_Mg-1Y_t and G/G E100 for AM_WE43_t. This may indicate that some cells were still alive even though their metabolic activity was affected.

To understand how the metals affect cell viability, one of the most influencing factors of metal corrosion on cells was studied, i.e. the alteration of cell media pH. We evaluated the pH change induced by the metal incubation (**Figure VI 10 a) and b)**). This was done for both ratios of exposed surface area/volume tested (27.5 and 300 mm^2/ml). With a ratio of 27.5 mm^2/ml, G/G media (used for G/G cells) presented a statistically significant increase when incubated with all stent prototypes. This increase was higher than the one recorded for DMEM (used for L929 cells) in the case of AM tubes, while for extruded wires and WE43, the increase was more significant for DMEM. For G/G cells, the lowest viability values were with e_Mg-1Y, even though that was not the metal that led to the highest pH value. For L929 cells, the lowest viability values were with AM_Mg-1Y_t and e_Mg-1Y, and those were in fact the metals that caused a higher pH increase.

Regarding the 300 mm^2/ml condition, the pH of both media (DMEM and G/G media) increased substantially, both being higher than 10. In both cases, the AM_Mg-1Y_t sample caused the highest pH

(almost 11). Interpretating these results in light of the cell viability ones, for G/G cells, AM_Mg-1Y_t indeed appeared to be the most toxic metal. For L929, AM_Mg-1Y_t also appeared to be slightly more toxic than the other two, although already at 50% dilution, no difference was found Both the metal release and pH increase may have led to a loss of cell viability. Nitinol did not cause a significant pH increase as its corrosion rate is lower and the formed surface layer stabilized the pH at lower values, even though it negatively affected the cells. Thus Nitinol did probably release elements, such as Ni, that were responsible for the cells' loss of viability(56).

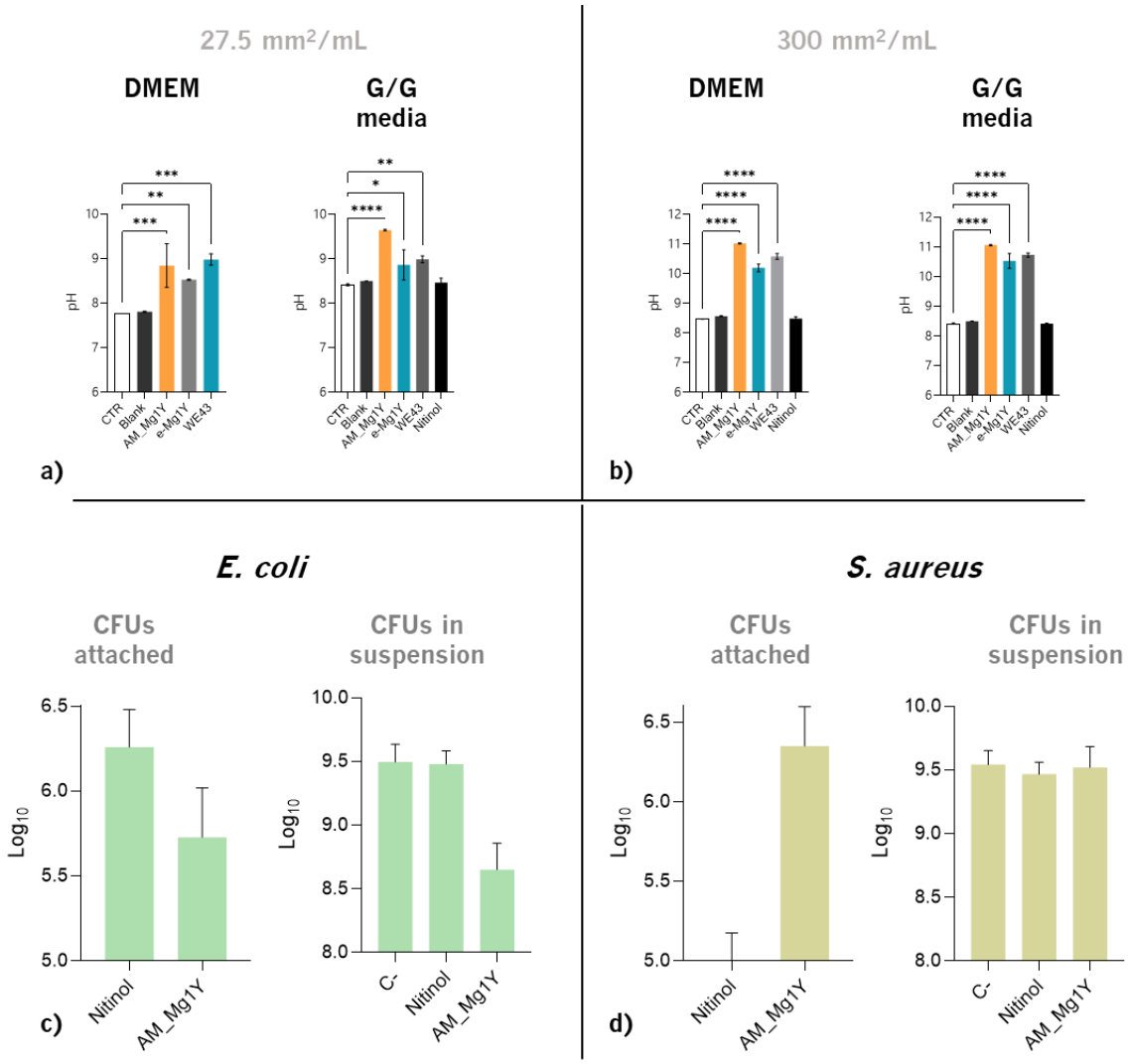


Figure VI 10 pH variation in the cell culture media used when exposed to the tested stent prototypes (AM_Mg-1Y_t, e_Mg-1Y and AM-WE43_t) with two exposed surface area/volume ratios, 27.5 mm²/ml and 300 mm²/ml and antibacterial activity of AM_Mg-1Y_t against *E. coli* and *S. aureus*.

VI-3.5. Antibacterial activity

Finally, we evaluated the possible antibacterial effect of AM_Mg-1Y_t against *E. coli* and *S. aureus*, common strains found in urinary tract infections32. We used a concentration of 27.5 mm^2/ml, which was considered non-toxic for cells in this study. The bacteria were placed in contact with the metals for 24 h and then the viability was evaluated by CFU counting. We assessed the CFUs attached to the samples' surface as well as the CFUs in suspension. Nitinol was used as control. AM_Mg-1Y_t was found to have an antibacterial effect against *E. coli* (**Figure VI 10 c)**). More cells attached to the Nitinol surface than on AM_Mg-1Y_t sample's and there were less CFUs in the media of the samples containing AM_Mg-1Y_t. These results indicated that the AM_Mg-1Y_t sample's surface was less prone to bacteria attachment than Nitinol and that the compounds released during corrosion also hamper *E. coli* growth. For *S. aureus*, no antibacterial effect was seen (**Figure VI 10 d)**). This strain had more ability to attach to the AM_Mg-1Y_t surface than on Nitinol's and the products released during AM_Mg-1Y_t corrosion did not impact the bacterial growth.

VI-4. Discussion

In this work, Mg-1Y-based tubes were successfully produced as simple representations of ureteral stent prototypes in the form of AM-meshes and Extr-coiled samples. This enabled an investigation of two different designs and manufacturing techniques for production of biodegradable metallic ureteral stents. The tubes' corrosion was studied in dynamic conditions with constant flow of fresh AUS, which is an in vitro close representation of the urinary tract. The cytotoxicity of the released corrosion components was studied with standard L929 cells as well as a urinary tract derived cell line, G/G, and the antibacterial potential of the AM tubes was also assessed using relevant bacterial strains. In summary, this study is a complete in vitro investigation on the functional performance of Mg-1Y based stent prototypes, bringing us closer to the development of a biodegradable metallic ureteral stent.

VI-4.1. Corrosion properties

The alloying of Mg with Y is considered a good strategy to improve the corrosion resistance of Mg, as has previously been verified by conventional manufacturing techniques(24–26), although some studies have showed the opposite(15,18,29,57). Indeed, corrosion of Mg alloys is highly dependent on the composition, microstructure, immersion fluid, sample surface conditions and experimental conditions (i.e., stagnant or dynamic)(8,15,18). Therefore, in this study the corrosion behavior was explored in vitro of ureteral stent prototypes of the same base material but produced through different manufacturing

techniques. This way, the properties of each of them were addressed and their individual suitability for ureteral stents was investigated.

The Mg corrosion improvement conferred by the addition of Y is related to the high affinity of Y to oxygen, compared to Mg, which results in the rapid formation of an oxide surface film composed of O and Y (Y2O3)(26). The existence of dissolved Y in the Mg matrix hence typically contributes to a better corrosion protection. In AM, the feedstock material is in the form of powder and upon contact with air, the powder surface will be covered by an oxide layer, which in this case would be MgO and Y_2O_3. Indeed, in a previous work where the same powder as the one used here was characterized, EDS results revealed that the powder surface is composed of Mg, Y and O, confirming that an oxide layer including these elements is covering the powder particles(40). During the printing process, the oxide shells of the particles are disrupted by the thermal expansion and partial evaporation of Mg. These oxides do not melt as their melting point is too high (around 2438 °C), which would lead to excessive evaporation of Mg during the process, as its boiling point is much lower (1091°C)(57). The oxides will hence end up being dispersed in the matrix and not dissolved. Bär et al. have hypothesized a similar event in their studies, where the microstructure of PBF-LB and cast WE43 was described in detail(57). The authors concluded that most of the Y in the PBF-LB-fabricated samples is in the form of oxides (due to the already oxidized surface of the powder), contrasting the cast samples that presented a higher Y concentration dissolved in the Mg matrix. In the present work, the amount of Y was low (around 1%), and it is likely that much of it is in the form of dispersed oxides and not dissolved in the Mg matrix, thus, not conferring the expected corrosion protection.

In this study, the corrosion data revealed that AM-meshes degraded too fast, considering the average indwelling time of ureteral stents (2 – 6 months). This can be related not only with the structure design but also the manufacturing technique,. The AM-meshes presented a larger surface area compared with the Extr-coiled sample, which may also have been a significant accelerator of corrosion. The Extr-coiled samples may had an adequate degradation time since they maintained the tubular structure during the 7 days tested, however, areas of preferential crevice corrosion due to the coiling were present, indicating that those points would lead to stent failure (break), thereby highlighting the importance of selecting the adequate stent design as well as the most adequate manufacturing method when developing biodegradable urinary devices..

Analysis of composition along the corrosion layer of the samples was also carried out. Similar elements were revealed for both geometries, which was expected given the same base Mg alloy

composition, as well as the same corrosion medium (AUS), and testing conditions. However, the amount of some elements was slightly different. This included Y (see EDS analysis on **Figure VI 5 d)**), which was found at high concentrations in the corrosion layer of AM-meshed tubes but not in that for Extr-coils. Moreover, Na and Cl- were present in higher amounts in the corrosion layer for Extr-coils than in that of the AM-meshed tubes. This can be related to differences in microstructure, particularly since different feedstock materials were used. In the case of AM-meshes, the powder feedstock likely contained a high content of Y2O3 present along the surface of the powder particles. Moreover, given the low content of Y in the base alloy (1%), it is probable that most of the Y was present as Y2O3, leaving little Y solute within the Mg matrix. Hence during corrosion, it is likely that such oxides did not dissolve, resulting in a Y-enriched corrosion layer for the AM-meshed tubes. This indicated that even though samples have similar base composition, the different corrosion pattern (given the different manufacturing techniques and geometries) will lead to a slightly different corrosion layer, which in turn will directly impact the surface protection against the surrounding media, and thus, corrosion.

Despite the fast degradation, localized corrosion was not visible on the AM samples, although one side of the tube degraded faster than the other. This, however, seems to not be related with the sample's structure itself but rather with the way AUS flows through the samples. As briefly mentioned in the results section, the AUS flow is not enough for the tube to be completely immersed in AUS all the time, which means that the sample is only partially exposed to the AUS. However, this AUS flow rate was selected based on previous studies and on the normal amount of urine production(58,59). Therefore, the part of the sample through which the AUS flow passes mostly will degrade faster. The AM-meshed samples' surface was also very rough due to non-melted powder particles. This factor may as well influence the corrosion, so future work should include post process treatments to improve the surface smoothness and evaluate the impact on corrosion. The rate of corrosion for the Extr-coiled sample seems to be more adequate but localized corrosion was present. For this study a thinner extruded wire, with similar chemical composition and same process setup, was used as that in a previous study from the authors, where the corrosion of Mg-based extruded wires was investigated under the same dynamic conditions(8). In that study, the Mg-1Y was the wire with the better corrosion profile given its homogeneous corrosion. In the present study, the same extruded wire was used to produce the coiled tubes, the only difference was that this wire had a smaller diameter. The coiling process may be a determinant factor for the appearance of localized corrosion due to the plastic deformation that may lead to surface layer rupture and a higher propensity for localized corrosion. Additionally, localized corrosion was primarily limited to the spaces between two consecutive coils, which likely inhibited fluid flow in these

confined spaces, thereby allowing for extensive build-up of the corrosion products over time, that could not be easily washed away with the AUS flow. Therefore, even though the localized corrosion appearance may be also related with the coiling process, the fluid flow may also have had a significant influence. These results revealed that the fluid flow on the stent's surface will also dictate the corrosion pattern, thus having a direct effect on the efficiency of the stent drainage. The extruded Mg-1Y wire hence still seems to be a good option as base material for ureteral stent development, but improvement of the wire coiling process and coiling structure is necessary.

VI-4.2. Cytotoxicity evaluation

Cytotoxicity evaluation assays should represent the real environment to as large extent as possible and be standardized so that different studies with different biomaterials and cells could be compared. However, for biodegradable metals and specifically for the urinary tract, there is currently no standard available. In our work, the objective was to fabricate a non-expandable biodegradable metallic ureteral stent, so the urothelium cells will not be constantly touching the stent, given the constant peristaltic movements and continuous urine passage, but they would constantly be exposed to the metal corrosion products released. So, as a first approach for cytotoxicity evaluation of the ureteral stent prototypes, and to best simulate the real conditions, we performed an indirect test where the cells were exposed to metal extracts. The chosen cell lines were the standard L929(60) and a cell line isolated from mouse bladder, G/G cell line. Two different concentrations were used, since there is not a recommended specific value for these kinds of studies. First, 27.5 mm^2/ml and then 300 mm^2/ml was used, following the recommendations of the ISO 10992-12 (for non-degradable material). At the low concentration, AM_Mg-1Y_t led to a decrease in cell viability to 60-70 % for L929 and to 70-80 % for the G/G cell line, with the most concentrated extract (100 %). e_Mg-1Y samples were more toxic to G/G cell lines compared with AM samples, leading to a decrease of cell viability to 30 % with the direct extract. L929 were more sensitive to AM_Mg-1Y_t and AM_WE43_t. Considering the ISO 10993-5(60), if the cell viability is more than 70 % with the undiluted extract (100 %), it should be considered that the sample is non-toxic, i.e. the AM samples could be considered toxic to L929 but not to G/G and extruded samples were toxic to both cell lines, at these specific metal concentrations. This can be explained by several factors. First, the culture media is different for the two cell lines, so the samples may degrade differently, which can justify the variation in toxicity of the AM samples to the different cell lines. The cells themselves may have different responses to the alloy's extracts, and the amount of corrosion products released may vary, given the distinct corrosion profile of each sample, likely attributed to the different manufacturing methods. These factors may in turn, influence the cell viability differently. At the higher concentration of 300 mm^2/ml,

AM_Mg-1Y_t' direct extract was toxic to the L929 cells, but already at 50% concentration, the cell viability was around 80 %. This was not observed for the G/G cell lines, where a high toxicity was seen also for the 25 % extract. Only the 12.5 % AM_Mg-1Y_t' extract was non-toxic to these cells. For e_Mg-1Y samples, the 50 % concentration resulted in around 90 % L929 viability, while for G/G at 50 % extract the viability was around 60 %. Only at 25 % extract the G/G cell viability was more than 70 %. The AM_WE43_t results were very similar to those obtained for e_Mg-1Y samples. These results indicate that AM_Mg-1Y_t are more toxic to G/G cell lines than AM_WE43_t or e_Mg-1Y samples.

Measurements of pH were also maintained to understand the effect of alkalinity on the cell lines. For 300 mm^2/ml, a more alkaline pH was induced by AM_Mg-1Y_t, which suggests that pH may have been influential in causing cell damage. However, at low metal concentrations (27.5 mm^2/ml), the increase of pH in media for G/G cell lines induced by AM_Mg-1Y_t was slightly higher than the increase induced by e_Mg_1Y or AM_WE43_t. Nevertheless, at these low metal concentrations, the samples that led to higher toxicity to G/G were the e_Mg-1Y_t ones. Hence, it seems that the difference in alkalinity given by the different samples was not sufficient to impact the cell viability. In this case, other factors may be leading to cytotoxicity, such as excessive concentration of Mg2+ ions(61). For higher concentrations of extract (300 mm^2/ml), all the prototype stents induced a considerable increase in the media pH, but AM_Mg-1Y_t gave the highest. These results are in accordance with those of corrosion, where we found that AM-meshes samples degrade considerably faster than Extr-coiled ones. If the samples corrode faster, the corrosion products released to the media, namely OH- ions, will be higher, promoting a fast pH increase(18,19).

The lack of standardization of cytotoxicity assays of biodegradable metals for urinary applications makes the comparison of different works difficult, but some aspects can help understanding the results. Tian et al have studied three culture methods to represent the interaction of human urothelial cells (HUCs) with Mg-based stents (Mg-4Y, AZ31 and pure Mg), and found that the different culture methods lead to different cell responses(18). This study also involved an exploration of the impact of the media pH on the HUCs growth and it was found that at a certain pH (8.6), the cell density considerably decreased and at higher pH (9), the cells had a round shape, indicative of the severity of the damage the high pH was creating. Here, we could see that a higher pH than 9 was obtained, which can be one main reason for cell toxicity. It should also be kept in mind that other components released during the corrosion will contribute to a harsh local environment that may be unfavorable to the cells6. Mg2+ for example can

cause the depolarization of the cell membrane if the concentration is too high (more than 10 mM in a previous study)(18).

The deviation of the test conditions from actual in vivo conditions should also be taken into account. In the ureter, the urine will be constantly flowing and dragging away the released corrosion products, i.e. the metal will not be confined to a specific volume, as in the cytotoxicity studies. We believe that in vivo the increase in the local pH will not be as high due to the constant urine flow, so it is likely that the metals will be non-toxic from this aspect. Indeed, at the high metal surface area/media volume ratio, even the non-degradable, biocompatible Nitinol caused cell death. Nitinol is known as a biocompatible material and largely used for stent development(62,63).

The cell responses obtained in this study also highlight that the fabrication method and sample corrosion time will impact the biocompatibility of the stent, despite the utilization of the same base material and the same environmental conditions.

VI-4.3. Antibacterial properties

USATI are very common in stented patients and one of the reasons for stent failure, stent associated pain and increased treatment time(2). For this reason, a large portion of research on ureteral stents has focused on avoiding bacterial contamination(29,64). In this work, we evaluated the antibacterial properties of the additively manufactured Mg-1Y, given the antibacterial properties associated with Mg and the alloyed MgY(17,29). One of the first works reporting the use of Mg alloys for urinary stent application was the work by Lock et al, where the antibacterial potential of Mg-4Y, AZ31 (Mg–3wt% Al-1wt% Zn) and pure Mg against *E. coli* was explored(29). Herein, the AM_Mg-1Y_t samples were selected based on the previous cytotoxicity results, where at low concentrations (27.5 mm^2/ml), these samples showed no toxicity for the bladder derived cell line (G/G). For the bacterial assays we used the same exposed sample surface area/volume ratio and two of the most common strains found in urinary tract infections, *E. coli* and *S. aureus*, representing Gram negative and Gram positive bacteria, respectively(2). The AM_Mg-1Y_t samples showed antibacterial activity against *E. coli*, both by the release of corrosion products to the cell media, given the lowest CFUs formed in suspension compared with control and Nitinol, and by the surface corrosion activity, that was more efficient in avoiding bacteria attachment, compared with Nitinol. On the other hand, the same was not true for *S. aureus*. This strain was more efficient in attaching to the AM_Mg-1Y_t surface than on Nitinol and it grew normally in the presence of AM_Mg-1Y_t samples' corrosion products. The antibacterial activity associated with Mg is reported to be associated with its corrosion activity, specifically the high alkalinity promoted by the release

of OH- and the release of Mg^{2+}ions(17,31). For *E.coli*, one possible mechanism leading to its sensitivity to Mg corrosion products is the high amounts of H^+ that these bacteria cells produce to neutralize the formation of OH^- during Mg corrosion, which results in damage of the proton electrochemical gradient in the intermembrane space of bacteria(17). Besides, release of high concentrations of Mg^{2+} can also compromise the bacteria viability, whereby the osmotic stress generated leads to bacteria death. In the case of Mg corrosion, both events occur simultaneously, i.e. the pH increase and the Mg^{2+} ion release, so the bacteria killing mechanisms are more efficient, since one potentiates the other(31). In this study, it is possible that the phenomenon behind the antibacterial activity against *E.coli* is related with both events, since the AM_Mg-1Y_t samples have a fast corrosion, liberating OH- and Mg2+ ions in high quantities, which is sufficient to cause *E. coli* cell death or compromised cell growth. The *S. aureus* strain seems to be more resistant to these conditions, which can be related with the cell wall structure. Gram-positive and Gram-negative bacteria differ mostly on their cell wall structure; while Gram-negative bacteria have a thin peptidoglycan layer separating the cytoplasmatic membrane from the outer cell membrane, the Gram-positive bacteria present a thick peptidoglycan layer covering the cytoplasmic membrane, and does not present an outer cell membrane. This different cell wall structure is in some cases the reason for the different sensitivities of bacteria to antibiotic agents(30). An additional antibacterial coating covering a wider bacterial spectrum can be considered in future studies(65).

Overall, this study indicated that AM_Mg-1Y_t samples can be non-toxic to cells and also antibacterial against specific strains, which is a very good characteristic for ureteral stents. The fast corrosion and rough surface are, however, aspects that must be improved, through stent design and/or alloy development and surface treatments. Nevertheless, we must bear in mind that improving corrosion resistance, means a reduction in the released corrosion products (the antibacterial ions OH^- and Mg^{2+}), so this can decrease the antibacterial potential. However, it is known that even a slow corrosion means constant OH^- and Mg^{2+} release at the sample's surface, so while a slow corrosion may not contribute to an antibacterial activity in the environment surrounding the sample it could at least do so at the surface, indicating that biofilm formation, which is one of the most problematic events in urinary infections, can become compromised(31). This antibacterial potential can contribute to a general reduction of antibiotic administration. On the other side, the Extr-coiled samples seem to have a more adequate degradation time for ureteral stent applications due to the shape maintenance over time, despite the events of localized corrosion that must be avoided to prevent stent failure. Additionally, Extr-coiled samples showed some toxicity against urinary tract derived cells, which should be investigated in further studies.

Overall, the development of a biodegradable metallic ureteral stent is a complex process given the large number of factors that influence the corrosion and subsequent stent performance and biological interaction. Thus, the ideal biodegradable ureteral stent would provide an efficient drainage for at least 2-3 months, not cause any harm to the urinary tract and be resistant to biofilm development. This is a substantial challenge, especially in the urinary tract, which is a harsh environment and with a constantly changing fluid composition, volume and flow rate. Notwithstanding, this study provided a complete evaluation of the performance of two ureteral stent candidates and an understanding of their corrosion patterns, cytocompatibility, and possible antibacterial activity, thereby advancing the development of a biodegradable metallic ureteral stent toward clinical reality.

VI-4.4. Limitations

Besides further work needed on the material and designs, this study had some limitations related to the experimental set-up, namely the use of AUS to eliminate the random variation of human urine, the use of representative stent parts rather than and full length stents, and the non-consideration of the peristaltic movements, that will considerably affect the stent corrosion. Therefore, in further studies using a full length stent and human urine pools may be considered, as well as using an intermittent fluid flow to better mimic the natural conditions and, finally, in vivo experiments may be performed.

VI-5. Conclusion

In this work we successfully produced two MgY based ureteral stent prototypes, through PBF-LB (AM-meshes) and extruded coiled wires (Extr-coiled). The AM-meshes degraded considerably faster and especially one side of the sample, due to the non-homogeneous fluid flow, indicating an early loss of efficiency. Extr-coiled samples showed localized corrosion, especially in the sites between two consecutive coils, probably due to a poorer fluid flow and due to the coiled structure itself, but a slower overall corrosion rate. The AUS flow was a determinant factor on the samples' corrosion and further studies should be conducted on this topic.

At low metal concentrations, AM-meshes did not show toxicity against L929 or G/G cell lines. The Extr-coiled samples presented toxicity, and especially against the G/G cell line. While AM-meshes did not show antibacterial activity against *S. aureus*, it showed antibacterial effects against one of the other most common strains found in stent-related urinary tract infections, *E. coli*.

Altogether, this study gave important details on the corrosion patterns of two biodegradable metallic ureteral stent candidates produced by two different methods, as well as their respective cytotoxicity and antibacterial activity.

VI-6. BIBLIOGRAPHY

1. Soria F, Rako D, Graaf P de. Urinary Stents. Soria F, Rako D, de Graaf P, editors. Cham: Springer International Publishing; 2022.

2. Pérez-Fentes D, Aranda-Pérez J, de la Cruz JE, Soria F. Indications, Complications and Side Effects of Ureteral Stents. In: Urinary Stents. Cham: Springer International Publishing; 2022. p. 5–20.

3. Wang X, Ji Z, Yang P, Li J, Tian Y. Forgotten ureteral stents: a systematic review of literature. BMC Urol. 2024 Mar 5;24(1):52.

4. Lombardo R, Guidotti A, Turchi B, Nacchia A, Santoro G, Romagnoli M, et al. Trends and incidence of reported events associated with ureteral stents: an analysis of the food and drug administration's manufacturer and user facility device experience (MAUDE) database. World J Urol. 2024 Sep 14;42(1):524.

5. Pacheco M, Silva JM, Aroso IM, Lima E, Barros AA, Reis RL. Biomaterials for Ureteral Stents: Advances and Future Perspectives. In: Urinary Stents. Cham: Springer International Publishing; 2022. p. 197–208.

6. Tian Q, Zhang C, Deo M, Rivera-Castaneda L, Masoudipour N, Guan R, et al. Responses of human urothelial cells to magnesium-zinc-strontium alloys and associated insoluble degradation products for urological stent applications. Mater Sci Eng C. 2019 Mar;96:248–62.

7. Tie D, Liu H, Guan R, Holt-Torres P, Liu Y, Wang Y, et al. In vivo assessment of biodegradable magnesium alloy ureteral stents in a pig model. Acta Biomater. 2020 Oct;116:415–25.

8. Pacheco M, Aroso IM, Silva JM, Lamaka S V., Bohlen J, Nienaber M, et al. Understanding the corrosion of Mg alloys in in vitro urinary tract conditions: A step forward towards a biodegradable metallic ureteral stent. J Magnes Alloy. 2023 Dec;

9. Mei D, Wang C, Nienaber M, Pacheco M, Barros A, Neves S, et al. Corrosion behavior of Mg wires for ureteral stent in artificial urine solution. Corros Sci. 2021 Aug;189:109567.

10. Rola P, Włodarczak S, Doroszko A, Lesiak M, Włodarczak A. The bioresorbable magnesium scaffold (Magmaris)—State of the art: From basic concept to clinical application. Catheter Cardiovasc Interv. 2022 Nov 13;100(6):1051–8.

11. Seitz J-M, Lucas A, Kirschner M. Magnesium-Based Compression Screws: A Novelty in the Clinical Use of Implants. JOM. 2016 Apr 7;68(4):1177–82.

12. Shin WJ, Chung YW, Kim S Do, An K-Y. Additional fixation using a metal plate with bioresorbable screws and wires for robinson type 2B clavicle fracture. Clin Shoulder Elb. 2020 Dec 1;23(4):205–9.

13. Waizy H, Diekmann J, Weizbauer A, Reifenrath J, Bartsch I, Neubert V, et al. In vivo study of a biodegradable orthopedic screw (MgYREZr-alloy) in a rabbit model for up to 12 months. J Biomater Appl. 2014 Jan 3;28(5):667–75.

14. Windhagen H, Radtke K, Weizbauer A, Diekmann J, Noll Y, Kreimeyer U, et al. Biodegradable magnesium-based screw clinically equivalent to titanium screw in hallux valgus surgery: short term results

of the first prospective, randomized, controlled clinical pilot study. Biomed Eng Online. 2013 Dec 3;12(1):62.

15. Johnson I, Liu H. A Study on Factors Affecting the Degradation of Magnesium and a Magnesium-Yttrium Alloy for Biomedical Applications. PLoS One. 2013;8(6).

16. Liu C, Ren Z, Xu Y, Pang S, Zhao X, Zhao Y. Biodegradable Magnesium Alloys Developed as Bone Repair Materials: A Review. Scanning. 2018;2018(1).

17. Lin Z, Sun X, Yang H. The Role of Antibacterial Metallic Elements in Simultaneously Improving the Corrosion Resistance and Antibacterial Activity of Magnesium Alloys. Mater Des. 2021 Jan;198:109350.

18. Tian Q, Deo M, Rivera-Castaneda L, Liu H. Cytocompatibility of Magnesium Alloys with Human Urothelial Cells: A Comparison of Three Culture Methodologies. ACS Biomater Sci Eng. 2016 Sep 12;2(9):1559–71.

19. Kim J, Pan H. Effects of Magnesium Alloy Corrosion on Biological Response- Perspectives of Metal-Cell Interaction. Prog Mater Sci. 2022 Nov;101039.

20. Paramitha D, Chabaud S, Bolduc S, Hermawan H. Biological Assessment of Zn–Based Absorbable Metals for Ureteral Stent Applications. Materials (Basel). 2019 Oct 12;12(20):3325.

21. Lin G, Chen M, Zhao Y, Sasikumar Y, Tie D. The Mechanical Properties and Corrosion Resistance of Magnesium Alloys with Different Alloying Elements for Bone Repair. Crystals. 2018 Jun 28;8(7):271.

22. Xie J, Zhang J, You Z, Liu S, Guan K, Wu R, et al. Towards developing Mg alloys with simultaneously improved strength and corrosion resistance via RE alloying. J Magnes Alloy. 2021 Jan;9(1):41–56.

23. Liu X, Shan D, Song Y, Han E. Influence of yttrium element on the corrosion behaviors of Mg–Y binary magnesium alloy. J Magnes Alloy. 2017 Mar;5(1):26–34.

24. Li J, Chen Z, Jing J, Hou J. Effect of yttrium modification on the corrosion behavior of AZ63 magnesium alloy in sodium chloride solution. J Magnes Alloy. 2021 Mar;9(2):613–26.

25. He W, Zhang E, Yang K. Effect of Y on the bio-corrosion behavior of extruded Mg–Zn–Mn alloy in Hank's solution. Mater Sci Eng C. 2010 Jan;30(1):167–74.

26. Hanzi A, Gunde P, Schinhammer M, Uggowitzer P. On the biodegradation performance of an Mg–Y–RE alloy with various surface conditions in simulated body fluid. Acta Biomater. 2009 Jan;5(1):162–71.

27. Johnson I, Liu H. A Study on Factors Affecting the Degradation of Magnesium and a Magnesium-Yttrium Alloy for Biomedical Applications. Zheng J, editor. PLoS One. 2013 Jun 14;8(6):e65603.

28. Sharma SK, Saxena KK, Malik V, Mohammed KA, Prakash C, Buddhi D, et al. Significance of Alloying Elements on the Mechanical Characteristics of Mg-Based Materials for Biomedical Applications. Crystals. 2022 Aug 12;12(8):1138.

29. Lock JY, Wyatt E, Upadhyayula S, Whall A, Nuñez V, Vullev VI, et al. Degradation and antibacterial properties of magnesium alloys in artificial urine for potential resorbable ureteral stent applications. J Biomed Mater Res Part A. 2014 Mar;102(3):781–92.

30. Nguyen N-YT, Grelling N, Wetteland CL, Rosario R, Liu H. Antimicrobial Activities and Mechanisms of Magnesium Oxide Nanoparticles (nMgO) against Pathogenic Bacteria, Yeasts, and Biofilms. Sci Rep. 2018 Nov 2;8(1):16260.

31. Feng H, Wang G, Jin W, Zhang X, Huang Y, Gao A, et al. Systematic Study of Inherent Antibacterial Properties of Magnesium-based Biomaterials. ACS Appl Mater Interfaces. 2016 Apr 20;8(15):9662–73.

32. Domingues B, Pacheco M, Cruz JE, Carmagnola I, Teixeira - Santos R, Laurenti M, et al. Future Directions for Ureteral Stent Technology: From Bench to the Market. Adv Ther. 2022 Jan 17;5(1):2100158.

33. Cerqueira L, Oliveira JA, Nicolau A, Azevedo NF, Vieira MJ. Biofilm formation with mixed cultures of Pseudomonas aeruginosa / Escherichia coli on silicone using artificial urine to mimic urinary catheters. Biofouling. 2013 Aug;29(7):829–40.

34. Ikuta KS, Swetschinski LR, Robles Aguilar G, Sharara F, Mestrovic T, Gray AP, et al. Global mortality associated with 33 bacterial pathogens in 2019: a systematic analysis for the Global Burden of Disease Study 2019. Lancet. 2022 Dec;400(10369):2221–48.

35. Zhang S, Bi Y, Li J, Wang Z, Yan J, Song J, et al. Biodegradation behavior of magnesium and ZK60 alloy in artificial urine and rat models. Bioact Mater. 2017 Jun;2(2):53–62.

36. Dev Singh D, Mahender T, Raji Reddy A. Powder bed fusion process: A brief review. Mater Today Proc. 2021;46:350–5.

37. Korei N, Solouk A, Haghbin Nazarpak M, Nouri A. A review on design characteristics and fabrication methods of metallic cardiovascular stents. Mater Today Commun. 2022 Jun;31:103467.

38. ASTM F-1828-97 Standard Specification for Ureteral Stents. 2006.

39. Zelenko N, Coll D, Rosenfeld AT, Smith RC. Normal Ureter Size on Unenhanced Helical CT. Am J Roentgenol. 2004 Apr;182(4):1039–41.

40. Pacheco M, Hassila C-J, Francesco D, Persson C, Lima E, Barros AA, et al. Additive manufacturing of biodegradable Mg1%Y-based ureteral stents: Understanding the corrosion under simulated urinary tract environment. In: 15th Symposium on Biodegradable Metals for Biomedical Applications. Cetraro; 2023.

41. Autodesk. Fusion 360. 2022. Available from: https://www.autodesk.com/

42. Gu Y, Liu Y, Bühring J, Tian L, Koblenzer M, Schröder K-U, et al. Biocompatibility and osteogenic capacity of additively manufactured biodegradable porous WE43 scaffolds: An in vivo study in a canine model. Biomater Adv. 2024 Nov;164:213984.

43. Åhman HN, Larsson L, Wahman C, Mellin P, D'Elia F, Persson C. Higher laser power improves strength but reduces corrosion resistance of Mg WE43 processed by powder bed fusion. Mater Today Commun. 2024 Jun;39:108979.

44. Nienaber M, Yi S, Kainer KU, Letzig D, Bohlen J. On the Direct Extrusion of Magnesium Wires from Mg-Al-Zn Series Alloys. Metals (Basel). 2020 Sep 9;10(9):1208.

45. Deger M, Kapila V, Denys MA, Aridogan IA, Everaert K, Herve F. The impact of movement, physical activity and position on urine production: A pilot study. Int J Clin Pract. 2021 Nov 28;75(11).

46. ASTM G1-03. Standard Practice for Preparing, Cleaning, and Evaluating Corrosion Test Specimens. 2003.

47. Chou D-T, Hong D, Saha P, Ferrero J, Lee B, Tan Z, et al. In vitro and in vivo corrosion, cytocompatibility and mechanical properties of biodegradable Mg–Y–Ca–Zr alloys as implant materials. Acta Biomater. 2013 Nov;9(10):8518–33.

48. Bao G, Fan Q, Ge D, Sun M, Guo H, Xia D, et al. In vitro and in vivo studies on magnesium alloys to evaluate the feasibility of their use in obstetrics and gynecology. Acta Biomater. 2019 Oct;97:623–36.

49. Lovašiová P, Lovaši T, Kubásek J, Jablonská E, Msallamová Š, Michalcová A, et al. Biodegradable WE43 Magnesium Alloy Produced by Selective Laser Melting: Mechanical Properties, Corrosion Behavior, and In-Vitro Cytotoxicity. Metals (Basel). 2022 Mar 10;12(3):469.

50. Chen H-B, Cui L-Y, Liu W-N, Zhang S-C, Wang Y, Li S-Q, et al. In vitro degradation, antibacterial activity and drug release of levofloxacin-loaded coatings on Mg alloy AZ31: The effect of chain length. Prog Org Coatings. 2024 Apr;189:108327.

51. Wang X-M, Lu G-J, Cui L-Y, Liu C-B, Kannan MB, Zhang F, et al. In vitro degradation and biocompatibility of vitamin C loaded Ca-P coating on a magnesium alloy for bioimplant applications. Corros Commun. 2022 Jun;6:16–28.

52. Wilson EV, Bushiri MJ, Vaidyan VK. Characterization and FTIR spectral studies of human urinary stones from Southern India. Spectrochim Acta Part A Mol Biomol Spectrosc. 2010 Oct;77(2):442–5.

53. Channa NA, Ghangro AB, Soomro AM, Nooran L. Analysis of kidney stones by FTIR spectroscopy. J Liaquat Univ Med Heal Sci. 2007;6(2):66–73.

54. Krishnamoorthy N, Dey B, Arunachalam T, Paramasivan B. Effect of storage on physicochemical characteristics of urine for phosphate and ammonium recovery as struvite. Int Biodeterior Biodegradation. 2020 Sep;153:105053.

55. ASTM G1-03. Standard Practice for Preparing, Cleaning, and Evaluating Corrosion Test Specimens. 2003.

56. Haider W, Munroe N, Tek V, Gill PKS, Tang Y, McGoron AJ. Cytotoxicity of Metal Ions Released from Nitinol Alloys on Endothelial Cells. J Mater Eng Perform. 2011 Jul 1;20(4–5):816–8.

57. Bär F, Berger L, Jauer L, Kurtuldu G, Schäublin R, Schleifenbaum JH, et al. Laser additive manufacturing of biodegradable magnesium alloy WE43: A detailed microstructure analysis. Acta Biomater. 2019 Oct;98:36–49.

58. Kim K-W, Choi YH, Lee SB, Baba Y, Kim H-H, Suh S-H. Analysis of Urine Flow in Three Different Ureter Models. Comput Math Methods Med. 2017;2017:1–11.

59. Kim H-H, Kim K, Choi YH, Lee SB, Baba Y. Numerical Analysis of Urine Flow with Multiple Sizes of Double-J Stents. Appl Sci. 2020 Jun 23;10(12):4291.

60. ISO. Biological evaluation of medical devices — Part 5: Tests for in vitro cytotoxicity. 2009.

61. Zhen Z, Liu X, Huang T, Xi T, Zheng Y. Hemolysis and cytotoxicity mechanisms of biodegradable magnesium and its alloys. Mater Sci Eng C. 2015 Jan;46:202–6.

62. Bach C, Kabir MN, Goyal A, Malliwal R, Kachrilas S, Howairis ME El, et al. A Self-Expanding Thermolabile Nitinol Stent as a Minimally Invasive Treatment Alternative for Ureteral Strictures in Renal Transplant Patients. J Endourol. 2013 Dec;27(12):1543–5.

63. Mosayyebi A, Manes C, Carugo D, Somani BK. Advances in Ureteral Stent Design and Materials. Curr Urol Rep. 2018 May 10;19(5):35.

64. Ma Z, Gao M, Na D, Li Y, Tan L, Yang K. Study on a biodegradable antibacterial Fe-Mn-C-Cu alloy as urinary implant material. Mater Sci Eng C. 2019 Oct;103:109718.

65. Shao Y, Zeng R-C, Li S-Q, Cui L-Y, Zou Y-H, Guan S-K, et al. Advance in Antibacterial Magnesium Alloys and Surface Coatings on Magnesium Alloys: A Review. Acta Metall Sin. 2020;33:615–29.

SUPPLEMENTARY INFORMATION

Towards biodegradable Mg-based ureteral stents: a comprehensive in vitro study of two Mg-1Y stent prototypes

Margarida Pacheco[1,2], Francesco D'Elia[3], Maria Nienaber[4], Jan Bohlen[4], Zahra Jafari[5], Sviatlana V. Lamaka[5], Estêvão Lima[6], Alexandre Barros[1,2], Rui L. Reis[1,2], Cecilia Persson[3*]

[1]3B's Research Group—Research Institute on Biomaterials, Biodegradables and Biomimetics, University of Minho, Guimarães, Portugal. [2]ICVS/3B's-PT Government Associate Laboratory, Braga/Guimarães, Portugal. [3]Division of Biomedical Engineering, Department of Materials Science and Engineering, Uppsala University, Uppsala, Sweden. [4]Institute of Material and Process Design, Helmholtz-Zentrum hereon GmbH, Germany. [5]Institute of Surface Science, Helmholtz-Zentrum hereon GmbH, Germany. [6]School of Health Sciences, Life and Health Sciences Research Institute (ICVS), University of Minho, Braga, Portugal

.

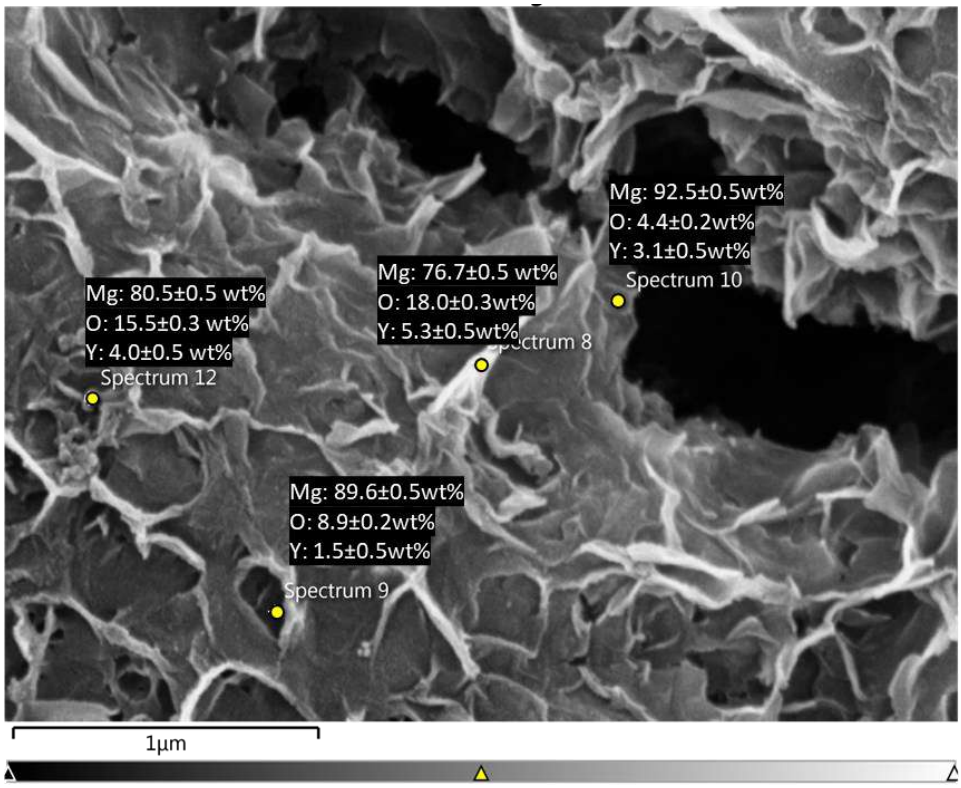


Figure VI S 1 EDS analysis on the SEM image of the AM-mesh cross section, highlighting the composition of the brighter and darker spots of the sample.

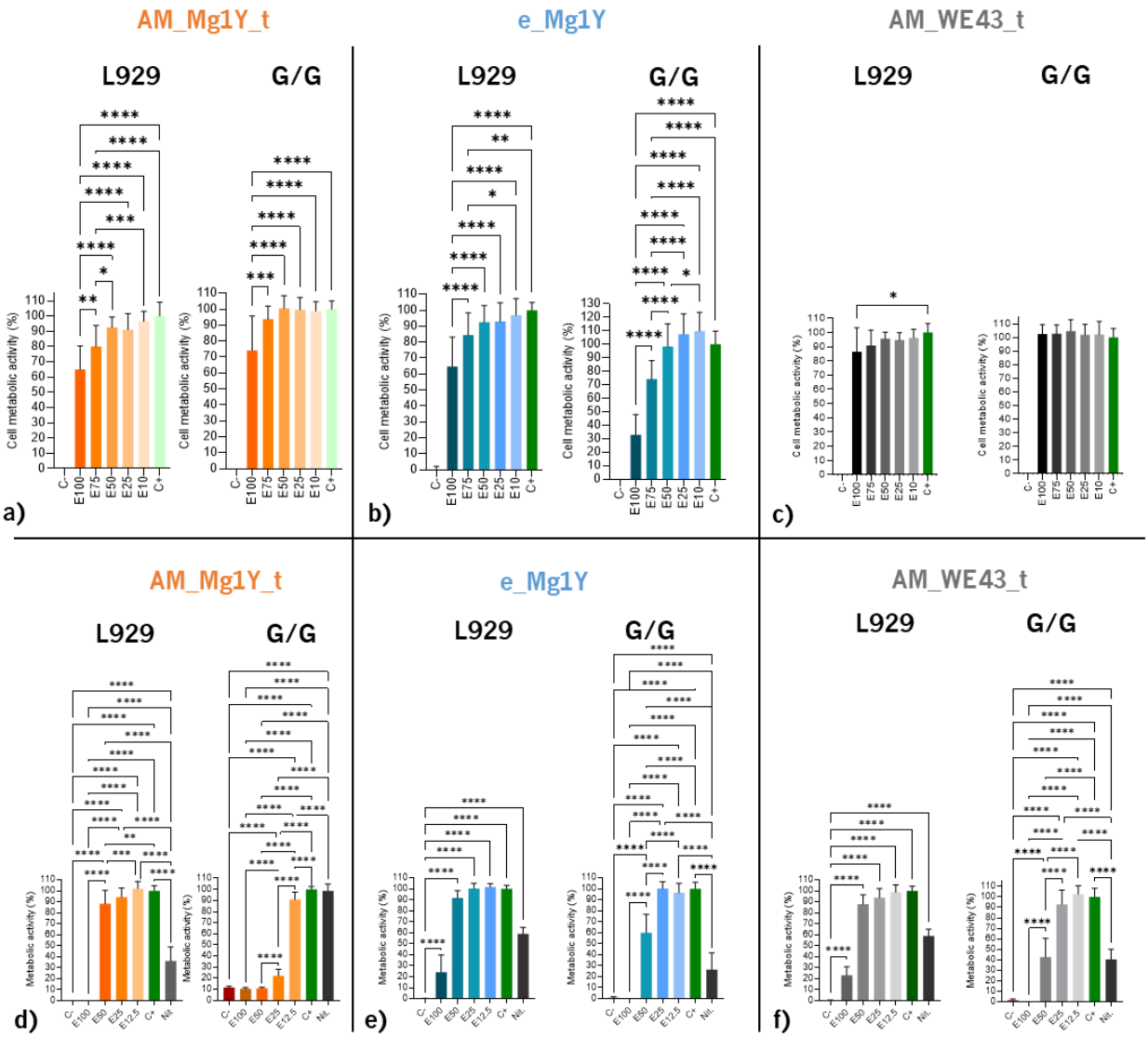


Figure VI S 2 Cell viability assay (MTS) for L929 and G/G cell lines after 24h contact with metal extracts (AM_Mg-1Y_t, e_Mg-1Y and AM_WE43_t), for 24h at a exposed surface area/volume ratio of 27.5 mm^2/ml, a), b) and c) and 300 mm^2/ml, d), e) and f). E100 represents the direct extract (100%) and E75 to E10 the different dilutions of the original extract (75% to 10%). CTR_Nit is the Nitinol control, extract with 100% Nitinol. C+ represents the positive control, cells with cell culture media only and C- the negative control, cells with 25% DMSO.

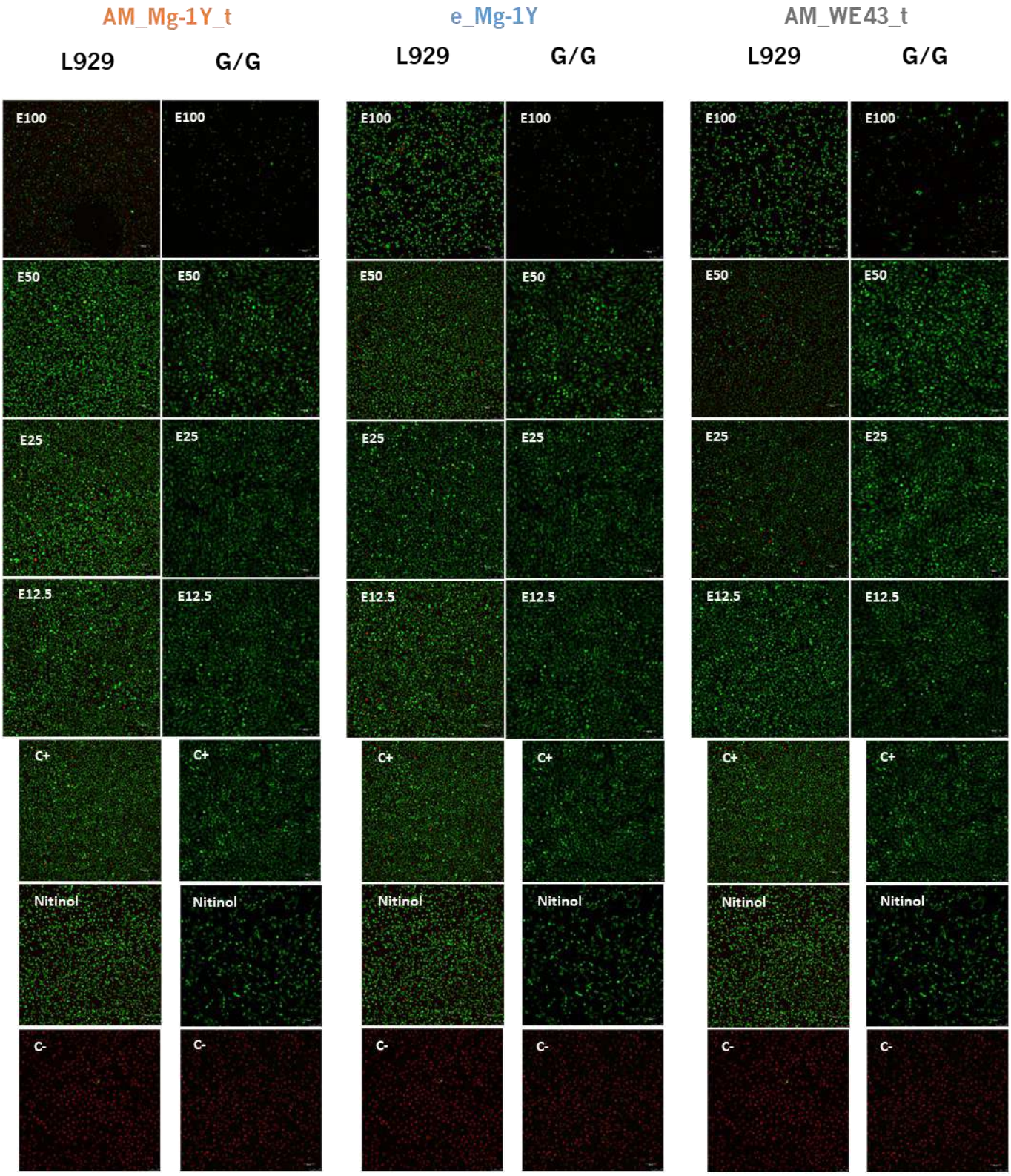


Figure VI S 3 Cell viability assay (Live/Dead) for L929 and G/G cell lines after 24h contact with metal extracts (AM_Mg-1Y_t, e_Mg-1Y and AM_WE43_t), for 24h at a exposed surface area/volume ratio of 300 mm^2/ml. The cels were exposed to direct extract (E100) and several dilutions of the main extract, 50% (E50), 25% (E25) and 12.5% (E12.5). A positive control (C+), without extract and a nevative control (C-), with DMSO were used as well. Nitinol was used as reference material, only with the direct extract.

SECTION 4

GENERAL CONCLUSIONS

CHAPTER VII

GENERAL CONCLUSIONS

Chapter VII

GENERAL CONCLUSIONS AND FUTURE PERSPECTIVES

VII-1. General conclusions

Ureteral stents are indispensable medical devices in urology, widely used to ensure the proper drainage of urine from the kidney to the bladder. These devices are used in the management of several conditions such as urolithiasis, tumor in or near the ureter, providing structural support during ureter reconstruction or healing. Additionally, ureteral stents play a vital role in facilitating healing after surgical interventions on the urinary tract, preventing post-surgical complications such as hydronephrosis or obstruction caused by swelling.

Despite their clinical utility, conventional stents often pose significant challenges, including encrustation, infection, the forgotten stent problem and the need for secondary procedures to remove them. These limitations have driven extensive research into the development of biodegradable alternatives that can provide temporary support and degrade safely within the body, eliminating the need for additional surgeries. Besides, it is expected that biodegradable materials have lower propensity of encrustation and bacteria attachment due to the constantly eroding surface.

Magnesium-based biodegradable stents offer a promising solution, combining the mechanical strength required for effective ureteral support with controlled biodegradability. The use of magnesium and its alloys ensure favorable biocompatibility and has the potential to mitigate common complications associated with traditional stents by the biodegradability and antibacterial properties reported for some Mg alloys. This thesis focuses on the investigation of Mg and Mg alloys for the development of biodegradable metallic ureteral stents (BMUS).

In **Chapter III**, pure Mg and 4 Mg alloys (AZ31, Mg-1Zn, Mg-1Y and Mg-4Ag) in the form of extruded wires were studied in static and simulated dynamic urinary tact conditions, aiming at characterizing the corrosion profile of these materials and respective biocompatibility. The results revealed that in dynamic conditions the corrosion was considerably faster compared static conditions, which highlighted the importance of using dynamic environment to study urinary devices. Furthermore, the alloys exhibited distinct corrosion behaviors: most of them showed severe localized corrosion, indicating higher susceptibility to uneven degradation. In contrast, Mg-1Y displayed a homogeneous corrosion, indicating that it can be a promising candidate as base material for the production of a BMUS. The

subsequent studies started to focus on ureteral stent designs, specially through additive manufacturing (AM) using powder bed fusion laser beam (PBF-LB). In **Chapter IV**, the potential of AM was explored using WE43 powder, a well-established biodegradable metal for biomedical applications. WE43 was chosen for this phase of the study due to its extensive documentation in PBF-LB processes and its proven efficacy in manufacturing medical implants. Representative ureteral stent designs, thin wires (1 mm diameter) and tubes were produced to evaluate the feasibility of this approach. The early stages of corrosion in artificial urine solution (AUS) under dynamic conditions were investigated, revealing that different stent designs exhibited varying corrosion layer coverage, which in turn influenced their corrosion profiles—even though identical printing parameters were employed. Additionally, thinner samples were observed to be less stable and more susceptible to structural pore formation. This work served as base for the following works on AM-based urinary stent designs exploration using Mg-1Y, since this was the alloy with better corrosion performance in the first part of the study. On **Chapter V**, a comprehensive optimization study was conducted to refine the printing process for thin structures, paving the way for the future development of thin-walled ureteral stent designs. This phase compared the use of conventional continuous wave (CW) laser mode with the modulated wave (MW) laser mode, the latter being suggested as a more effective method for printing thin-walled constructs. Various combinations of printing parameters were tested and characterized for both laser modes, with the resulting samples further evaluated for their corrosion behavior in artificial urine solution (AUS). MW-printed samples exhibited slightly rougher surfaces compared to CW samples; however, CW samples demonstrated more inhomogeneous corrosion. These findings suggest that MW laser mode may produce structures with greater stability and improved corrosion resistance. Based on these findings, **Chapter VI** focused on production of thin-walled ureteral stent designs through PBF-LB, leading to the development of a Mg-1Y based meshed tube. The corrosion in dynamic conditions, biocompatibility and antibacterial potential of these samples was investigated. For comparison, Mg-1Y-based extruded wires, coiled into a spring-shaped tube, were evaluated to assess differences in corrosion profiles and biological activity between the two manufacturing techniques and to determine the suitability of each one for the manufacturing of a BMUS. The results revealed that AM-produced samples degraded significantly faster than the extruded coiled ones, although they didn't exhibit severe localized corrosion. In contrast, the extruded coiled samples showed localized corrosion, particularly in the spaces between adjacent coils. Interestingly, while Mg-1Y as-extruded wires displayed even corrosion in earlier studies, the coiling process induced localized corrosion spots. Despite the faster degradation, AM-produced samples demonstrated lower cytotoxicity toward the standard L929 cell line and a cell line isolated from the rat urinary tract, at concentrations

that also exhibited antibacterial activity against *E. coli.* These findings highlight the advantages and limitations of each manufacturing technique. Additive manufacturing (AM) offers considerable design flexibility, making it an excellent tool for exploring and optimizing stent designs. However, the rapid corrosion rates of AM samples remain a significant challenge. On the other hand, extruded coiled samples degrade more slowly but suffer from severe localized corrosion, which poses a risk of stent breakage. Given that the design of coiled stents relies on a single wire, any breakage could result in the stent fracturing into two pieces—a critical issue for clinical applications.

Overall, these results emphasize that not only the material and stent design but also the manufacturing technique play a crucial role in determining the corrosion behavior and performance of biodegradable metallic ureteral stents. This study underscores the significant potential of Mg alloys for the production of biodegradable urinary tract devices, while also demonstrating the importance of tailoring manufacturing methods to optimize their functionality.

FUTURE PERSPECTIVES

Magnesium alloys demonstrate significant potential as base materials for urinary tract implants, owing to their exceptional biocompatibility, corrosion tailorability, and the antibacterial properties reported for some alloys. Despite these advantages, several challenges must be addressed, particularly the rapid corrosion of magnesium. This issue is especially pronounced in AM-produced samples, where post-treatment strategies are necessary to slow the corrosion process. Additionally, as-printed AM-produced samples currently lack the flexibility required for ureteral stents, limiting their immediate applicability.

One approach to address these limitations could involve employing surface treatments or other post-printing modifications to enhance the corrosion resistance and flexibility of AM-constructed stents such as post printing heat treatment.

For extruded coiled wires, while this manufacturing technique provides the required flexibility, localized corrosion remains a critical issue. This localized degradation poses a significant risk of stent failure, as the design relies on the integrity of a single wire. Future work should focus on optimizing the coiling process to mitigate microstructural changes that lead to localized corrosion sensitivity. Enhancing this technique to support alternative designs could also increase its clinical applicability, addressing its current limitation of producing only one type of stent design.

In conclusion, while the results of this study are highly promising, future research should prioritize optimizing both AM and extrusion-based approaches. For AM, the focus should be on post-treatment strategies to achieve improved corrosion resistance and flexibility. For extrusion-based methods, efforts should aim at minimizing the impact of the coiling process on corrosion and exploring ways to diversify design capabilities. These advancements will be crucial to fully unlock the potential of magnesium alloys for biodegradable urinary tract devices.